COMPUTATIONAL FLUID DYNAMICS AND ANALYTICAL MODELING OF SUPERSONIC RETROPROPULSION FLOWFIELD STRUCTURES ACROSS A WIDE RANGE OF POTENTIAL VEHICLE CONFIGURATIONS

A Thesis
Presented to
The Academic Faculty

By

Christopher E. Cordell, Jr.

In Partial Fulfillment
Of the Requirements for the Degree
Doctor of Philosophy in Aerospace Engineering

Georgia Institute of Technology

December 2013

COMPUTATIONAL FLUID DYNAMICS AND ANALYTICAL MODELING OF SUPERSONIC RETROPROPULSION FLOWFIELD STRUCTURES ACROSS A WIDE RANGE OF POTENTIAL VEHICLE CONFIGURATIONS

Approved by:

Dr. Robert D. Braun, Advisor
School of Aerospace Engineering
Georgia Institute of Technology

Dr. Jerry M. Seitzman
School of Aerospace Engineering
Georgia Institute of Technology

Dr. William L. Kleb
Computational Aerosciences Branch
NASA Langley Research Center

Dr. Alan W. Wilhite
School of Aerospace Engineering
Georgia Institute of Technology

Dr. Stephen M. Ruffin
School of Aerospace Engineering
Georgia Institute of Technology

Date Approved:
November 13, 2013

ACKNOWLEDGEMENTS

I would not be the person I am today without the support of my family throughout the years. Through the ups and the downs, the good times and the bad, I always knew that I had strong support behind me. I would need the full length of this dissertation many times over to have enough space to adequately express my gratitude to Mom, Dad, and Amy for everything they've done for me over the years. Thank you all for being there for me every step of the way along this journey.

Thank you to my advisor, Dr. Robert Braun, for the support and assistance over the years. I feel like I've come a long way from the student in your Space Senior Design class to completing this dissertation, and it would not have been possible without your guidance along the way. Even when I questioned my own work, you would not let me get down and continued supporting the path I was on, for which I am extremely grateful. Thank you to Dr. Stephen Ruffin for introducing me to the topic of supersonic retropropulsion during my time as an undergraduate researcher, as well as the support and knowledge passed on about the computational side of my work. Thank you to Dr. Bil Kleb for the support and assistance with FUN3D and using it as my primary analysis tool over the years. Thank you to Dr. Jerry Seitzman for the lessons provided in class as well as the direction for the dissertation. Thank you to Dr. Alan Wilhite for the insight into the systems design aspects of my thesis work.

The Space Systems Design Laboratory has provided an amazing work environment throughout my time here, and I have really appreciated getting to know you all on a personal level too. I would like to thank all of my labmates over the years for the support and encouragement. Thank you to Dr. Ashley Korzun for all the help and support as we

worked in the same research area. Thank you, Allison Hutchings, Scott Martinelli, and Zarrin Chua for being awesome cubemates over the years. Thank you, Brad Steinfeldt, Jenny Kelly, Milad Mahzari, and others for being willing to provide feedback, criticisms, and commendations as my thesis developed and evolved over the years.

I owe particular thanks to a few friends who have been with me throughout my time in school. Thank you, Josh Forrest and Andrew Hardin, for being awesome hallmates in high school and continuing to be great friends throughout my time at Georgia Tech. I do not know how I would have made it through my undergraduate and graduate studies without you both being around. Thank you, Jessica Forrest and Jackie Mitchell, for providing wonderful friendship throughout my time at Georgia Tech. Josh and Andrew may have brought you both into my life, but I am eternally grateful that I have all four of you to lean on.

I would like to extend thanks to the FUN3D development team and to the NASA SRP community. To the FUN3D team, I think by this point that I have interacted with all of you over the years, with all kinds of questions ranging from silly to serious. I am sure you appreciate my finding so many obscure bugs in the code that increased your work load. Thank you for assistance in compiling and running the code, and helping me understand the computational processes to generate my solutions. To the NASA SRP team, it has been a pleasure to work with you all and assist however I am able with furthering NASA's own research into SRP technology. I gained a lot of valuable insight during my internships with you all, interacting with the CFD team, assisting with the wind tunnel experiment, and generally gaining a view of the process by which you all approached your research. It has helped guide my own research in many different ways.

TABLE OF CONTENTS

LIST OF TABLES

LIST OF FIGURES

LIST OF SYMBOLS AND ABBREVIATIONS

A	body reference area, m^2
A_1	nondimensional shock parameter
A_2	nondimensional shock parameter
$A_{i,j}$	matrix for solving source strengths
$\vec{A}$	area vector, m^2
$\vec{A}_i$	area vector for point along barrel shock, m^2
A_{exit}	nozzle exit area, m^2
A/A_{throat}	nozzle area ratio
B	axial density distribution parameter
B_B	body bluntness term
B_S	shock bluntness term
C	barrel shock scaling parameter
C_D	drag coefficient
$C_{D,net}$	net deceleration force coefficient
C_i	constant vector for solving source strengths
$C_{M\alpha}$	static pitch stability derivative
C_P	pressure coefficient
$C_{P,sub}$	pressure coefficient relative to subsonic conditions in panel method
C_T	total thrust coefficient ($T/q_\infty A$)
d	distance from nozzle throat to point along barrel shock, m
d_i	distance from nozzle throat to point along barrel shock, m
d_{throat}	throat diameter, m
dm	differential mass, kg

dr_i	differential radial distance for point on barrel shock, m
ds	differential arc length, m
dt	differential time, sec
dx_i	differential axial distance for point on barrel shock, m
dV	differential velocity, m/s
D	drag, N
D_B	body base diameter, m
g_0	Earth surface gravity, m/s^2
$I_{1\text{-}5}$	terms for solving integral in panel method
$I_{i,j}$	integral term in panel method
I_{sp}	engine specific impulse, sec
L_{cone}	length of conical diverging section of nozzle, m
m	mass, kg
m_{pay}	payload mass, kg
m_{prop}	propellant mass, kg
m_s	structural mass, kg
$\dot{m}$	mass flow rate, kg/s
$\dot{m}_{barrel}$	barrel shock mass flow rate, kg/s
$\dot{m}_i$	mass flow rate at point along barrel shock, kg/s
$\dot{m}_{terminal}$	terminal shock mass flow rate, kg/s
M_{barrel}	Mach number along barrel shock for mass flow rate calculation
M_{edge}	jet edge Mach number
M_{exit}	jet exit Mach number
M_s	Mach number at point along plume arc length
$M_{terminal}$	terminal shock Mach number

M_∞	freestream Mach number
MR	mass ratio
$\vec{n}_i$	normal vector for panel in panel method, m
N	number of panels along surface
P_{barrel}	pressure along barrel shock for mass flow rate calculation, Pa
P_{exit}	nozzle exit pressure, Pa
P_s	pressure along plume arc length, Pa
$P_{terminal}$	pressure before jet terminal shock, Pa
$P_{T,1}$	stagnation pressure behind freestream normal shock, Pa
$P_{T,1,jet}$	stagnation pressure behind jet terminal shock, Pa
$P_{T,jet}$	jet chamber total pressure, Pa
$P_{T,\infty}$	freestream stagnation pressure, Pa
P_∞	freestream static pressure, Pa
q_∞	freestream dynamic pressure, Pa
r	dimensional jet radial coordinate, m
$r_{terminal}$	terminal shock radius, m
r'	scaled barrel shock coordinate, m
r_{exit}	nozzle exit radius, m
r_{ij}	distance between control points in panel method
r_{shock}	bow shock radial coordinate, m
R_{gas}	specific gas constant, J/kg-K
R_{ND}	non-dimensional jet radial coordinate
R_S	bow shock nose radius, m
Re	Reynolds number
Re_c	Reynolds number per unit length

Re_x	Reynolds number at distance along flat plate
s	arc length along barrel shock, m
S_j	length of panel in panel method, m
T	thrust, N
$T_{T,jet}$	jet chamber total temperature, K
$\vec{V}$	velocity vector, m/s
$\vec{V}_{cross}$	crossflow velocity vector, m/s
V_{final}	final velocity, m/s
$\vec{V}_i$	velocity vector at point along barrel shock, m/s
$V_{initial}$	initial velocity, m/s
$\vec{V}_{jet}$	jet exit velocity vector, m/s
$\vec{V}_{\parallel}$	crossflow parallel component of velocity vector, m/s
$\vec{V}_{\perp}$	crossflow perpendicular component of velocity vector, m/s
V_{barrel}	velocity along barrel shock for mass flow rate calculation, m/s
V_s	velocity at point along plume arc length, m/s
$V_{s,i}$	tangential flow velocity in panel method, m/s
V_{sub}	subsonic velocity behind freestream normal shock, m/s
$V_{terminal}$	velocity before jet terminal shock, m/s
x	dimensional jet axial coordinate, m
x_0	bow shock coordinate, axial shock location, m
x_b	bow shock coordinate, axial body location, m
x_c	bow shock coordinate, axial focus location, m
x_i	axial coordinate of point along barrel shock, m
x_j	coordinate of center of panel, m

x_{plate}	flat plate distance for Reynolds number calculation, m
x_{shock}	bow shock axial coordinate, m
X	body fixed coordinate, corresponds to vehicle axis
X_0	body fixed coordinate, axial shock location, m
X_b	body fixed coordinate, axial body location, m
X_c	body fixed coordinate, axial focus location, m
X_j	coordinate of endpoint of panel, m
X_{ND}	non-dimensional jet axial coordinate
y_j	coordinate of center of panel, m
Y	body fixed coordinate, directed out right side of vehicle
Y_j	coordinate of endpoint of panel, m
Z	body fixed coordinate, directed up in pitch plane
α	angle of attack
β_i	angle between normal and subsonic velocity vectors in panel method, rad
γ	ratio of specific heats
δ	turbulent boundary layer thickness
η	nondimensional shock coordinate system
η_{body}	nondimensional shock coordinate for body axial location
θ_0	initial jet expansion angle, rad
θ_{cant}	nozzle cant angle, rad
θ_i	angle between panel and subsonic velocity vector in panel method, rad
θ_{nozzle}	conical nozzle half angle, rad
θ_∞	maximum jet expansion angle, rad
λ	source strength per unit length along surface
μ	dynamic viscosity, kg/m-s

ν	Prandtl-Meyer function
ν_{edge}	jet edge Prandtl-Meyer function
ν_{exit}	jet exit Prandtl-Meyer function
ν_{∞}	maximum jet Prandtl-Meyer function
ξ	nondimensional shock coordinate system
ρ_a	jet shape function scaling parameter
ρ_{barrel}	density along barrel shock for mass flow rate calculation, kg/m^3
ρ_i	density at point along barrel shock, kg/m^3
ρ_s	density at point along plume arc length, kg/m^3
$\rho_{terminal}$	density before jet terminal shock, kg/m^3
$\rho/\rho_{T,jet}$	jet density ratio
φ	jet shape function scaling parameter
φ_{cross}	crossflow deflection angle, rad
$\varphi(x,y)$	velocity potential along surface
Φ_{body_roll}	body roll angle, rad
Φ_{nozzle}	nozzle angular location, rad
Φ_{total}	total nozzle angular location relative to pitch plane, rad
ψ	jet boundary constant
ψ_{∞}	maximum jet expansion solid angle, rad

CFD	Computational Fluid Dynamics
CG	Center of Gravity
DRA	Design Reference Architecture
EDL	Entry, Descent, and Landing
EDL-SA	Entry, Descent, and Landing Systems Analysis

FUN3D	Fully Unstructured Navier-Stokes 3-Dimensional
OML	Outer Mold Line
RANS	Reynolds Averaged Navier-Stokes
RCS	Reaction Control System
SRP	Supersonic Retropropulsion
UPWT	Unitary Plan Wind Tunnel

SUMMARY

For the past four decades, Mars missions have relied on Viking heritage technology for supersonic descent. Extending the use of propulsion, which is required for Mars subsonic deceleration, into the supersonic regime allows the ability to land larger payload masses. Wind tunnel and computational experiments on subscale supersonic retropropulsion models have shown a complex aerodynamic flow field characterized by the interaction of underexpanded jet plumes exhausting from nozzles on the vehicle with the supersonic freestream. Understanding the impact of vehicle and nozzle configuration on this interaction is critical for analyzing the performance of a supersonic retropropulsion system, as deceleration will have components provided by both the aerodynamic drag of the vehicle and thrust from the nozzles.

This investigation focuses on the validity of steady state computational approaches to analyze supersonic retropropulsion flowfield structures and their effect on vehicle aerodynamics. Wind tunnel data for a single nozzle and a multiple nozzle configuration are used to validate a steady state, turbulent computational fluid dynamics approach to modeling supersonic retropropulsion. An analytic approximation to determining plume and bow shock structure in the flow field is also developed, enabling more efficient grid generation for computational fluid dynamics analysis by predicting regions of importance in the computational domain. Results for both the computational fluid dynamics and analytic approaches show good agreement with the experimental datasets. Potential limitations of the two methods are identified based on the comparisons with available data.

Eight geometries are defined to investigate the extensibility of the analytical model and determine the variation of supersonic retropropulsion performance with configuration. These validation geometries are split into two categories: three geometries with nozzles located on the vehicle forebody at varying nozzle cant angles, and three geometries with nozzles located on the vehicle aftbody at varying nozzle cant angles and number of nozzles.

The forebody nozzle configurations show that nozzle cant angle is a significant driver in performance of a vehicle employing supersonic retropropulsion. Aerodynamic drag preservation for a given thrust level increases with increasing cant angle. However, increasing the cant angle reduces the contribution of thrust to deceleration. The tradeoff between these two contributions to the deceleration force is examined. Static pitch stability characteristics are investigated for the lowest and highest cant angle configurations, indicating that the stability performance of a supersonic retropropulsion vehicle is independent of cant angle for forebody nozzles.

The aftbody nozzle configuration results show that removing the plume flow from the region forward of the vehicle results in less interaction with the bow shock structure. This impacts aerodynamic performance, as the surface pressure remains relatively undisturbed for all thrust values examined. Static pitch stability characteristics for each of the aftbody nozzle configurations are investigated; noting that supersonic retropropulsion for these configurations creates insensitivity to center of mass locations near the vehicle axis, while exhibiting a transition point from static stability to instability as a function of this center of mass location along the axis.

CHAPTER I

INTRODUCTION AND MOTIVATION

1.1 Supersonic Retropropulsion

Supersonic retropropulsion (SRP) involves the use of forward facing nozzles to provide deceleration forces during the entry, descent, and landing (EDL) sequence of a trajectory. Generally, SRP is characterized by highly underexpanded plumes that interact with the oncoming freestream flow to create a complex flow field around the entry vehicle. This modified flow field affects the surface pressure along the vehicle, and the subsequent aerodynamic forces generated during this stage of flight [1]. The interaction between the thrust provided by the nozzles and the vehicle aerodynamics varies with vehicle configuration and is difficult to predict.

SRP is of particular importance for the EDL sequence in a low density atmosphere, such as the one experienced at Mars. Due to the thin Martian atmosphere, deceleration occurs lower in the atmosphere, reducing the timeline available for landing maneuvers [2]. All Mars missions to date have relied on Viking heritage technology to provide the necessary deceleration for a safe landing on the surface. There is an upper limit to the mass that can be landed on Mars due to continued use of Viking era technology, which is well below the estimated sizes required for large robotic missions or future human missions [2,3]. Another consequence of sending larger missions is that the landing trajectory may not pass through a flight condition capable of deploying current parachute technology, which prevents those systems from being feasible [2]. This is demonstrated

in Figure 1 where increasing ballistic coefficient results in deceleration lower in the atmosphere than the acceptable flight conditions for current parachute technology.

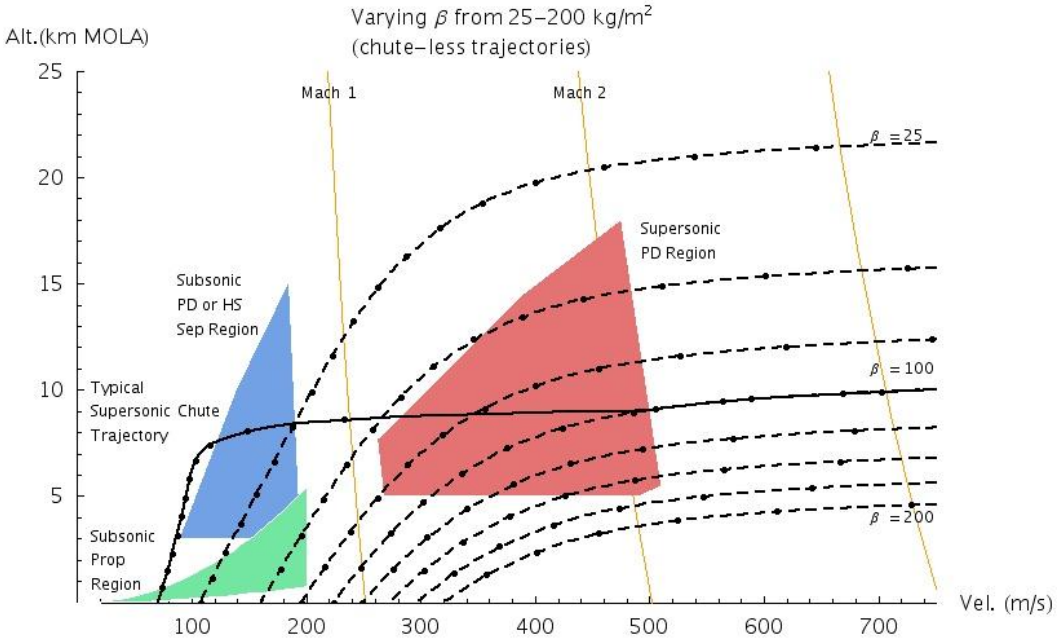

Figure 1: Limitations of current parachute technology for Martian descent [2]

Improvements to deceleration technology are required for landing large missions on Mars [4]. SRP can provide significant deceleration benefits through thrust, at the expense of fuel required to generate the thrust. Understanding the propulsive-aerodynamic interaction of an SRP system is critical to determining the flight implications of employing such a system for deceleration. By increasing the total deceleration force through a combination of thrust and drag contributions, a vehicle can decelerate higher in the atmosphere, allowing for the possibility of a combination of technologies to be used for descent of high mass missions at Mars. An example of this is shown in FIG, where

half of the concepts shown contain SRP to some extent, with three of the options employing both SRP and some other technology for supersonic deceleration.

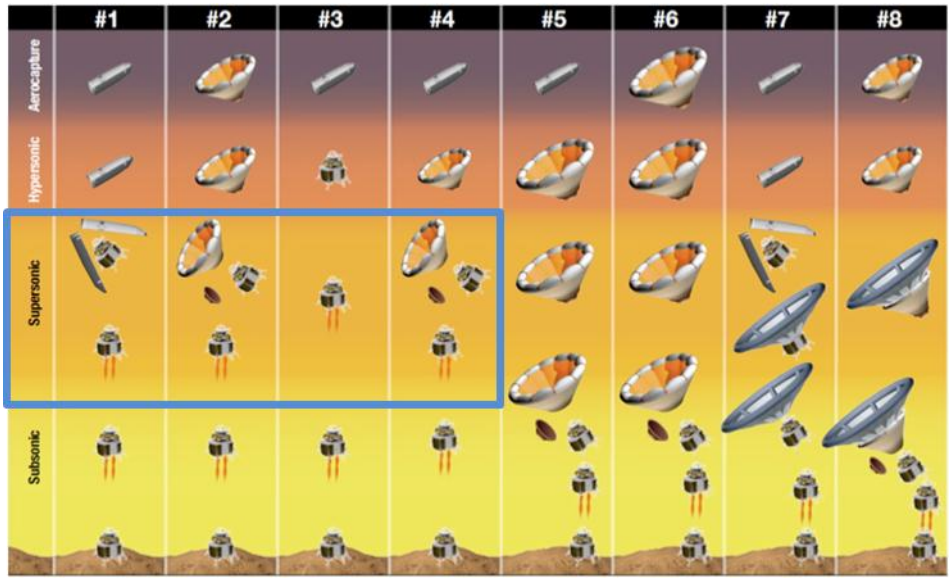

Figure 2: Entry, Descent and Landing Systems Analysis group architectures of interest [3] with supersonic retropropulsion inclusions highlighted in blue

The SRP investigations performed to date have characterized the general flowfield structure and aerodynamics expected for jets exhausting into a supersonic freestream. Currently available SRP data is limited to a few configurations, restricting the conclusions that can be drawn from system and trajectory analysis. The work presented in this dissertation seeks to further the understanding of configuration effects on SRP performance by employing computational approaches to determine flowfield structure and surface pressure characteristics for a variety of design parameters. An analytical method is developed to provide an initial estimate of the expected flow field for an input vehicle design at input thrust conditions, which serves as a precursor to computational fluid dynamics (CFD) analyses. An investigation of the effects that SRP design variables

have on system performance is then performed on novel vehicle configurations. These configurations extend the knowledge of SRP performance characteristics such that configuration can be leveraged to obtain a desired total deceleration.

1.2 Flowfield Structure

Design of systems employing SRP will require detailed knowledge of the variation of flowfield structure and its impact on SRP system performance. As the freestream and thrust conditions vary, the plume and bow shock structure will be impacted. This section provides a more detailed discussion of the components of an SRP flow field, as well as how nozzle configuration is expected to impact each feature. The thrust level from each engine will affect the extent of plume expansion from the nozzle exit. The freestream condition and the entire plume structure will determine how the bow shock forms during SRP. The overall flowfield structure will determine the pressure on the vehicle, resulting in a coupling between thrust and aerodynamics to achieve the desired total force for deceleration.

1.2.1 Plume Expansion

Nozzles will be designed to achieve a desired thrust force to apply to the entry vehicle, which is dependent on the flow conditions at the nozzle exit. These conditions will also determine the flow field created by the exhausted jet flow based on the total pressure of the engine and the freestream conditions into which the jet exhausts. An ideal nozzle would be designed to perfectly expand the jet flow such that the pressure at the exit exactly equals the ambient pressure into which the nozzle exhausts. If the nozzle expands

the flow more than is required, then the flow is deemed overexpanded and the flow separates inside the nozzle. If a nozzle does not sufficiently expand the jet flow, then the pressure at the exit is higher than the ambient environment and the flow is deemed underexpanded [5]. While a static engine design will only have ideal expansion at a certain flight condition, underexpanded flow is more desirable than overexpanded as the shock structure is external to the nozzle and performance is impacted less by the nonideal expansion [5]. These underexpanded flow fields are likely to exist in SRP flows due to the large thrusts required for deceleration and the relatively low ambient pressure into which the nozzles are exhausting. The schematic shown in Figure 3 represents the underexpanded plume structure generally expected for SRP systems [1].

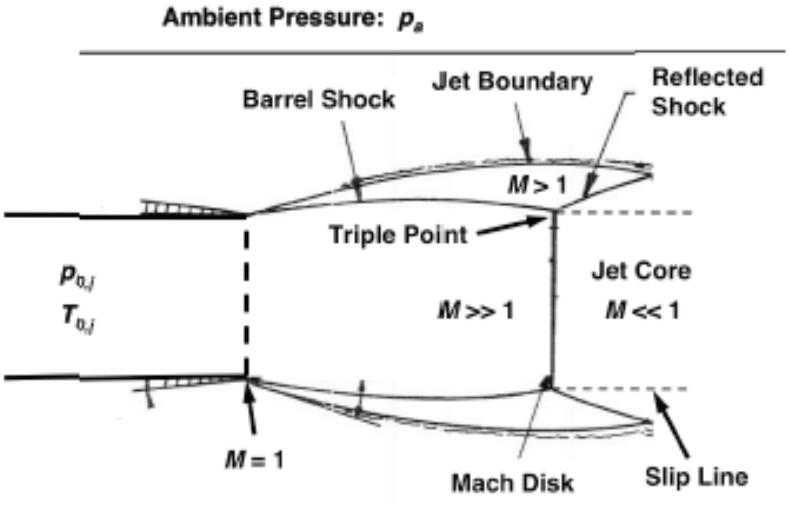

Figure 3: Axisymmetric underexpanded plume structure seen in SRP flow fields [1]

Since the flow is underexpanded, an expansion fan occurs at the nozzle exit where the flow continues to expand past the nozzle exit [6]. A barrel shock forms near the plume boundary, separating the ambient flow from the expanding jet exhaust [7]. A terminal

shock forms at the extent of the plume expansion which reduces the total pressure of the jet flow to equal that of the ambient environment [1,8,9]. The characteristics as shown in Figure 3 hold true for high thrust nozzle flow exhausted directly into the supersonic freestream from the nose of the vehicle. Low thrust conditions, defined by the ratio of nozzle exit pressure to freestream pressure, demonstrate a markedly different plume structure [10]. For these plumes, the distinct terminal shock does not form. Rather, the plume is elongated and the flow dissipates through mixing. Schematic representations of these two types of flows are shown in Figure 4 [10].

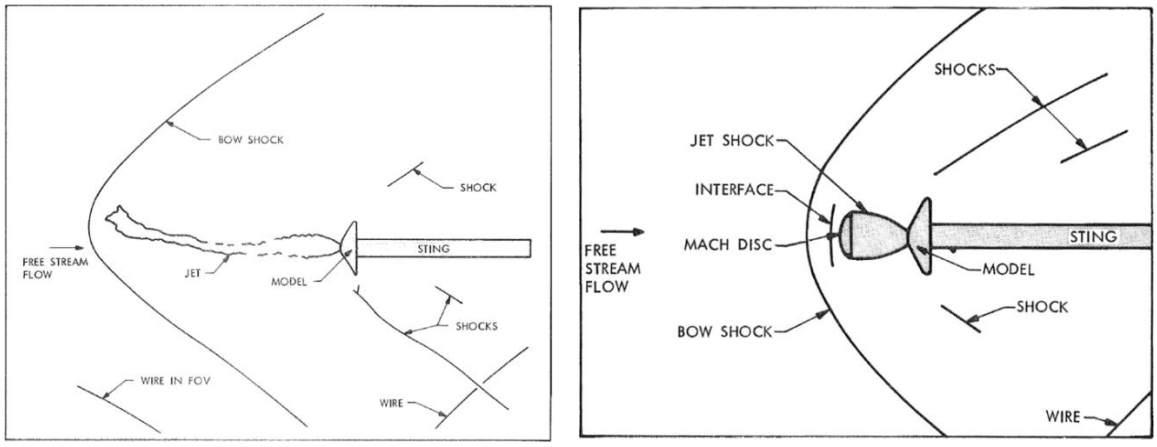

Figure 4: Single nozzle flow regimes for low thrust (left) and high thrust (right) [10]

For plumes that do not meet the flow criteria resulting in the basic axisymmetric shape shown in Figure 3, perturbations to the plume will create a more complex structure. Primarily, these perturbations result from the nozzle exhausting at an angle to the local flow path, creating what is in essence a jet in crossflow. This behavior can result from a combination of nozzle canting, vehicle angle of attack, or nozzle location away from the nominal vehicle stagnation point. Much of the work done to analyze a jet in crossflow

focuses on the effects of the plume on the pressure on the plate from which it exhausts, though a characterization of the flow structure of the plumes has also been performed. The presence of a crossflow results in a plume whose inboard side is compressed as the jet flow reacts to the increased pressure in this region. The plume is turned such that the jet is directed more downstream, in line with the local flow path [11-16]. These same types of effects are seen for SRP flow fields, where nozzles located away from the vehicle axis can exhibit a modified inboard shape due to the presence of the high pressure in this region [1,10]. A schematic representation of the flow field for a peripherally located nozzle is shown in Figure 5, demonstrating that the plume is turned outboard for these configurations [18]. As plumes grow larger due to an increased expansion of the jet flow, two possible effects can occur for configurations with multiple plumes. Plume interaction refers to plumes which have expanded near each other such that the boundary conditions along each plume boundary are altered due to the presence of plumes affecting the flow between each other. The plumes remain distinct; however, their boundaries may be perturbed due to the close proximity of other plumes. Plume coalescence refers to plumes actually intersecting each other and creating a single, joined plume rather than distinct, individual plumes.

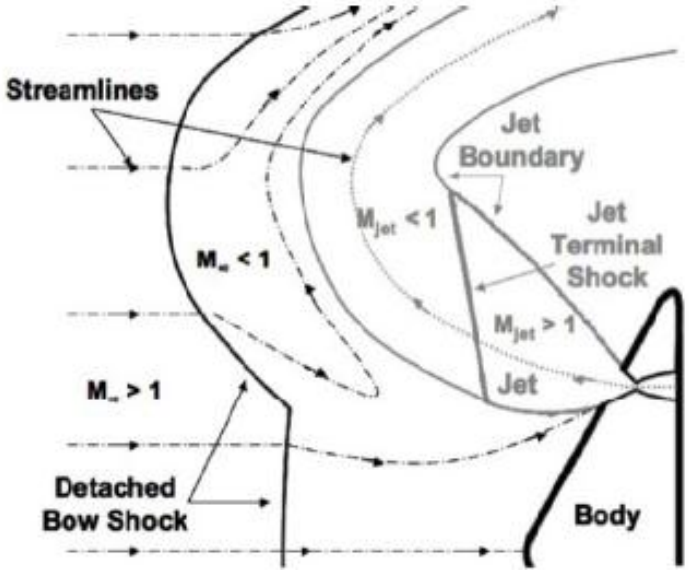

Figure 5: Notional flow structure for a peripherally located nozzle [18]

1.2.2 Bow Shock

For supersonic flow, the presence of an obstruction such as an entry vehicle causes a bow shock to form so that the flow can decelerate forward of the vehicle [19]. The plume structure for a SRP system creates additional complexities for the formation of the bow shock. Each jet plume acts like an additional surface in the flow field, combining with the aeroshell shape to create a larger effective obstruction to the freestream supersonic flow. The bow shock formation responds to this effective obstruction by forming differently than it would for a vehicle with no jet exhaust. Plumes forward of the vehicle cause the bow shock to form further upstream of the entry body. The extent of this upstream distance depends on the size of the plumes, as there must be enough space for the exhaust flow to decelerate and turn around the vehicle. Additionally, plumes located more outboard on the vehicle create a larger effective cross sectional area of obstruction. Depending on the plume structure, this can result in a wider bow shock, or a shock

structure where plumes appear to penetrate the shock and cause structures similar to that sketched in Figure 5.

Another aspect of bow shock formation for SRP systems is the formation of a contact surface between the jet exhaust and the freestream flow, which each flow regime follows without crossing. The turned jet exhaust flowing along this surface defines an effective obstruction seen by the supersonic freestream. Figure 6 demonstrates the formation of this surface for a single nozzle exhausted directly into the freestream from the nose of the entry body. The jet exhaust decelerates through the Mach disk of the plume then turns to flow axisymmetrically back around the vehicle. The freestream flow turns in response to the effective obstruction created by the exhaust flow, treating the contact surface as if it were a solid impediment to the flow [18]. For peripheral configurations, this surface becomes more complex as the jet flow does not flow axisymmetrically around the vehicle. Instead, the contact surface can be thought of as a combination of the jet flow boundary and the vehicle surface that defines the physical boundary of the obstruction to the freestream supersonic flow.

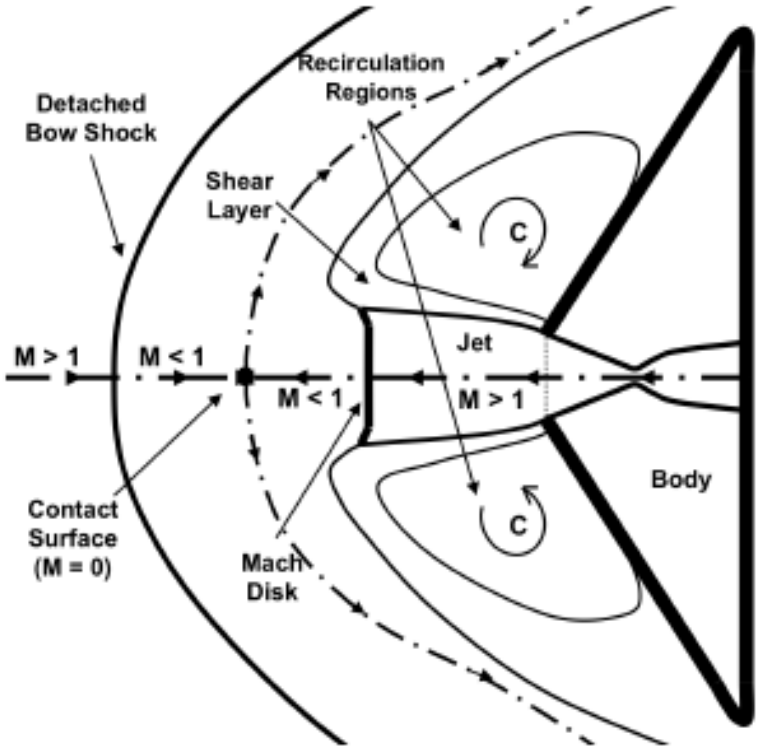

Figure 6: Single nozzle schematic demonstrating contact surface and turned jet flow [18]

1.2.3 Propulsive-Aerodynamic Interaction

The presence of the flowfield structure created by the jet exhaust from an SRP system alters the pressure along the surface of the vehicle. As the plume expansion and subsequent flow field varies with nozzle configuration and thrust provided by the engines, this creates a coupling between the thrust and aerodynamic components of the forces and moments created on the vehicle during SRP. For a single nozzle located at the nose of the vehicle, the vehicle is effectively shielded from the freestream flow, and the resultant pressure decreases with increasing thrust [1,10]. In terms of net deceleration force on the vehicle, thrust provides the majority of the force, even for relatively low thrusts, as the aerodynamic drag component is significantly reduced. For a three nozzle peripheral configuration at low thrust values, when thrust is approximately equal to the

aerodynamic drag with no jets, pressure is preserved inboard of the nozzles [10]. Since the jet flow turns outboard, the vehicle surface inboard of the nozzle exits is still exposed to freestream flow and the pressure in this region is not reduced. Thus aerodynamic drag is preserved for some thrust coefficients, as shown in Figure 7. This type of behavior is similar to the results for a jet in crossflow, where the crossflow can be thought to originate at the stagnation point on the vehicle surface. The pressure forward of the jets, or in this case inboard, is higher than that seen outboard of the plumes [11-16].

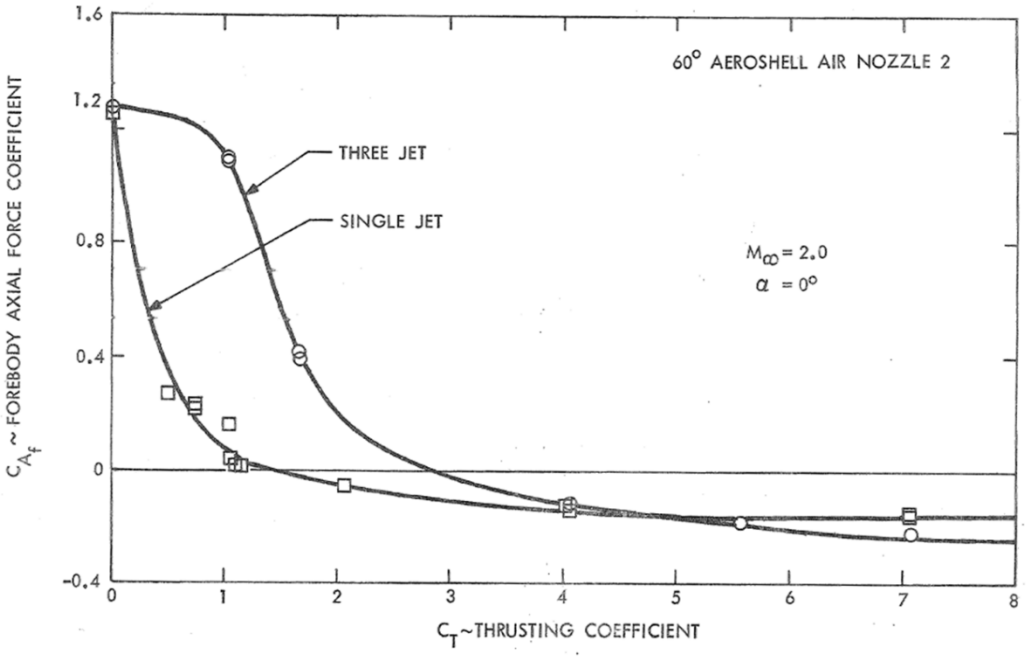

Figure 7: Drag comparison of single and three nozzle configurations from the Jarvinen and Adams wind tunnel experiment [10]

Aerodynamic drag is limited by the freestream conditions, as only so much pressure is available to be preserved on the vehicle. Thrust, being governed by the engine design, is not limited to the same degree and can be taken to much higher values than the possible

aerodynamic contributions to vehicle dynamics [17]. For large thrust values, vehicle dynamics will be driven primarily by thrust performance of the SRP system. Depending on the degree of aerodynamic preservation for given thrust conditions and nozzle configuration, an aerodynamic contribution to forces and moments may exist that would need to be accounted for during system design. Effectively modeling the SRP flow environment for a wide range of freestream conditions, nozzle configurations, and thrust conditions allows for further understanding of the interaction between the propulsion system and the resultant vehicle aerodynamics.

1.3 SRP Modeling Efforts

To model the flow fields that exist for a vehicle employing SRP, multiple simulation methods have been examined. Wind tunnel testing on scale models allows for visualization of the actual flowfield structure using schlieren or shadowgraph images. Pressure ports on the body allow for data to be taken to characterize the effects of configuration and thrust levels on the aerodynamics of the vehicle. In addition to characterizing the SRP environment, these datasets provide a validation database against which other modeling techniques can be compared. CFD approaches numerically solve the underlying flow equations to generate solutions of the expected flow structure and vehicle aerodynamics. To ensure accurate modeling of SRP flow fields, the results are validated against the known wind tunnel datasets to build confidence for generating computational simulations of geometries for which no physical data exists. CFD solutions can require a significant amount of time to achieve the desired results, so analytical approaches provide a lower fidelity estimate of flow properties. These analytical methods

also need to be validated, but can provide more information prior to higher fidelity CFD approaches. This information could be used to create a better initial computational grid, reducing the time required to converge on a reasonable solution.

1.3.1 Wind Tunnel Experiments

Wind tunnel investigation of SRP has occurred during two distinct time periods. First, prior to selection of Viking parachute technology, SRP was of interest as an entry technology. More recently, as the limits of current parachute technology are being approached, SRP has again emerged as a potential deceleration technology for Martian entry [2,18]. Thrust effects in these wind tunnel efforts are primarily reported as a function of thrust coefficient (C_T) as defined in Eq. (1). Note that this is a force coefficient with the same normalization as is seen for drag coefficient (C_D) rather than a value dependent on the nozzle chamber pressure.

$$C_T = \frac{T}{q_\infty A} \tag{1}$$

Retropropulsion work prior to the Viking era primarily focused on a single nozzle exhausting into a supersonic freestream. Much of this work focused on low thrust coefficients, noting a generally unsteady behavior of the plume structure. Pressure taps on the various test models confirmed that pressure on the vehicle decreases for this configuration, even at these low thrust values [20-23]. For higher thrusts, a transition to a steadier flowfield structure resembling that shown in Figure 4 is noted. The ratio of jet

total pressure to freestream total pressure and the relative size of the nozzle exit to the body diameter affect the transition conditions between the two flow regimes. The experimental results note a sharp change from the elongated plume which penetrates the bow shock to the shortened plume with a Mach disk for a single jet exhausting into a supersonic freestream [24-26].

In addition to the single nozzle experiments, some tests focused on configurations with multiple nozzles. Peterson and McKenzie investigated a configuration with four nozzles clustered near the axis of a semiellipsoid body with a flat face. It was noted that varying flow regimes existed with abrupt changes in the flow field occurring for varying thrust. The flow field transitioned from small plume expansions, to a large bow shock standoff distance, and a return to a nearer bow shock standoff. The presence of the jets caused a significant reduction in surface pressure, relatively independent of thrust level [27]. These nozzles resemble the behavior of a single nozzle configuration as the plumes coalesce into a single combined structure. Keyes and Hefner investigated a configuration with three nozzles completely outboard of the blunted forebody. For increasing jet total pressure, equivalent to an increase in thrust, an increase in drag coefficient is noted [28]. This shows that nozzles located near the periphery of a vehicle have the capability of preserving pressure inboard of the nozzles.

Jarvinen and Adams performed an extensive wind tunnel experiment to compare a single and a three nozzle configuration [10]. The single nozzle tests covered C_T ranging from 0-7 and exhibited both the unsteady flow field at low thrust conditions and the steady flow field for higher thrusts, consistent with the results discussed previously. The three nozzle configuration tested in this experiment had the nozzles located at 80% of the

base radius with a total thrust coefficient ranging from 0-7. Lower thrust conditions with small plumes exhibited the same type of surface pressure preservation noted by Keyes and Hefner, while continuing to increase thrust eventually caused significant reduction in surface pressure [10].

Recent wind tunnel experiments have built on the information learned from the historical experiments to provide more insight into the SRP flow field. Daso et al. investigated a centrally located nozzle on an Apollo capsule, noting the same types of flow structure transitions seen previously [29]. Additionally, radiative heat transfer effects were noted; with high thrust conditions providing a cooling effect to the model [29]. McDaniel et al. investigated the use of SRP at hypersonic speeds, finding similar aerodynamic performance trends for both a single and four nozzle configuration as were seen at supersonic freestream conditions [30]. Additional investigations on a similar model by Codoni et al. showed the differences in flow field of a sonic and supersonic nozzle, with the supersonic nozzle resulting in a larger flowfield structure [31]. Berry et al. performed experiments in the NASA Langley Unitary Plan Wind Tunnel (UPWT) and NASA Ames UPWT at various conditions on a model capable of a single nozzle, three nozzle, and four nozzle configuration [32-34]. The thrust conditions reported for the single nozzle configuration only exhibit the steady flow structure. The three nozzle configuration had nozzles located at 50% of the base radius, which showed surface pressure preservation for some thrust conditions. Due to the proximity of the nozzles to each other, significant coalescence was noted between the plumes which limited the amount of pressure preservation possible and provided unsteadiness in the flow field. The four nozzle configuration, consisting of a combination of the single and three nozzle

configurations, provided potential steadying benefits to the flow field for some low thrust conditions. These wind tunnel results were used as baseline cases for the computational efforts described in Section 1.3.2 and for uncertainty analysis to determine potential errors from a range of sources [35].

1.3.2 Computational Fluid Dynamics Studies

The wind tunnel results described above demonstrate the effects of SRP on a subscale vehicle. For mission planning, where multiple vehicle and nozzle configurations may be of interest, a quicker and more cost effective means of analyzing SRP flow field is required. Computational fluid dynamics provides a means of simulating resultant flow structures and vehicle aerodynamics for a wide range of SRP conditions at the expense of computational time. Additionally, varying assumptions can be made within the governing equations of a CFD simulation that will affect the time required to generate a solution as well as the flow properties that will be captured. The wind tunnel results provide a database against which CFD can be validated to ensure that the proper physics are sufficiently captured within an SRP flow field. Past computational work has focused on generating varying fidelity solutions for SRP configurations, including inviscid and viscous flow as well as steady and unsteady solutions.

Studies of SRP using inviscid flow demonstrated potential limitations of this assumption while generating reasonable approximations of SRP flow fields. Bakhtian and Aftosmis showed that inviscid solutions could capture the surface pressure effects for the single and three nozzle Jarvinen and Adams geometry [36]. Korzun et al. noted a potential unsteadiness associated with inviscid analysis of SRP as compared to laminar

and turbulent flow assumptions for the same geometries [1]. Inviscid and laminar solutions for a single nozzle configuration showed significant asymmetry in the steady state flow field, which could be due to unsteadiness associated with the flow assumptions. Viscous flow assumptions provided increased dissipation to the flow field that resulted in smoother plume boundaries and increased steadiness in the flow field [1]. This is also apparent in another study by Bakhtian and Aftosmis, where the geometries of Berry et al. were investigated. The inviscid solutions showed significant unsteadiness that is not seen in all of the comparison viscous solutions; however, the underlying plume structure was still somewhat captured [37].

Viscous CFD approaches account for turbulence that may exist within an SRP flow field. Analyses on the Jarvinen and Adams geometries indicated that steady, turbulent solutions generally captured the flow structure and pressure trends seen in the wind tunnel experiment. Low thrust conditions on a single nozzle demonstrated potentially unsteady behavior, and the more complicated flow field for the three nozzle configuration also limited the potential for the steady flow assumption. There may be time varying properties and unsteady behavior that would not be captured by a steady state analysis [1,38,39].

Using a time-accurate CFD approach allows for the simulation to capture unsteady characteristics of the flow field at the expense of more time to generate a solution. Alkandry et al. investigated both single and multiple nozzle configurations using a reacting flow CFD code and found aerodynamic performance trends in agreement with the expectations of the wind tunnel experiments [40,41]. Using the wind tunnel models of Berry et al., many time accurate CFD analyses were performed. Kleb et al. demonstrated

potential effects from sting modeling and turbulence modeling on the simulations [42]. Korzun et al. investigated all nozzle configurations of this test series at similar thrust levels, showing good qualitative agreement, though the three nozzle configuration showed poorer agreement than the other geometries [43]. Schauerhamer et al. demonstrated the effects of angle of attack on SRP simulations and found that variations in turbulence modeling affected levels of unsteadiness seen in the solutions. This in turn affected the ability to create appropriate time averages for comparison with experimental data [44]. Zarchi et al. demonstrated that capturing different time-varying properties from various codes did not affect overall time-averaged comparisons between CFD results and experimental results [45].

1.3.3 Analytical Approaches

While high fidelity CFD solutions or wind tunnel tests for SRP systems are required to evaluate configurations late in the design process, leveraging more rapid analytical approaches can provide information to better drive these investigations early in the process. For example, a first order understanding of the expected plume structure of a given SRP configuration allows for more efficient grid generation for CFD by predicting regions in the flow field which should contain higher grid resolution. This can potentially reduce the number of grid iterations required to reach grid convergence and generate an acceptable solution, reducing the amount of computational time required. Many analytical approaches have been performed on underexpanded plumes, namely for investigating high altitude performance at Earth or plume shape in a vacuum [46-50]. The

models themselves are not designed for forward facing rockets, as would be seen in an SRP system, though the assumptions are potentially extensible to that scenario.

Work by Alden described the jet flow behind a missile using inviscid flow models to determine the boundary of the plume. A normal shock was assumed at the termination of the plume to equate the jet exhaust pressure with freestream and an asymptotic expansion was used for radial velocity components. Additionally, a second-order differential equation was used to model the full idealized plume surface [46]. A series of papers reported approximations of underexpanded jet structures by assuming radial flow from a source at the nozzle exit. Albini used a homogenous shock layer to approximate the boundary between the jet flow and ambient environment [47]. Hubbard extended the concept to account for laminar flow in the shock layer [48], and Boynton showed that the results for both methods show good agreement with numerical calculations [49]. Hill and Draper took a similar approach, assuming nearly radial flow far from the nozzle with a mass flux inversely proportional to the radius squared. Using density decay along the plume axis, constant density contours were generated to define the plume boundary [50]. Charwat assumed that the flow along the boundary was nearly isentropic and that the jet edge Mach number is constant along this boundary. Using Prandtl-Meyer expansion at the nozzle exit, this Mach number was calculated and the shape of the boundary was integrated for given input conditions [51]. Using a similar method, Sibulkin and Gallaher determined the axial density distribution as a function of radius by allowing the jet flow to undergo a Prandtl-Meyer expansion to an infinite Mach number [52]. Salas investigated a method to determine the entire plume structure, including the possibility of multiple Mach disks present in the jet structure [53]. Abbett expanded on plume

formation to define when a Mach disk is expected to form in addition to determining its location by determining where the triple point of the plume should exist [54].

Finley used a momentum balance to estimate flow properties and vehicle aerodynamics for a single nozzle configuration [55], which Korzun extended to apply to multiple nozzles [56]. This extension to multiple nozzles assumes that the plumes from each nozzle in the configuration coalesce to form a single effective plume, as shown in Figure 8. This assumption allows for the calculation of the surface pressure caused by the effective single plume structure. This assumption is true for nozzles in close proximity to each other, or in configurations similar to the Jarvinen and Adams three nozzle, peripheral configuration at high thrust. This flow assumption is not true for nozzles spaced far from each other and operating at thrust conditions with plumes that do not coalesce into a single plume.

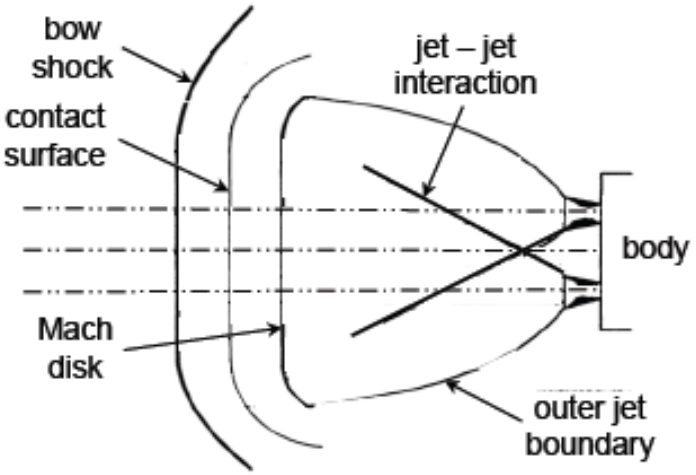

Figure 8: Plume coalescence into a single effective plume used by Korzun to approximate surface pressure and vehicle aerodynamics for multiple nozzle configurations [56]

Bakhtian assumed an oblique shock cascade to model possible drag augmentation associated with SRP as shown in Figure 9; however, that analysis was independent of SRP configuration [57]. This model assumes that local plume shocks distinctly form forward of the jet exhaust and that the pressure effects from the shock-shock interactions at the intersection of these local plume shocks are consistent across the entire vehicle. The formation of these plume shocks is not directly tied to an input SRP configuration, which may not exhibit this plume structure depending on the nozzle location and the thrust value output from each engine. The shock-shock interaction also does not drive the entire surface pressure of the vehicle, as different regions are exposed to different flow regimes along the surface.

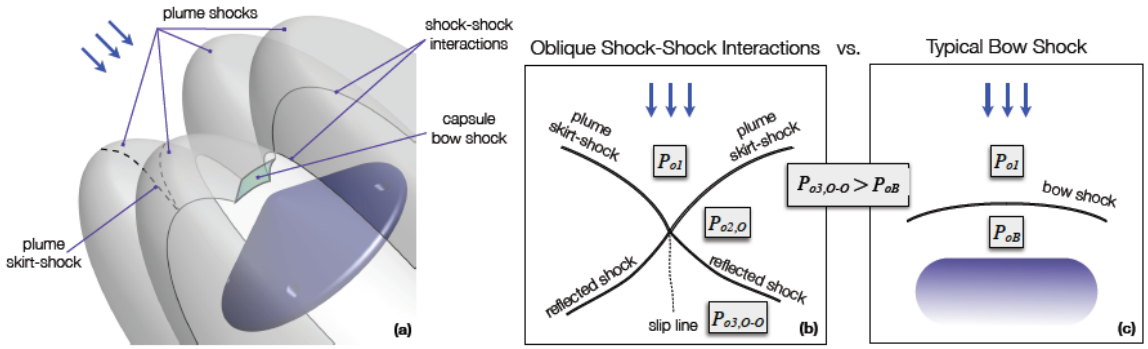

Figure 9: Flow field assumptions for Bakhtian's approach to modeling drag augmentation in SRP systems [57]

Work by Skeen extended the model of Bakhtian to attempt to account for the variation in flow regime along the vehicle surface by investigating a single CFD solution and defining regions on the vehicle which exhibit certain pressure effects [58], as shown in Figure 10. For example, the oblique shock cascade of Bakhtian is only applied in the regions between the nozzle exits, defined as regions 4 and 5 in Figure 10. While this

approach begins to consider the effects of flowfield structure on surface pressure, no flowfield structure is actually modeled in this approach. The regions along the vehicle are for a single operating condition (C_T = 1), for a single configuration (4 peripheral nozzles), and based on a CFD pressure distribution rather than an extensible analytical definition.

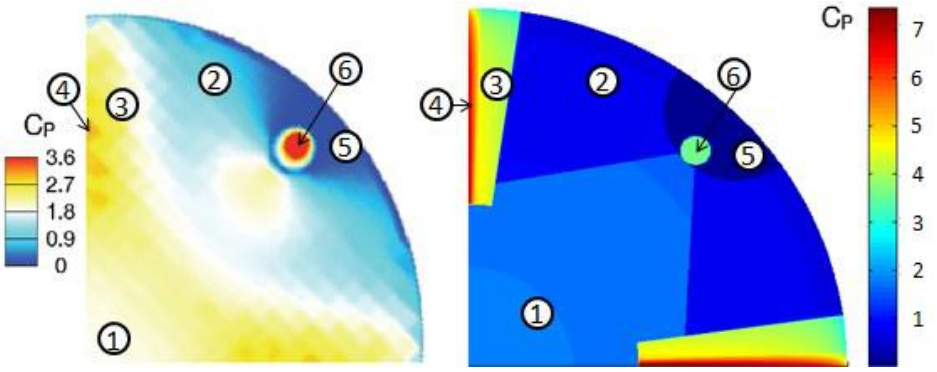

Figure 10: Surface regions proposed by Skeen for C_T = 1 on a four nozzle configuration [58]

Jarvinen and Adams performed some basic comparison of analytical approaches to modeling the flowfield structure with schlieren imagery from their wind tunnel results. The method of Hill and Draper was used to define the nozzle flow and terminal shock location, and the method of Charwat was used to define the jet boundary. The bow shock and contact surface were also approximated as part of this analysis [10]. A sample comparison from the report is shown in Figure 11. By defining the contact surface as an approximate shape, such as a hemisphere as proposed by Romeo [59] or Gilles [60], methods similar to those proposed by Love [61] or Van Dyke [62] were used to estimate the location and shape of the detached bow shock forward of the jet structure. This analysis was limited to a single nozzle configuration, with no discussion of extensibility to multiple nozzle configurations.

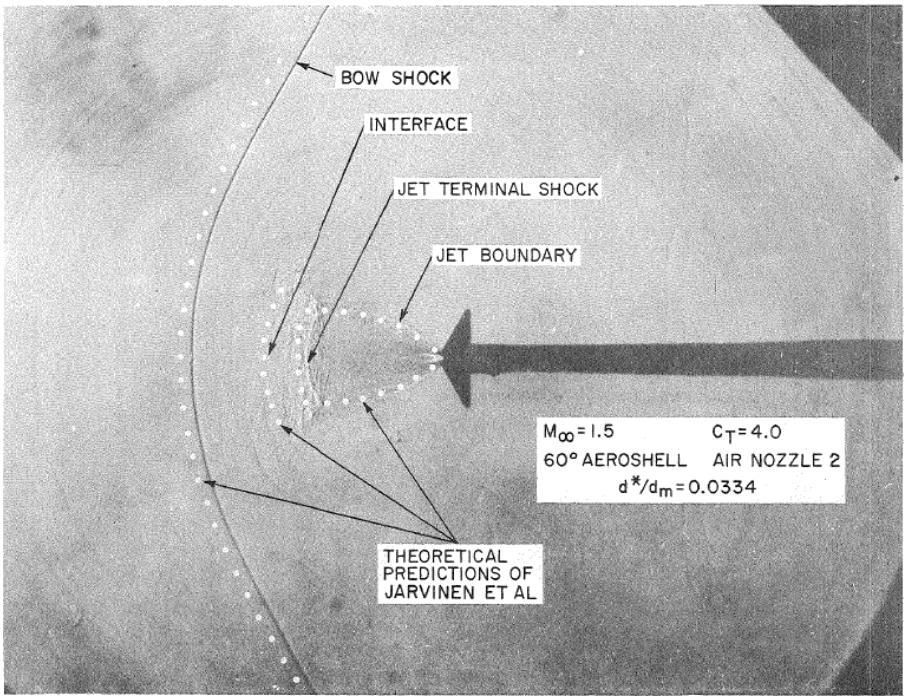

Figure 11: Application of analytical methods to approximating SRP flowfield structure for a single nozzle configuration [10]

1.4 System Design and Vehicle Integration

Design of a vehicle employing SRP will depend on a wide range of factors. As nozzle configuration and performance are varied and constrained due to system integration implications, the resulting propulsive-aerodynamic interaction inherent in an SRP system will vary. Identifying and understanding the effect of system design choices on the overall performance of SRP is key to designing an effective deceleration system.

Within the NASA Mars Design Reference Architecture (DRA) 5.0, a fully propulsive descent was considered, including thrust during supersonic flight, but this option was deemed to have too low of a payload mass fraction due to the large propellant mass

requirements [63]. Future work by the Entry, Descent, and Landing Systems Analysis (EDL-SA) group identified eight potential architectures for Mars EDL. One of these architectures was a derivative of the fully propulsive option considered for DRA 5.0, with a total of four out of the eight architectures involving some form of SRP [3]. The design of these architectures hinged on analysis of SRP performance relative to other potential technologies for supersonic descent [64,65].

1.4.1 Trajectory Effects

Fundamentally, SRP is a technology that could be used to enhance the deceleration characteristics of an entry vehicle. As the thrust required to achieve an acceptable trajectory varies, the design of the SRP system will be impacted. Lower thrust implies smaller nozzles and less propellant. Since the aerodynamic characteristics of the vehicle are coupled to the flowfield structure and thrust generated by the nozzles, understanding how a particular vehicle configuration affects the propulsive-aerodynamic interaction is important to matching vehicle performance to a desired trajectory.

Simulations performed as part of the EDL-SA study did not model aerodynamic drag dependence on thrust during SRP, noting an increase in arrival mass to accommodate the propellant requirements for descent [66]. Work done by Korzun and Braun analyzed potential trajectory effects due to SRP by maximizing the final landed mass of an entry vehicle [67]. Cases were run with no drag preservation (thrust provides all of the deceleration force), assumed drag preservation percentage, and a thrust dependent model based on the wind tunnel results of Jarvinen and Adams [10]. The results showed that preserving aerodynamic drag reduces the propellant requirements of the SRP system by

allowing a lower thrust to achieve the same total deceleration force, though the mass savings were only a few percent of the total vehicle weight. Using the thrust dependent drag model, high mass systems tended to operate at conditions at which no drag would be present due to the large thrusts required [67]. Steinfeldt et al. examined SRP as a candidate deceleration technology by empirically modeling the propulsive-aerodynamic interaction and maximizing mass to the surface. SRP architectures required a higher mass due to the propellant requirements, and increasing thrust available allows for SRP solutions to exist for larger entry masses [68].

Terminal descent guidance using propulsive deceleration could be thought to extend into the supersonic phase of flight [69]. Studies by Christian et al. [70] allowed for gravity turn descent to initiate during supersonic flight for configurations that did not employ parachutes, resulting in a lower payload mass fraction due to the increased propellant requirements. Propellant mass fraction was reduced for larger arrival masses, indicating that propulsive descent may scale better for larger missions [70]. Additional descent considerations, such as Smart Divert use propulsive descent to redirect vehicle motion to land in different locations [71]. In Ref. [71], divert was initiated at Mach 0.8, but that could be extended to higher Mach numbers. During supersonic flight, effects of the propulsive-aerodynamic interaction need to be considered, as well as the configuration and its divert capabilities. SRP behavior has also been investigated as a drag modulation device for hypersonic entry, with Grenich et al. noting that relatively low jet flow rates could be used to sufficiently alter drag characteristics of the vehicle at hypersonic speeds [72]. The potential for guided landing of reusable rocket stages has been investigated by SpaceX for the Falcon launch vehicles, where the first stage

propulsion system could be reignited at supersonic conditions to perform thrusted guidance to safely return the launch vehicle stage for reuse [73].

1.4.2 Nozzle Configuration

Trajectory design gives useful information for determining the thrust levels required to achieve a given mission design. Using the thrust requirements, nozzle configuration and design can be performed. Factors such as number of nozzles and nozzle cant angle will impact the performance necessary from the SRP system to follow a given trajectory. More nozzles implies that the thrust from any individual engine would be reduced, resulting in a smaller engine size. However, that size reduction is offset by the need for more engines. Many past studies have investigated empirical engine sizing with mass and volume being linearly dependent on nozzle thrust [67,68,70]. Generally, in this type of analysis, an increase in the number of nozzles results in a larger total mass due to the constant term in the linear sizing estimate being multiplied over multiple engines. However, lower individual thrust levels result in smaller plumes per nozzle, which has benefits for the propulsive-aerodynamic interaction during SRP. Another approach to mass sizing was used by EDL-SA, where response surface equations were used to approximate mass models for configurations employing SRP. Empirical data was also used to determine the size of various structural supports for the SRP system [74].

In addition to nozzle thrust considerations, orientation and location of the engines affect performance of the SRP system. As was shown in the Jarvinen and Adams wind tunnel experiment, nozzles located outboard on a vehicle have the potential to preserve aerodynamic drag for some thrust levels [10]. While an SRP system may not be designed

to explicitly take advantage of drag preservation, consideration of other aspects of system design, such as packaging constraints, could drive a vehicle toward configurations where outboard engine placement is beneficial. All wind tunnel testing to date has investigated nozzles exhausting opposite to the freestream flow. This results in zero thrust loss as the total force is directed for deceleration. Canted nozzles orient the thrust vector and the resulting plume structure in a different direction, resulting in thrust losses. A parametric study by Bahktian and Aftosmis detailed how cant angle could affect the ability of SRP to preserve pressure. It was noted that canting nozzles outward creates a bow shock which is normal over a larger expanse of the vehicle, decreasing aerodynamic drag loss on the forebody [36]. Thus, there may be design approaches that reduce the losses inherent to a system with canted nozzles.

As nozzle location, number, and configuration are determined for a given system, there is the possibility that the nozzle exits will be scarfed if the nozzle is mounted flush to the aeroshell. This type of configuration is common in the wind tunnel experiments described previously [10,32,33] as well as in reaction control systems (RCS) on entry vehicles [75-79]. Scarfed nozzles exhibit more complex flow paths than axisymmetric nozzles and result in thrust aligned off-axis from the nozzle, as demonstrated by Lilley using the method of characteristics [80].

Nozzle configuration is inherently tied to vehicle design, as packaging constraints affect the locations where nozzles can be placed and cant angles at which the nozzles can be set. The Dragon capsule under development by SpaceX, for example, locates the nozzles on a conical aftbody at a cant angle [81,82]. These nozzles have aerodynamic housings surrounding each engine, such that a more complex outer mold line is created

than the scarfed and integrated nozzles seen in the wind tunnel experiments and on other vehicle configurations.

1.4.3 Force and Moment Effects

The deceleration force provided by the SRP system is fundamentally tied to the propulsive-aerodynamic interaction of the plume structure and freestream flow, with the possibility of both aerodynamic and thrust contributions to the net deceleration force [17]. The thrust contribution to deceleration depends on nozzle design as well as the cant angle of the nozzles. By canting the nozzles such that the flow is not directed parallel to the vehicle axis for zero angle of attack, a cosine loss will reduce the contribution of thrust to deceleration. Some component of the thrust vector for each nozzle will create a side force. For a symmetric nozzle distribution with symmetric thrusting, a zero net side force results. An asymmetric nozzle distribution or differential throttling can create scenarios where some side force is generated, providing out of plane control to the SRP system. The presence of plumes alters the flow paths of the decelerated freestream which affects the aerodynamic contribution to drag as discussed in Section 1.2.3 for SRP configurations with nozzles on the forebody. Work on RCS engines showed that this type of flow modification also exists for engines located on an aftshell [75,77,78], as might be seen for an SRP configuration on a slender vehicle.

For static pitch stability, the derivative of the pitching moment coefficient with respect to angle of attack ($C_{M\alpha}$) needs to be less than zero. For blunt bodies such as sphere-cones, the entry vehicle generally exhibits static pitch stability [83-88]. For more slender vehicles, the stability characteristics have a dependence on the location of the

center of gravity (CG), as the vehicle transitions from statically stable to unstable in pitch motion [68,87,88]. The ability of the vehicle to reach trim conditions, where the net moment on the vehicle is zero, at a given angle of attack is also important for vehicle control. Steinfeldt et al. showed that a 70° sphere-cone is generally insensitive to near-axial CG location for the vehicle to be capable of reaching trim conditions, while a slender ellipsled shows a strong sensitivity to CG location [68] as shown in Figure 12. Static pitch stability and ability of the vehicle to trim are both necessary to ensure that the entry vehicle performs as expected.

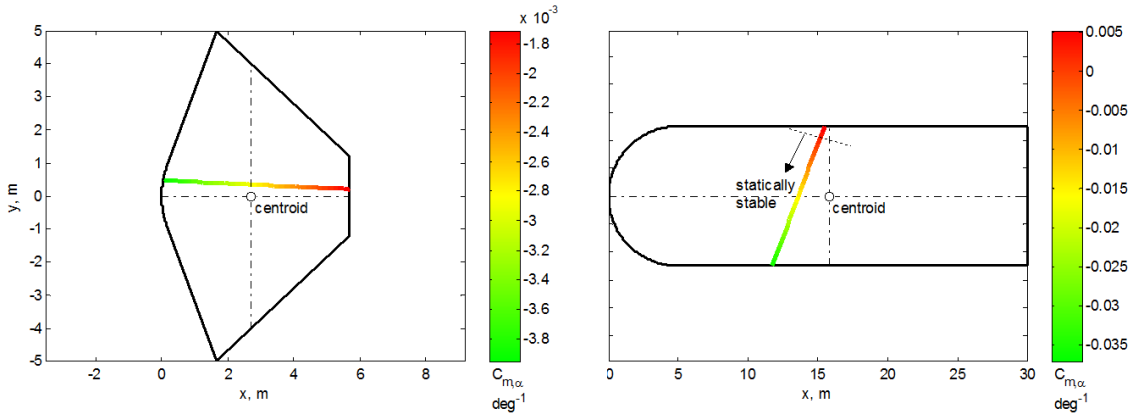

Figure 12: Example CG trim lines for blunt (left) and slender vehicles (right) [68]

1.5 Study Overview

1.5.1 Research Goals

Performance of supersonic retropropulsion is governed by the propulsive-aerodynamic interaction of the resultant plume structure from exhausting jets into a supersonic freestream. Thrust provided by the engines and the surface pressure distribution created

by the decelerated freestream results in vehicle forces and moments. The presence of jet plumes within the flow field alters the aerodynamic characteristics of the body, creating a coupled effect between thrust and aerodynamic contributions to the net forces and moments during SRP. Location of the nozzles on the vehicle and the resulting jet plumes have a significant impact on the degree of interaction between the plume structure and the vehicle surface pressure.

Past investigations into supersonic retropropulsion across all types of modeling efforts have been limited to small variations in vehicle and nozzle configuration, primarily focused on single nozzle configurations. The few multiple nozzle configurations examined tend to demonstrate significant plume interaction, with the potential for plume coalescence to occur at high thrust values. The primary goal of this dissertation is to extend the analysis of SRP to a wider range of possible configurations across both CFD and analytical analysis methods. SRP configurations variables such as number of nozzles, nozzle location, and nozzle cant angle are varied across eight configurations to determine variability in SRP performance with configuration. Past analytical models have been limited to configurations which exhibit a particular shock structure or a single effective plume structure. This dissertation advances the state of the art by providing an analytical model for investigating configurations which do not exhibit the flowfield structures assumed in past work.

1.5.2 Chapter Layout

Chapter II of this dissertation demonstrates the capabilities of steady state CFD analysis by using FUN3D to capture relevant flow physics associated with SRP. Two

configurations have been investigated: a single nozzle and a three nozzle configuration. The resulting CFD simulations are compared to existing wind tunnel data. Solutions covering a range of thrust conditions on each configuration at zero angle of attack are examined to identify key features in the SRP flow field. Variations in SRP performance with thrust and grid properties are investigated to generate reliable SRP simulations.

Chapter III describes an analytical approach to estimating the components of a SRP flow field, including both the plume structure and the resultant bow shock. Each nozzle creates a plume which is defined using a determination of the terminal shock standoff distance for that plume as well as a calculation of the plume barrel shock. An effective hemispherical obstruction to the local freestream flow is created for each plume which can be used to define the local bow shock structure forward of each nozzle. A model of the free shear layer in the plume relies on basic turbulent shear layer approaches which have been modified to account for the barrel shock as an effective surface. An approximation of the crossflow deflection angle for each plume takes into account the fact that each nozzle exhausts into a local crossflow that creates perturbations on the plume structure.

Chapter IV discusses the design of validation geometries for the analytical model which cover a wide range of potential SRP configurations to examine the extensibility of this model. Eight geometries are used for validation, with nozzle location, number of nozzles, nozzle cant angle, and vehicle shape varied amongst the configurations. Comparison of the analytical flowfield structure with CFD solutions for each geometry at various thrust coefficients and angles of attack is performed, with the CFD simulations used as truth data for validating the analytical model.

Chapter V presents the flowfield structure and aerodynamic performance variation for configurations which have nozzles located on the forebody of a blunt entry vehicle at various nozzle cant angles. The total deceleration force is examined for each configuration, taking into account both aerodynamic drag contributions and thrust contributions with losses due to nozzle canting. Static pitch stability performance and trim capabilities for two configurations are also examined.

Chapter VI presents the flowfield structure and aerodynamic performance variation for configurations with nozzles located on the aftbody of an entry vehicle. These configurations exhibit more of a slender vehicle shape, and variations in both nozzle cant angle and the number of nozzles are examined. Total deceleration force as a function of thrust coefficient and static pitch stability characteristics as a function of angle of attack are found for each configuration.

1.5.3 Computational Code Description

The computational fluid dynamics work in this dissertation is performed using FUN3D as the analysis tool. FUN3D is a NASA developed fully unstructured Navier-Stokes 3-dimensional flow solver [89]. The code can solve both the Euler and Reynolds Averaged Navier-Stokes (RANS) equations under either compressible or incompressible perfect gas assumptions. A second order, node based finite volume discretization with implicit time stepping is used to solve the flow for a given grid. A variety of upwind flux functions, limiters, and turbulence models are available. A description of the relevant computational properties used for the solutions shown in this dissertation is included in each chapter for the solutions shown therein.

CHAPTER II

COMPUTATIONAL FLUID DYNAMICS AS A SUPERSONIC RETROPROPULSION ANALYSIS TOOL

2.1 Methodology

In order to confidently apply CFD to the analysis of supersonic retropropulsion, solutions must be validated against existing experimental data. The following validation efforts are based on the experimental results of Jarvinen and Adams [10]. A twofold approach has been taken to demonstrate the effects of grid properties on the computational solution for a range of thrust coefficients. Preliminary solutions demonstrate the effects of grid resolution and exit plane location on both single and three nozzle configurations. These results provide guidelines to generate higher resolution grids to investigate the effect of varying thrust coefficient on both configurations. For the single nozzle configuration, the thrust coefficient range covers both expected flowfield structures, the long jet penetration and the blunt flow interaction, to determine if both types can be modeled effectively on the same grid. For the three nozzle configuration, the thrust coefficient range extends from low thrust to a level high enough for the jet plumes to coalesce. The effects on flowfield structure and surface pressure are investigated for each configuration and thrust value.

2.1.1 Vehicle Geometries

For both configurations, the forebody and nozzle geometries used in the computational solutions are identical to the Jarvinen and Adams wind tunnel models [10]. The single

nozzle configuration, shown in Figure 13 below, is a 60° sphere-cone with a base radius of 2". The nozzle has a 15° cone angle and an exit diameter of 0.5". In the experimental setup, the exhaust gas is supplied by a line running through the sting apparatus. To simulate the presence of the sting, a cylinder has been appended to the back of the vehicle. This cylinder is not as long as the sting in the experiment, but should serve to provide a more representative flow field aft of the vehicle than if no sting is included. The full length of the supply line is also not modeled in the computational geometry. Rather, a short cylindrical plenum is placed prior to the converging section of the nozzle. The jet total pressure and temperature can be provided at the inflow boundary to set the thrust for each run condition.

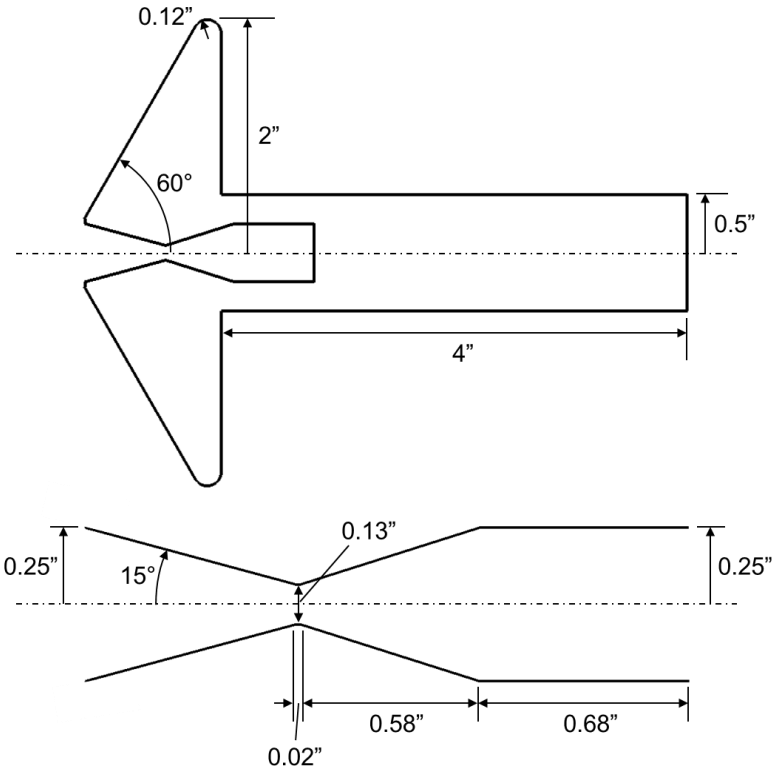

Figure 13: Single nozzle geometry dimensions used to generate CFD simulations

For the three nozzle configuration, as shown in Figure 14, the forebody is a 60° sphere-cone with a 2” base radius. Each nozzle centerline is located at the 80% radial location (1.6”) and the three nozzles are equally spaced around the vehicle. The nozzles are scarfed for this configuration, as the nozzle axis is not perpendicular to the surface. The cone angle for each nozzle is 15°. In the wind tunnel experiment, each nozzle shared a common supply line from the sting with the plenum casing exposed to the flow field. Rather than try to model the complicated flow field around each nozzle casing, a cylindrical aftshell has been placed around the nozzle plena to simplify the geometry exposed to the flow field. Each nozzle is given its own inflow boundary, where total temperature and pressure determine each nozzle’s thrust value.

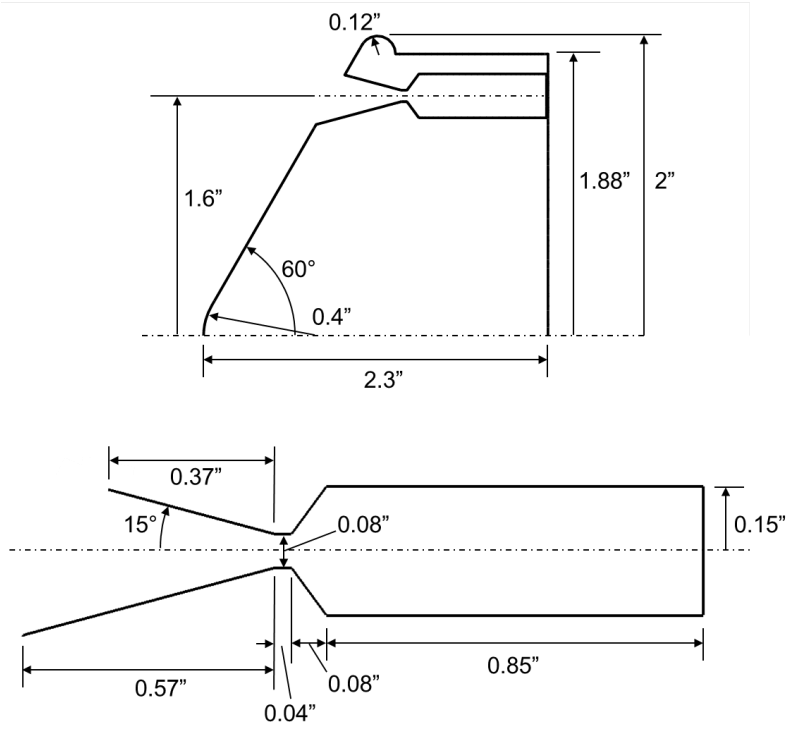

Figure 14: Three nozzle geometry dimensions used to generate CFD simulations

2.1.2 FUN3D Flow Parameters

Freestream flow conditions are taken from the wind tunnel data and input as farfield boundary conditions within FUN3D [89]. Freestream temperature is not explicitly stated in the experimental report, and as such has been set to 173.4 K, a value consistent with other CFD efforts on the same geometry [38]. The wind tunnel report does give freestream Mach number and total pressure for each run. This is converted into a Reynolds number per grid unit for input into FUN3D. For the preliminary solutions, the grids have been built in units of millimeters. The later solutions have grids with units of meters. Thus two Reynolds numbers are required, as shown in Table 1.

Table 1: Freestream flow inputs for CFD simulations

Property	Freestream Value
Mach Number	2
Temperature	173.4 K
Total Pressure	2 psia
Reynolds Number	1589.88 mm^{-1}
Reynolds Number	1589877 m^{-1}

The jet flow is established based on inflow boundary conditions within FUN3D. The flow solver enforces subsonic flow normal to the inflow plane for a given pressure and temperature. These boundary conditions are input into FUN3D via ratios of jet total pressure and temperature to freestream static pressure and temperature, respectively. Run conditions from the wind tunnel report are recorded in terms of thrust coefficient, which need to be converted to the corresponding pressure and temperature conditions. Isentropic

relations allow for determination of the required jet stagnation pressure to generate a given C_T value. For peripheral configurations, C_T from the experimental report represents a total thrust for all three nozzles. Jet temperature does not directly affect the thrust coefficient, and is not provided in the wind tunnel dataset. Jet total temperature has been set to 294 K, consistent with prior computational efforts on these models [38]. The input pressure ratios for each configuration and run condition are shown below in Table 2. When possible, the flow conditions are set to match data points within the experimental results. Additional runs are included to fill in the cases which were not experimentally investigated to determine the continuity of flow field and aerodynamic trends for varying thrust.

Table 2: Jet inflow boundary conditions for the single and three nozzle configurations

C_T	Single Nozzle $P_{T,jet}/P_\infty$	C_T	Three Nozzle $P_{T,jet}/P_\infty$
0.47	712.4	1.0	1504.0
0.75	1131.8	1.7	2556.9
1.05	1581.2	3.0	4512.1
2.00	3004.3	4.0	6166.5
3.00	4502.3	5.0	7520.2
4.04	6060.2	6.0	9024.3
5.00	7498.3	7.0	10678.7
6.00	8996.3	8.0	12032.3
7.00	10494.2	9.0	13536.4
8.00	11992.2	10.0	15040.4
9.00	13490.2		
10.00	14988.2		

Each solution shown has been generated using local time stepping within FUN3D. Thus, time evolution of the flow field is not determined, but rather a steady state solution is shown for each thrust value. All solutions are calculated assuming turbulent flow using the LDFSS flux function with the Van Albada limiter and the Menter-SST turbulence model. These settings are consistent with previous SRP investigations [38]. Convergence is determined by a leveling of the residuals with iteration history and investigation of the flowfield structure to ensure that it is unchanging. For the preliminary single nozzle solutions, the flow solver is set to use first order spatial differencing due to issues encountered in establishing the flow fields. All other solutions use second order spatial differencing.

2.2 Preliminary Investigation of Grid Properties

2.2.1 Grid Generation

The preliminary grids for both configurations have been generated using Gridtool and VGrid. A fully tetrahedral mesh with anisotropic boundary layer cells is generated throughout the computational volume. For the single nozzle configuration, the preliminary grids have the exit plane located directly on the shoulder of the vehicle. This was done since the primary flowfield structures are forward of the vehicle, and it was thought that the aft flow would be unimportant in determining forebody surface pressures and plume structures. However, this creates an ill-posed exit plane boundary condition as will be shown in Section 2.2.2. Scaling parameters within Gridtool and VGrid have been used to create four levels of grid resolution from the same cell source locations around the single nozzle geometry. Sources along the vehicle surface and a linear source along

the axis of the jet concentrate cells in the plume region and near the forebody. The cell sizes increase with distance from the vehicle. The computational boundaries are identical for all four grids. The total node count for each grid as well as the thrust values run on each are shown below in Table 3. The thrust levels of interest for these grids focus on conditions which have available experimental data for comparison. Initially, a sweep of C_T values was run on grid 1 to examine the effects of varying thrust on the flowfield structure and surface pressures. Increasingly fine grids were run on a select number of cases to examine the effects of grid resolution on the solutions.

Table 3: Grid node count and thrust conditions for each preliminary single nozzle grid

Grid	Number of Nodes	C_T Values Run
1 (coarse)	0.30×10^6	0.47, 0.75, 1.05, 1.50, 2.00, 4.04, 5.50, 7.00
2	0.40×10^6	0.75, 1.05, 2.00, 4.04
3	0.55×10^6	0.75, 1.05, 2.00, 4.04
4 (fine)	1.63×10^6	1.05, 4.04

A comparison of the differences in grid resolution for these preliminary single nozzle configuration grids is shown in Figure 15, with the grids built in units of millimeters. As Gridtool and VGrid generate the computational mesh throughout the entire domain as a single component, there is no planar boundary to clearly denote triangular sides of the cells. Rather, the entire volume has tetrahedral cells filling out the computational domain, and these cells are interpolated onto the *X*-*Z* plane shown in Figure 15. From grid 1 to grid 4, the increase in cell resolution is clearly visible, as the cells become more densely packed in the expected plume region. This increase in the number of cells near $Z = 0$

forward of the vehicle is the primary driver in the increase number of cells shown in Table 3.

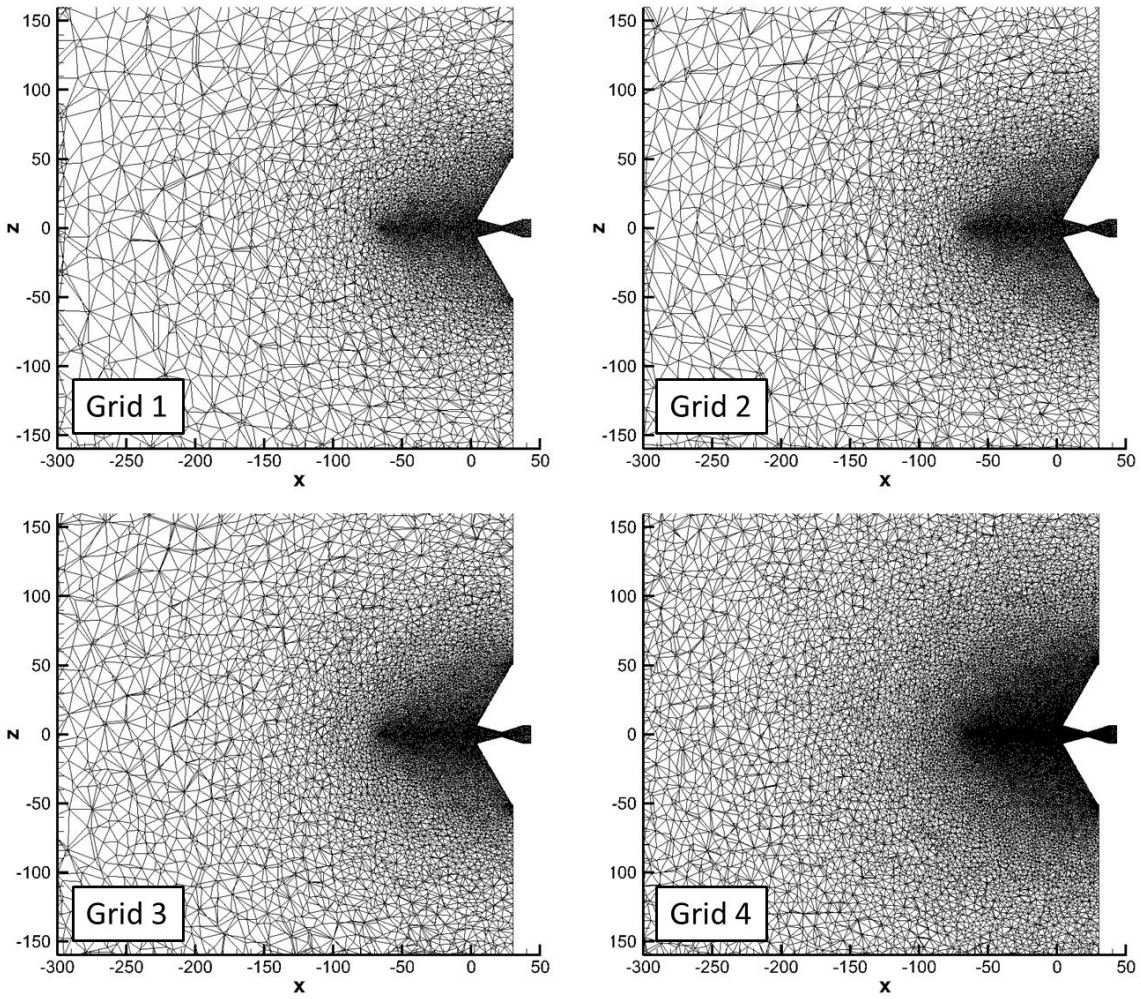

Figure 15: Comparison of preliminary single nozzle configuration grid resolutions

For the three nozzle configuration, four preliminary grids are created to examine the effects of exit plane location on the solution. Extending the exit plane further aft of the vehicle allows for more of the wake region to be captured within the computational domain, which can potentially affect the flow solution around the vehicle. The wake

region is of particular importance for a configuration with peripheral nozzles as the apparent body size to the freestream flow is larger, creating the potential for a longer wake region than would ordinarily be seen for the vehicle alone. The cell size source locations and parameters are unchanged between the first three grids in order to keep their cell sizes relatively similar, though grids with a further aft exit plane will have more total cells since the computational domain is larger. The fourth grid does have an altered cell source to provide more resolution in the plume region. Due to the advancing front method used to generate the grids, the cell structure is not identical between the grids for each exit plane location. Table 4 shows the exit plane locations as measured from the nose of the vehicle in body diameters, the number of nodes, and thrust values run for each grid.

Table 4: Grid properties and thrust conditions for each preliminary three nozzle grid

Grid	Exit Plane Location	Number of Nodes	C_T Values Run
A	$2.5D_B$	0.58×10^6	0.0, 1.0, 7.0
B	$5D_B$	1.00×10^6	0.0, 1.0, 1.7, 7.0
C	$7.5D_B$	1.17×10^6	1.0, 1.7, 7.0
D	$20D_B$	2.97×10^6	1.0, 1.7, 2.4, 3.0, 3.6, 4.1, 4.8, 5.5, 6.3, 7.0, 8.0, 9.0, 10.0

A comparison of the three nozzle configuration grids in the region near the vehicle is shown in Figure 16, with these grids in units of millimeters. The first three grids, grids A-C, have their *X* axes oriented in the opposite direction of FUN3D convention due to improper axis definition during the geometry creation process. This has been corrected

when running the solutions by specifying a sideslip angle of 180° such that the freestream flow is correctly aligned with the vehicle. Grid D has had the axes corrected in the geometry definition, such that *X* is aligned in the direction of freestream flow and no sideslip angle is necessary. The thick black areas in the grids represent cells near the source lines defined in Gridtool and VGrid, which have been placed in the expected plume region for each nozzle. The increase in cell resolution for grids A-C is a function of both the increase exit plane distance aft of the vehicle as well as variations in the size and strength of the source line for cell sizes. Grid D attempts to correct for the discrepancies seen in grids A-C by varying the source line length, location, and strength, including the inclusion of an additional source line to keep cell size smaller near the expected bow shock location. The increase in the number of nodes for grid D is a function of this variation in source properties and the large increase in exit plane distance aft of the vehicle.

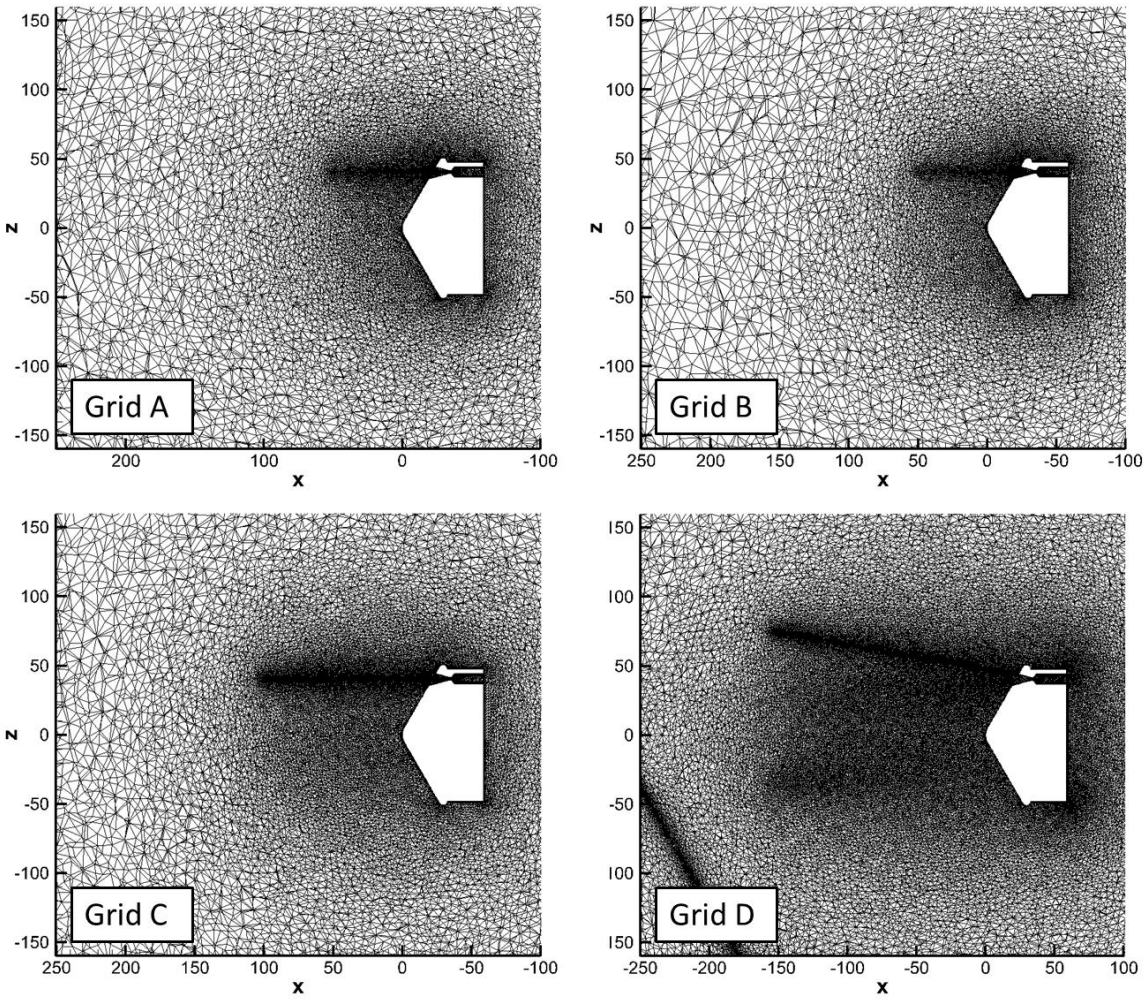

Figure 16: Comparison of preliminary three nozzle configuration grid resolutions

2.2.2 Single Nozzle Configuration

For this configuration, the available experimental data show the variation of terminal shock standoff distance, stagnation point location, and bow shock standoff distance as a function of thrust coefficient. Additionally, pressure coefficient along the forebody is provided for certain run conditions. Due to the lack of clear schlieren imagery in the wind tunnel report, direct comparison of the flowfield structure between computational and

experimental results is not possible; however, grid to grid comparisons can be made to investigate grid resolution effects.

The flowfield structures for common C_T values of 1.05 and 4.04 are shown in Figure 17 for the coarsest and finest grids. Mach contours are shown, which clearly distinguish the bow shock, jet boundary, and stagnation point. The C_T = 1.05 solutions show no clear jet terminal shock for any grid resolution. This is not necessarily unexpected, as the boundary between the two jet flow regimes is around a thrust coefficient of 1. In fact, the wind tunnel report shows both flow regimes as being possible at this condition, but does not explain how that was achieved in the experimental results. The sharp nature of the transition between the regimes suggests that a small variation in flow conditions can drastically alter the flowfield structure that should exist. Thus, this run condition could represent a situation where the jet flow should extend far upstream and not terminate in a distinct normal shock. Since neither type of flow structure is definitively seen, these levels of grid resolution may not be sufficient to fully capture the flow structure at this low thrust value. Increasing grid resolution shows a longer jet plume more consistent with the long jet penetration mode as well as a smoother bow shock due to the smaller cell size.

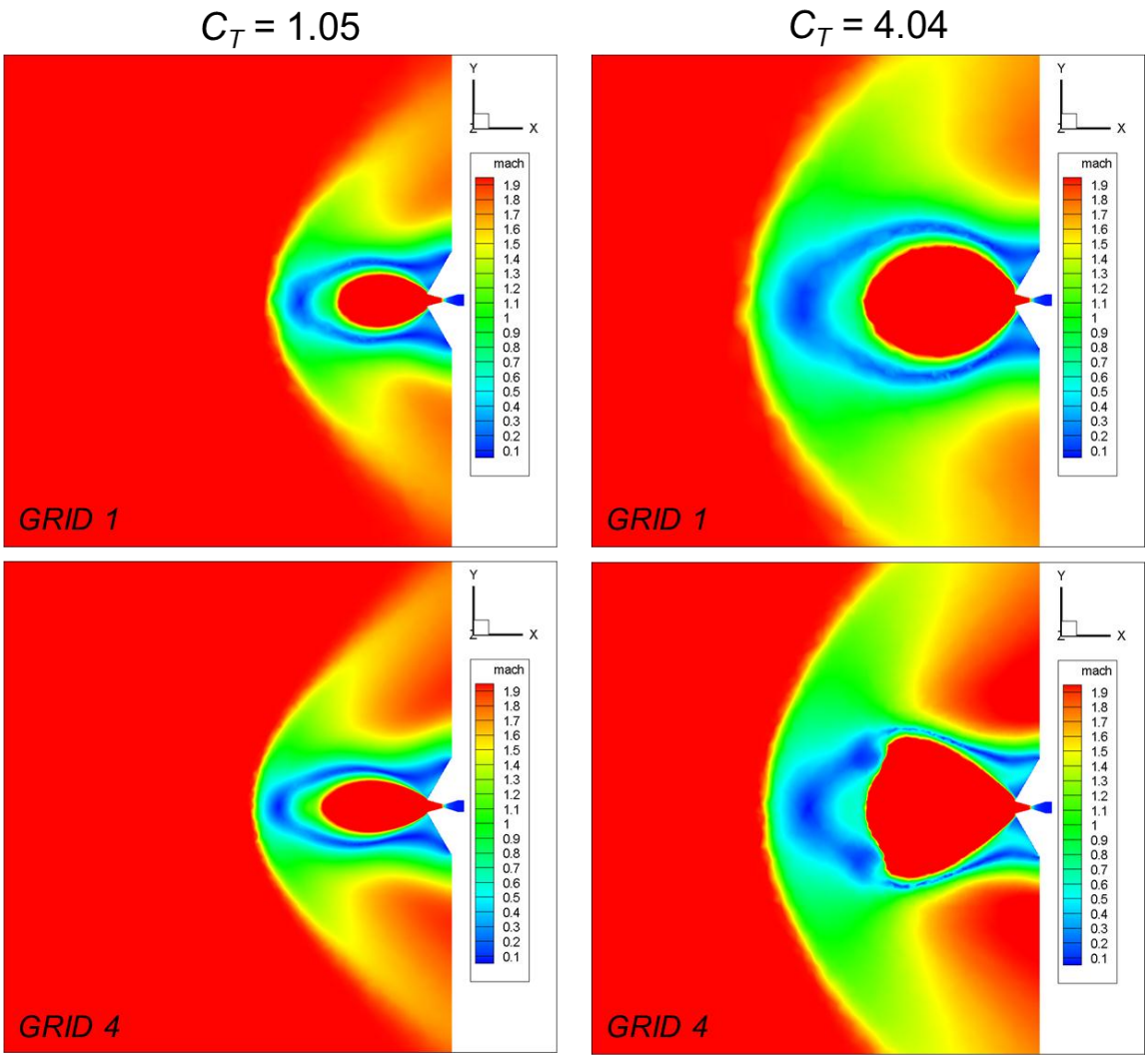

Figure 17: Mach contours for coarsest and finest single nozzle grids at C_T = 1.05 and C_T = 4.04

For C_T = 4.04, a distinct jet terminal shock is only seen on the finest grid. All three lower grid resolutions show a flow structure similar to that of grid 1, where the jet plume has a rounded termination region. This shape means that no triple point and Mach disk form at the termination of the jet plume, indicating that at higher thrust coefficient, grid resolution becomes a significant driver in accurately determine the flow structure. Grid resolution does not only impact the smoothness of the flow features, but also their shapes.

A low grid resolution may not provide an adequate solution for preliminary analysis of an SRP configuration because the plume structure may be inaccurate compared to what should exist due to the coarseness of the grid.

Axial flow structure locations are shown in Figure 18 and Figure 19 for the jet terminal shock and bow shock respectively for each grid. Standoff distances are measured from the nozzle exit plane and have been normalized by the vehicle base diameter for comparison with experimental data. For the jet terminal shock locations, if the solution does not have a distinct terminal shock, then the location is determined by the axial distance at which the jet flow transitions from supersonic to subsonic flow. Grids 1-3, the three coarsest grids, show a consistent plume shape that does not have a distinct terminal shock, and the standoff distances are consistently overpredicted. No jet penetration mode is seen for C_T values less than 1, and the jet terminal shock standoff distance continues to decrease with decreasing thrust in this region. For grid 4, a terminal shock does form in solutions with a thrust coefficient larger than 1. While C_T = 4.04 shows a better terminal shock agreement than the coarser grids, the standoff distance is still overpredicted as the plume shape is not as expected. Increasing grid resolution does have a beneficial effect on the axial terminal shock location, but further resolution is likely required to reasonably determine the entire plume shape. This will be investigated in Section 2.3.2.

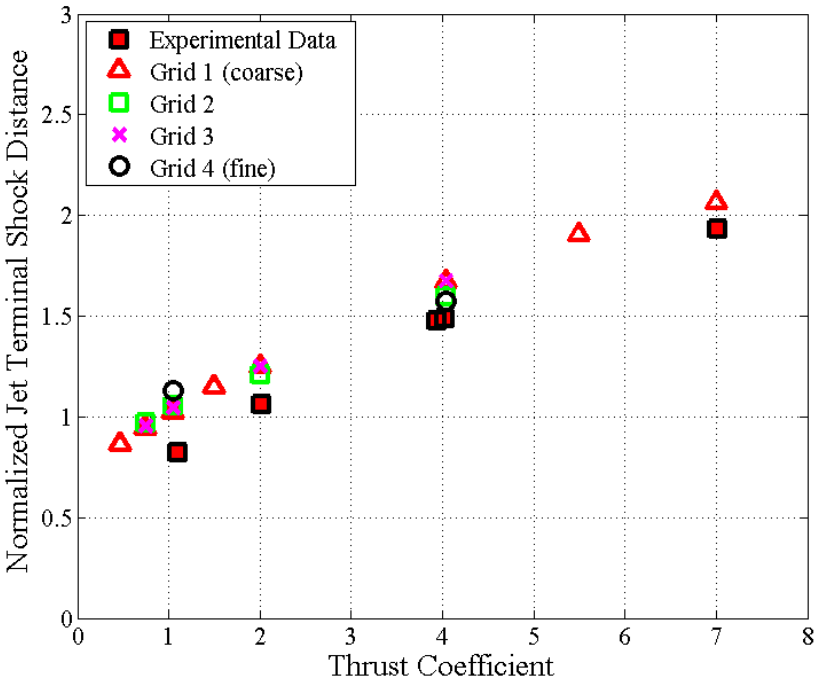

Figure 18: Jet shock location variation with grid and C_T for the single nozzle configuration

Bow shock standoff distances are clearly seen in the CFD solutions as the transition from the Mach 2 freestream flow to a subsonic flow behind the shock. Due to the resolution in all four grids, the bow shock is not a sharp discontinuity, but rather exhibits a deceleration of the flow over a few cells. The bow shock location is taken to be roughly the average location of the transition from freestream to decelerated flow. Consistent with the jet terminal shock and stagnation point locations, the bow shock location is overpredicted as compared to the experimental data for all high thrust conditions. $C_T <$ 1.05, as discussed in Section 1.2.1 for the Jarvinen and Adams wind tunnel experiment [10], should result in unsteady plume structures with large standoff distances. For these lower C_T values, because there is no jet penetration in the CFD solutions, the bow shock is not located as far off the vehicle as the experimental data suggests.

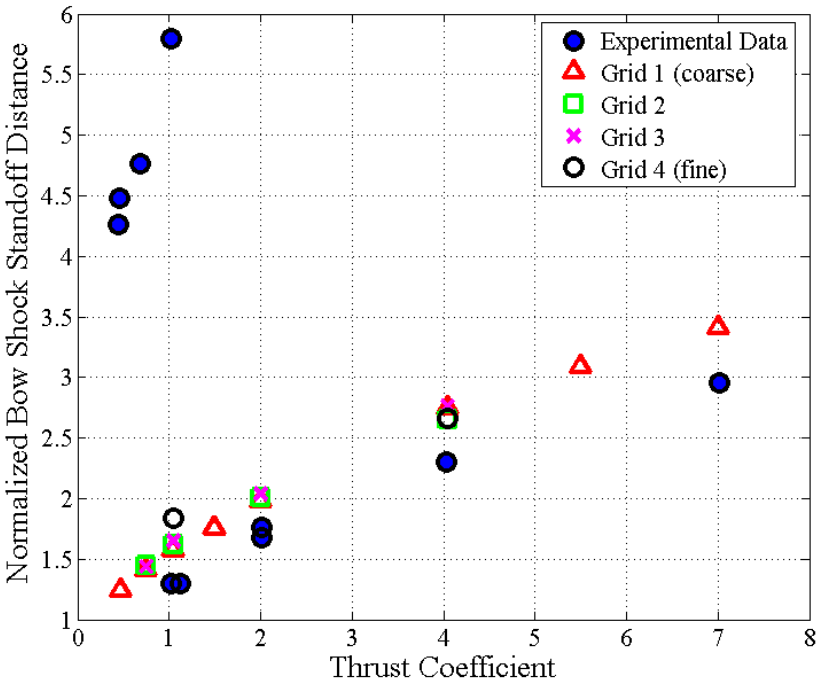

Figure 19: Bow shock location variation with grid and C_T for the single nozzle configuration

Surface pressure distributions from grid 1 are compared to the wind tunnel results in Figure 20 and Figure 21. As thrust coefficient increases, the pressure on the forebody decreases due to the jet plume blocking the oncoming freestream flow. As thrust is increased beyond C_T = 4.04 in the experimental results, the pressure becomes nearly independent of thrust coefficient as the vehicle is immersed in a wake type flow. A significant pressure rise is seen near the jet exit plane due to the plume expansion. Of particular note is the CFD pressure distribution for C_T = 1.05, which falls between the two distributions shown in the experimental data. This further supports that the steady state CFD solution for this condition is not representative of either flow regime, but rather some intermediate flow structure. For higher thrust coefficients, the drop to a nearly constant pressure independent of thrust coefficient is seen in the CFD solutions

even though the plume shapes for this grid resolution are not in agreement with the experimental schlieren images.

These preliminary solutions illustrate the significant effects grid resolution can have on an SRP simulation. Increasing grid resolution creates a flow field that better agrees with experimental results. Too coarse of a grid can provide a flow field which is not even a rough approximation of the correct flow field, but rather a completely different plume shape. The plume may be wider than expected if the resolution is not sufficient to appropriately calculate the expansion from the nozzle exit and the shear layer that forms along the plume boundary, or the plume may be lacking a terminal shock. These discrepancies in jet structure affect the bow shock structure as well as the surface pressures.

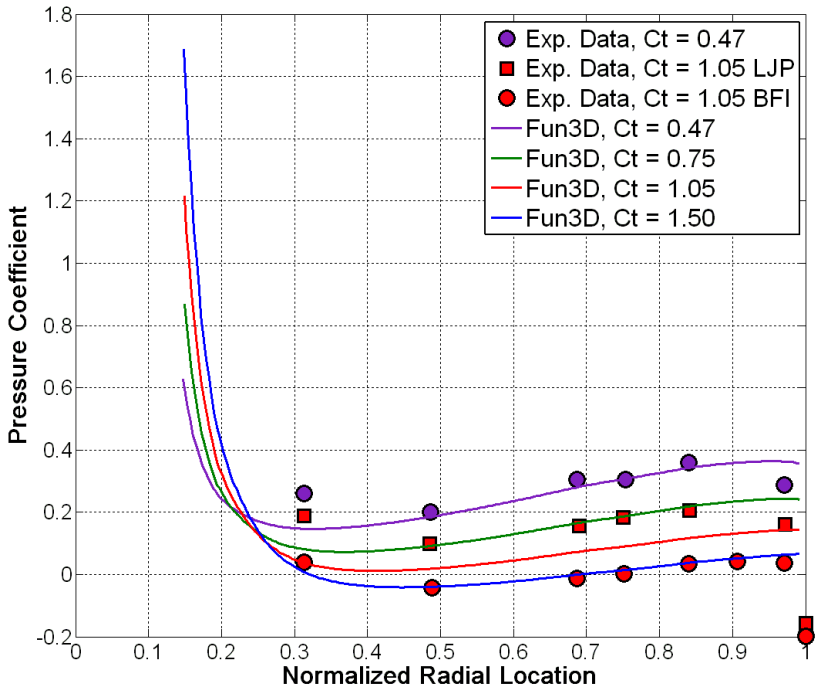

Figure 20: Low thrust radial C_P distributions for coarse single nozzle grid

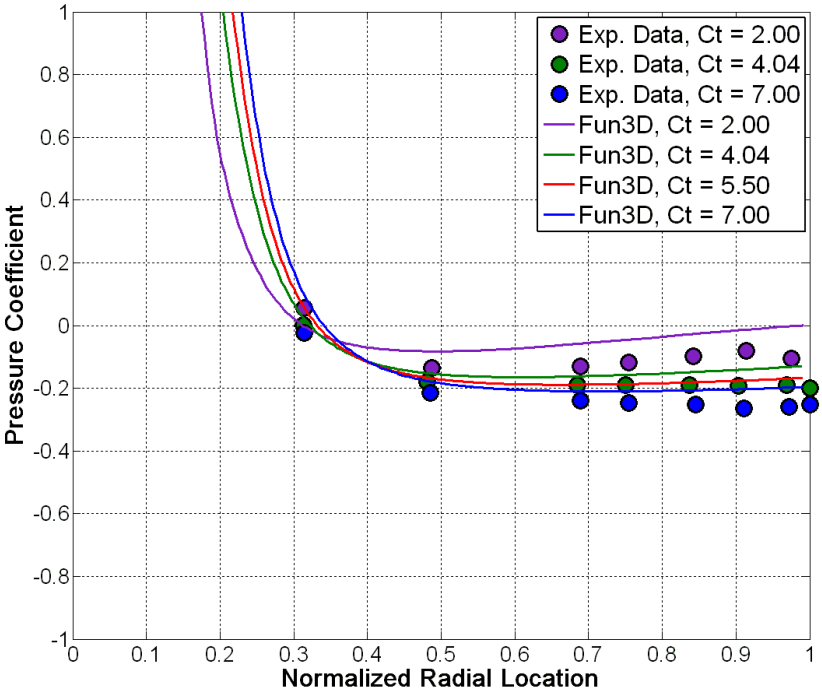

Figure 21: High thrust radial C_P distributions for coarse single nozzle grid

2.2.3 Three Nozzle Configuration

From the single nozzle configuration solutions, grid resolution in the plume region and exit plane location has a significant effect on an SRP simulation. For the three nozzle configuration, cells are more concentrated in the plume regions, though the total number of cells is on the same order of magnitude as for the single nozzle configuration. Additionally, each grid has an increasingly distant exit plane to allow for analysis of exit plane effects. For Grid A, with the nearest exit plane to the vehicle, the subsonic wake does not close within the computational domain for the thrust coefficients examined, creating an ill-posed exit plane boundary condition. For low thrust solutions on grids B and C, the subsonic wake does close within the computational domain; however, the higher thrust conditions still show an ill-posed exit plane boundary condition. Grid D sufficiently removes the exit plane from the vehicle to prevent this ill-posed boundary condition across all thrust coefficients examined.

Flowfield structures for common thrust coefficients of 1.0 and 7.0 are shown in Figure 22. These images represent a slice through the axis of the vehicle and the centerline of one nozzle, showing a single jet plume. If one of the out of plane plumes expands and intersects this cut plane, then it will be seen as a region of increased Mach number not associated with the cut plane plume. For C_T = 1.0, the solution does not noticeably vary between each of the four grids. This thrust condition results in a relatively small expansion and does not create a large wake aft of the vehicle. The exit plane interaction with the wake is negligible, and the flow field forward of the body is unperturbed. The jet plume shapes generally agree with the experimental schlieren, where each plume is independent and a normal shock is seen inboard of the nozzles.

For C_T = 7.0, the solutions vary significantly between each of the four grids. There is significant coalescence of the jet plumes seen for grids A-C, as seen by the increased Mach number region below the primary visible plume. This results in a bow shock extended far upstream of the vehicle, with no clear terminal shock structure forming from the coalesced plumes. The plume expansions themselves differ between all four grids, which is most likely a combined effect from grid resolution and exit plane location. Grids A and C show a wide plume structure, with a thick and thin jet boundary respectively. Grid B shows a narrower and longer plume structure which serves to offset the bow shock to a larger distance. Grid D shows a much different plume structure from any of the other three. There is no plume coalescence, which causes the bow shock to be much closer to the vehicle. Additionally, the independent plumes demonstrate that a local crossflow exists for each plume, as the plume flow turns outboard somewhat and is not aligned with the nozzle axis. The stagnation region at the nose of the vehicle creates a flow outboard along the surface which causes this crossflow. The subsonic wake is fully enclosed within the computational domain for this solution, which eliminates the ill-posed boundary condition created by subsonic wake flow intersecting the exit plane.

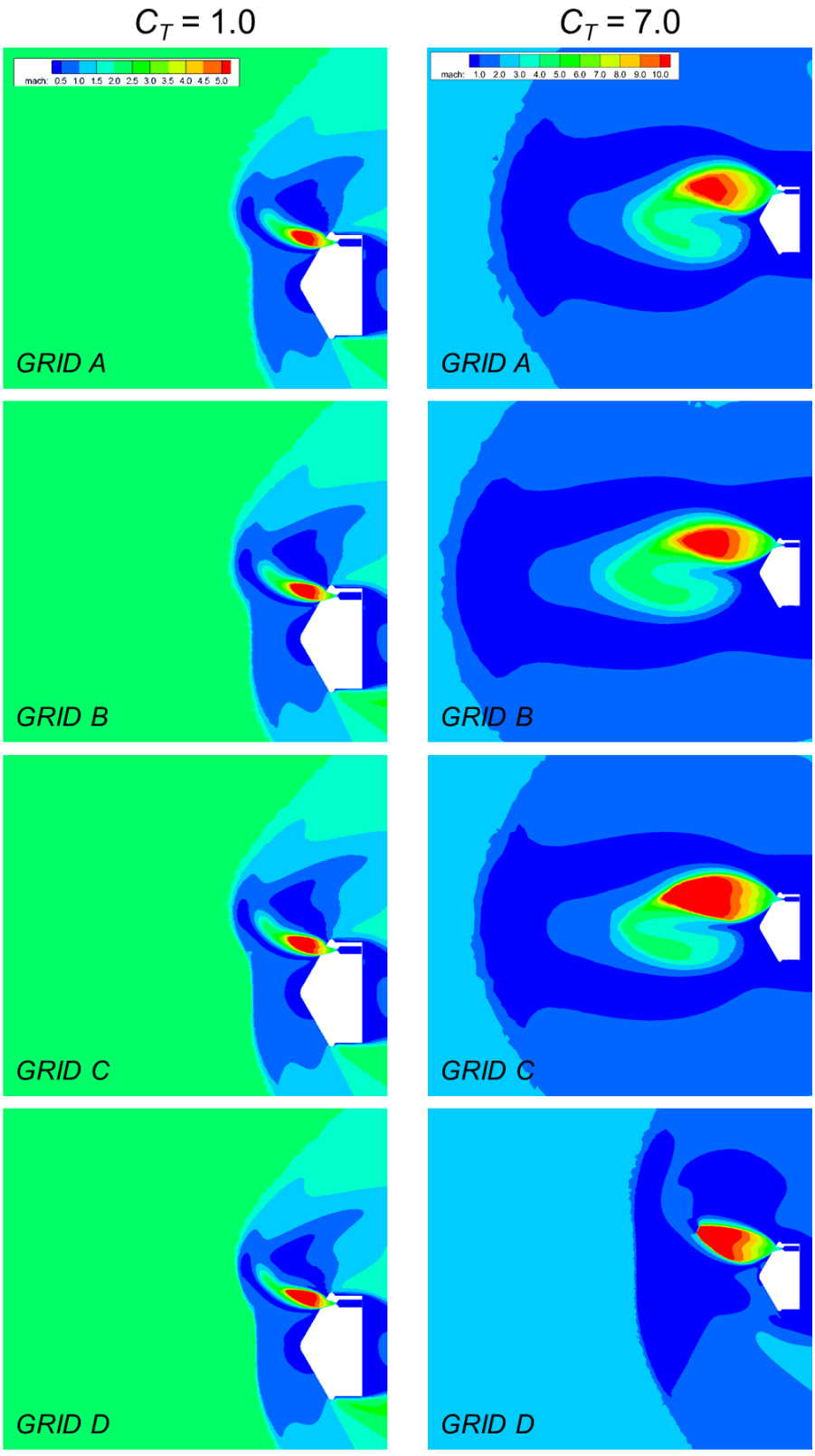

Figure 22: Mach contours for preliminary three nozzle grids at C_T = 1.0 and C_T = 7.0

Pressure distribution plots are shown for thrust coefficients of 1.0 and 7.0 in Figure 23. For C_T = 1.0, the similarity seen in the flowfield structure is also seen in the pressure distributions. Outboard of the nozzle exits, the pressure drops significantly due to the plume expansion shielding that region of the forebody from the oncoming freestream flow. Higher pressure is seen near the nose of the vehicle since the plumes do not expand sufficiently to shield that region.

As the flow field varies significantly from grid to grid for C_T = 7.0, so does the pressure distribution on the vehicle. Grids A through C all show plume coalescence in the flowfield structure, which causes a significant reduction in forebody surface pressure. The value of this pressure for each grid depends on the extent of the coalesced plume as it expands from the nozzle exits. Grid B, which shows the largest plume extent, has a slightly higher pressure than A and C, which have similar length extents into the flow field. Grid D, with no plume coalescence, shows a more significant difference in pressure distribution than grids A-C which conceptually resembles the effects seen for the lower thrust coefficient. Here, the independent jet plumes allow for some pressure to be preserved inboard of the nozzles. Since C_T = 7.0 creates larger plumes than C_T = 1.0, the region of preserved pressure is smaller and the peak pressure coefficient is smaller. The available wind tunnel data suggests that the pressure distribution should more resemble that seen in grids A-C. Uncertainties in grid resolution effects on the flowfield structure and pressure distribution indicate that this agreement may be coincidental.

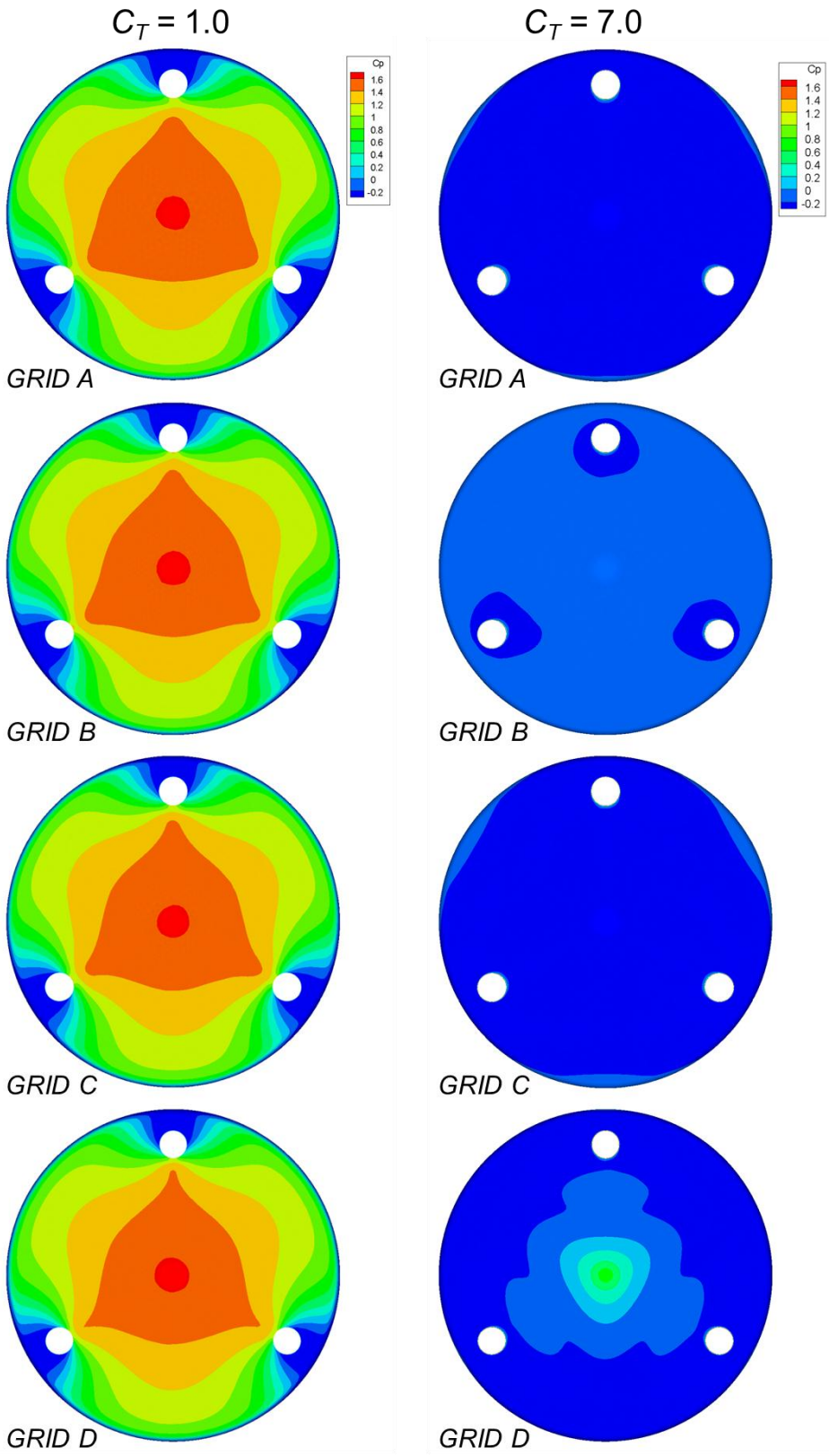

Figure 23: C_P distributions for preliminary three nozzle grids at C_T = 1.0 and C_T = 7.0

From the solutions shown here, it is difficult to say with certainty that the exit plane location alone has a significant effect on the flow field forward of the vehicle. Because cell density varies between the grids, there may be a coupling of effects from the grid resolution and exit plane. There is a definite effect on the wake region of the flow field due to the exit plane location. As shown in Figure 24 for C_T = 1.0, the subsonic wake is completely enclosed for grids B and C, and nearly so for grid A. Interaction between the exit plane and the wake is minimal, and the flow field is not significantly perturbed.

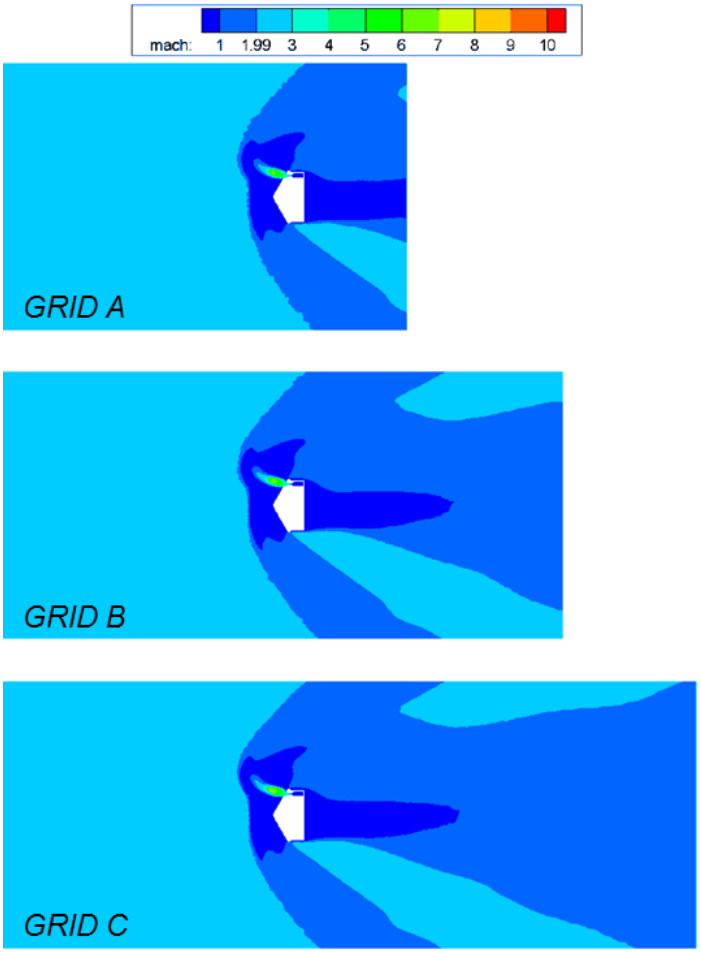

Figure 24: Exit plane effects on preliminary three nozzle grids for C_T = 1.0

The exit plane effects for C_T = 7.0 are shown in Figure 25 for grids A-C. In these solutions, there is significant interaction between the subsonic wake and the exit plane. For grid C in particular, the subsonic wake can be seen to expand at the exit plane, a non-physical effect. The shape of the subsonic wake is altered as far forward as the shoulder of the vehicle, indicating that it is possible that the plume structure is being altered. There is also an interaction of the flow field with the outflow boundaries along the sides of the computational domain. Though grid D is not shown in the comparison due to the large extent of the exit plane, moving the exit plane far aft of the vehicle causes the wake to completely close within the computational domain.

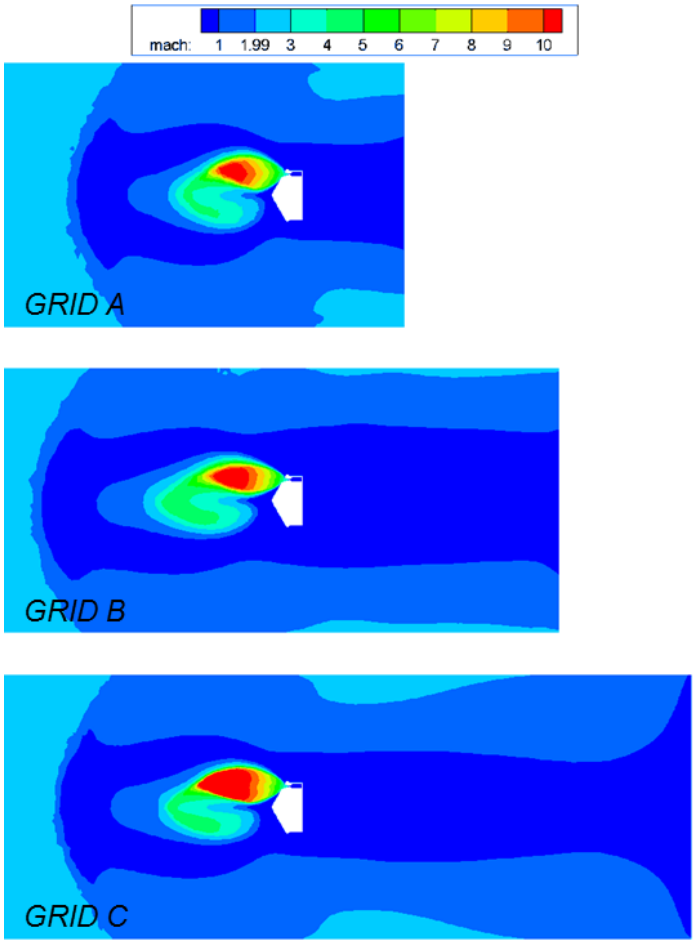

Figure 25: Exit plane effects on preliminary three nozzle grids for C_T = 7.0

2.3 Effects of Varying Thrust Coefficient

2.3.1 Grid Generation

Both the single nozzle and three nozzle grids for this study have been generated using Gridgen V15.15. Pentahedral cells are used in the boundary layer region along the vehicle surface, with tetrahedral cells used to fill in the rest of the computational volume. The grid properties are shown in Table 5. For both grids, the number of nodes within the grid is increased by a factor of 10 compared to the preliminary results. While this is a

result of an enlarged computational domain, the majority of the increase is due to refinement of cells relative to the preliminary grids.

Table 5: Grid properties and thrust conditions for both the single and three nozzle grids

Configuration	Exit Plane	Number of	C_T Values Run
Single Nozzle	$10D_B$	19.7×10^6	0.47, 0.75, 1.05, 2.00, 3.00, 4.04, 5.00, 6.00, 7.00, 8.00, 9.00, 10.00
Three Nozzle	$20D_B$	19.4×10^6	1.0, 1.7, 3.0, 4.0, 5.0, 6.0, 7.0, 8.0, 9.0, 10.0

As this grid has been generated with Gridgen, the source lines that are seen in the preliminary grids are no longer present since Gridgen creates a grid by defining blocks within the flow field. Two views of the grid are shown in Figure 26, with dimensions of meters, to detail the significant increase in cell resolution for this grid. Regions have been defined where the plume is expected to exist, with additional regions for capturing the bow shock structure and near-vehicle aftbody flow field sufficiently. The cells shown in Figure 26 are interpolated onto the *X-Z* plane, as the actual tetrahedral cells do not have a symmetry plane in the grid generation process. Figure 27 shows a slice of the entire computational domain for the single nozzle configuration.

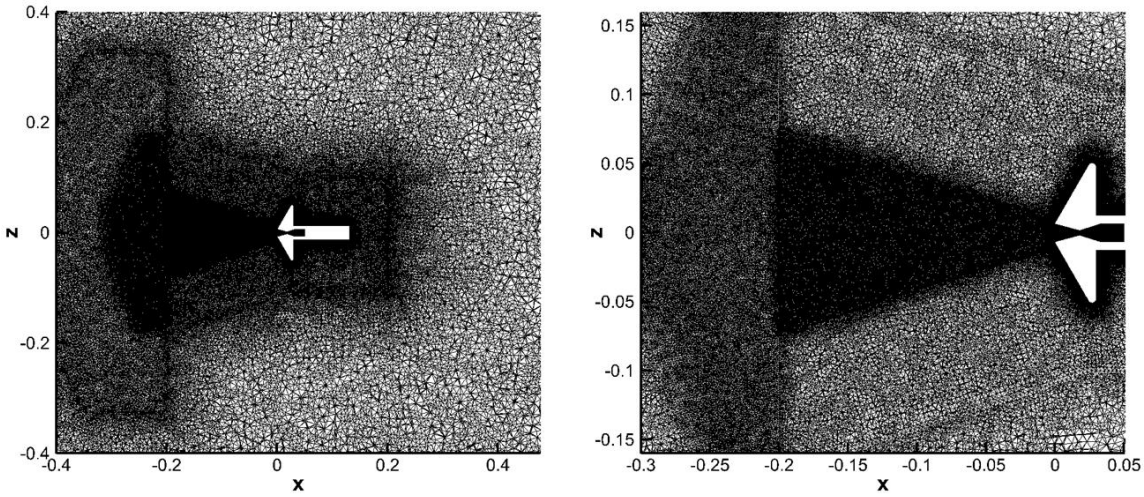

Figure 26: Near-vehicle grid for the single nozzle configuration

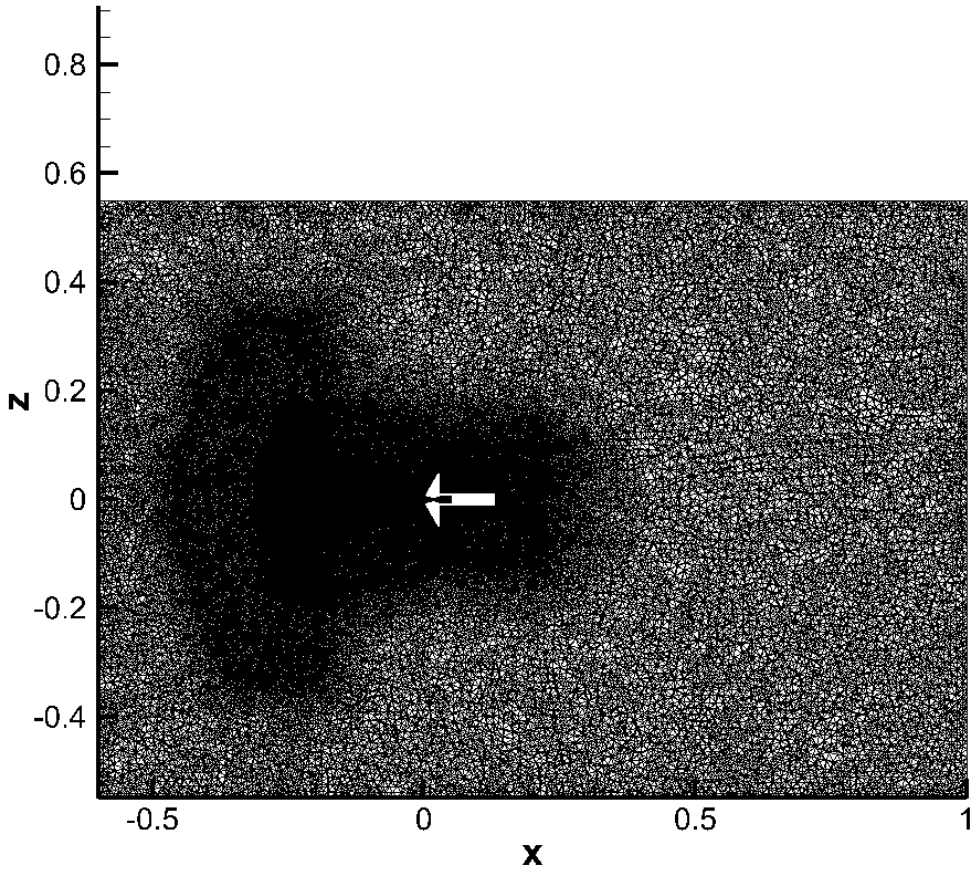

Figure 27: Full computational domain for the single nozzle configuration

The grid for the three nozzle configuration has also been generated using Gridgen, so the source lines seen in the preliminary grids are no longer present. The blocks within this grid defining the plume and bow shock regions have been created in sets of three for each location, so a symmetry plane is present in some regions as seen in Figure 28. As with the single nozzle configuration, this grid represents a significant increase in cell resolution to better capture the underlying flow physics which occur during SRP. The zoomed in image of the computational mesh on the right in Figure 28 shows variations in the cell structure at some locations in the mesh due to Gridgen continuously varying the cell lengths from the small cells near the vehicle to the larger cells at the boundaries of the regions. These local cell irregularities are small and do not appear to have any effect on establishing the solutions shown in Section 2.3.3. Figure 29 shows a slice of the entire computational domain for the three nozzle configuration with the exit plane far removed from the vehicle to ensure that the subsonic wake is fully enclosed within the computational domain.

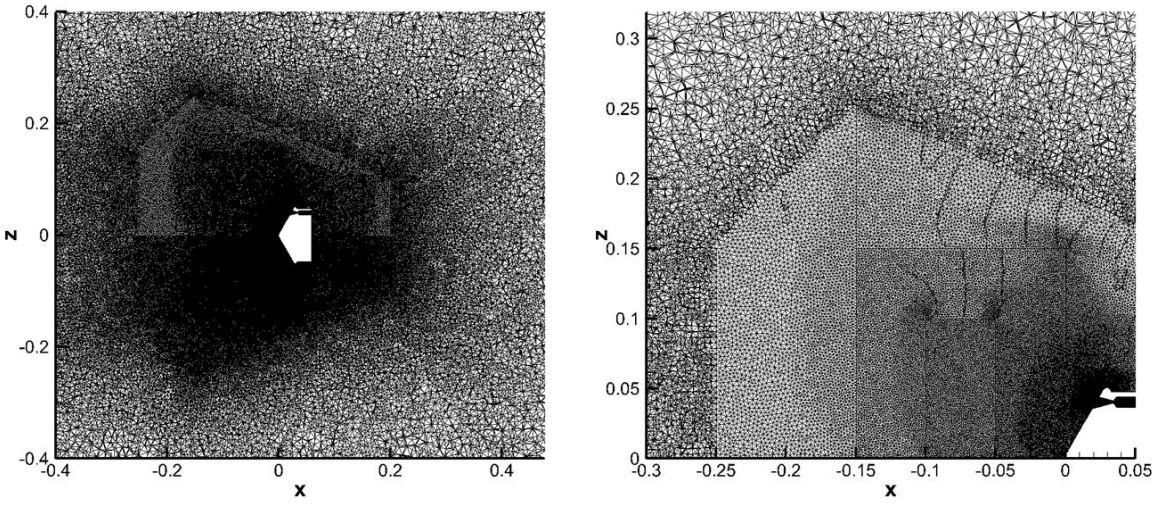

Figure 28: Near-vehicle grid for the three nozzle configuration

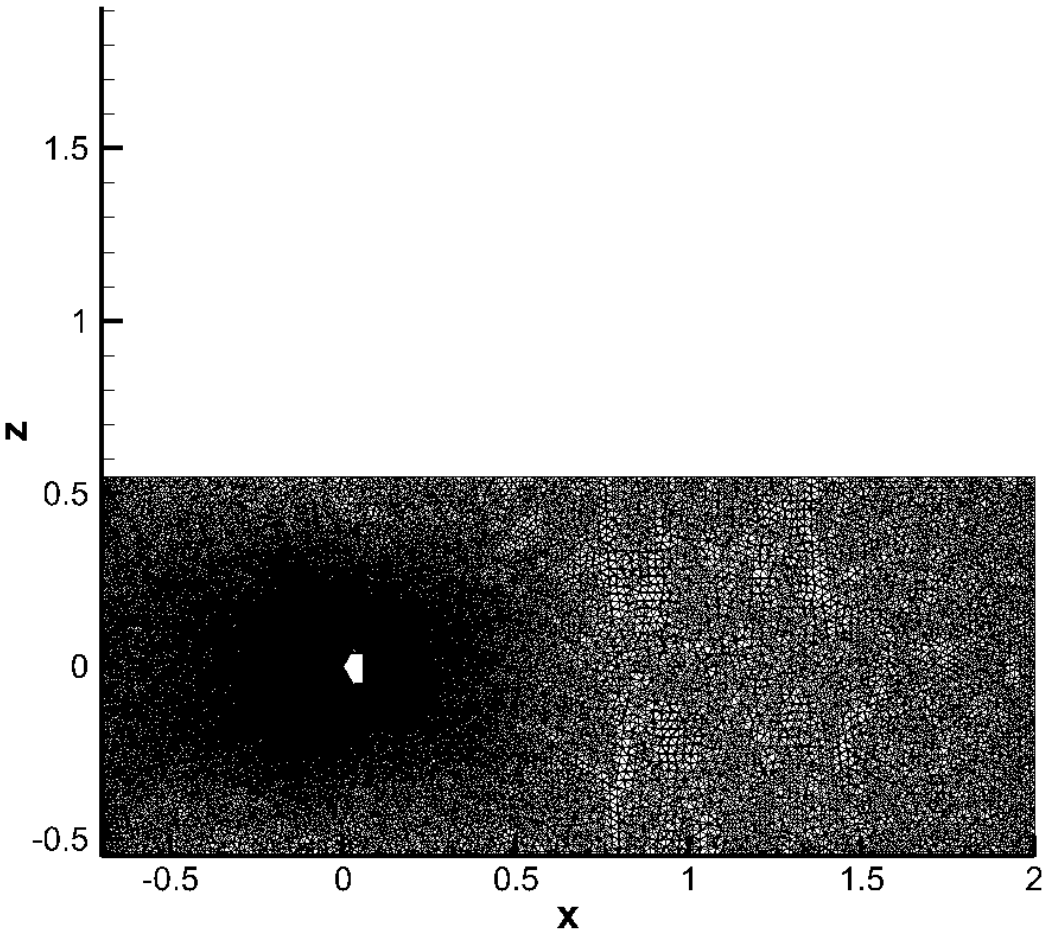

Figure 29: Full computational domain for the three nozzle configuration

2.3.2 Single Nozzle Configuration

The flow structures for varying thrust coefficient are more clearly defined on this grid as compared to the preliminary solutions, as shown in Figure 30. For C_T < 1.05, the beginnings of a jet penetration mode are seen in the plume structure. This supports the trend seen in the preliminary solutions, where increasing grid resolution showed elongated plumes for a thrust coefficient of 1.05. Even the level of grid resolution in this higher resolution grid is not sufficient to generate jet penetration to the extent reported in the wind tunnel results as discussed in Section 1.2.1 for the Jarvinen and Adams

experimental results [10]. For these low thrust values, the CFD solutions show a clear plume cell, with the possibility that an additional cell is attempting to form. The schlieren imagery from the experimental data does not clearly distinguish the shape that this flow field should exhibit, though the sketches shown indicate that there may not be a well-established flow structure and that it is a highly unsteady flow regime. From the CFD solution, there may be dissipative effects from the turbulence model and cell size that prevents the full jet penetration mode from forming.

For $C_T > 1.05$, the flow field shows a distinct terminal shock for all thrust coefficients tested. As thrust coefficient increases, the plume expansion becomes larger and the terminal shock forms further from the vehicle. Unlike the solutions seen on the preliminary grids, these plumes have a narrow expansion out of the nozzle, which allows for the correct jet boundary to form. Each plume on the higher resolution grid shows a smooth transition from nozzle exit to jet boundary up to the terminal shock, which is not seen in any of the preliminary solutions. Though the extent of plume expansion varies drastically from the low to high thrust coefficients tested, the plume shape and flowfield structure tends to remain similar amongst all of the solutions under the same flowfield structure mode. Creating a grid that is sufficient to resolve the largest expected plume also allows for the determination of lower thrust coefficient solutions on the same grid. If multiple flow modes are expected, such as a jet penetration mode and a blunt flow mode, then the same grid may not be capable of fully resolving both flow fields, particularly if the cell sizes are based on the high thrust plume structures as is done with this grid. The plume structure does still show signs of creating a jet penetration mode, but it is not to the extent that is expected from the experimental data.

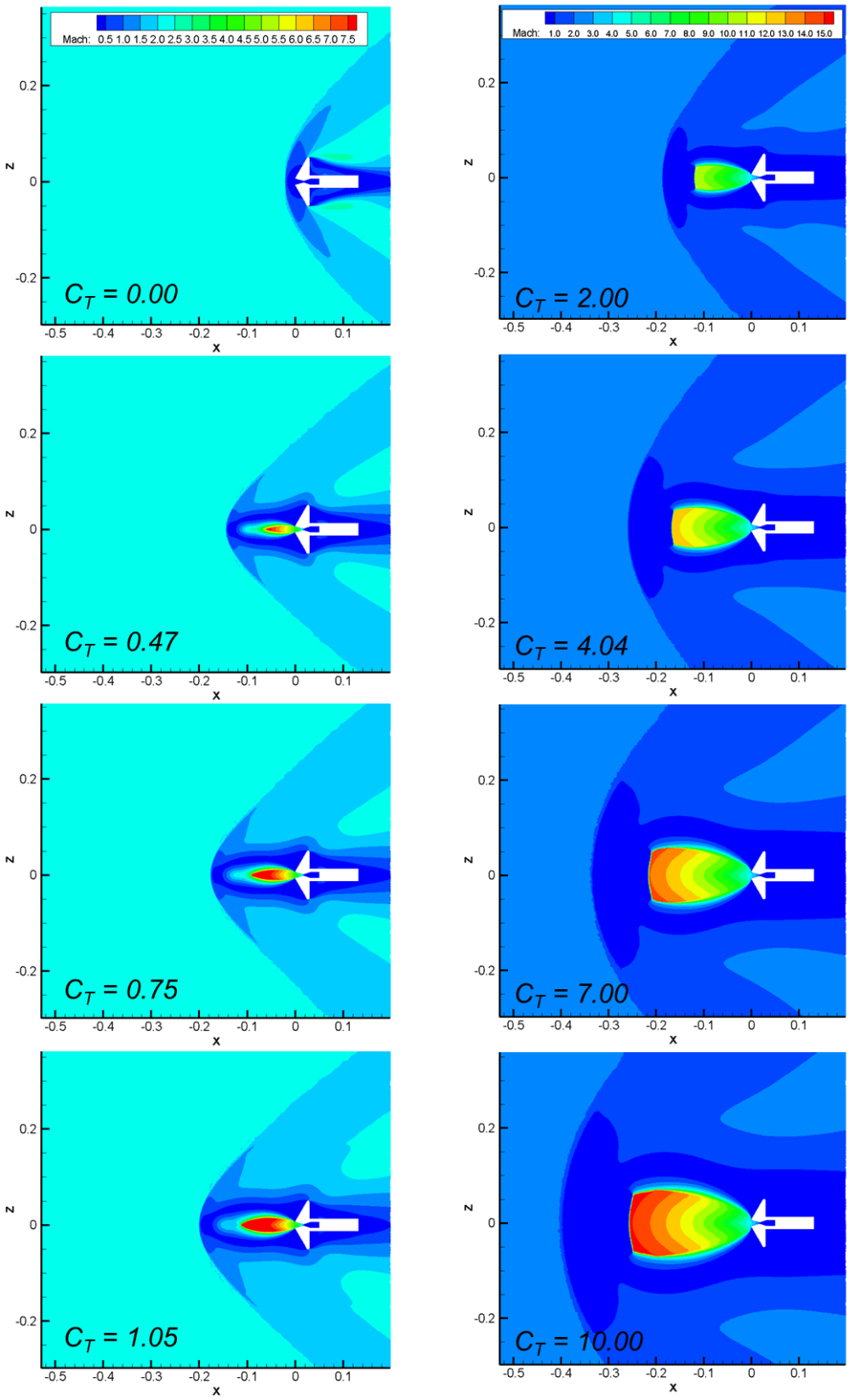

Figure 30: Mach contours for increasing C_T for the single nozzle configuration

Comparisons of the axial locations of the terminal shock, stagnation point, and bow shock with experimental data is shown in Figure 31. There is still a consistent overprediction of the flow feature locations for the higher C_T values as is seen on the preliminary grids. Since there is no extended jet penetration mode seen in the CFD solutions, the low C_T cases show a significant underprediction of flow structure locations. It is unclear if this discrepancy is due mainly to the CFD simulation, the experimental data, or both. Since the wind tunnel results do not dictate a methodology used to determine the flow structure properties, no remark can be made on the expected accuracy of those data points. This is particularly important for the low thrust coefficients, where the experimental report notes that the flow field was highly unsteady. The length of time used to create a time averaged data point from the experimental schlieren imagery could significantly alter the reported data values.

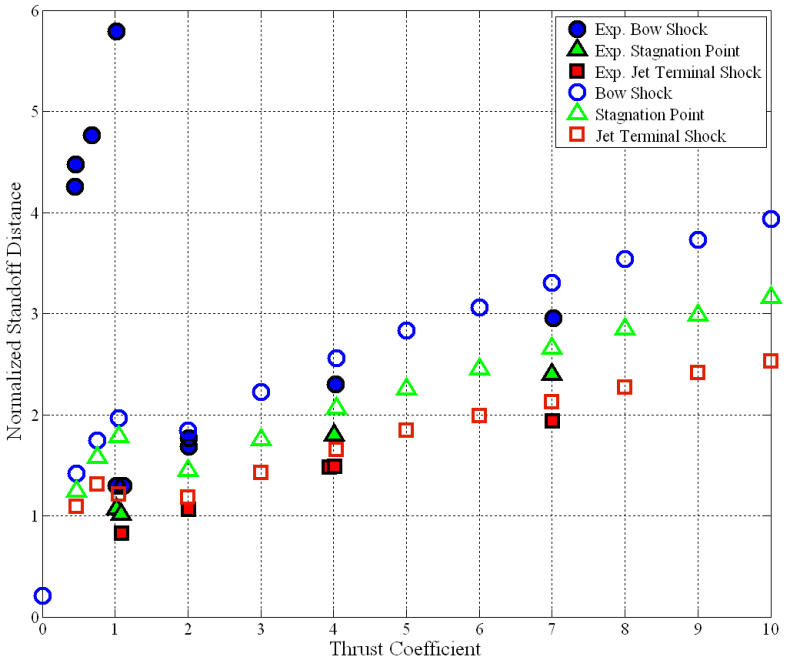

Figure 31: Axial flow structure locations for varying C_T for the single nozzle configuration

Surface pressure distributions are shown in Figure 32 and Figure 33 for the higher resolution solutions. These follow the expected trends from the experimental data where increasing thrust coefficient results in more shielding of the forebody and a drop in pressure along the surface. While the jet off condition generally agrees well with the experimental data, the low thrust coefficient solutions significantly underpredict the surface pressure. In particular, the C_T= 1.05 solution shows better agreement with the lower pressure associated with a blunt flow structure rather than the jet penetration mode. Since the jet penetration mode does not fully form in the CFD simulations, then corresponding pressure distribution should be altered. Along with the results from the preliminary grids, the shape of the jet plume clearly has a large effect on the forebody pressure distribution.

For higher thrust coefficients that are clearly within the blunt flow regime, the pressures show a better comparison far from the nozzle exit. The pressure rises near the nozzle do not agree between the CFD solutions and the experimental data points. Since grid 4 of the preliminary solutions showed agreement with this first data point, but with a widely expanded jet plume, it is evident that accurate determination of the plume expansion drives the forebody pressure near the nozzle exit. Increasing thrust coefficient eventually causes a plateau in the surface pressure, as the vehicle becomes surrounded by a wake type flow field.

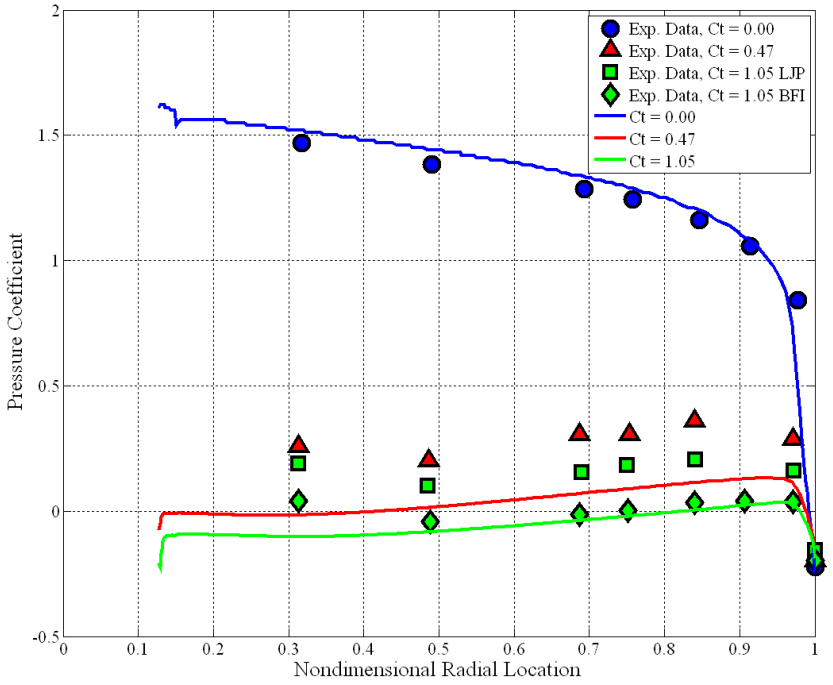

Figure 32: Low thrust radial C_P distributions for the single nozzle configuration

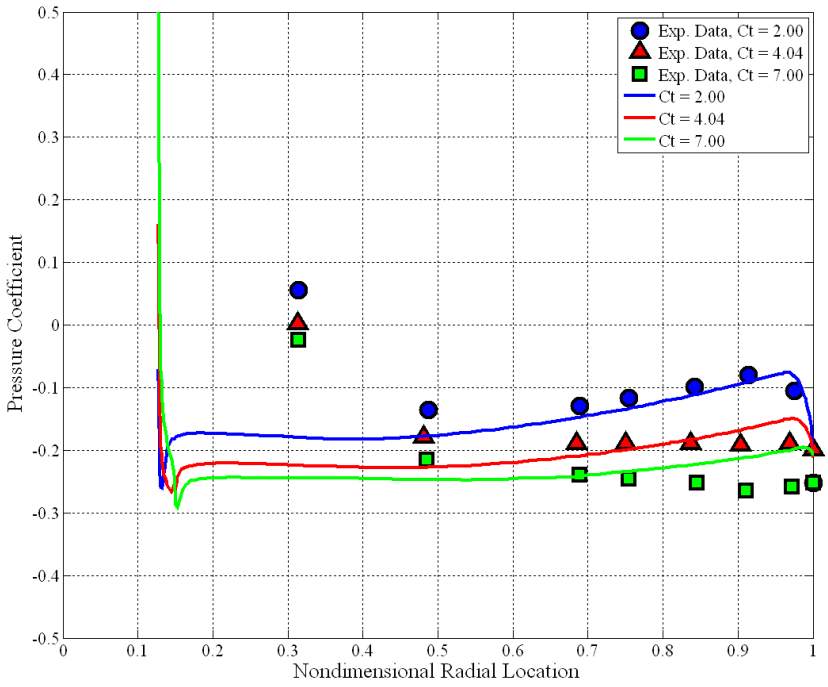

Figure 33: High thrust radial C_P distributions for the single nozzle configuration

For all thrust coefficients, the integrated forebody drag coefficient is shown in Figure 34. Across all thrust coefficients and flow regimes, good agreement is seen with the experimental data, even with the low thrust discrepancies in the flowfield structure and the high thrust discrepancies in the nozzle exit expansion. For the jet low C_T values, the slight underprediction of C_D is most likely due to the lack of establishment of the jet penetration mode. For the high C_T values, the drag coefficient does show a slight decrease with increasing thrust coefficient, though it does not vary significantly for $C_T >$ 7. For $C_T > 1$, there is essentially no drag preservation.

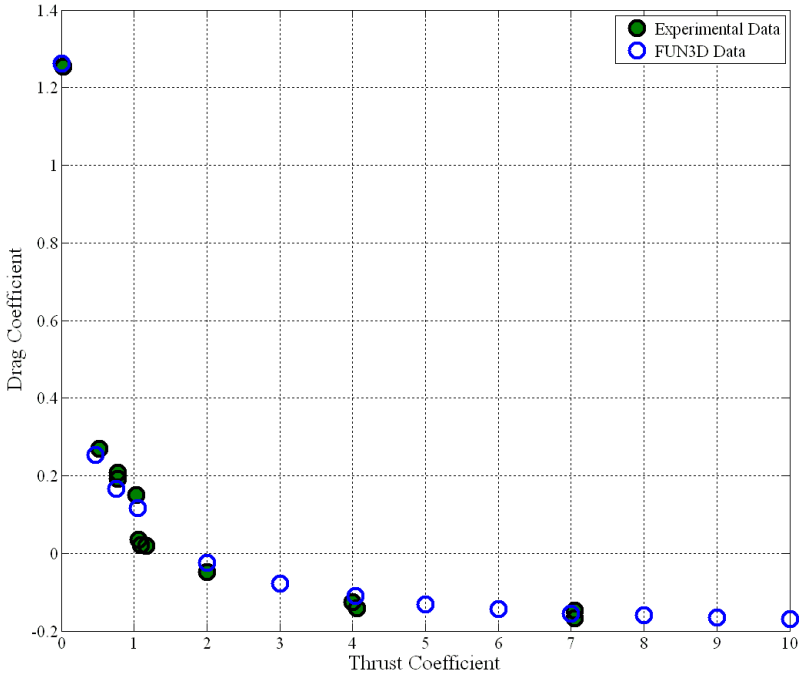

Figure 34: Integrated forebody C_D variation with C_T for the single nozzle configuration

2.3.3 Three Nozzle Configuration

With the increased grid resolution and sufficiently extended exit plane location, the flowfield structure is able to form across a wide range of thrust coefficients. A sampling of these flow fields are shown in Figure 35, along with their corresponding pressure distributions. The C_T = 1.0 solution resembles that seen in the preliminary investigation, with small jet plumes that preserves pressure inboard of the nozzle. This is characteristic of low thrust applications, where the plume is not large enough to noticeably alter the bow shock structure.

As C_T is increased, the plumes grow larger and shield a greater portion of the forebody surface area. This causes a decrease in the peak surface pressure on the forebody in addition to the overall decrease in surface pressure caused by the plume

expansion. For C_T = 4, a significant region of pressure is still evident as the plume expansion is still somewhat small. Increasing the thrust to C_T = 7 results in nearly total shielding of the forebody and a drop in surface pressure to a nearly constant, low value. The inboard expansion of the plume has nearly reached the vehicle axis, which is why this significant reduction in pressure is noted.

For C_T = 10, the plumes have coalesced and created a single large plume. The coalescence is evident in the Mach number contours due to the presence of a high Mach region below the primary visible plume. For this situation, the plumes have joined together and act as a single plume, and the standoff distance of both the terminal shock and the bow shock greatly increases. The effect on surface pressure for this thrust level is similar to that seen for the single nozzle configuration, where the entire vehicle exhibits a total loss of surface pressure. As the plumes have coalesced, even the surface near the nose is now shielded by the plume structure and the decelerated freestream has no flow path to reach the surface.

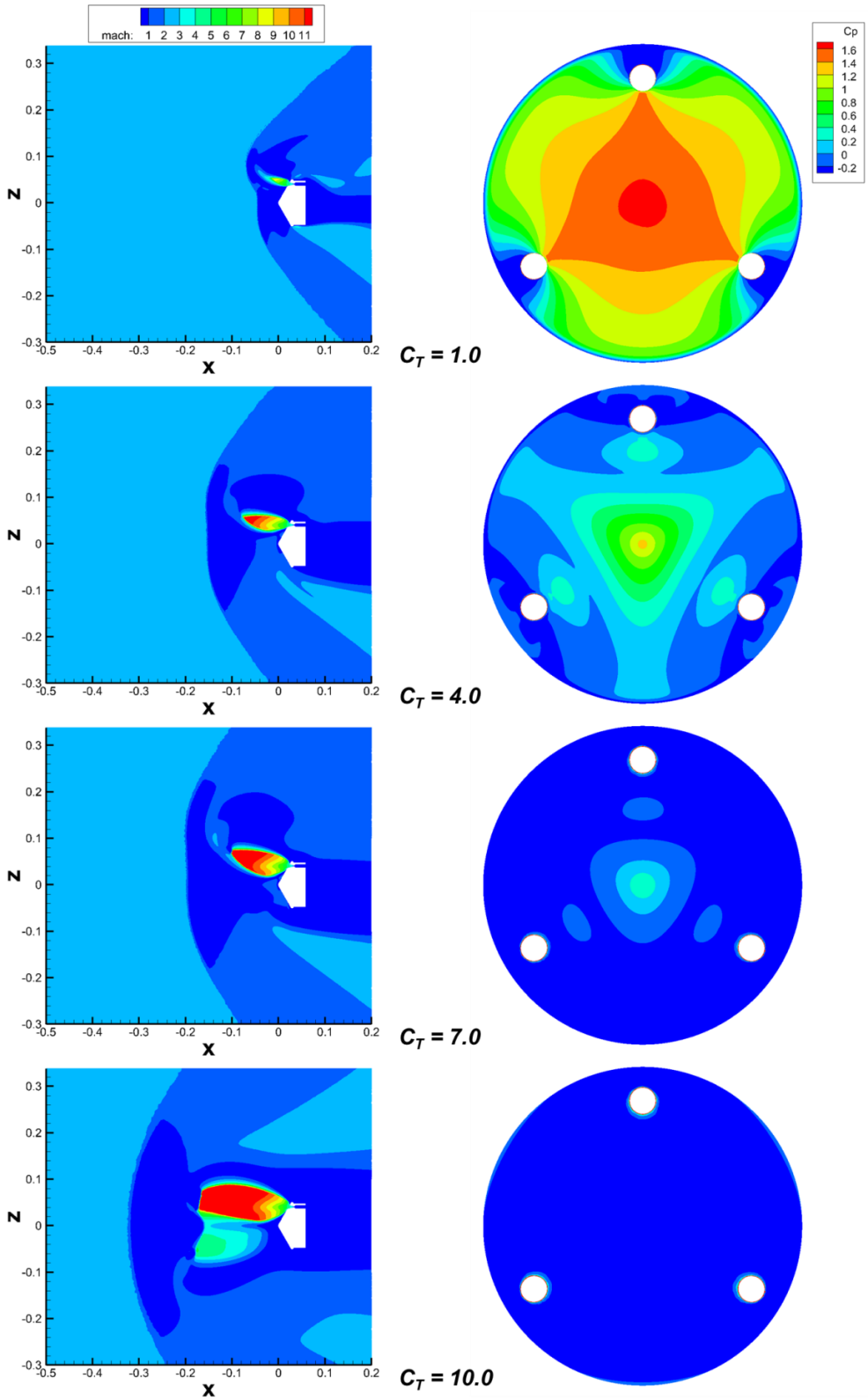

Figure 35: Mach contours and C_P distributions for varying C_T for the three nozzle configuration

A comparison of the bow shock and jet terminal shock standoff distances with the experimental data is shown in Figure 36. The bow shock standoffs represent the shock axial location, and the terminal shock locations represent an average distance since the terminal shock is not perpendicular to the vehicle axial direction. Thus a direct comparison between the experimental data points and the CFD solutions may not be valid, though the trends in the data should be comparable. In general, as thrust is increased the plumes become larger, causing the shocks to form farther from the vehicle. Once the plumes coalesce, which is seen in the CFD solutions for C_T values of eight and above, a significant rise is seen in the shock locations due to the larger effective plume. The experimental report does not indicate why C_T = 5.5 shows a larger bow shock standoff distance, and this increase is not seen in the steady state CFD solutions.

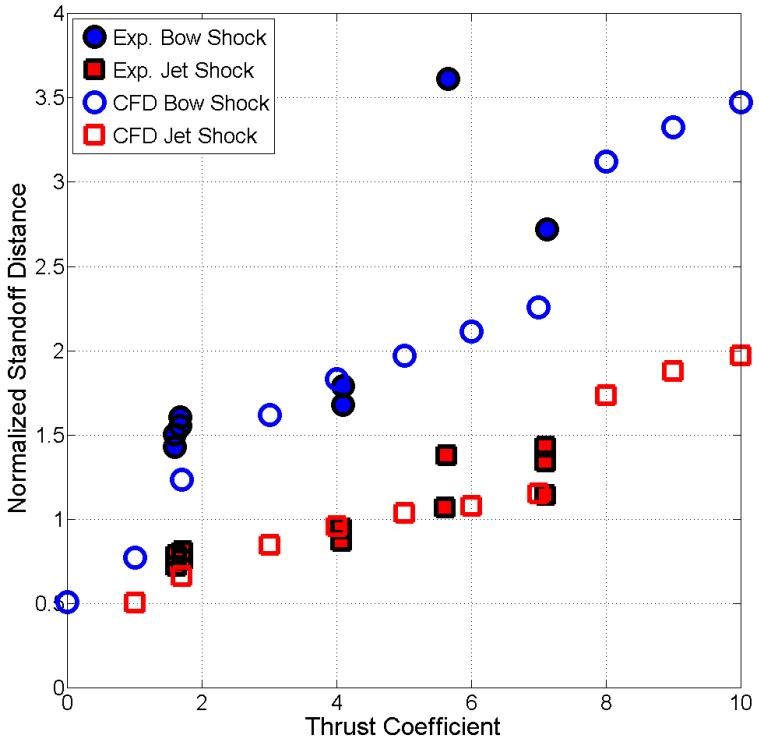

Figure 36: Flow structure locations for varying C_T for the three nozzle configuration

Integrated drag coefficient values are shown in Figure 37 for varying thrust levels on the three nozzle configuration. Low thrust coefficients (C_T < 4) result in some drag preservation with drag preservation significant for C_T < 1. Increasingly larger plumes create lower pressure over more of the forebody. C_D eventually levels out to a nearly constant value with varying thrust coefficient as the vehicle becomes immersed in a wake type flow.

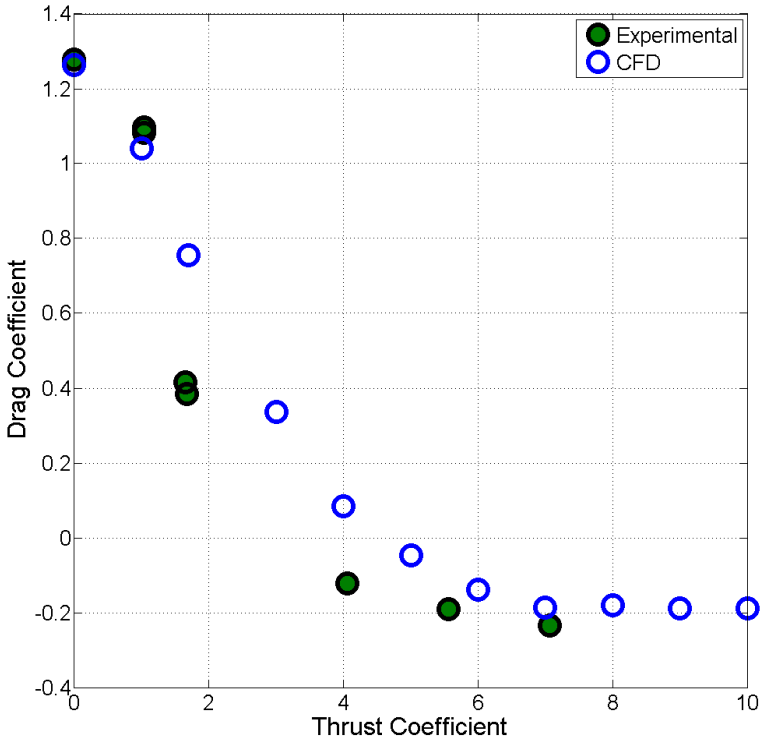

Figure 37: Integrated forebody C_D for varying C_T for the three nozzle configuration

CHAPTER III

ANALYTICAL DETERMINATION OF SUPERSONIC RETROPROPULSION PLUME STRUCTURES

3.1 Overview of Analytical Approach

While the steady state CFD analysis in Chapter II shows good agreement with experimental data for generating SRP simulations, it is a time intensive process. Significant time is required to generate a grid, run a solution, determine the validity of the grid, and iterate until a converged, reasonable solution is achieved. While this type of analysis is useful once a vehicle and nozzle configuration have been chosen, it requires too much time commitment earlier in the design process. For configuration pruning, more rapid approaches are necessary to compare various SRP systems and reduce the design space to a subset of potential designs for higher fidelity analysis. To that end, leveraging information from analytical approaches to simulating plume structures allows for configuration comparisons to be made in a time efficient manner.

Analytical methods for determining SRP flowfield structures have many uses which can benefit the early stages of the design process. First, an understanding of the approximate locations for the plumes, with a given nozzle orientation and location, can allow for qualitative prediction of the possible aerodynamic implications of a given configuration. As is shown in the analysis of Chapter II, moving nozzles outboard of the vehicle axis creates a scenario where surface pressure is preserved on the vehicle. As thrust increases, the plume expansion increases and more of the vehicle is shielded. The resulting surface pressure decreases until the entire vehicle is eventually shielded for

large thrust values. While an analytic solution for the surface pressure distribution of a general configuration is beyond the scope of this work, knowledge of the plume locations can be used to identify potentially shielded areas of the vehicle. Thus, information can still be inferred as to whether it is expected for significant surface pressure preservation to be possible. Additionally, understanding the plume structure allows for more informed grid generation prior to creating CFD simulations. Knowledge of the expected location of plume structures allows for more efficient concentration of cells in a computational domain to target the regions of interest for a given SRP configuration. Predictions of the bow shock structure can be used to set upstream and radial computational boundaries such that the shock structure created by a given SRP configuration is fully contained within the computational volume without the need to create a large mesh due to unknown flowfield structure.

Two other predictive capabilities of the analytical model relate to plume structure in particular. As previous analytical approaches tend to deal with single effective plumes, investigating the ability of the analytical approach developed in this thesis for predicting plume coalescence can be used to determine the applicability of past analytical approaches for a given configuration at a given thrust level. Additionally, for nozzles with low incidence angles relative to the surface from which they exhaust, predicting the potential for significant plume-surface interaction allows for system designers to consider additional aerodynamic and thermal effects that may exist for a plume that expands along a surface of the vehicle. All of these considerations can be used as a screening tool for conceptual design, where a wide range of configurations can be analyzed rapidly with the

analytical approach to determine configurations of interest for higher fidelity analysis with CFD or wind tunnel experiments.

The analytical model developed in this chapter builds on prior work for nozzles exhausting into a vacuum with the plumes assumed to be axisymmetric and to terminate in a normal shock. One analytical model is used to determine the terminal shock location relative to the nozzle exit. A separate model is used to generate the plume barrel shock, which is then scaled such that the mass flow out of the entire plume balances with that of the nozzle plenum. Prior analytical work on bow shock shape is utilized to determine a local bow shock structure for each plume based on an assumed effective obstruction to the freestream flow. Each local bow shock structure is then combined to create an approximation of the full bow shock present for a given SRP configuration. Approximations of the shear layer thickness based on traditional boundary layer theory applied to the jet flow provide a context for determining potential cell sizes within the computational domain. A velocity triangle approach based on surface flow and jet exit velocities is used to determine the perturbations to each plume structure due to the effects of each jet exhausting into a local crossflow.

3.2 Determining Plume Terminal Shock Location

An analytical relationship from Sibulkin [52] is used as the basis for determining the location of the terminal shock. This relationship assumes that the flow at large radial distances appears to have streamlines emanating from a common source and that the flow exhausts into a vacuum. The axial density distribution is found from the maximum turn angle of the nozzle exit flow and a scaling parameter, which was determined with a fit to

available method of characteristics data. For SRP flow fields, which do not exhaust into a vacuum, a normal shock is assumed for both the freestream and jet flows to determine the required pressure behind each shock to balance the two decelerated flows.

3.2.1 Plume Axial Density Distribution

Sibulkin's approach to analyzing a nozzle exhausting into a vacuum assumes that the flow emanates radially from a common point as shown in Figure 38 [52]. For this flow assumption, mass flux varies inversely to the square of the radial distance, and the axial density distribution can be related to this distance by Eq. (7). As the jet flow expands, the pressure ratio will vary until the flow reaches conditions at which a shock can decelerate the fluid to the ambient conditions into which the plume exhausts.

$$\frac{\rho}{\rho_{T,jet}} = B\left(\frac{x}{d_{throat}}\right)^{-2} \tag{7}$$

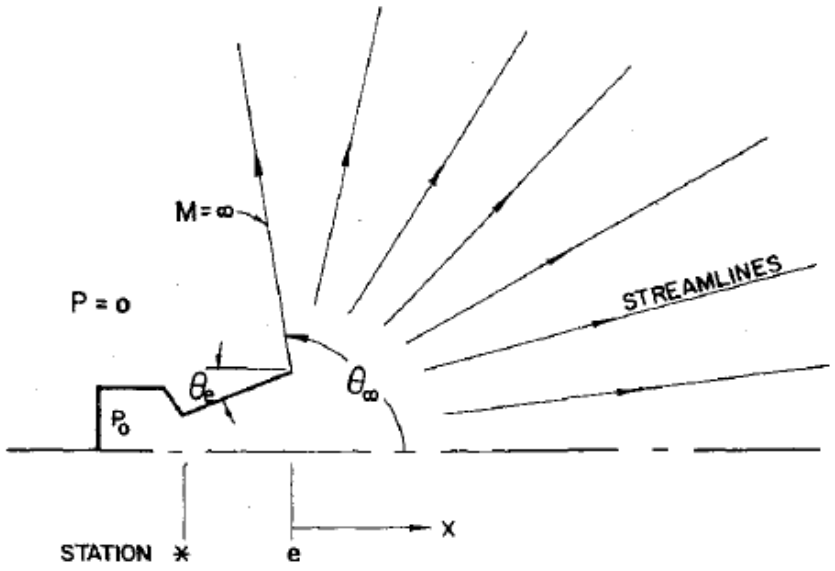

Figure 38: Assumed flow paths for Sibulkin model of plume exhausting into a vacuum [52]

Since the Sibulkin model assumes that the nozzle exhausts into a vacuum, the parameter *B* is based on the maximum flow angle of the nozzle exhaust from a Prandtl-Meyer expansion. Eq. (8) gives the Prandtl-Meyer function for the maximum flow angle, and Eq. (9) gives the Prandtl-Meyer function to calculate the nozzle exit conditions. Eq. (10) can be used to relate these to the physical flow angle based on the nozzle cone angle. The turn angle of the exhaust flow defines a solid angle given in Eq. (11) which Sibulkin uses to determine *B* as shown in Eq. (12).

$$\nu_\infty = \frac{\pi}{2}\left(\sqrt{\frac{\gamma+1}{\gamma-1}}-1\right) \tag{8}$$

$$\nu = \sqrt{\frac{\gamma+1}{\gamma-1}}\tan^{-1}\left[\sqrt{\frac{(M^2-1)(\gamma-1)}{\gamma+1}}\right] - \tan^{-1}\left[\sqrt{M^2-1}\right] \tag{9}$$

$$\theta_\infty = \nu_\infty - \nu_{exit} + \theta_{nozzle} \tag{10}$$

$$\psi_\infty = 2\pi(1-\cos\theta_\infty) \tag{11}$$

$$B = \frac{0.4\pi}{\psi_\infty} \tag{12}$$

3.2.2 Normal Shock Pressure Balance

In addition to the scaling parameter in Eq. (12), the density ratio at the jet terminal shock is required to determine the standoff distance. A stagnation pressure balance of the expanded and decelerated jet flow with the resulting stagnation pressure behind the freestream bow shock will set the location of the jet terminal shock because the flow speed at the interface equals zero and pressure is equal to stagnation pressure, as shown in Figure 39.

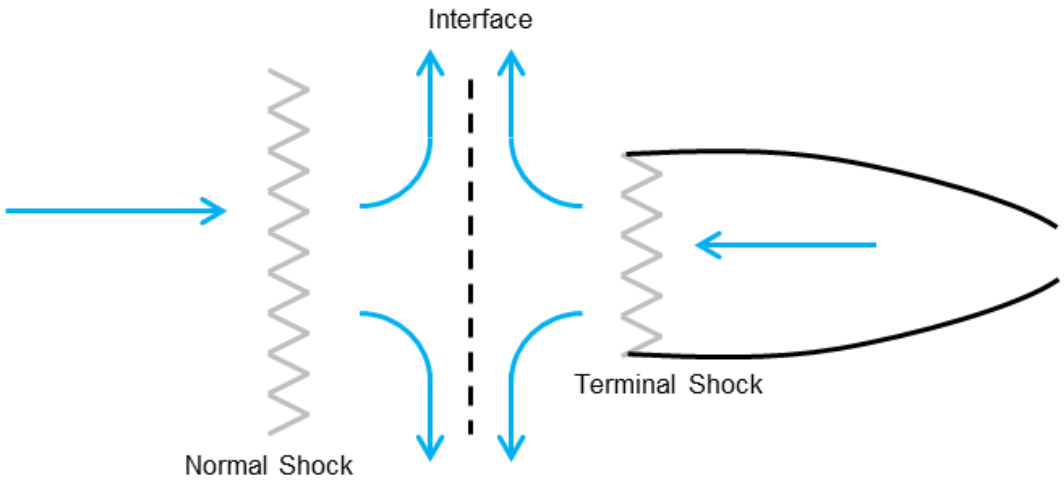

Figure 39: Assumed shock structure and flow paths for determining the stagnation pressure balance between freestream and jet flows

Assuming a freestream normal shock, the stagnation pressure before the bow shock can be determined from Eq. (13), with the stagnation pressure after the shock given in Eq. (14). The Mach number at which the terminal shock occurs sets the pressure at the terminal shock and the subsequent pressure of the decelerated jet flow. This Mach number is iterated upon until the resulting stagnation pressure of the decelerated jet flow through a normal shock equals that of the decelerated freestream. The stagnation pressure of the decelerated jet flow is given in Eq. (15). Once the terminal Mach number is found, the density ratio at the normal shock is given by Eq. (16) for use in determining the shock location with Eq. (7).

$$P_{T,\infty} = P_{\infty}\left[1+\frac{(\gamma-1)M_{\infty}^{2}}{2}\right]^{\frac{\gamma}{\gamma-1}} \tag{13}$$

$$P_{T,1} = P_{T,\infty}\left[\frac{(\gamma+1)M_\infty^2}{(\gamma-1)M_\infty^2+2}\right]^{\frac{\gamma}{\gamma-1}}\left[\frac{\gamma+1}{2\gamma M_\infty^2-(\gamma-1)}\right]^{\frac{1}{\gamma-1}} \tag{14}$$

$$P_{T,1,jet} = P_{T,jet}\left[\frac{(\gamma+1)M_{terminal}^2}{(\gamma-1)M_{terminal}^2+2}\right]^{\frac{\gamma}{\gamma-1}}\left[\frac{\gamma+1}{2\gamma M_{terminal}^2-(\gamma-1)}\right]^{\frac{1}{\gamma-1}} \tag{15}$$

$$\frac{\rho_{terminal}}{\rho_{T,jet}} = \left(\frac{P_{terminal}}{P_{T,jet}}\right)^{\frac{-1}{\gamma}} \tag{16}$$

3.3 Generating Plume Barrel Shock

The underlying plume barrel shock model is based on that described by Charwat [51]. That model determines the barrel shock for a jet exhausting into still air, assuming a nearly isentropic flow along the jet boundary with a constant jet edge Mach number. The model generates a consistently narrower plume since the plume is truncated at the terminal shock location. To correct the barrel shock, the shape given by the Charwat approach is assumed to be accurate. This shape is then scaled such that the mass flow rate out of the barrel shock and out of the jet terminal shock is equal to the input mass flow rate of the nozzle. To be consistent with the terminal shock location determined in Section 3.2, the direction of the flow along the barrel shock is assumed to radially emanate from the nozzle throat. The same relationship for density distribution is used to determine the conditions along the shock to calculate the mass flow rate.

3.3.1 Barrel Shock Shape Function

The equations for the Charwat model [51] describing the plume shape are described below. In addition, additional equations are shown to determine model flow parameters based on the SRP flow conditions. To determine the jet edge Mach number, a Prandtl-Meyer expansion is calculated at the nozzle exit, with final flow conditions set by the conditions behind the bow shock. The bow shock is assumed to be a normal shock, which sets the stagnation pressure into which the plume exhausts as shown in Eq. (14). Based on the jet total pressure and the nozzle geometry, the jet exit Mach number and exit pressure are calculated using Eq. (17) and Eq. (18). These two values allow for the jet edge Mach number to be calculated using Eq. (19).

$$\frac{A_{exit}}{A_{throat}} = \frac{1}{M_{exit}}\left[\frac{2+(\gamma-1)M_{exit}^{2}}{\gamma+1}\right]^{\frac{\gamma+1}{2(\gamma-1)}} \tag{17}$$

$$P_{exit} = P_{T,jet}\left[1+\frac{(\gamma-1)M_{exit}^{2}}{2}\right]^{\frac{-\gamma}{\gamma-1}} \tag{18}$$

$$M_{edge} = \sqrt{\frac{2}{\gamma-1}\left\{\left[1+\frac{(\gamma-1)M_{exit}^{2}}{2}\right]\left(\frac{P_{T,1}}{P_{exit}}\right)^{\frac{1-\gamma}{\gamma}}-1\right\}} \tag{19}$$

Charwat defines a function ψ which is constant along the jet boundary and is dependent on the jet edge Mach number and the nozzle exit Mach number and their respective isentropic area ratios as shown in Eq. (20). Additionally, the initial expansion angle of the

plume is calculated based on a Prandtl-Meyer expansion from the nozzle exit. The Prandtl-Meyer function is calculated using Eq. (9) for both the exit Mach number and jet edge Mach number, and the initial expansion angle is calculated using Eq. (21).

$$\psi = \frac{2}{\gamma+1}\frac{\sqrt{M_{edge}^2-1}}{M_{edge}^2\left(\frac{A}{A_{throat}}\right)_{edge}}\left(\frac{A}{A_{throat}}\right)_{exit} \tag{20}$$

$$\theta_0 = \nu_{edge} - \nu_{exit} + \theta_{nozzle} \tag{21}$$

Based on these parameters, Charwat goes on to define two scale parameters to be used in determining the barrel shock shape. These parameters are given in Eq. (22) and Eq. (23). The coordinates of the barrel shock are normalized via Eq. (24) for the axial coordinate and Eq. (25) for the radial coordinate. The axial coordinate is measured outward along the nozzle axis, with the origin at the nozzle exit. The radial coordinate is perpendicular to the nozzle axis, and represents the extent of expansion of the jet plume. Lastly, the integral relationship between the nondimensional plume coordinates is given by Eq. (26).

$$\rho_a = \sqrt{1+\frac{\theta_0}{\psi}} \tag{22}$$

$$\varphi = \psi + \theta_0 \tag{23}$$

$$X_{ND} = \frac{x}{r_{exit}\rho_a} \tag{24}$$

$$R_{ND} = \frac{r}{r_{exit}\rho_a} \tag{25}$$

$$X_{ND} = \int_{1/\rho_a}^{R_{ND}} \cot\left[\varphi\left(1 - R_{ND}^2\right)\right] dR_{ND} \tag{26}$$

Within Eq. (26), the plume shape is governed by the cotangent function, which tends to infinity as its argument tends to zero. As R is increased from its minimum value of $1/\rho_a$ at the nozzle exit to a value nearing 1, the cotangent function creates a large value for X. For the region near R = 1, the plume radius does not vary significantly with the axial coordinate due to this cotangent effect. Thus, to avoid the singularity at R = 1, the plume shape function is integrated until R = 0.999 to set the maximum radius of the jet flow. R is discretized from the lower limit of $1/\rho_a$ to this upper limit, and Simpson's rule is used to determine the integral over each interval. The final axial coordinate of the plume is based on the terminal shock location calculated previously, and the plume shape function is extended to that location with the maximum radius determined from the upper limit of R = 0.999.

3.3.2 Mass Flow Rate Scaling

For any plume structure, the mass flow rate input from the nozzle plenum conditions should be balanced by the mass flow through the boundaries of the plume. As described

in Section 3.3.1, the Charwat approach [51] to determining the barrel shock nominally assumes a plume of infinite length to create this mass flow rate balance. However, by truncating the plume at the location of the terminal shock as found using the method described in Section 3.2, the overall mass flow rate out of the barrel shock includes the flow through the boundary up to the terminal shock and the flow through the shock itself as illustrated in Figure 40. To ensure conservation of mass flow rate, the barrel shock is scaled such that the total mass flow out of the plume is equal to that which is defined as an input for a given thrust condition.

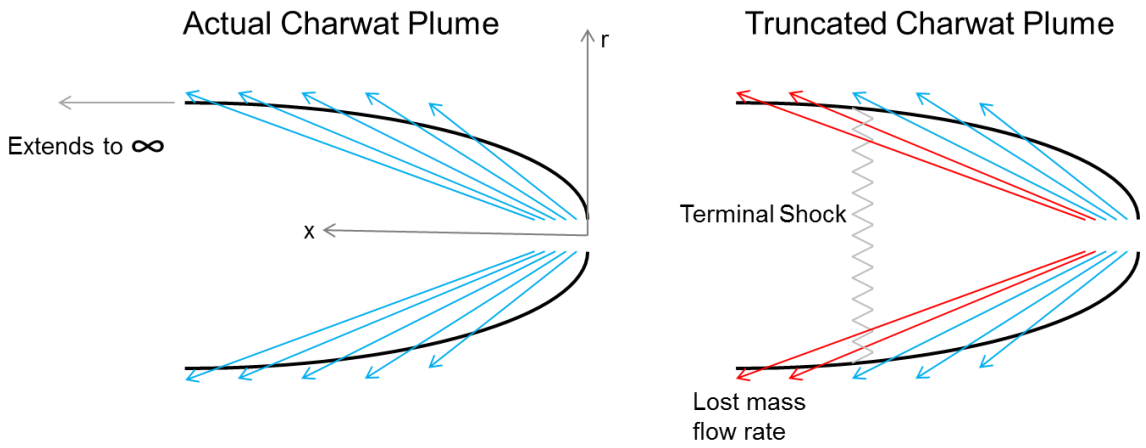

Figure 40: Comparison of boundary mass flow rate accounted (blue) and unaccounted (red) for between actual Charwat plume model and truncated plume with a terminal shock

This analysis assumes that the Charwat approach gives an appropriate shape function for the barrel shock, namely that the radial components as a function of distance from the nozzle exit can be uniformly scaled from the values calculated using the method detailed in Section 3.3.1. This is shown in Eq. (27) where r is the dimensional coordinate of the

barrel shock used previously in Eq. (25) and C is the scale factor which will be varied to create the mass flow rate balance.

$$r' = Cr \tag{27}$$

The mass flow rate out of the plume is then split into two components. For the assumed terminal shock, the flow direction is set to be normal to the shock, as shown in Figure 41. The second component, the outward flow through the barrel shock, is assumed to have a direction set by a radial extension from the nozzle throat to each point along the barrel shock, as shown in Figure 41. As the plume is assumed to be axisymmetric for this analysis, these vectors can be treated two dimensionally with a 360° rotation to account for the three-dimensional nature of the plume structure. Eq. (7), which sets the density ratio along a radial streamline as a function of distance, is used to determine the Mach number and subsequent velocity and pressure along the shock.

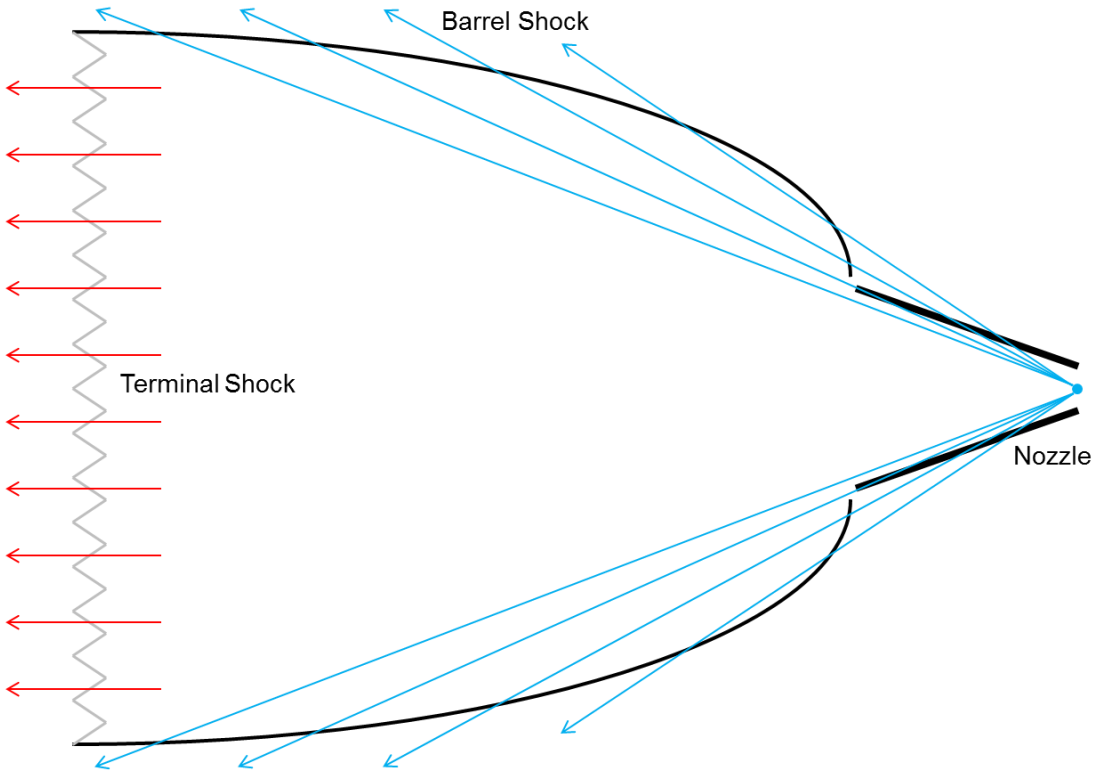

Figure 41: Vector representation of plume flow through barrel shock (blue) and terminal shock (red) used to calculate total mass flow rate out of the plume

There are three key assumptions for determining the flow directions through the plume boundaries. First is that the flow through the terminal shock is normal to the shock. Investigation of the single nozzle CFD solutions from Chapter II shows this to be a reasonable assumption, as the plume flow tends to expand and straighten out to roughly parallel the nozzle axis. The second assumption is that the direction of plume flow at the barrel shock can be represented by the vectors shown in Figure 41. Note that this assumption is not implying that the actual flow path follows these lines exactly, as that would require the flow to pass through the solid wall of the nozzle for some locations. Rather, this assumption use a virtual origin to model the flow direction of the jet exhaust as it passes through the barrel shock. The location of the virtual origin depends on where

the flow direction is needed. As the flow tends to turn as it passes through the barrel shock, the nozzle throat has been used as the virtual origin for the analytical model as the lines from that point are nearly tangent to the flow passing through the barrel shock, as shown in Figure 42. Investigation of the CFD solutions shown in Chapter II shows that this is a reasonably accurate assumption far from the nozzle exit as the plume flow establishes itself. Both of these assumptions are shown in Figure 42 with an example single nozzle CFD solution for C_T = 10.

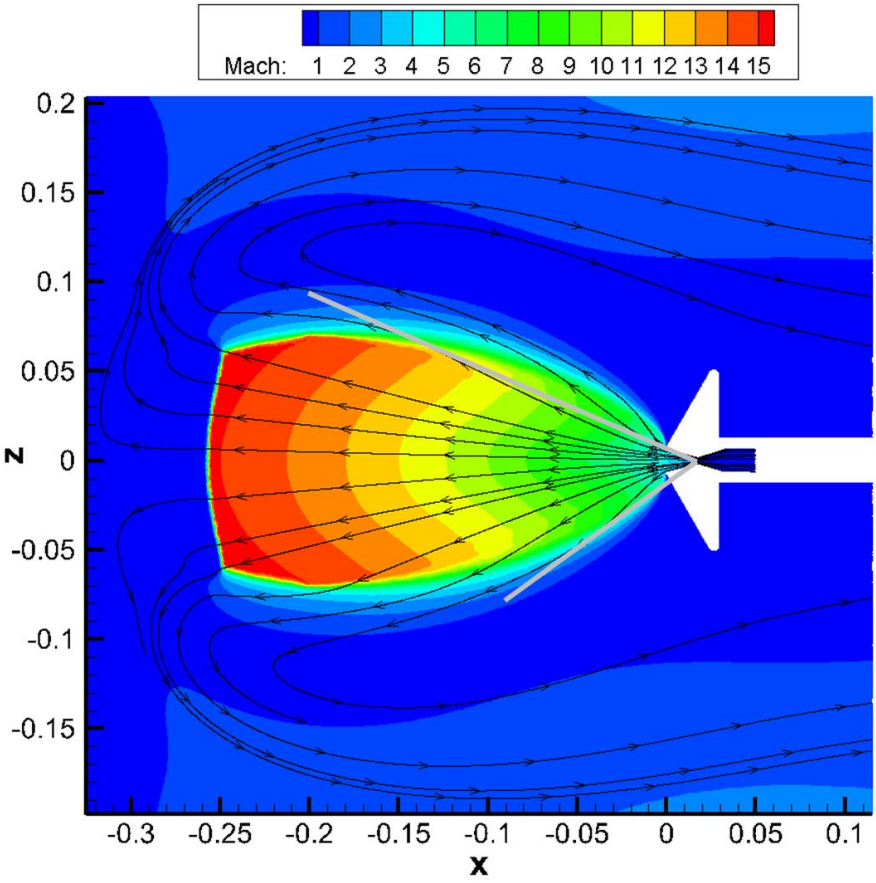

Figure 42: C_T = 10 CFD solution with streamlines and two example tangent lines (gray) demonstrating reasonability of nozzle throat assumption for determining flow direction

The third assumption relates to the flow through the barrel shock near the nozzle exit. This flow has turned out of the nozzle and would not actually appear to emanate from the assumed point at the throat. Figure 43 shows a linear fit of the calculated mass flow rate per differential axial length through the barrel shock as a function of distance along the axis from the nozzle exit for the CFD case shown in Figure 42. Integrating the CFD data represented by this linear fit gives the total mass flow rate through the barrel shock equal to 0.32 kg/s. The analytical model for this same case returns a mass flow rate through the barrel shock of 0.37 kg/s. Figure 43 shows that mass flow near the nozzle exit is a small percentage of the total mass flow rate. As a result, any errors associated with discrepancies in the flow direction approximation for this region will cause negligible differences in the integrated mass flow rate for the entire shock.

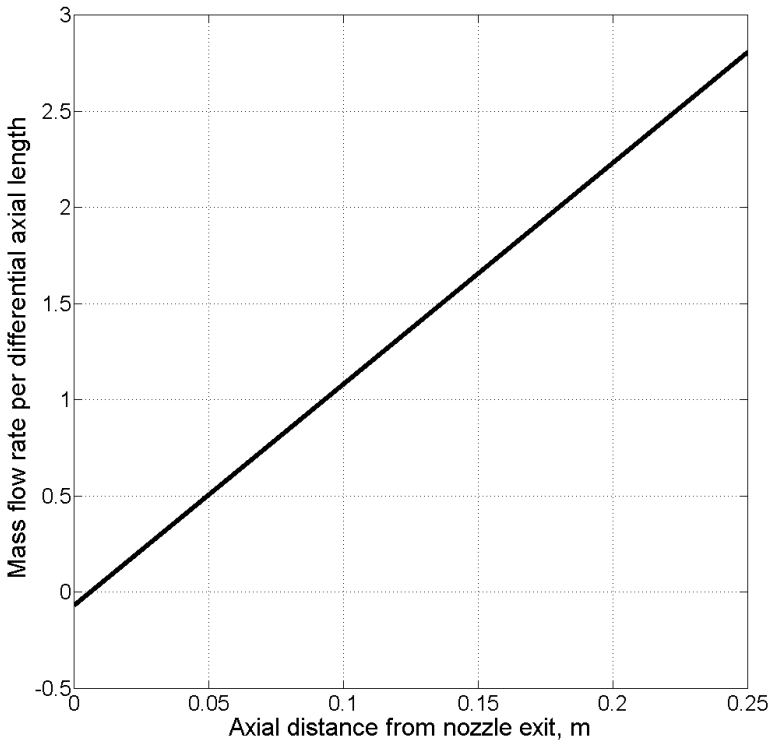

Figure 43: Trend line of mass flow rate per differential axial length for CFD solution of single nozzle configuration at $C_T = 10$

In general, mass flow rate over a given area is defined as shown in Eq. (28), where the area vector is defined to be an outward normal vector with magnitude equal to the area represented by the vector. Density and velocity of the flow are assumed to be constant across the represented area in this formulation.

$$\dot{m} = \rho\left(\vec{V} \cdot \vec{A}\right) \tag{28}$$

For the plume terminal shock, all flow is assumed to pass perpendicularly through the shock. Thus the mass flow rate will depend only on the density and flow speed at the shock, as well as the total exit area of the plume at this location. The terminal shock

Mach number is known from the stagnation pressure balance given in Eq. (15), which sets the flow conditions at the shock. The density ratio in Eq. (16), as well as the known total density for a given thrust condition as calculated in Eq. (29) set the density at the terminal shock. The pressure ratio, also used in Eq. (16), sets the pressure at the terminal shock. This can be used with the Mach number and density to calculate velocity, as shown in Eq. (30). The area of the terminal shock is determined from the scaled barrel shock radius, as calculated in Eq. (27), at the location of the terminal shock. The total outward mass flow rate for the plume terminal shock is given in Eq. (31).

$$\rho_{T,jet} = \frac{P_{T,jet}}{R_{gas} T_{T,jet}} \tag{29}$$

$$V_{terminal} = M_{terminal} \sqrt{\frac{\gamma P_{terminal}}{\rho_{terminal}}} \tag{30}$$

$$\dot{m}_{terminal} = \rho_{terminal} V_{terminal} \pi \left(Cr_{terminal} \right)^2 \tag{31}$$

For the flow through the barrel shock, the flow is assumed to pass through in a direction defined along a line extending from the center of the circular nozzle throat, as previously illustrated in Figure 41. The distance from this location to a point on the barrel shock, denoted as *d* and calculated using Eq. (32), determines the flow conditions at each point along the barrel shock using Eq. (7) to calculate the density ratio. The Mach number can be calculated using Eq. (33), and the pressure ratio can be calculated using Eq. (16).

Using the known total conditions for the jet, pressure and density can be calculated for use in Eq. (34) to determine the speed of the flow at the barrel shock.

$$d = \sqrt{\left(x + L_{cone}\right)^2 + \left(Cr\right)^2} \tag{32}$$

$$M_{barrel} = \sqrt{\frac{2}{\gamma - 1}\left[\left(\frac{\rho}{\rho_{T,jet}}\right)^{-(\gamma-1)} - 1\right]} \tag{33}$$

$$V_{barrel} = M_{barrel}\sqrt{\frac{\gamma P_{barrel}}{\rho_{barrel}}} \tag{34}$$

To determine the mass flow rate through each location along the barrel shock, the velocity direction and the normal vector to the shock need to be found. The velocity vector, being oriented along the line connecting the nozzle throat to a point on the shock, can be defined using the coordinates of the barrel shock, x_i and r_i, and the length of the conical nozzle section, L_{cone}, as shown in Eq. (35). The area vector can be defined for a given point *i* using central numerical differencing as shown in Eq. (36-38). Finally, the local mass flow rate can be rotated by 360° to account for the circular plume shape in three-dimensional space as shown in Eq. (39) and summed over each interior point along the shock to determine the total mass flow rate through the barrel shock as shown in Eq. (40). Adding the barrel shock mass flow rate to the terminal shock mass flow rate gives the total mass flow rate out of the plume.

$$\vec{V}_i = \frac{V_{barrel}}{d_i}\left[x_i + L_{cone}, \quad Cr_i\right] \tag{35}$$

$$dx_i = \frac{x_{i+1} - x_{i-1}}{2} \tag{36}$$

$$dr_i = \frac{r_{i+1} - r_{i-1}}{2} \tag{37}$$

$$\bar{A}_i = \frac{dx_i}{\sqrt{C^2 dr_i^2 + dx_i^2}}\left[-C \cdot dr_i, \quad dx_i\right] \tag{38}$$

$$\dot{m}_i = \left(2\pi C r_i\right)\rho_i\left(\bar{V}_i \cdot \bar{A}_i\right) \tag{39}$$

$$\dot{m}_{barrel} = \sum_{i=2}^{N-1} \dot{m}_i \tag{40}$$

3.4 Generating Bow Shock Shape

Supersonic flow will generally respond to a blunt obstruction in the flow field by creating a bow shock to decelerate the flow to stagnation conditions forward of the obstruction. Nominally, the obstruction seen by the supersonic freestream consists of a vehicle. In the case of SRP, this obstruction consists of both the vehicle and the jet exhaust flow, including the plume structure as well as the turned and decelerated jet flow. Work by Van Dyke [62] is used as the basis of the following analytical approach to modeling bow

shock structure for SRP flow fields. The decelerated and turned plume flow is assumed to create a hemispherical obstruction for each nozzle in a configuration, which provides geometry information for Van Dyke's approach to defining the bow shock. The location of each local hemispherical obstruction is based on the plume geometry and direction of the oncoming supersonic freestream. Each local obstruction, along with an approximation for the bow shock of the vehicle with no jets firing, is then combined into an overall three-dimensional shock structure by assuming that the furthest offset shock at a given radial location is the primary and sole shock that will be present at that location.

3.4.1 Bow Shock Shape Equations

Van Dyke assumes that a two-dimensional bow shock, i.e. a cross section of some three-dimensional bow shock, can be functionally represented as a conic section [62]. The governing equation for such a surface is given in Eq. (41), where R_S is the nose radius of the shock and B_S is the bluntness, similar in concept to the more traditional eccentricity of a conic section. For the bluntness factor, a negative value represents a hyperbola, zero represents a parabola, and a positive value represents an ellipse. These parameters and a coordinate system for the shock structure are noted in Figure 44.

$$r_{shock}^2 = 2R_S x_{shock} - B_S x_{shock}^2 \tag{41}$$

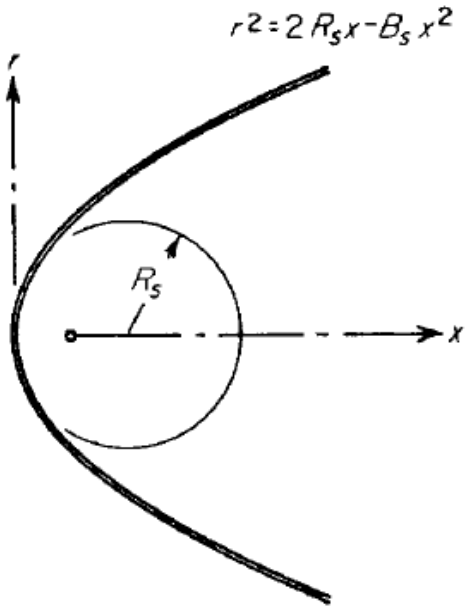

Figure 44: 2-dimensional bow shock formulation and relevant coordinate system [62]

Van Dyke proposes a second orthogonal coordinate system that contains the shock wave as one of its coordinate surfaces [62]. The coordinate transforms between the shock coordinate system (ξ, η) and the Cartesian system (x_{shock}, r_{shock}) are shown in Eq. (42) and Eq. (43). In this formulation, the shock wave itself is defined along η = 1, as shown in Figure 45. The focus of the conic section lies at $\xi = \eta = 0$.

$$\frac{x_{shock}}{R_S} = \frac{1}{B_S}\left[1 - \sqrt{\left(1 - B_S\xi^2\right)\left(1 - B_S + B_S\eta^2\right)}\right] \tag{42}$$

$$\frac{r_{shock}}{R_S} = |\xi|\eta \tag{43}$$

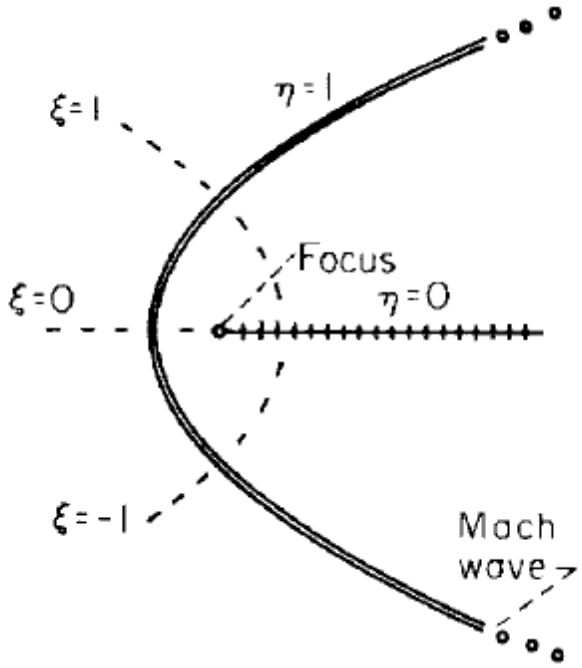

Figure 45: Shock aligned coordinate system for bow shock definition [62]

Van Dyke then describes a numerical finite difference scheme which propagates the flow from an assumed shock shape until the surface of the body can be defined along each constant ξ line. The η value at which the body appears will vary along each of these constant ξ lines. For a range of freestream Mach numbers, shock shape, and specific heat ratio values, results are tabulated to determine the bluntness of the body that would create the assumed shock structure. While the results are sparse over the entire set of all possible variable combinations, many of the results are reported for body bluntness, B_B, equal to 1 [62]. This would indicate a circular body in the two-dimensional sense. Appendix B contains tabulated values for B_S as a function of M and γ for hemispherical obstructions that are used in Section 3.4.3 to determine the approximate bow shock structure for SRP configurations.

3.4.2 Defining an Effective Hemispherical Obstruction

An SRP configuration with multiple nozzles will create multiple plumes and local obstructions to the supersonic freestream that affect the bow shock structure. These effects will vary with nozzle conditions, freestream conditions, and vehicle configuration. Past works have relied on hemispherical obstructions for defining flow field components for single nozzle configurations. This is being extended to multiple nozzle configurations by assuming that each plume is independent of all other plumes such that there is no jet coalescence or interaction associated with pressure boundary conditions effects from the presence of other plumes. The method determines an effective hemisphere for each plume to represent the boundary between the decelerated and turned jet flow after the plume terminal shock and the decelerated freestream behind the bow shock. This interface between the two flow regimes defines the obstruction seen by the freestream flow.

As noted in Section 1.2.1, a high pressure stagnation region inboard of a nozzle causes the plume flow to turn and flow outboard of the nozzles. As configuration and freestream relative flow angle (including both angle of attack and body roll angle) vary, the direction of relative flow between the supersonic freestream and the jet exhaust changes. Thus, the first consideration is to determine which direction the decelerated plume flow will turn based on the expected influence of the freestream. Traditional flight mechanics analysis denotes the freestream flow angle relative to an axis system where X is defined pointing out of the front of the vehicle, Z is directed downward, and Y completes the right handed coordinate system. Flow angles are defined using angle of attack and sideslip angle, which represent the flow angle in the X-Z plane and the flow

angle in the *Y-Z* plane respectively. For the following analysis, rather than deal with these two angles to create a full three-dimensional vector, a body roll angle and total angle of attack are used. The total angle of attack represents the angle between the freestream flow vector and the body *X* axis, while the body roll angle represents a rotation about the body *X* axis to align the freestream flow vector such that it is only in the *X-Z* plane.

Nozzle location on the vehicle is defined using both a radial component and an angular component. The radial distance specifies how far outboard (as measured perpendicular to the body *X* axis) the centerline of each nozzle intersects the vehicle outer mold line. The angular component represents a clockwise location, as viewed from in front of the vehicle, with zero degrees meaning that the nozzle centerline intersects the vehicle in the *X-Z* plane. To take into account body roll angle, the physical angular location can be combined with the body roll to create a total effective angular location for each nozzle using Eq. (44). Any nozzle with a total angular location of 0° or 180° will lie within the plane where total angle of attack is measured. Any other angles will result in nozzles that are out of this plane.

$$\Phi_{total} = \Phi_{nozzle} + \Phi_{body\_roll} \tag{44}$$

For nozzles which are located out of the angle of attack plane, the decelerated jet exhaust flow is assumed to turn outboard perpendicularly to the *X* axis along a vector passing through the *X* axis. Since the stagnation point on the vehicle will lie somewhere in the angle of attack plane, flow along the body will radiate away from this plane, thus causing these plumes to turn outboard. The analytical plume flow is assumed to be axisymmetric,

though the CFD simulations from Chapter II show asymmetric plume structures due to a variable pressure boundary condition around the three-dimensional plume structure which is beyond the scope of this analytical model. Nozzles which are located within the angle of attack plane will have their plume turning direction determined by the relative approach direction of the freestream flow to the nozzle exit location, as illustrated in Figure 46 for a four nozzle configuration with two nozzles in the angle of attack plane. The decelerated plume exhaust is assumed to flow in the same general direction as the oncoming freestream relative to the nozzle exit. For a plume exhausting directly into the freestream, no overall direction is assumed, as this situation should result in a uniform flow of the decelerated plume exhaust in all directions around the plume structure.

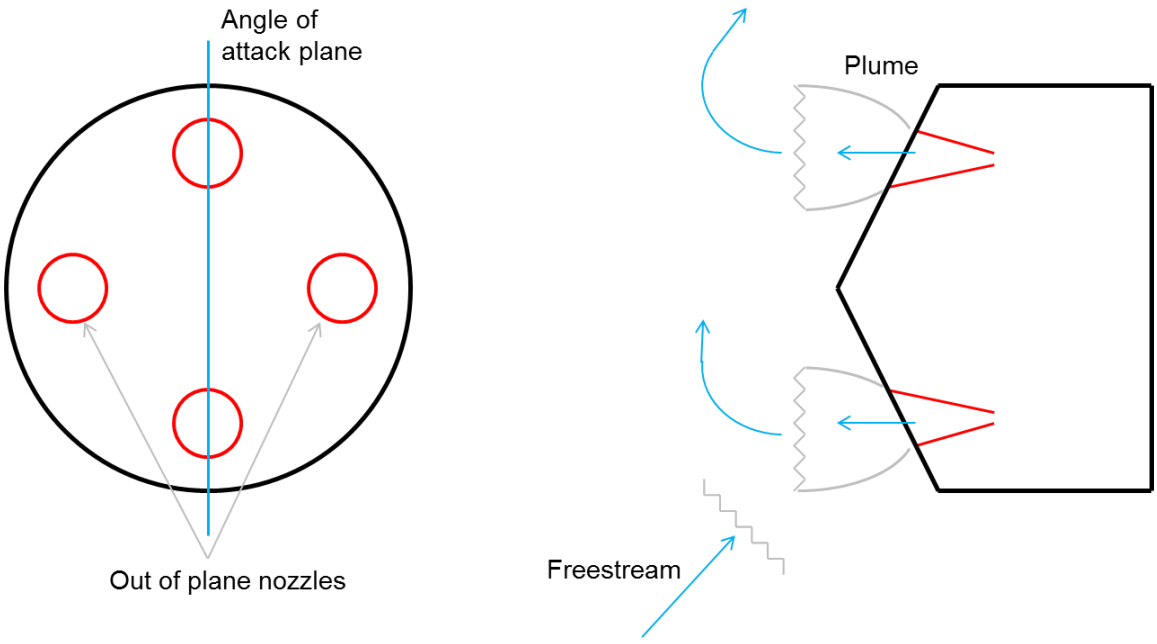

Figure 46: Example four nozzle configuration at angle of attack with two nozzles in the angle of attack plane (left) and assumed turning of decelerated plume exhausts (right)

Once the flow direction is determined, the effective hemispherical obstruction can be defined. In this work, the decelerated plume flow is assumed to begin turning immediately after passing through the plume terminal shock with a turning radius of zero. In actuality, the physical turning radius of the decelerated jet flow will be greater than zero as the flow requires some distance in order to isentropically change its flow direction. Calculating the turning radius as a function of the input vehicle configuration, freestream conditions, and thrust conditions should be more accurate in defining the plume obstruction; however, this requires increased knowledge of the streamlines in the flow field as the conditions into which this turn occurs will vary significantly with nozzle orientation and flow conditions. Thus, to simplify the model and use predicted flow structures that are already calculated as part of the analytical model, the center of the effective hemisphere is set to be the point on the barrel shock corresponding to the location of the plume terminal shock about which a rotation of the flow away from the stagnation point is seen as shown in Figure 46. The hemispherical radius is set equal to the diameter of the plume terminal shock to represent that all of the jet exhaust flow must turn due to the presence of a supersonic freestream. This is illustrated in a two-dimensional sense in Figure 47. The actual flow path has some minimum positive turning radius which will cause the hemisphere to be centered further outboard and have a larger maximum radius than this model assumes. Assuming a hemisphere centered along the barrel shock does not required more complicated modeling of the interface between the plume flow and the decelerated freestream flowing around the plume, which would set this outboard hemisphere center.

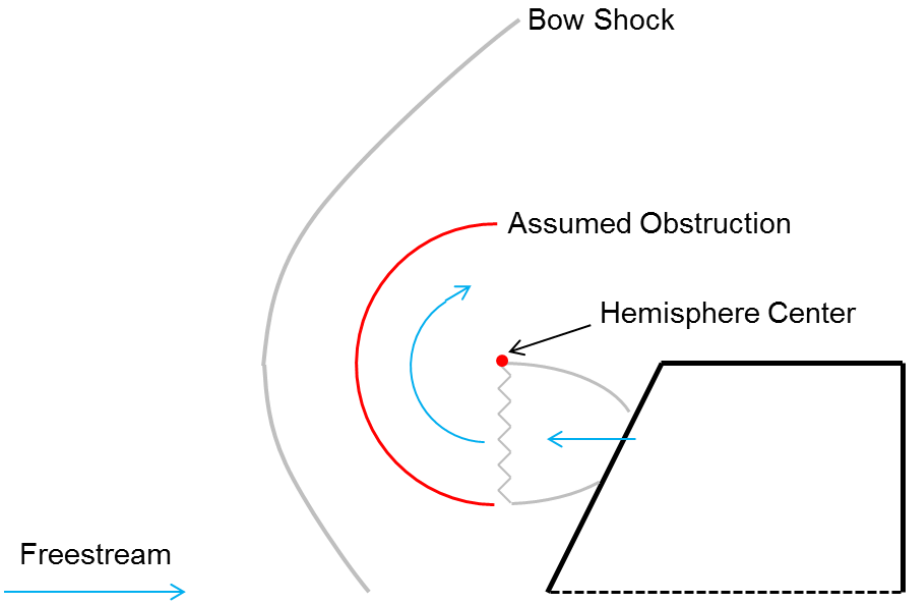

Figure 47: 2-dimensional illustration of location of hemisphere center and definition of the radius used to create the hemispherical obstruction

A schematic view directly into the plume terminal shock is shown in Figure 48. This is to illustrate the overpredictive nature of this assumption of a hemispherical obstruction in the three-dimensional sense. The plume flow is not expected to have significant out of plane expansion, though the hemispherical obstruction necessarily models behavior in this manner. Thus an overprediction of each plume in the out of plane directions is expected when compared with experimental or CFD solutions. Knowing that there is a consistent possibility of overprediction means that the flow features of interest will be bounded within the calculated bow shock structure.

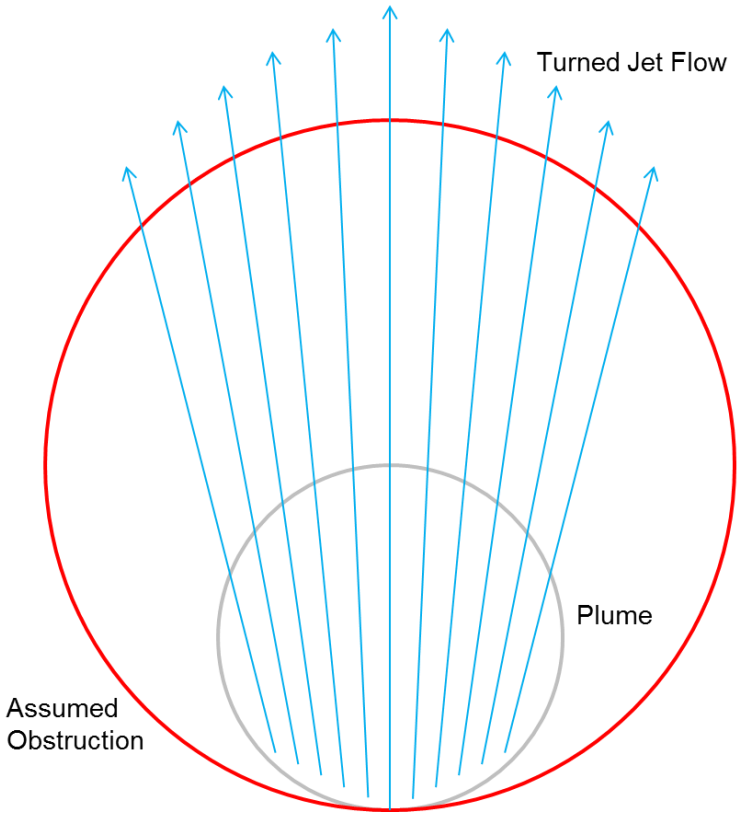

Figure 48: Head-on view of notional expected plume flow and hemispherical obstruction demonstrating that obstruction should overpredict out of plane bow shock structure

3.4.3 Calculating Three-Dimensional Bow Shock Structure

Once the effective hemispherical obstruction is defined for each plume flow, the three-dimensional bow shock structure can be calculated. Examining Eq. (42) and Eq. (43) reveals that the local shock structure requires knowledge of B_S, R_S, ξ, and η to solve for x_{shock} and r_{shock}. The shock bluntness term is found by interpolating the data in Appendix B for the input freestream Mach number and γ. Along the shock, $\eta = 1$, and ξ can be varied to calculate the distribution of x_{shock} and r_{shock} as functions of ξ. Rather than perform the numerical integration of Van Dyke for the entire bow shock structure, the

assumption of a hemispherical obstruction means that only the flow along $\xi = 0$ needs to be solved to determine R_S. The geometry for this calculation is shown in Figure 49.

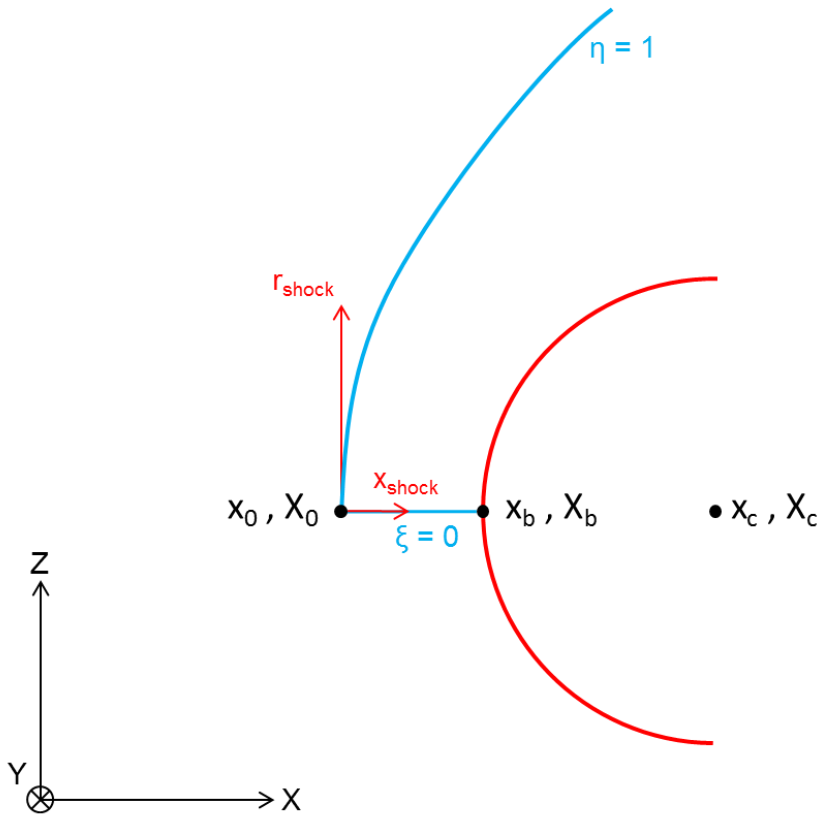

Figure 49: Nondimensional coordinate system (blue), dimensional shock space (red), and actual dimensional coordinate system (black) with key axial points for determining shock nose radius

There are three coordinate systems of interest to the problem, as noted in Figure 49. First, there is the nondimensional (ξ, η) space, within which $\eta = 1$ for the shock is known as well as $\xi = 0$ along the line between the shock and the body on the axis. Unknown in this frame is η_{body}, which specifies the nondimensional location of the body along this axis. The next space of interest is the dimensional shock space (x_{shock}, r_{shock}) with the origin at the intersection of the shock with the axis (corresponding to $\xi = 0$ and $\eta = 1$). In this

space, x_0 is known to be zero, while x_b and x_c are unknown. The last coordinate system of interest is the actual, dimensional coordinate system related to the physical location of the plume in the (X, Y, Z) space of the entire vehicle. In this system, the location of the focus, X_c, is known to be the center of the hemisphere found in Section 3.4.2. The distance between this point and the hemisphere is equal to the diameter of the terminal shock, which means that X_b is known. The only unknown in this coordinate system is X_0, which would be the actual standoff location of the bow shock in front of the effective hemispherical obstruction. The final unknown which will be calculated is the shock nose radius, R_S, which is a function of the unknowns listed here. A summary of the known and unknown geometry variables and their associated coordinate systems is summarized in Table 6.

Table 6: Known and unknown variables for each coordinate system used to solve for shock nose radius parameter

	Nondimensional (ξ,η)	Dimensional Shock (x_o, r_{body})	Physical Space (X, Y, Z)
Knowns	ξ = 0 on axis η = 1 on shock B_S	$x_o = 0$	X_c X_b
Unknowns	η_{body} R_S	x_b x_c	X_0

The coordinate transform noted in Eq. (42) and some geometrical relationships provide enough equations to solve for all of the unknown variables in this problem. First, Eq. (45) and Eq. (46) show applications of Eq. (42) to calculate the points x_c and x_b as functions of

R_S along the shock axis, denoted as A_1 and A_2 respectively. The relationship shown in Eq. (47) can then be used to determine the value for R_S. Lastly, Eq. (48) is used to calculate X_0 based on a known x_0 and a calculated x_c.

$$A_1 = \frac{x_c}{R_S} = \frac{1}{B_S}\left(1 - \sqrt{1 - B_S}\right) \tag{45}$$

$$A_2 = \frac{x_b}{R_S} = \frac{1}{B_S}\left(1 - \sqrt{1 - B_S + B_S \eta_{body}^2}\right) \tag{46}$$

$$\left|X_b - X_c\right| = \left|x_b - x_c\right| = R_S \left|A_2 - A_1\right| \tag{47}$$

$$\left|X_0 - X_c\right| = \left|x_0 - x_c\right| = \left|x_0 - R_S A_1\right| \tag{48}$$

With a known center point for the effective hemispherical obstruction, known geometrical parameters for the shock equations given in Eq. (42) and Eq. (43), and various values of ξ, the local bow shock structure profile can be calculated in the actual, dimensional coordinate system of the SRP geometry. This profile can then be rotated by 360° to approximate the full three-dimensional effect caused by the local obstruction created by each plume and the vehicle. To determine the global bow shock structure for the entire SRP configuration, the furthest offset bow shock from the vehicle as a function of radius and rotation angle about the axis is assumed to be the primary bow shock that will exist in the actual flow field. No shock-shock interaction of the bow shocks from

each hemispherical obstruction is assumed in this analysis. Rather, the intersection of two different local bow shocks is treated as a continuous, but not necessarily differentiable, transition from one bow shock structure to the other.

3.5 Model Enhancements

The analytical model as described to this point provides the basic flow features expected to exist within an SRP flow field. Two enhancements to this model have also been developed to further refine the analytical plume structure for each nozzle. First, an approximation of the free shear layer thickness is calculated along the barrel shock. This provides insight into the expected thickness of the plume boundary beyond the assumed infinitesimally thin barrel shock in the analytical model. Second, an estimation of the crossflow velocity of the nominal flow along the surface if no plumes are present is used in conjunction with the exit conditions of a nozzle to determine a deflection angle for the plume due to the local crossflow experienced at the nozzle exit.

3.5.1 Free Shear Layer Approximation

The free shear layer approximation used in this analytical model is based on the turbulent boundary layer equations for flow over a flat plate, as described by Anderson [90]. The underlying equation for the boundary layer thickness as a function of distance along a flat plate is given in Eq. (49), where Re_x is the Reynolds number based on the distance along the plate.

$$\delta = \frac{0.37 x_{plate}}{\mathrm{Re}_x^{1/5}} \tag{49}$$

In an SRP plume, there is no solid flat plate; however, the boundary between the plume and the external flow field can be thought of as a constant boundary since there is assumed to be no mixing between the two flow regions. Rather than treat the plume as an exact flat plate, the distance x_{plate} in Eq. (49) is assumed to be the arc length along the barrel shock calculated in Section 3.3. Rearranging Eq. (49) allows for the calculation of a Reynolds number per unit length as shown in Eq. (50). This can be calculated at each point along the barrel shock, then applied to Eq. (51) to determine the shear layer thickness as a function of arc length, *s*.

$$\mathrm{Re}_c = \frac{\rho_s V_s}{\mu} \tag{50}$$

$$\delta = \frac{0.37 s^{4/5}}{\mathrm{Re}_c^{1/5}} \tag{51}$$

The density and velocity in Eq. (50) are based on the flow properties at each location along the barrel shock. Equation (7) is used to find the density based on the distance the flow travels to reach a point along the barrel shock, consistent with the plume flow assumptions from Section 3.2.1. The pressure ratio for each point can be calculated by applying Eq. (16), and the Mach number can be found using Eq. (52). The velocity at

each point, which is needed in the Reynolds number calculation, is then found using Eq. (53).

$$M_s = \sqrt{\frac{2}{\gamma - 1}\left(\frac{\rho_s}{\rho_{T,jet}}\right)^{\frac{\gamma-1}{-1}-1}} \tag{52}$$

$$V_s = M_s \sqrt{\gamma \frac{P_s}{\rho_s}} \tag{53}$$

To further account for the fact that the barrel shock is not a flat plate, the shear layer thickness is applied to each point on the surface as a distance normal to the barrel shock and directed outward from the plume flow. This assumes that the barrel shock is the innermost plume structure, and is consistent with using the plume flow properties to determine the local Reynolds number, as the plume flow acts as local freestream conditions for use in the boundary layer thickness equation.

3.5.2 Effect of Nozzles Exhausting at an Angle to Freestream Flow

In an SRP flow field, the plumes do not exhaust into a purely stagnant flow. Rather, the plumes encounter the existing flow field around the entry vehicle which creates perturbations to the plume flow. This is effectively a jet in a local crossflow, and the strength of the crossflow depends on both the angle between the nozzle axis and the freestream flow vector and the angle between the nozzle axis and the surface of the vehicle. Both angles are needed as the direction of the freestream flow vector sets the

stagnation point on the vehicle, and the incidence angle of the nozzle axis to the surface determines the relative angle of the surface flow to the jet flow. In addition to these orientation considerations, the physical cause of perturbations to a jet in crossflow is due to the static pressure, velocity, and stagnation pressure of the flow into which the nozzle exhausts. These effects manifest themselves across the entire length of the plume, as the direction of the crossflow will depend on how far removed from the surface the plume reaches. Modeling the entire flow field and the interaction between the decelerated freestream that causes the crossflow and the plume flow for each nozzle is beyond the capabilities of analytical approaches.

Simplifying assumptions have been made in this model to account for these perturbations. First, the decelerated freestream flow which causes the crossflow deflection is assumed to always be parallel to the vehicle surface at the location where the nozzle intersects the vehicle. This is true near the surface, but not as valid in the flow field far from the vehicle where the flow reacts to the plume structure. Additionally, the static pressure contribution to the plume deflection is considered to be minimal, such that the primary driver of the crossflow deflection angle is the relative velocity of the decelerated freestream surface flow to the jet exit flow. This allows for vector relationships to be used to define the deflection angle. Lastly, the entire plume is assumed to rotate due to the local crossflow perturbations. In actuality, the pressure boundary condition that alters the plume structure varies as a function of the angular location around the plume, such that the inboard plume boundary has the largest perturbation while the outboard plume boundary is less disturbed. Attempting to model this variable

deflection effect requires knowledge of the flow as it passes around the plume obstruction, which is beyond the scope of this model.

To model the effects of crossflow on the plume structure, the numerical source panel method for nonlifting flows described by Anderson [90] is adapted for an SRP flow field. This method assumes a subsonic freestream flow with a distribution of sources and sinks defined piecewise along an arbitrary surface. The method returns both a surface pressure coefficient relative to the subsonic freestream conditions and a velocity at each point along the surface. To recreate the subsonic freestream, the flow behind the bow shock in the SRP flow field is used as a local effective freestream, assumed to be conditions caused by a normal shock to be consistent with prior assumptions in the analytical model. The velocity potential for this flow is given in Eq. (54) assuming a continuous body. The angle of attack here is assumed to be nearly zero, such that the stagnation point on the vehicle remains close to the nose. By breaking the body up into panels, the discrete form of the governing velocity potential can be found as shown in Eq. (55) for a given panel *i* based on the effects of every panel *j*. This form assumes the control point for each panel is the center of the panel. The distance from each control point is given in Eq. (56).

$$\phi(x,y) = \int_a^b \frac{\lambda ds}{2\pi} \ln(r) \tag{54}$$

$$\phi(x_i, y_i) = \sum_{j=1}^{N} \frac{\lambda_j}{2\pi} \int_j \ln(r_{ij}) ds_j \tag{55}$$

$$r_{ij} = \sqrt{\left(x_i - x_j\right)^2 + \left(y_i - y_j\right)^2} \tag{56}$$

For an inviscid flow or the flow external to a viscous boundary layer, the normal component of velocity to the surface equals zero. This is used as the boundary condition in the panel method to obtain the normal velocity equation given in Eq. (57) for one panel. By populating this equation for each panel, *N* linear equations are formed with *N* unknowns, namely the source strength for each panel, λ_j. This can be described in a general matrix form shown in Eq. (58).

$$\frac{\lambda_i}{2} + \sum_{\substack{j=1 \\ j \neq i}}^{N} \frac{\lambda_j}{2\pi} \int_j \frac{\partial}{\partial n_i} \left(\ln\left(r_{ij}\right)\right) ds_j + V_{sub} \cos\beta_i = 0 \tag{57}$$

$$\left[A_{i,j}\right]\left[\lambda_j\right] = \left[C_i\right] \tag{58}$$

A schematic of the relevant parameters for a given panel *i* is shown in Figure 50. The vector n_i represents the outward normal to a panel. The angle β_i is the angle between this outward normal and the freestream flow direction. Another angle θ_i represents the angle between the panel itself and the freestream flow direction.

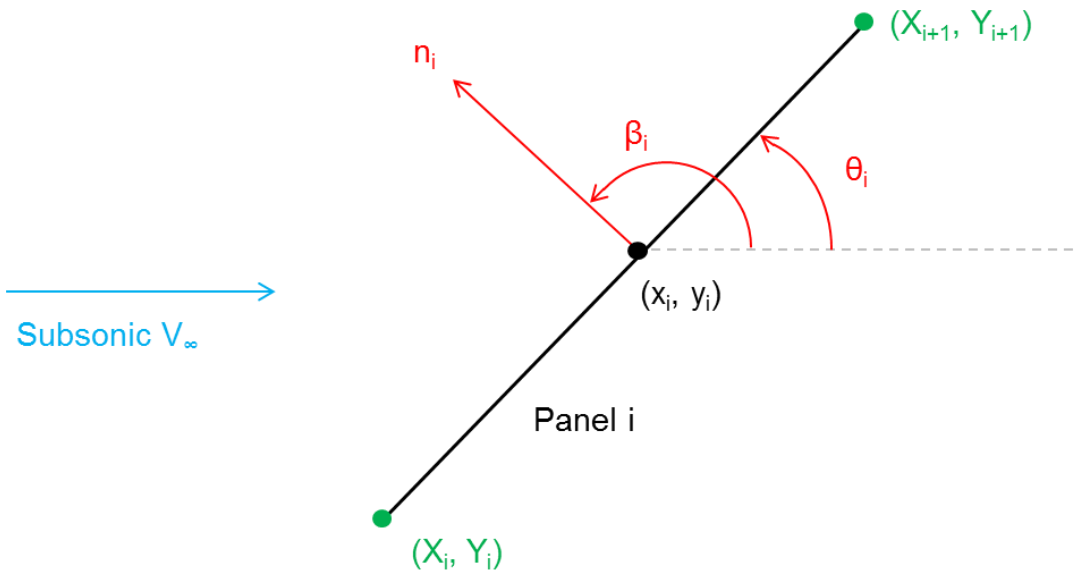

Figure 50: Schematic of a single panel with relevant points and angles relative to the freestream flow direction for the subsonic panel method

In Eq. (57), there are three terms which will be used to populate the matrix and vectors in Eq. (58). The first term defines the diagonals of the matrix $A_{i,j}$, as shown in Eq. (59) since this terms represents the contribution of a given panel's source term to its own velocity. The second term, which is a summation of the contribution of all other panels to the normal velocity, populates the other terms in the matrix $A_{i,j}$, as shown in Eq. (60), where $I_{i,j}$ represents the integral in the term. The last term of Eq. (57) populates the constant vector C_i, as shown in Eq. (61).

$$A_{i,i} = \frac{\lambda_i}{2} \tag{59}$$

$$A_{i,j} = \frac{\lambda_j}{2\pi} I_{i,j} \tag{60}$$

$$C_i = -V_{sub}\cos\beta_i \tag{61}$$

The integral term can be solved for this equation using integral tables and defining certain intermediate variables. Equations (62)-(67) give the definitions of the intermediate variables, and Eq. (68) gives a close formed expression for the integral expression in the normal velocity equation shown in Eq. (57). The intermediate variables are functions of the geometry shown in Figure 50, including the control point of the panel, each endpoint of the panels, and the incidence angle of the panel surface to the subsonic freestream. The panel being examined is panel *i* in this notation, while *j* represents another panel whose impact on panel *i* is being evaluated.

$$I_1 = -(x_i - X_j)\cos\theta_j - (y_i - Y_j)\sin\theta_j \tag{62}$$

$$I_2 = (x_i - X_j)^2 + (y_i - Y_j)^2 \tag{63}$$

$$I_3 = \sin(\theta_i - \theta_j) \tag{64}$$

$$I_4 = (y_i - Y_j)\cos\theta_j - (x_i - X_j)\sin\theta_j \tag{65}$$

$$I_5 = \sqrt{I_2 - I_1^2} \tag{66}$$

$$S_j = \sqrt{\left(X_{j+1} - X_j\right)^2 + \left(Y_{j+1} - Y_j\right)^2} \tag{67}$$

$$I_{i,j} = \frac{I_3}{2}\ln\left(\frac{S_j^2 + 2I_1S_j + I_2}{I_2}\right) + \left(\frac{I_4 - I_1I_3}{I_5}\right)\left[\tan^{-1}\left(\frac{S_j + I_1}{I_5}\right) - \tan^{-1}\left(\frac{I_1}{I_5}\right)\right] \tag{68}$$

After populating the matrix $A_{i,j}$ and constant vector C_i, the matrix equation given in Eq. (58) can be solved to obtain the required source strength for each panel. These can then be used to solve for the tangential velocity of the flow along the surface, as given in Eq. (69) generally and Eq. (70) in terms of the intermediate variables defined previously. A pressure coefficient relative to the subsonic local freestream can be calculated using Eq. (71). In order to determine the actual pressure coefficient relative to the supersonic freestream of the SRP problem, the subsonic local freestream conditions will need to be used to determine the dimensional pressure, which can then be substituted back into the definition of C_P to get the pressure coefficient relative to the supersonic freestream conditions.

$$V_{s,i} = V_{sub}\sin\beta_i + \sum_{j=1}^{N}\frac{\lambda_j}{2\pi}\int_j \frac{\partial}{\partial s}\left(\ln\left(r_{ij}\right)\right)ds_j \tag{69}$$

$$V_{s,i} = V_{sub}\sin\beta_i + \sum_{j=1}^{N}\frac{\lambda_j}{2\pi}\left[\left(\frac{I_4 - I_1I_3}{2I_5}\right)\ln\left(\frac{S_j^2 + 2I_1S_j + I_2}{I_2}\right) - I_3\left[\tan^{-1}\left(\frac{S_j + I_1}{I_5}\right) - \tan^{-1}\left(\frac{I_1}{I_5}\right)\right]\right] \tag{70}$$

$$C_{P,sub} = 1 - \left(\frac{V_{s,i}}{V_{sub}} \right)^2 \tag{71}$$

A comparison of surface pressure distributions for the 60° sphere-cone used as the baseline geometry in Chapter II is shown in Figure 51 to demonstrate the accuracy of the panel method in determining the surface properties when the subsonic flow behind the normal shock is used as a local effective freestream. Results from a baseline CFD simulation with no thrust from the nozzles and modified Newtonian flow are used for validation. The analytical panel method captures the peak surface C_P value at the nose that is seen in the CFD solution. Overall, the shape of the analytical panel method pressure distribution has a similar shape as that of modified Newtonian flow. Modified Newtonian flow is designed for hypersonic flows, and as such may not be as accurate for the supersonic, Mach 2 flow simulated in the CFD solution. The primary discrepancy between the analytical panel method and the other two pressure distributions is at the shoulder, where the pressure is not predicted to drop as low as is seen in either the CFD solution or modified Newtonian pressure distribution. This is likely related to the acceleration of the flow around the shoulder, which may not be accurately captured by the analytical panel method using a local effective subsonic freestream.

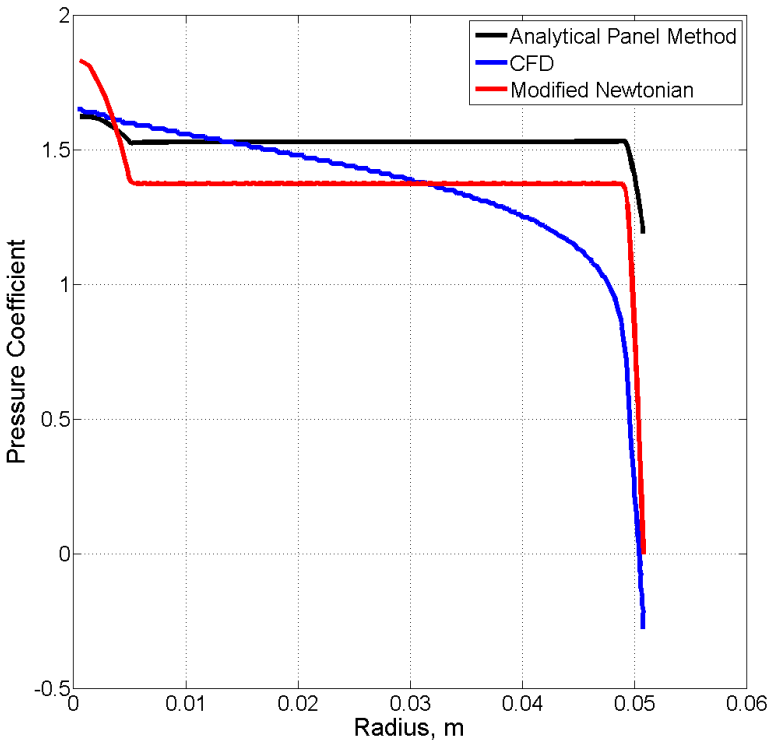

Figure 51: Comparison of surface pressure distribution for the baseline, 60° sphere-cone geometry for the analytical panel method, CFD solution, and modified Newtonian

Once the surface velocity that would exist without the presence of the plumes is known at the location of the nozzle exit, this is assumed to be the speed of the flow which causes the crossflow effects on the plume. This flow is assumed to emanate from near the nose, meaning that the flow velocity should always be directed outboard, causing the plume to turn away from the stagnation point. A velocity triangle is used to determine the deflection angle of the plume caused by the local crossflow, as shown in Figure 52. The parallel velocity component is defined to be the component of the crossflow velocity in the direction of the jet exit velocity, as defined in Eq. (72). The perpendicular velocity is any velocity from the crossflow which does not flow along the jet exit velocity vector, as defined in Eq. (73). The crossflow angle of deflection can then be calculated using Eq.

(74). To include the crossflow angle in the plume definition, the barrel shock described in Section 3.3 is rotated outboard by the crossflow angle about the intersection of the nozzle axis with the vehicle surface. This assumes that the flow within the nozzle is unperturbed by the crossflow and only the flow that occurs outside of the nozzle should be affected.

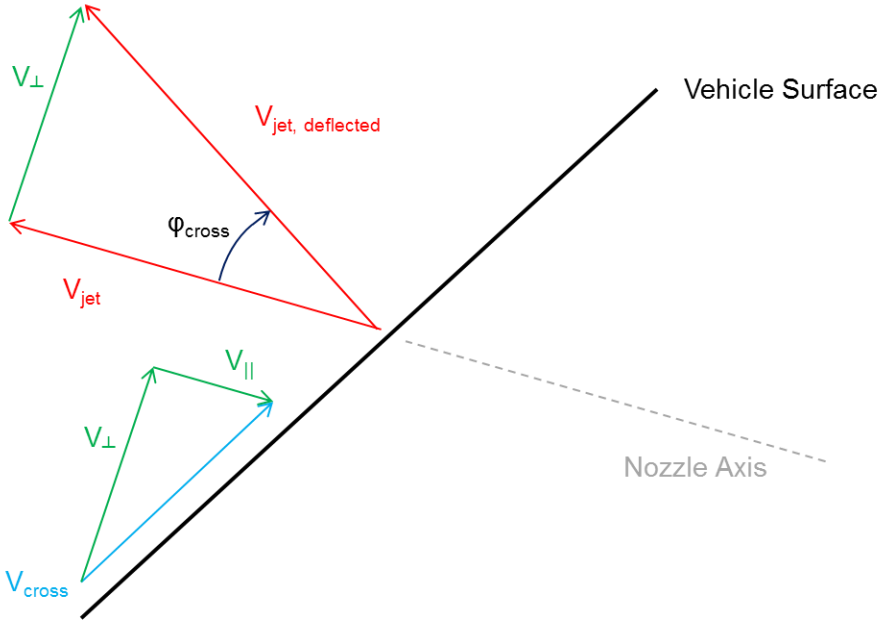

Figure 52: Schematic of the velocity triangle created to determine the deflection angle of the plume caused by the local crossflow

$$\vec{V}_{\parallel} = \frac{\left(\vec{V}_{jet} \cdot \vec{V}_{cross}\right)\vec{V}_{jet}}{\left|\vec{V}_{jet}\right|^2} \tag{72}$$

$$\vec{V}_{\perp} = \vec{V}_{cross} - \vec{V}_{\parallel} \tag{73}$$

$$\phi_{cross} = \tan^{-1}\left(\frac{\left|\vec{V}_{\perp}\right|}{\left|\vec{V}_{jet}\right|}\right) \tag{74}$$

CHAPTER IV

COMPARISON OF ANALYTICAL MODEL TO COMPUTATIONAL FLUID DYNAMICS SIMULATIONS

4.1 Trade Space Definition

The analytical model described in Chapter III does not assume a specific nozzle configuration or forebody shape. Experimental results to date have exclusively focused on geometries which have nozzles oriented parallel to the vehicle axis, with the majority of computational efforts focusing on similar configurations. While the analytical model will be validated against these available configurations, the lack of validation data for other configurations requires the development of vehicle geometries and nozzle configurations for which CFD simulations can be run to provide comparable data. The design of these vehicles for the purpose of this thesis is to cover a range of possible design variables to demonstrate the flexibility of the analytical model with respect to vehicle and nozzle configuration. Eight candidate geometries have been identified to investigate the effects of relevant SRP design variables on key flow field components.

4.1.1 SRP Design Variables

The design variables of interest for defining the comparison cases can be split into two distinct categories, those associated with freestream and jet flow conditions and those associated with vehicle geometry and configuration. Both sets of variables are shown in Table 7 along with possible settings for each variable. The flow condition variables are not used to define the validation geometries, but are instead used to determine run

conditions for each final configuration. Mach number and angle of attack define the freestream conditions of the SRP system, as nominally defined by some wind tunnel test condition or trajectory analysis. Thrust coefficient represents the performance of the SRP system as an enhancement to the deceleration force felt by the vehicle. Gamma represents variation in atmospheric and jet exhaust chemistry. Ideally, this variable would vary independently for both the freestream flow and the jet flow; however, FUN3D is limited to a single global value of gamma when solving the calorically perfect compressible Navier-Stokes equations.

Table 7: Matrix of SRP Design Variables for Determining Validation Cases

Property	Values			
Specific Heat Ratio (γ)	1.2	1.3	1.4	
Mach number	2	3	4	
Angle of attack	0	Negative	Positive	
Thrust coefficient	Low	Mid-low	Mid-high	High
Number of nozzles	1	3	4	6
Nozzle cant angle	0°	Low	Mid	High
Nozzle location	Forebody nose	Forebody outboard	Aftbody	
Aeroshell geometry	Sphere-cone	Capsule		
Aftshell geometry	Conical	Cylindrical		
Plume-vehicle interaction	Yes	No		

The geometric variables used to define the vehicle configurations are key parameters to be considered in the design of an SRP system. The number of nozzles affects how thrust is distributed for a given configuration, with a lower thrust generating a smaller plume for

a given engine design. Canting the nozzles outboard will affect the propulsive-aerodynamic interaction. Nozzle location on the forebody has been shown in past work to have a significant impact on the interaction between the exhaust plumes and the freestream flow. An aftbody nozzle location will further remove the plumes from interaction with the bow shock and potential forebody shadowing, which should result in more surface pressure preservation on the forebody.

Aeroshell geometry is included as a trade variable due to the variations in aerodynamic performance with aeroshell shape. While the shape is not expected to significantly affect the plume shadowing, if there is little to no shadowing then the aerodynamic characteristics of the vehicle will be preserved. For these geometries, all nozzles are assumed to be scarfed such that there are no protrusions from the outer mold line (OML) of the vehicle. The aftshell geometry will affect integration of aftbody nozzles with the vehicle. A conical aftshell necessitates higher cant angles, as the converging aftshell angle defines a theoretical lower limit on the nozzle orientation. A cylindrical aftshell provides the capability to integrate a lower cant angle nozzle with the aftshell geometry. If the nozzle exhaust is a hot gas, plume-vehicle interaction could have also thermal implications for regions of the vehicle and must be considered for vehicle design.

4.1.2 Trade Space Definition

In order to define the validation cases for the analytical model, a series of trade space reductions are performed. The first such reduction is to remove the flow condition variables from consideration and only investigate the vehicle geometries and nozzle

configurations. As FUN3D will be used to create a CFD simulation for each validation case, the number of geometries is critical since each geometry requires its own computational grid. Flow conditions will be important for determining the final list of run conditions, but do not need to be considered for the purposes of defining the validation vehicle configurations. Additionally, the single nozzle case has been removed from consideration in the trade space, as validation data for that configuration already exists for both wind tunnel experiments and computational simulations. In the present investigation, multiple nozzle configurations are the focus of the trade space.

A full factorial investigation of the vehicle geometry variables (minus the single nozzle configuration) would result in 144 possible combinations. The compatibility of each variable has been investigated to determine if certain configurations would not be physically possible to create, resulting in two compatibility criteria. First, any configuration that would result in nozzles with zero cant angle and a location on the aftshell has been eliminated. As the nozzles for all configurations are assumed to be integrated internally to the vehicle, it is not possible for a nozzle to intersect any aftshell shape while still directing its exhaust parallel to the vehicle axis. If the aftshell is conical, then low cant angles are also deemed incompatible. Second, any configurations with canted nozzles located at the nose of forebody have been eliminated due to vehicle packaging considerations, as there is not enough space in the nose region of the vehicle for multiple canted nozzles to coexist. A diagram showing these incompatibilities is given in Figure 53. Eliminating these incompatible solutions from the trade space leaves 90 possible vehicle and nozzle configurations.

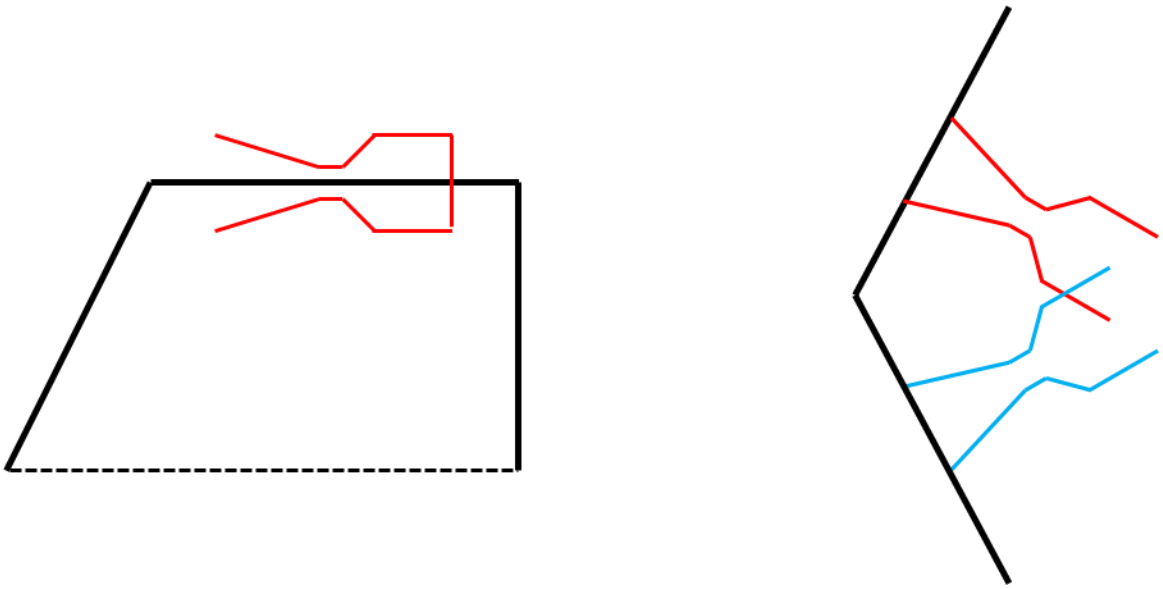

Figure 53: Zero cant angle on aftshell (left) results in incompatible nozzle integration and canted nozzles near nose (right) result in incompatible nozzle intersection

To further reduce the trade space and define the CFD validation geometries, relevance to the analytical model has been considered. Any number of nozzles near the forebody nose will result in significant plume coalescence for any appreciable thrust, as there is not enough volume for each plume to behave independently of each other. As the analytical model is not capable of modeling a single, coalesced plume from multiple nozzles, all configurations with nozzles at the nose have been removed from the trade space. Additionally, since the analytical model does not model plume-surface interactions, any configurations that may exhibit significant plume-surface interaction are removed. This includes low cant angle nozzles located on the aftbody as well as any cant angle nozzles on a conical aftbody. The conical aftbody results in significantly scarfed nozzles regardless of cant angle, which increases the likelihood of errors associated with the analytical model since it nominally uses the median exit radius to define the exit area of the nozzle.

In the morphological matrix shown in Table 7, three multiple nozzle counts are considered: three, four, and six nozzles. The three and four nozzle configurations do not result in drastically different thrust distributions to each nozzle. Comparing the effects of the highest and lowest multiple nozzle counts will provide sufficient information to determine the effects of thrust distribution on the flowfield structure for validation of the analytical model. All four nozzle configurations are removed from the trade space due to this consideration.

Lastly, consideration of shielding due to the plumes has been considered. For any nozzles located on the forebody, a lower cant angle should provide more forebody shielding, resulting in a decrease in pressure across the vehicle. This should not be strongly dependent on forebody shape as the lower pressure will result in a significantly reduced drag coefficient. For higher cant angles, the plumes should turn more outboard, thus shielding less of the forebody and preserving pressure on the vehicle. While the aerodynamic performance in this case will depend on the forebody shape, the overall effect of plume shielding should be evident regardless of the chosen forebody. For consistent comparison of surface pressure and plume effects, any configuration with nozzles located on the forebody will assume that the forebody shape is a sphere-cone to be consistent with the results shown in Chapter II. For nozzles located on the aftshell of the vehicle, the plumes are not expected to significantly affect any forebody surface properties, as the plumes will no longer be shielding the forebody of the vehicle. While aeroshell shape would be important in terms of the aerodynamics preserved on the forebody, the effects of the plumes on forebody surface pressure should be independent of forebody shape as the plumes are removed from the region forward of the vehicle. For

configurations with nozzles located on the aftbody, a capsule forebody shape will be used to demonstrate that the plumes have minimal impact on forebody surface pressure.

4.1.3 Selected Analysis Geometries

After reducing the SRP trade space to define the validation geometries and configurations, a total of eight possible configurations have been selected. The details of these configurations are shown in Table 8, and can be split into three distinct areas of interest. The first two geometries represent the models discussed in Chapter II, and have been used for the initial analytical model validation. The next three geometries perturb a single aspect of SRP design, the nozzle cant angle, to determine its effect on the flowfield structure and surface pressure. The last three geometries represent nozzles located on the aftshell of the vehicle. The three and six nozzle configurations will investigate the effect of thrust distribution on SRP performance, and the two cant angles have been selected to demonstrate the effects that plume impingement on the vehicle can have on SRP performance. Nominally, each of these configurations will be run at the same freestream conditions as the results presented in Chapter II so that comparisons between geometry effects will not be confounded with variations in freestream conditions. As detailed in Section 4.1.4, variation in freestream Mach number and the ratio of specific heats in the flow will also be investigated for select geometries to provide insight into the effects of flow conditions on the analytical model predictions.

Table 8: Validation geometries and configurations for analytical model

No.	Number of Nozzles	Nozzle Cant Angle	Nozzle Location	Aeroshell Geometry	Aftshell Geometry
1	1	0°	Forebody Nose	Sphere-cone	Sting
2	3	0°	Forebody Outboard	Sphere-cone	Housing
3	3	10°	Forebody Outboard	Sphere-cone	Cylindrical
4	3	20°	Forebody Outboard	Sphere-cone	Cylindrical
5	3	30°	Forebody Outboard	Sphere-cone	Cylindrical
6	3	30°	Aftbody	Capsule	Cylindrical
7	6	30°	Aftbody	Capsule	Cylindrical
8	6	60°	Aftbody	Capsule	Cylindrical

4.1.4 Validation Cases

To validate the components of the analytical model, the results from Chapter II will be used for geometries 1 and 2 in Table 8. The single nozzle geometry creates an axisymmetric plume structure which will be used for validation of the plume components of the analytical model. The three nozzle geometry will be used for validation of the entire analytical model, including the plume structure and the resulting bow shock structure.

The forebody nozzle canting geometries provide insight into the variations in flow physics due to changing the orientation of the jet exhaust to both the local crossflow on the vehicle surface and the freestream flow direction. As the nozzle canting increases for geometries 3-5, the plume flow becomes more normal to the forebody, meaning that the scarfing of the nozzle decreases. Additionally, the canting causes the jet flow to be initially turned outward, which should result in less shielding of the forebody. Both of these factors will affect the formation of the plume structure and the subsequent bow

shock, creating a more complex flow condition for validation of the analytical model. Table 9 details the cases which are run for geometries 3-5, with cases for C_T = 1, 4, 7, and 10 run at zero angle of attack for all configurations. For the 10° and 30° nozzle canting configurations, angle of attack cases are run to determine static pitch stability and trim capabilities of each configuration.

Nozzles located on the aftbody of an entry vehicle will have plumes exhausting into a much different flow regime than forebody nozzles. The plumes should have little to no impact on the forebody surface pressure, as the plumes are far removed from the forebody. These cases will be used to validate the analytical model for conditions where the plume is not exhausting into a stagnation region and where plume-surface interaction may occur. Table 10 details the flow conditions that are examined for geometries 6-8. The three nozzle aftbody configuration has the same pressure ratios for C_T = 1, 4, 7, and 10 as are used for the three nozzle, forebody located nozzle configurations. The six nozzle configurations have each nozzle provide half the thrust of a single engine in the three nozzle configurations, and the total pressure ratios input for the plenum flow have been adjusted. Additional cases at C_T = 20 are run on each of these geometries, where the nozzles have the same pressure ratio as C_T = 10 on the three nozzle configuration. Angle of attack cases are run on all three geometries to examine the static pitch stability and trim capabilities of these configurations.

Table 9: Validation cases for geometries with canted nozzles located on the vehicle forebody

Geometry	C_T	$P_{T,jet}/P_\infty$	Angle of Attack
3	1	1504.0	0°
3	4	6166.5	0°
3	7	10678.7	0°
3	10	15040.4	0°
3	10	15040.4	-10°
3	10	15040.4	10°
4	1	1504.0	0°
4	4	6166.5	0°
4	7	10678.7	0°
4	10	15040.4	0°
4	10	15040.4	-20°
5	0	--	0°
5	1	1504.0	0°
5	1	1504.0	-10°
5	1	1504.0	10°
5	1	1504.0	-30°
5	4	6166.5	0°
5	7	10678.7	0°
5	10	15040.4	0°
5	10	15040.4	-10°
5	10	15040.4	10°
5	10	15040.4	-30°

Table 10: Validation cases for geometries with canted nozzles located on the vehicle aftbody

Geometry	C_T	$P_{T,jet}/P_\infty$	Angle of Attack
6	0	--	0°
6	1	1504.0	0°
6	4	6166.5	0°
6	7	10678.7	0°
6	10	15040.4	0°
6	10	15040.4	-10°
6	10	15040.4	10°
6	10	15040.4	-30°
7	1	752.0	0°
7	4	3008.1	0°
7	7	5264.2	0°
7	10	7520.2	0°
7	10	7520.2	-10°
7	10	7520.2	10°
7	20	15040.4	0°
8	1	752.0	0°
8	4	3008.1	0°
8	7	5264.2	0°
8	10	7520.2	0°
8	10	7520.2	-10°
8	10	7520.2	10°
8	20	15040.4	0°

In addition to the validation cases which investigate the effect that geometry has on SRP flowfield structure, cases are run for varying freestream conditions to investigate the

effects of Mach number and ratio of specific heats on the analytical solution and computational SRP flow field. Both nozzle thrust and freestream total pressure are held constant as Mach number is varied to simulate a vehicle flying in the same ambient atmosphere with the same mass flow rate through the nozzles. Holding these values constant means that the freestream static pressure and dynamic pressure change, subsequently changing the freestream Reynolds number and nozzle thrust coefficient. These variations are summarized in Table 11. The variation in Mach number is investigated for Geometry 6, the three nozzle configuration with the nozzles located on the aftbody. This has been chosen due to the limited interaction of the plumes with the bow shock structure, demonstrated in Chapter VI. An increase in Mach number should result in a bow shock closer to the vehicle and a change in the pressure region into which the nozzles exhaust, so the extent of this interaction can be examined as a function of Mach number.

Table 11: Flow conditions for varying freestream Mach number while holding nozzle thrust and freestream total pressure constant

Mach	P_∞ (Pa)	*Re/m*	C_T	$P_{T,jet}/P_\infty$
2	1762.3	1589877.0	10	15040.4
3	375.4	508006.6	20.8	70609.2
4	90.8	163832.4	48.5	291863

Variation in the ratio of specific heats, γ, is also investigated. This simulates variations in the atmospheric composition as well as the jet flow composition. FUN3D assumes a constant γ throughout the flow field, so the effects of varying composition flow fields

interacting with each other are not investigated here. The ratio of specific heats should affect the expansion of the plumes and the properties behind the bow shock. These cases are run at Mach 2 with the same freestream static pressure and temperature as the results presented in Chapter II. Thrust will again be held constant, and γ values of 1.2 and 1.3 are run in addition to the γ = 1.4 case. Table 12 shows the relevant input parameters for each of these cases.

Table 12: Flow conditions for varying γ with constant freestream Mach number and static pressure as well as constant thrust

γ	Re/m	C_T	$P_{T,jet}/P_\infty$
1.4	1589877.0	10	15040.4
1.3	1531923.0	10.8	22684.7
1.2	1471824.0	11.7	41493.6

4.1.5 Determining Primary Flow Features

In addition to overlays of the analytical model prediction with CFD solutions for the thrust conditions examined on each configuration, the agreement of the analytical model and CFD for the locations of three primary flow features will also be quantified. Maximum radial extent of the plume represents the maximum Z coordinate of the outboard barrel shock. To obtain this value from the CFD Mach contours, the jet edge Mach number as calculated in the analytical model for a given thrust condition and configuration will be used to define the location at which the barrel shock should form. Values of the jet edge Mach number for a given thrust condition and given number of nozzles are shown in Table 13. Maximum axial extent of the plume represents the largest distance in the X direction of the plume barrel shock or terminal shock as measured from

the origin at the vehicle nose. In the CFD solutions, which exhibit asymmetric plume structures, this will be found as the furthest upstream location of the barrel shock or terminal shock, depending on the orientation of the plume in the flow. Maximum bow shock axial extent represents the largest standoff distance of the bow shock structure in the *X* direction as measured from the origin at the vehicle nose. In the CFD solutions, this will either be measured to the local plume shock or the inboard bow shock structure, whichever is furthest upstream. Two metrics will be used to determine the accuracy of the analytical model for each primary flow feature. The absolute difference equals the value from CFD solution subtracted from the value predicted by the analytical model. The percent difference represents the analytical model value relative to the CFD solution value. For the maximum axial extent features, because the positive *X* direction is aligned with the freestream, overprediction by the analytical model will have a negative absolute difference and a positive percent difference. The maximum plume radial extent is measured in the positive *Z* direction, so an overprediction by the analytical model will be positive for both metrics.

Table 13: Jet edge Mach number data for varying number of nozzles

One Nozzle		Three Nozzles		Six Nozzles	
C_T	M_{edge}	C_T	M_{edge}	C_T	M_{edge}
0.47	3.86	1.0	4.43	1.0	3.90
0.75	4.21	1.7	4.87	4.0	5.01
1.05	4.47	3.0	5.36	7.0	5.50
2.00	5.01	4.0	5.65	10.0	5.84
3.00	5.36	5.0	6.84	20.0	6.53
4.04	5.63	6.0	6.01		
5.00	5.83	7.0	6.18		
6.00	6.01	8.0	6.30		
7.00	6.16	9.0	6.42		
8.00	6.30	10.0	6.53		
9.00	6.42				
10.00	6.53				

4.2 Analytical Model Validation for Wind Tunnel Configurations

Initial validation of the analytical model is performed using the CFD solutions shown in Chapter II in addition to corresponding experimental data available from the Jarvinen and Adams wind tunnel investigations [10]. Since these nozzles have 0° cant angles and the body angle of attack is 0°, these cases represent a less complex flow field than would be expected for non-zero values of these parameters while still covering a wide range of possible flowfield structures. The single nozzle geometry is used to validate the plume structure, including the plume terminal shock location, the barrel shock shape, and the

free shear layer. The three nozzle geometry is used to validate the plume structure as well as the effective obstruction and resulting bow shock caused by multiple independent plumes.

4.2.1 Plume Terminal Shock Location

The stagnation pressure balance used to define the terminal shock location, as described in Section 3.2, depends on the expansion of the nozzle exhaust to the Mach number at which the terminal shock forms. To validate this assumption, the Mach number near the terminal shock in the CFD solutions presented in Section 2.3.2 is found by probing the CFD flow field near the shock for each thrust coefficient. The calculated terminal shock Mach number from the analytical model is compared with the CFD results in Figure 54. As thrust increases, the terminal shock Mach number also increases due to the requirements of balancing stagnation pressure with the decelerated freestream. For low thrust conditions that exhibit no distinct terminal shock, the reported Mach number is the highest value seen in each CFD simulation. The analytical model for these cases shows good agreement in capturing this peak Mach number, even though the CFD shows that the plumes in these solutions decelerate through diffusion rather than a normal shock. For thrust conditions where a distinct terminal shock is seen, the analytical model and CFD are in good agreement. The lone discrepancy is at $C_T = 5$, which appears to be related to the CFD result rather than the model. Examining the flow field for this case shows the anticipated flow structure formation, but the Mach contours within the plume do not follow the trends of the other thrust coefficients run. For $C_T > 2$, the analytical model consistently overpredicts terminal shock Mach number relative to the CFD solutions. As

thrust increases, the difference between the analytical model and CFD solutions decreases, indicating that the assumption of radial flow along the axis is more correct as the plume grows larger. This is consistent with the theory used to develop the analytical model, where flow far from the nozzle exit resembles a radial flow field.

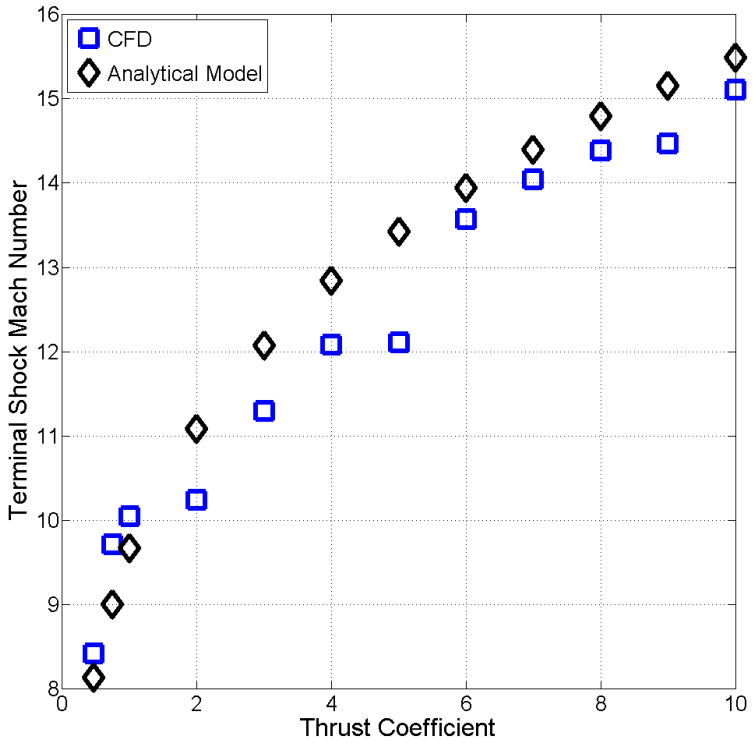

Figure 54: Comparison of terminal shock Mach number between CFD simulations and analytical model for the single nozzle configuration

The analytical model uses the terminal shock Mach number to calculate the density ratio at the shock, which sets the standoff distance as defined in Eq. (7). A comparison of the terminal shock location for varying thrust coefficient on the single nozzle configuration is shown in Figure 55. At low thrust coefficients ($C_T < 1$), the analytical model significantly underpredicts the total extent of the plume. This is due to the fact that the analytical

model assumes a normal shock while these thrust conditions decelerate the jet through diffusion. Even though the peak Mach number agrees well for these conditions, the inability of the analytical model to capture this low thrust effect means that the current model is not valid at these conditions. For higher thrust coefficients that exhibit a distinct terminal shock, the analytical model agrees well with the available data, though a slight consistent underprediction of the shock location is seen compared to both datasets. This underprediction is most likely related to the underlying assumption of fully isentropic flow of the nozzle exhaust. The actual flow field contains a plume boundary that constricts the jet flow and elongates the plume relative to the stagnation pressure balance approach of the model. As the difference between the CFD and analytical solutions appears to remain roughly constant over the C_T values examined, the percent error decreases with increasing thrust. This is consistent with the result seen when comparing terminal shock Mach number, where the larger thrust conditions create an environment that is in better agreement with the assumptions of the analytical model.

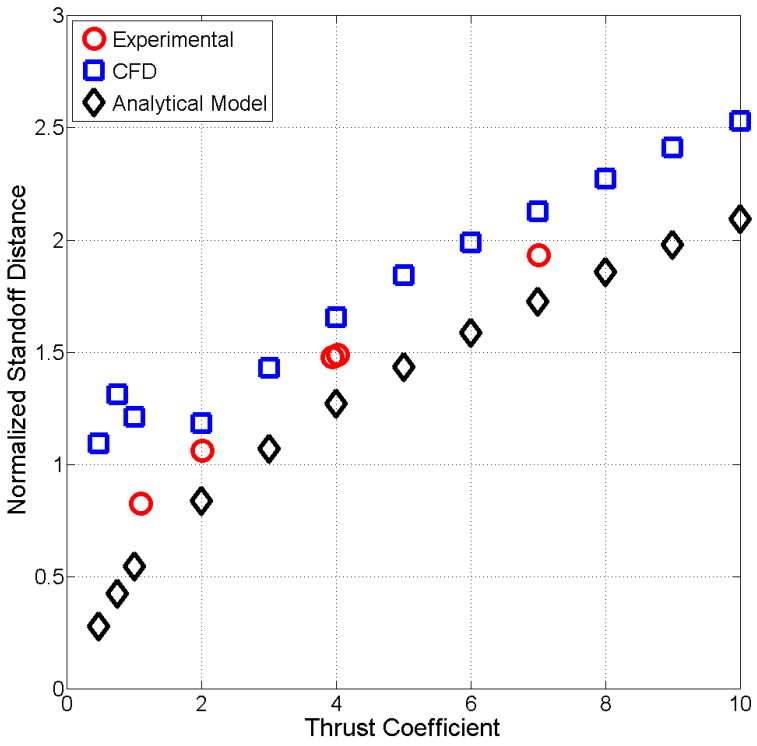

Figure 55: Comparison of terminal shock standoff distance between experimental data, CFD simulations, and analytical model for the single nozzle configuration

4.2.2 Axisymmetric Mass Flow Balance

The plume structure is defined by the method described in Section 3.3, where the overall plume shape is first determined assuming an infinitely long plume that is truncated at the terminal shock location. The truncated plume is then scaled such that the mass flow rate through both the terminal shock and barrel shock is equivalent to the input mass flow rate of the nozzle. To investigate the performance of the mass flow rate scaling far from the nozzle exit, a comparison of the plume radius at the terminal shock location is shown in Figure 56. The CFD simulations do not have a sharp barrel shock, but rather a barrel shock and free shear layer that form in the flow field. Thus, there is a thickness associated with the computational solutions that is represented in the plot as an upper and lower

bound. These bounds have been extracted from the CFD solutions by probing the contours shown in Chapter II. The lower bound represents the approximate boundary between the core plume flow and the transition through the barrel shock. The upper bound represents the outermost boundary between the plume flow and the recirculation region that forms for the single nozzle configuration.

For the low thrust solutions, where the plume is elongated, the free shear layer is thin and the analytical model agrees well with the upper bound of the CFD simulations. Even though these plume structures do not exhibit a distinct terminal shock, the mass flow rate scaling approach is still able to capture the maximum plume radius seen in the CFD solutions. For the higher thrust cases, where the plume structure exhibits a terminal shock, the analytical model consistently falls between the lower and upper bounds. As thrust increases, the shear layer grows larger and the spread between the bounds increases. The analytical model tends to approach the lower bound of the CFD data, which should occur since that bound is approximately taken to be the location of the barrel shock and the barrel shock is what is being modeled in the analytical method.

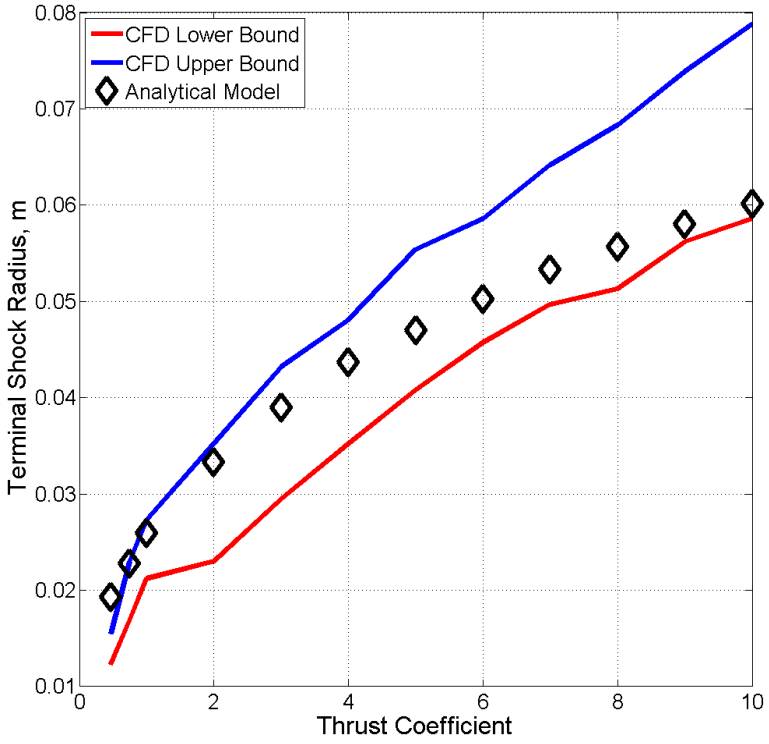

Figure 56: Comparison of terminal shock radius between lower and upper bounds in CFD simulations and analytical model for the single nozzle configuration

A comparison of the full plume is shown in Figure 57 for four thrust coefficients. As expected, the C_T = 1.05 analytical solution shows a significant underprediction of the extent of the plume due to this thrust level exhibiting a plume without a distinct terminal shock. For the analytical model, there is a consistent overprediction of the plume radius as a function of the distance along the plume axis compared to the CFD simulation near the nozzle exit. As thrust increases and the plume extends further upstream, the analytical prediction of the barrel shock slightly underpredicts the radius, as seen for C_T = 10. For higher thrusts, the initial expansion from the nozzle exit is well predicted by the scaled barrel shock of the analytical model. As noted in Section 4.2.1, the consistent underprediction of the terminal shock location is seen in Figure 57 by the analytical plume boundaries not extending to the same distance as the CFD Mach contours. The

computational solutions show a plume which increases in radius as the flow expands, then contracts prior to passing through the terminal shock. This behavior is not captured in the analytical model, which assumes a monotonically increasing plume radius with distance from the nozzle exit. Overall, the analytical model agrees well with CFD simulations in capturing the terminal shock radius and the initial plume expansion, while underpredicting the maximum plume expansion.

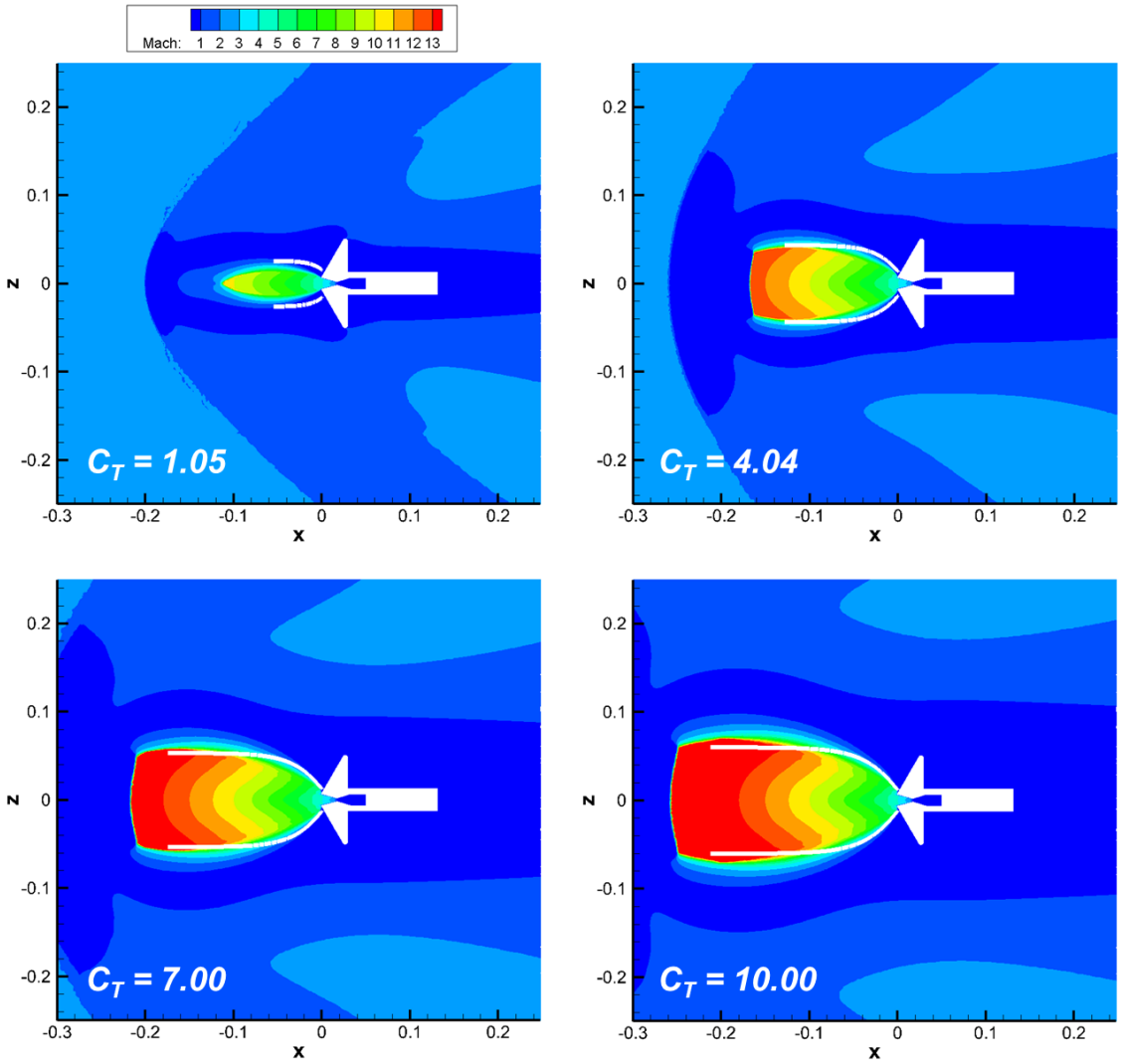

Figure 57: Comparison of overall plume structure for CFD simulations (Mach contours) and analytical model (white) for the single nozzle configuration

4.2.3 Peripheral Nozzle Plume and Bow Shock Structure

The CFD solutions presented in Chapter II for the three nozzle configuration are used to establish the extensibility of the analytical model to peripherally located nozzles for both the plume and bow shock structures. The solutions for four thrust coefficients are shown in Figure 58. These analytical solutions do not include crossflow perturbations, which will be discussed in Section 4.2.5. For thrust conditions where the plumes are independent, as is the case for C_T values of 1, 4, and 7, the outboard expansion of the jet flow agrees favorably between the CFD simulations and the analytical model. The total extent of the plume is underpredicted, and the initial expansion from the nozzle exit is well captured, both of which are consistent with the results seen for the single nozzle configuration. For C_T = 1 and C_T = 4, the overall outboard plume shape predicted by the analytical model agrees well with the barrel shock seen in the Mach contours of the CFD simulations. For C_T = 7, the analytical model slightly underpredicts the maximum radius of the outboard barrel shock, which could be due to the jet flow turning outboard for this configuration. As thrust and the extent of the plume increase, more distance and time are available for the plume flow to turn outboard which would cause the analytical model to underpredict the outboard barrel shock. The outboard barrel shock for this configuration at these thrust levels is not significantly altered by the presence of a local crossflow.

The inboard expansion of the plume shows a consistent discrepancy between the analytical model and the CFD simulations. The analytical model assumes an axisymmetric plume shape, which means that the outboard and inboard expansions would be identical. However, as noted in Chapter II, this peripheral configuration shows compression of the plume on the inboard side due to the presence of a stagnation region

at the vehicle nose and a local crossflow into which the nozzles exhaust. The analytical model consistently overpredicts the inboard barrel shock for thrust coefficients of 1, 4, and 7 due to this difference. The resulting bow shock for each of these thrust conditions slightly overpredicts the maximum standoff distance in the region local to the plumes, and shows a consistent, expected overprediction in the region between plumes as described in Section 3.4.2. The bow shock forward of the plume for C_T = 1 captures both the outboard bow shock shape and the maximum extent of the shock. As thrust increases, the outboard shock structure continues to agree well, although the analytical model begins to overpredict the maximum extent of the bow shock. This is due to the assumption of a hemispherical obstruction caused by the decelerated and turned plume flow. After passing through the terminal shock, the plume flow does not exactly follow a circular path (in the 2D sense of the Mach contours) as has been assumed. Thus the assumption of a hemispherical obstruction overpredicts the flow path of the decelerated plume flow.

For C_T = 10, the CFD simulations show plume coalescence due to the significant inboard expansion of the jet flow. This scenario is not captured in the analytical model, as the model assumes each plume has its own independent flow path. The analytical model does still capture the initial plume expansion from the nozzle exit, but significantly underpredicts the terminal shock standoff distance and maximum radius of the outboard plume expansion. The inboard plume expansion agrees slightly better than the lower thrust coefficients, as the presence of plume coalescence prevents the formation of the decelerated freestream flow stagnation region inboard of the nozzles. There is no local crossflow in the CFD solution to perturb the inboard barrel shock for this thrust

condition, though the plume coalescence does alter the pressure boundary condition along the inboard barrel shock in the CFD solution. This effect is not captured in the analytical model. The underprediction in plume extent also results in an underprediction of the bow shock structure, as the effective obstruction predicted by the analytical model is smaller than that of the CFD solution.

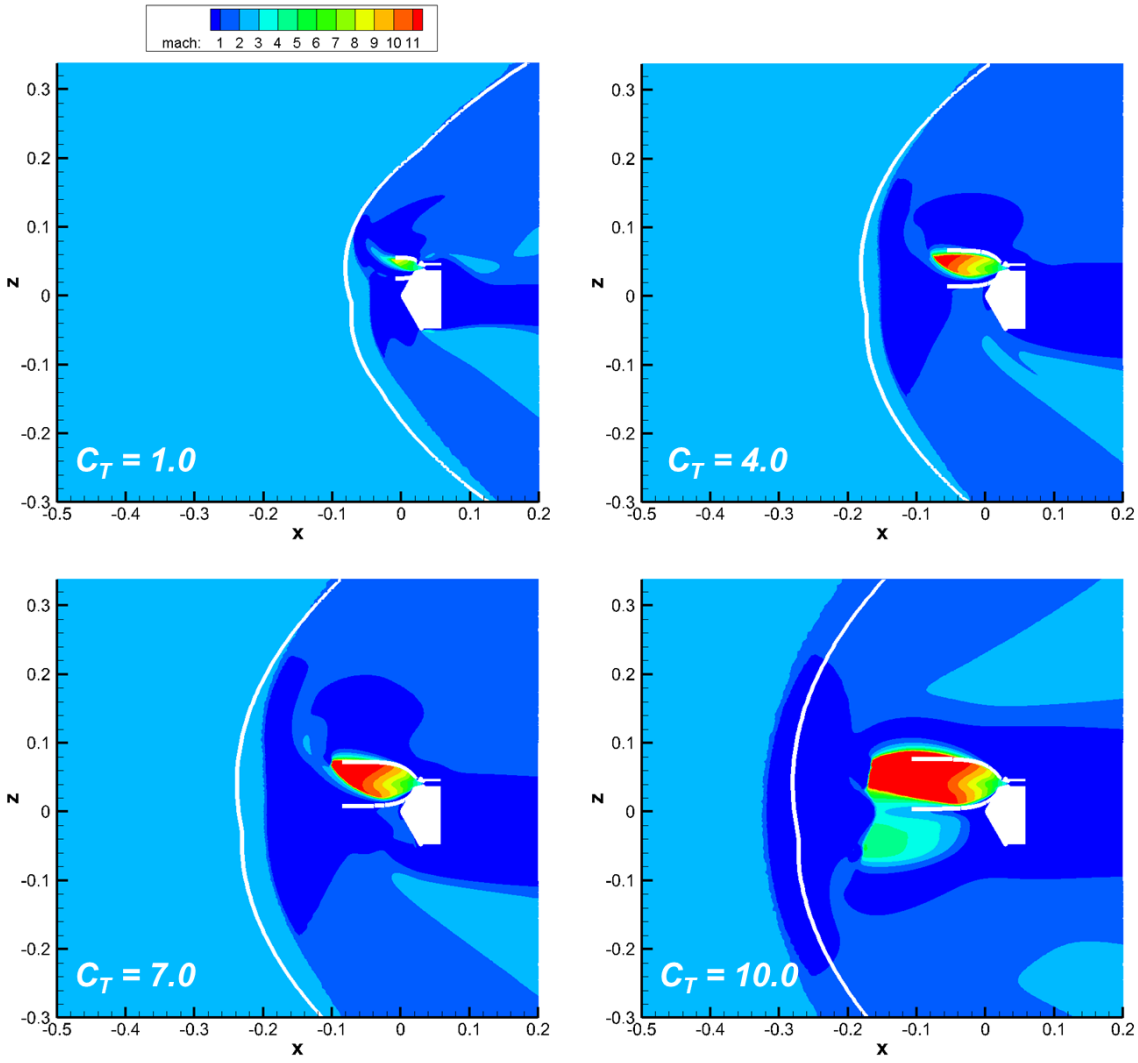

Figure 58: Comparison of plume and bow shock structures for CFD simulations (Mach contours) and analytical model (white) for the three nozzle configuration

4.2.4 Free Shear Layer

The method to determine free shear layer thickness in the analytical model results in a monotonically increasing thickness with distance along the plume for a given thrust coefficient. To compare the results for this model, the largest shear layer thickness from the analytical solution for the single nozzle configuration, corresponding to the shear layer thickness at the terminal shock location, is compared to the largest predicted shear layer thickness from the CFD solution for the same thrust level. Comparison for the single nozzle configuration is shown in Figure 59. Error bounds are included for the CFD solutions due to errors associated with taking the data from the CFD solutions with TecPlot. Mach 4 contour lines are used to determine the outmost extent of the shear layer, and the jet core is used as the inmost shear layer boundary. While the Mach 4 contours are easily seen in the CFD solutions, the transition from the shear layer to the core jet flow is not as noticeable. Overall, a reasonable error for probing the CFD Mach contours appears to be ±0.5 mm. The analytical model agrees well within the CFD error bounds for all C_T values that exhibit a steady plume structure. Only C_T = 1 shows a significant discrepancy between the CFD and analytical model, likely related to the fact that it is the transition thrust coefficient from the jet penetration mode to the steady plume structure.

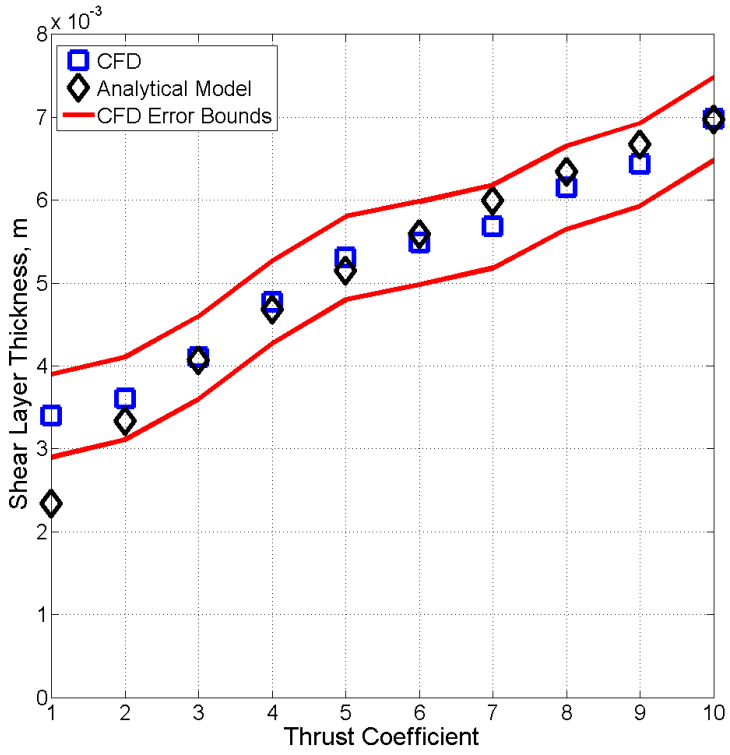

Figure 59: Comparison of shear layer thickness for the CFD solutions and the analytical model for the single nozzle configuration

A comparison of shear layer thickness for the three nozzle configuration is shown in Figure 60. As with the results for the single nozzle configuration, an error bound of ±0.5 mm is included to represent errors in the resolution of probing the CFD solutions, the location along the plume at which the shear layer thickness is found, and determining the jet core location. The shear layer thickness is consistently lower for the three nozzle configuration as compared to the single nozzle configuration due to the lower thrust provided by each nozzle to reach the same total C_T. The analytical model shows good agreement across all thrust coefficients examined, with a slight underprediction consistent across all thrust coefficients. This is likely related to the fact that the three

nozzle configuration results in a plume which is not axisymmetric, as the presence of a local crossflow perturbs the plume structure.

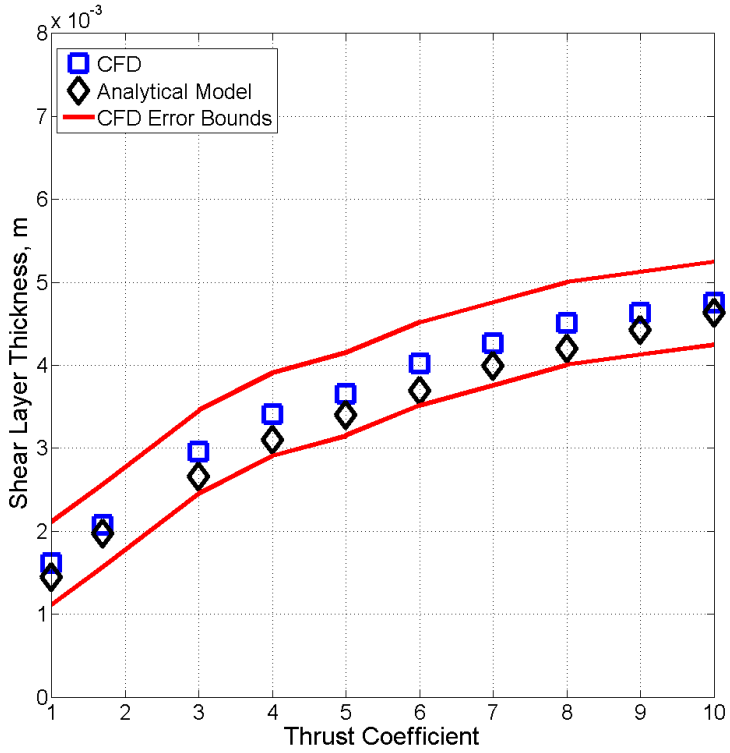

Figure 60: Comparison of shear layer thickness for the CFD solutions and the analytical model for the three nozzle configuration

4.2.5 Local Crossflow Perturbations

The results presented in Section 4.2.3 have no crossflow effects included, possibly causing the slight underprediction in the outboard barrel shock for those solutions. Including the crossflow perturbation angle as described in Section 3.5.2 results in a better overall agreement with the plume structure, as shown in Figure 61. For C_T = 1, the outboard plume structure agrees well, as the crossflow angle for this configuration is only 7.1°. The inboard barrel shock is still overpredicted; however, the rotation of the plume

does direct the analytical plume in more of the correct direction than the solution with no crossflow effects. Increasing to C_T = 4 results in a barrel shock with better inboard agreement across the entire analytical boundary, while the outboard barrel shock is slightly overpredicted. Further increasing to C_T = 7 shows good agreement for both plume boundaries. While the solution with no crossflow effects shown in Figure 58 underpredicts the outboard barrel shock, including the crossflow angle causes the boundary to rotate outboard and better capture the plume structure. The inboard plume expansion is also captured well, particularly the expansion of the plume near the nozzle exit. As the CFD plume structure becomes more complex, particularly since there is not a distinct, terminal normal shock, the analytical model overpredicts the barrel shock inboard of the nozzle axis. However, this plume still has better agreement between the analytical model and CFD solution than is seen if crossflow angle is not included. The crossflow angle causes the analytical plume flow to be directed more outboard for all three of these thrust coefficients, consistent with the results seen in the CFD solutions.

The C_T = 10 solution shows better outboard agreement when crossflow angle is included than when it is omitted. While the extent of the plume is still underpredicted due to the coalescence of the plumes, the outboard barrel shock shows a similar behavior as if the crossflow angle is still impacting the plume shape. The inboard barrel shock is well captured near the nozzle exit for this thrust condition, while the coalescence eventually results in the analytical model underpredicting the plume shape. This is a direct result of the analytical model being unable to capture the flow structure when the plumes coalesce, as the model assumes each plume to be independent of all other plumes.

A consistent widening of the bow shock and formation of the shock closer to the vehicle along the vehicle axis are seen when crossflow angle is included. This is due to the outboard shift in the effective obstruction for each plume, as the hemisphere center is set to be the furthest extent of the outboard barrel shock. For C_T = 1, 4, and 7, this results in a consistent overprediction of the bow shock standoff distance forward of the plume. However, the inboard standoff distance, while still overpredicted, is closer to the CFD solution than is seen if no crossflow angle is considered. For C_T = 10, the bow shock structure is underpredicted since the analytical model does not take into account the increase in plume axial extent due to plume coalescence.

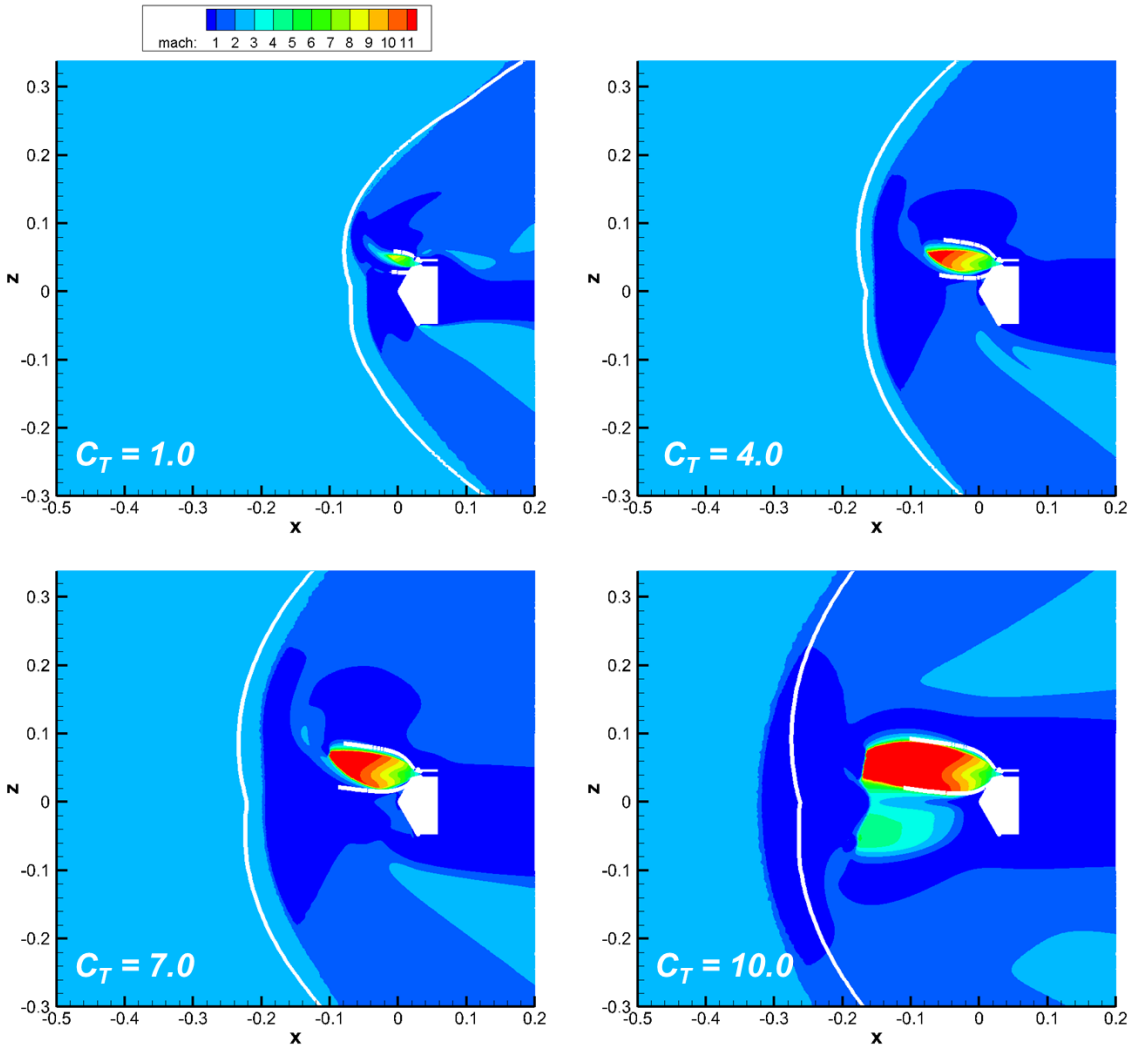

Figure 61: Comparison of plume and bow shock structures for CFD simulations and analytical model (white) for the three nozzle configuration with crossflow perturbations

Absolute and percent differences between the analytical model predictions and the CFD solutions for each thrust condition run on this geometry are shown in Figure 62. For all thrust coefficients, the jet edge Mach number is taken from Table 13 for the three nozzle calculations. The maximum plume radial extent has a peak percent difference of 13%, indicating that the analytical model generally captures the outboard expansion of the plume structure well regardless of plume coalescence. The absolute difference in both

plume axial extent and bow shock axial extent increase significantly when plume coalescence occurs, as the model is not capable of capturing this flow regime. For independent plumes, the magnitude of the absolute difference for both of these flow features drops by at least half as the analytical model better captures the flow environment at lower thrust coefficients.

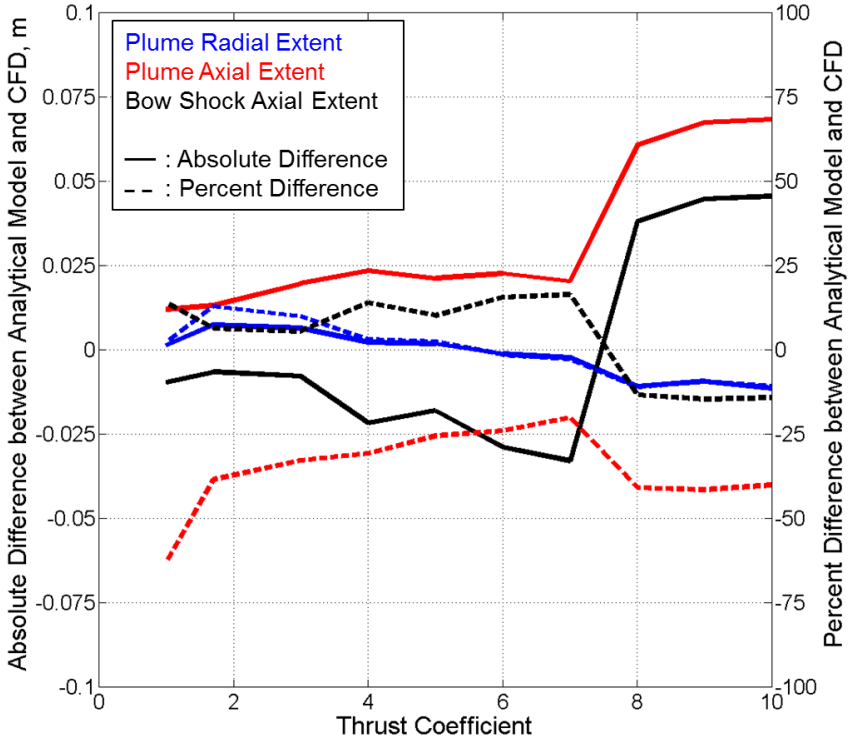

Figure 62: Absolute and percent differences for primary flowfield components between the analytical model and CFD for the three nozzle configuration

4.2.6 Prediction of Plume Coalescence

In the CFD data presented in Section 2.3.3, it is noted that plume coalescence initiates between C_T = 7 and C_T = 8 as the jet terminal shock and bow shock standoff distances increase significantly for C_T values of 8, 9, and 10. The analytical model treats all plumes

as independent of each other; however, plume coalescence may be predicted by examining situations where the predicted plume structures overlap. Figure 63 shows a comparison of two predictions at C_T = 10, with the one on the left allowing for the calculation of a crossflow deflection angle to the plume and the one on the right assuming that no crossflow is present. Both images show a view from upstream of the vehicle looking along the X axis toward the plumes. Including the crossflow deflection angle results in plumes directed outboard, and the predicted plume boundaries do not cross. However, by assuming that crossflow deflection is zero if plume coalescence occurs, the analytical model predicts that the plumes do intersect each other.

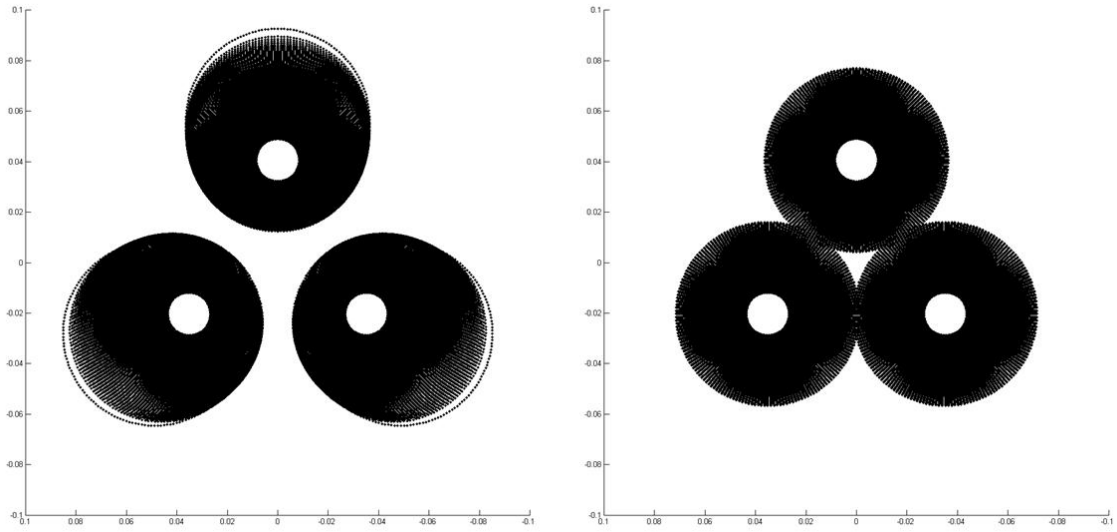

Figure 63: Effect of including crossflow deflection angle (left) versus no crossflow (right) for prediction of plume coalescence on the three nozzle configuration at C_T = 10

If the developed analytical model is capable of predicting plume coalescence, then the crossflow deflection angle for the model needs to equal zero according to Figure 63.

Physically, this means that the coalescence of the plumes prevents the decelerated freestream from reaching the vehicle surface to create the local crossflow. Predictions for $C_T = 8$ and $C_T = 10$ under this assumption are shown in Figure 64. For $C_T = 8$, the plumes do not intersect each other as is seen for $C_T = 10$. If plume coalescence is driven primarily by plume intersection, then the analytical model does not accurately capture the transition to a single effective plume structure. In actuality, the close proximity of the plumes will affect the boundary conditions for the formation of each plume structure, which may cause coalescence. Thus the analytical model predictions, by showing that the plumes expand to nearly intersect, can be used to qualitatively say that coalescence may occur, though no stronger statement is possible for the developed model.

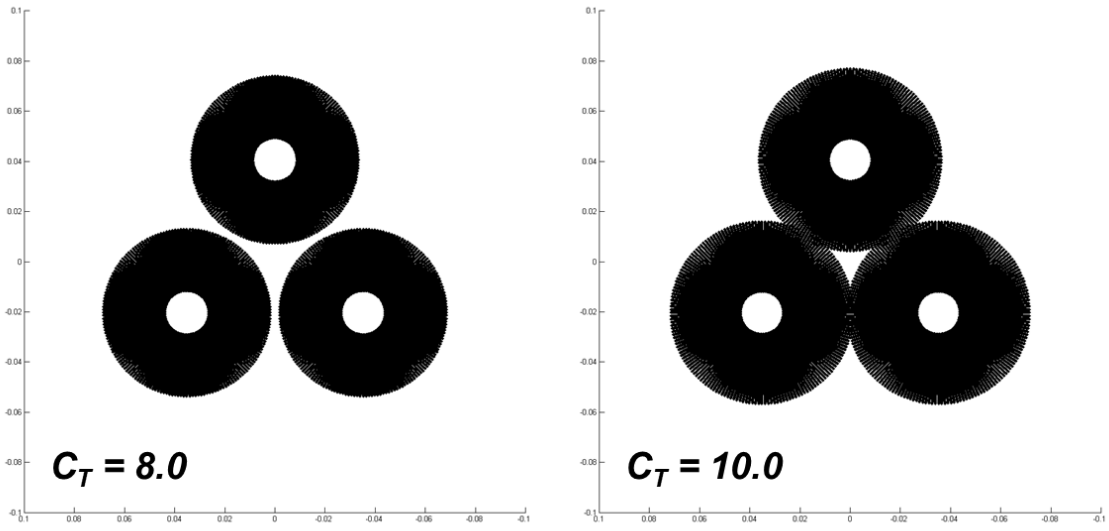

Figure 64: Effect of zero crossflow deflection angle for varying thrust coefficient to predict plume coalescence for the three nozzle configuration

4.3 Analytical Model Validation for Canted Nozzle Configurations

After validating the plume model against CFD solutions for geometries with no nozzle canting, the next step is to determine the accuracy of the model for canted nozzles. Increasing the nozzle cant angle outboard for forebody located nozzles should result in less scarfing of the nozzles due to a change in the angle between the nozzle axis and the surface, as well as an increase in the crossflow effect since the plume is more normal to the surface and less directed into the local crossflow. Three forebody nozzle cant angles, 10°, 20°, and 30°, are examined.

For canted nozzles located on the aftbody of the entry vehicle, the local flow environment should be less complex as the plumes are not expected to significantly interact with the bow shock since they are far removed from the forebody. Some crossflow should still be present as the decelerated freestream flows along the aftbody. The three geometries described in Section 4.1.3 with aftbody nozzles will be used to validate the analytical model under these flow conditions. Variations in Mach number and gamma will also be applied to the analytical model and CFD solutions to investigate the sensitivity of the analytical model to these input parameters.

4.3.1 Forebody Canted Nozzles

For a 10° nozzle cant angle, the comparisons of the analytical model with the CFD Mach contours for varying C_T values at zero angle of attack are shown in Figure 65. For all thrust coefficients, the bow shock standoff distance is overpredicted by the analytical

model, consistent with the results seen for the geometry with no nozzle canting when the plumes did not coalesce. This is due to a difference between the assumed obstruction shape of a hemisphere and the actual obstruction created by the jet plume. For this low nozzle cant angle, the barrel shock agrees well with the CFD solution. The analytical plume flow velocity has the same direction as the computational plume, with the outboard barrel shock agreeing well across the entire plume. The inboard barrel shock overpredicts the plume expansion, as the analytical model assumes an axisymmetric plume even when the crossflow angle is considered. The actual flow field shows an asymmetric plume, which is not captured in the assumptions of the model. The crossflow angle determined for this configuration is larger than for the zero nozzle canting geometry, with a calculated angle of 7.7°. The larger crossflow angle is due to the increase in relative angle of the jet exit flow to the local crossflow.

For all thrust coefficients, the radial extent of the plume in the Z direction is well captured by the outboard plume expansion, with a peak percent difference less than 5% as shown in Figure 66. The axial extent of the plume in the X direction is consistently underpredicted by the inboard analytical barrel shock due to the discrepancy in modeling the inboard plume compression, though the percent difference remains under 10% for all four thrust conditions and the absolute difference is nearly constant for C_T values of 4, 7, and 10. The consistent overprediction of the bow shock location has a steadily growing absolute difference magnitude, though the percent difference nearly levels out at approximately 20% for increasing thrust coefficient.

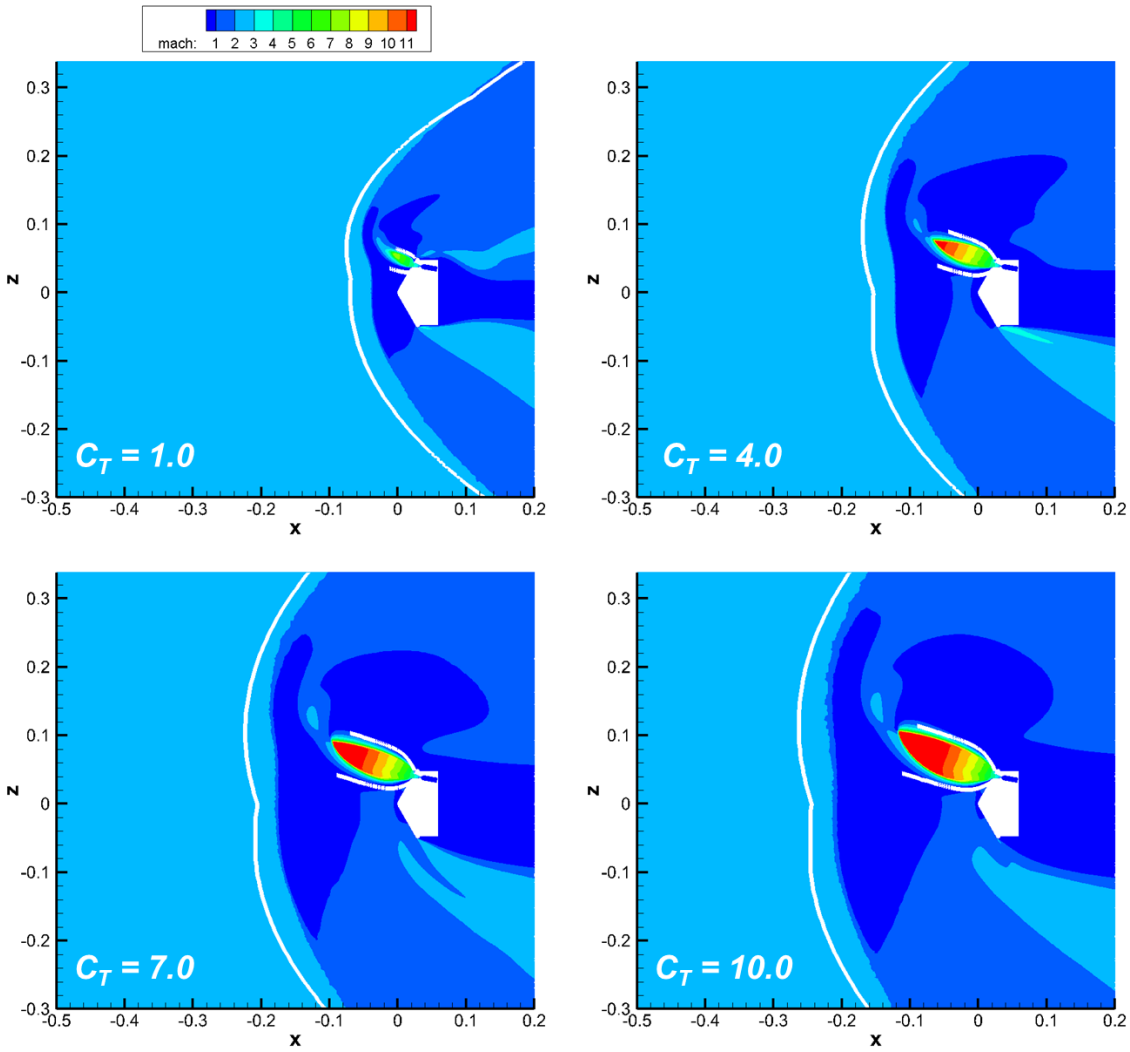

Figure 65: Comparison of plume and bow shock structures for CFD simulations and analytical model (white) for the three nozzle configuration with 10° nozzle canting

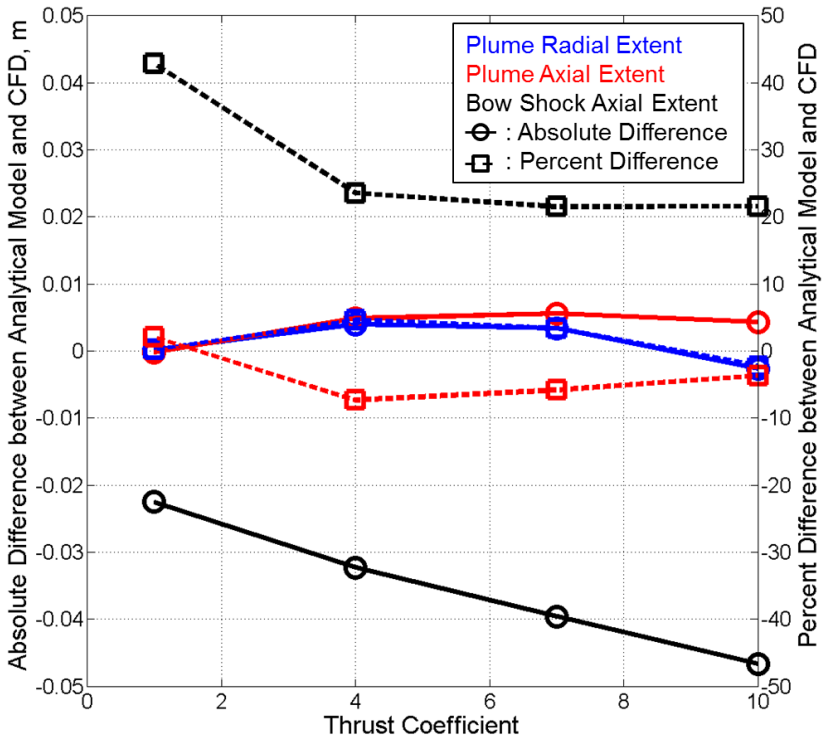

Figure 66: Absolute and percent differences for primary flowfield components between the analytical model and CFD for the three nozzle configuration with 10° nozzle canting

Figure 67 shows the flow field comparison for the 10° nozzle canting geometry at angles of attack of -10° and 10° for C_T = 10. When α = -10°, the jet flow of the visible nozzle and freestream flow are aligned, and the movement of the stagnation point on the vehicle results in a lower relative crossflow angle than for zero angle of attack in the CFD solution. The analytical model does not account for the movement of the stagnation point when determining the local crossflow velocity, though the comparison in Figure 67 shows that this is a minimal difference for this condition. The radial extent and axial extent of the plume flow are well captured by the analytical model, and the bow shock standoff distance is overpredicted.

For α = 10°, the shift in the stagnation point to the lower side of the vehicle creates a larger crossflow angle in the CFD solution since the flow along the vehicle will accelerate to a higher speed. The constant crossflow velocity results in a slight underprediction of the outboard barrel shock in the analytical model. The inboard barrel shock is not qualitatively different from other conditions in that the analytical model overpredicts the inboard plume expansion. The underprediction the outboard plume expansion indicates that a stronger local crossflow due to variation in the stagnation point location causes an increase in the deflection angle that is not captured by the analytical model. The radial and axial extents of the plume are still well captured for this angle of attack, and the bow shock location is still overpredicted due to the discrepancies in modeling the barrel shock.

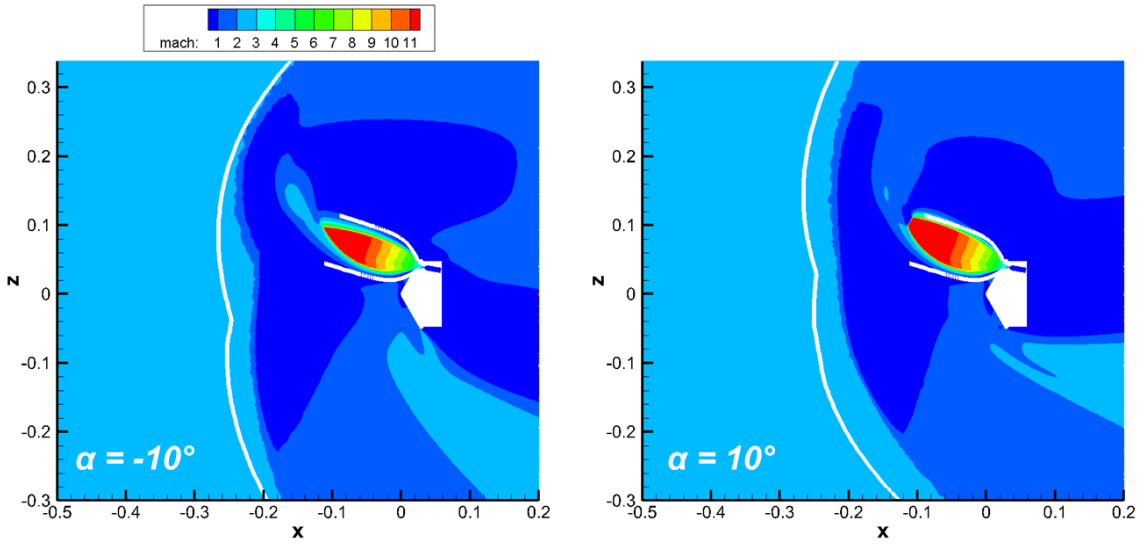

Figure 67: Effect of angle of attack on analytical plume and bow shock structures for the three nozzle configuration with 10° nozzle canting at C_T = 10

Increasing nozzle cant angle to 20° shows similar behavior in the analytical model as noted for the α = 10° case for the 10° nozzle canting configuration. Comparisons for C_T = 1, 4, 7, and 10 are shown in Figure 68 for the 20° nozzle canting configuration at zero angle of attack. The stagnation point for these conditions is located at the nose of the vehicle, and the relative orientation of the nozzle exit flow to the surface is more normal than for the 10° nozzle canting configuration. While the crossflow deflection angle calculated in the analytical model increases as expected, to a value of 8.0°, this is not sufficient to capture the CFD plume boundaries as well as in the lower cant angle solutions. The inboard barrel shock is significantly overpredicted across all thrust coefficients. The outboard barrel shock is underpredicted, particularly for the larger C_T values of 7 and 10. The initial expansion is well captured, and the low thrust condition of C_T = 1 shows good agreement across the entire plume structure due to the small plume created at this thrust level. The radial extent of the plume is underpredicted by the analytical model, as the crossflow angle does not sufficiently perturb the plume structure outboard. Since the analytical model creates a plume which is directed more upstream than the CFD solutions, the resulting bow shock standoff distance is significantly overpredicted as the effective obstruction forms further upstream. The presence of a local perturbation to the bow shock structure forward of the nozzle for all C_T values is captured by the analytical model, even if the exact location is not accurately captured.

Even though the orientation of the plume is not properly captured in the analytical model, the magnitude of the peak percent difference for the maximum plume radial extent is 11% at C_T = 4 as shown in Figure 69. For the thrust coefficients examined, both the absolute and percent differences decrease in magnitude for the maximum plume

radial extent as thrust increases from C_T = 4. The plume axial extent shows the largest disagreement for C_T = 1, consistent with the comparison in Figure 68, with a percent difference of 35%. The error levels off as thrust coefficient increases, with a percent difference for maximum plume radial extent of 6% for C_T = 10. The consistent overprediction of maximum bow shock standoff distance results in increasing magnitude of the absolute difference with C_T, though the percent difference does decrease with thrust coefficient as the CFD bow shock forms farther forward of the vehicle.

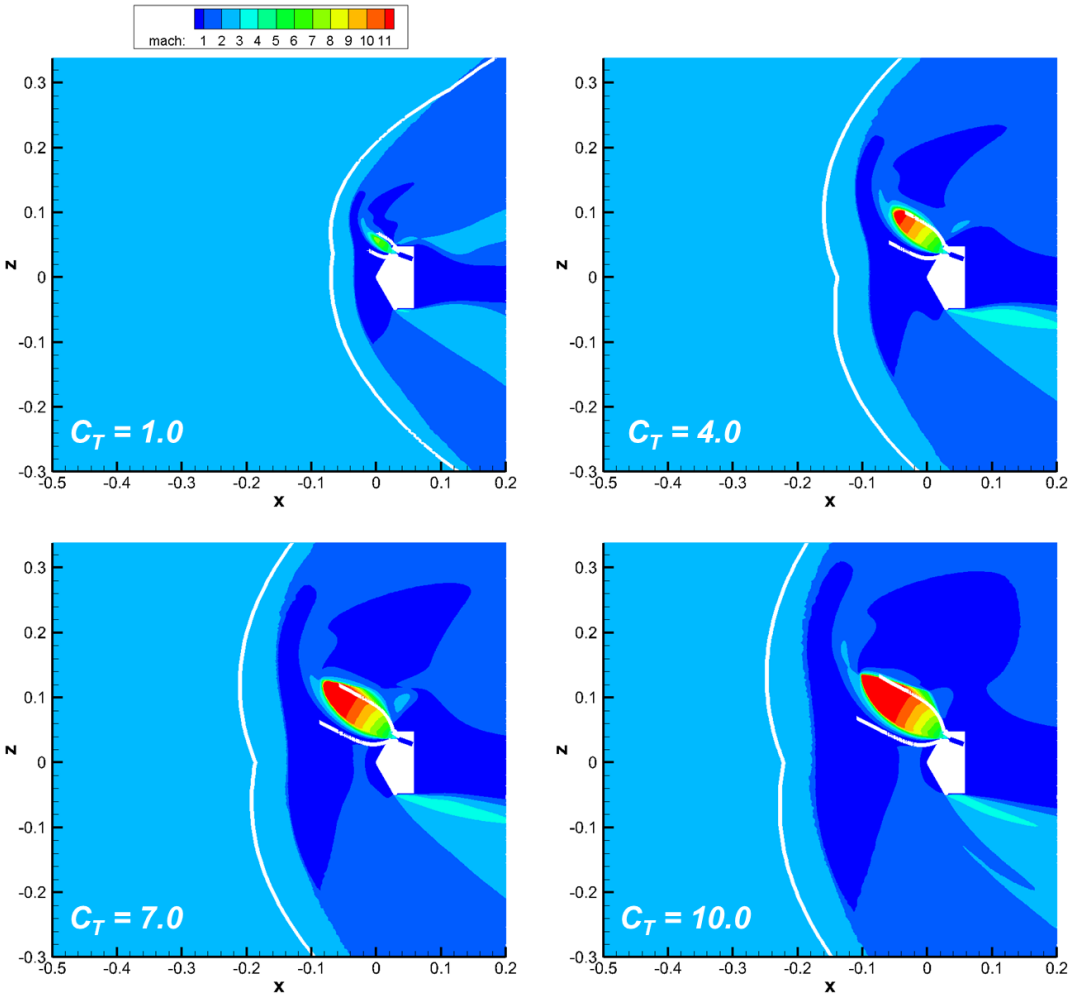

Figure 68: Comparison of plume and bow shock structures for CFD simulations and analytical model (white) for the three nozzle configuration with 20° nozzle canting

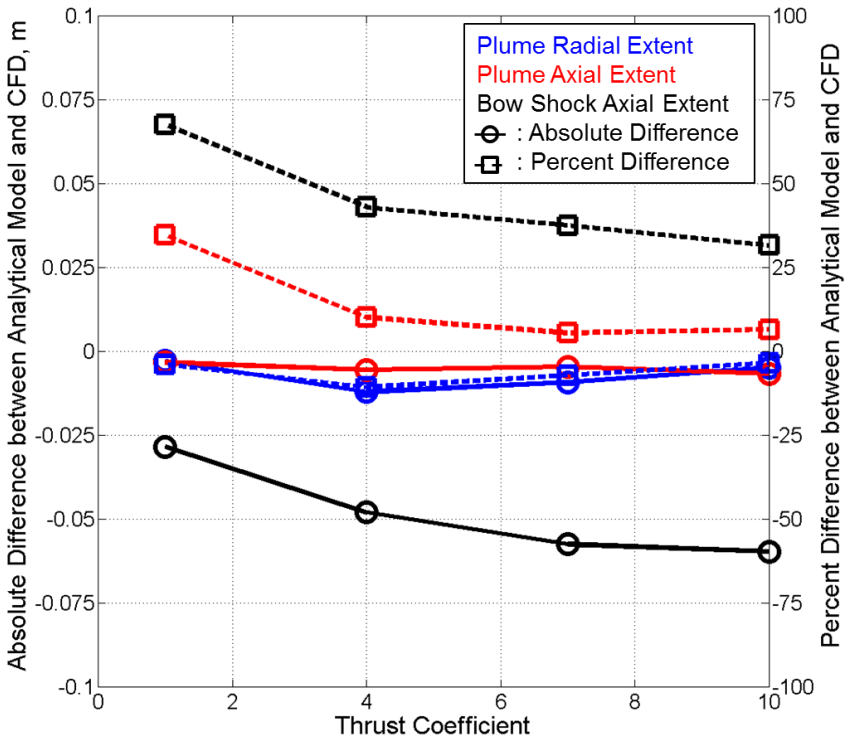

Figure 69: Absolute and percent differences for primary flowfield components between the analytical model and CFD for the three nozzle configuration with 20° nozzle canting

Further increase in the nozzle cant angle to 30° shows more discrepancy between the analytical plume model and the CFD Mach contours for zero angle of attack solutions, as shown in Figure 70. The nozzles in this configuration exhaust perpendicular to the vehicle surface, which causes the crossflow angle to increase to 8.2°. For C_T = 1, the small plume structure still agrees well between the analytical model and the CFD solution. The inboard barrel shock overpredicts the expansion of the plume in that direction. The radial extent of the plume is underpredicted, as the calculated crossflow angle is not sufficient to rotate the plume enough to match the full radial extent. For the higher thrust conditions, the underprediction of the outboard barrel shock by the analytical model is significant. The CFD solutions show a crossflow deflection angle

much larger than is calculated in the analytical model, and the plume expansion extends to a greater distance from the nozzle exit than the terminal shock assumption of the model captures. The inboard barrel shock shows the same consistent overprediction of the inboard expansion, resulting in an accurate capture of the axial extent of the plume structure. As the plume is directed more upstream in the analytical model than the CFD solutions, the resulting analytical bow shock also shows a larger standoff distance.

One cause of the discrepancy in the plume structure has to do with the interaction of the CFD plume structure with the flow around the vehicle, as is described in Section 5.3.1. The outboard barrel shock is perturbed by this interaction. Another cause of the discrepancy is the analytical approach to modeling crossflow deflection angle. The comparisons show that the crossflow angle should be a constant value for a given thrust condition, as the plume deflection appears to be a constant rotation about the intersection of the nozzle axis with the vehicle forebody. However, this angle is significantly underpredicted by the analytical model. The effect of the relative angle of the nozzle exit flow to the local surface flow direction is accounted for in the model, indicating that the assumption of a velocity triangle providing the crossflow deflection angle breaks down as the crossflow effect increases. An increase in crossflow deflection in the analytical model would direct the plume more outboard, causing the bow shock to form closer to the vehicle with the local shock perturbation further outboard.

Figure 71 shows the absolute and percent differences between the analytical model and the CFD solutions in determining the locations of primary flow features. The plume radial extent is consistently underpredicted by the analytical model with a percent difference near 25%. The plume axial extent shows good agreement, particularly for large

thrust coefficients. C_T = 1 shows a 15% difference in plume axial extent, while the other thrust coefficients examined all have errors less than 3%. The overprediction in bow shock location results in significant percent differences ranging from 22%-63%. The magnitude of the absolute error increases with thrust coefficient, therefore the decrease in percent difference with increasing thrust is primarily attributed to the larger overall bow shock standoff distance due to the large plume structure.

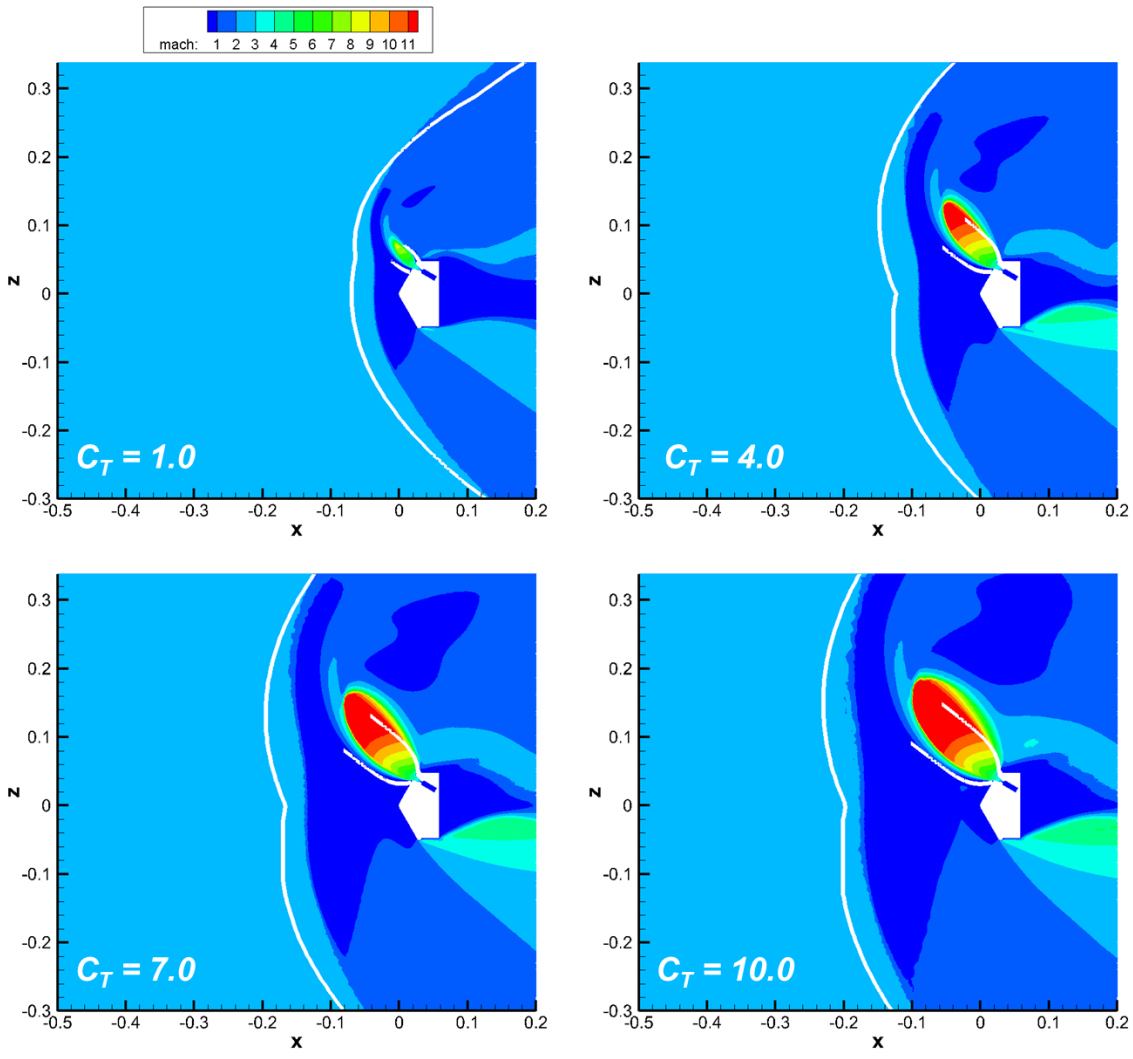

Figure 70: Comparison of plume and bow shock structures for CFD simulations and analytical model (white) for the three nozzle configuration with 30° nozzle canting

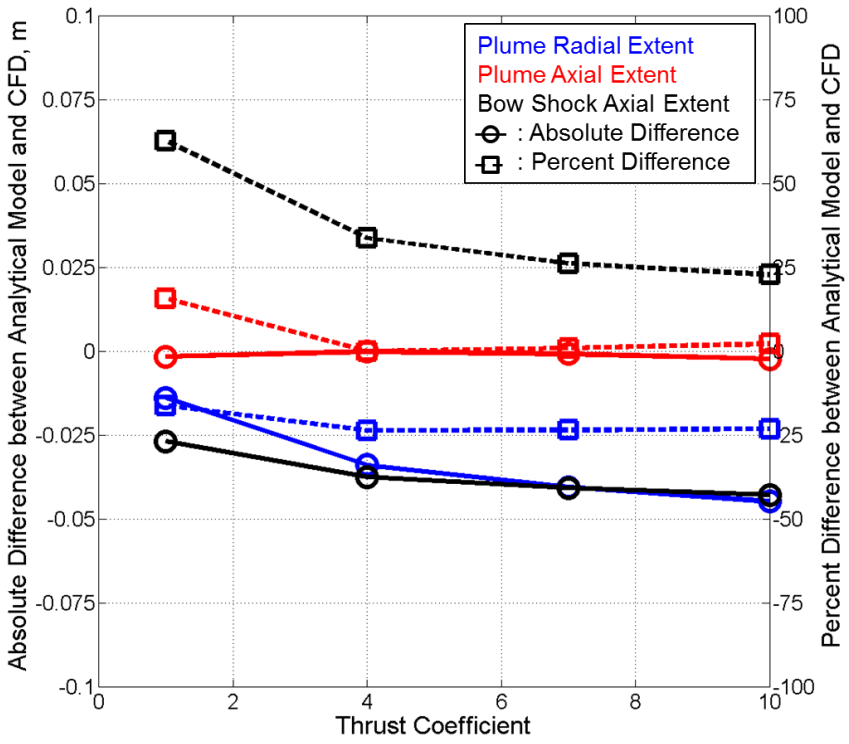

Figure 71: Absolute and percent differences for primary flowfield components between the analytical model and CFD for the three nozzle configuration with 30° nozzle canting

Comparisons of the analytical model with CFD Mach contours for C_T = 1 at angles of attack of -10° and 10° are shown in Figure 72. The α = -10° case moves the stagnation point closer to the nozzle shown, which should result in a lower crossflow deflection angle. The analytical model shows better agreement with the CFD solution since the calculated crossflow angle, which is independent of stagnation point location in the model, is closer to that of the computational flow field. The bow shock standoff distance is still overpredicted, though the maximum bow shock extent of the local perturbation forward of the nozzle is well captured.

For α = 10°, the shift in stagnation point should create a larger crossflow effect and the analytical model should underpredict the barrel shock. This is seen in Figure 72,

along with the overprediction of the inboard plume expansion. The bow shock structure shows a general overprediction as the plume structure is not directed sufficiently outboard in the analytical model. Thus, the obstruction and bow shock both form further upstream than in the CFD solution.

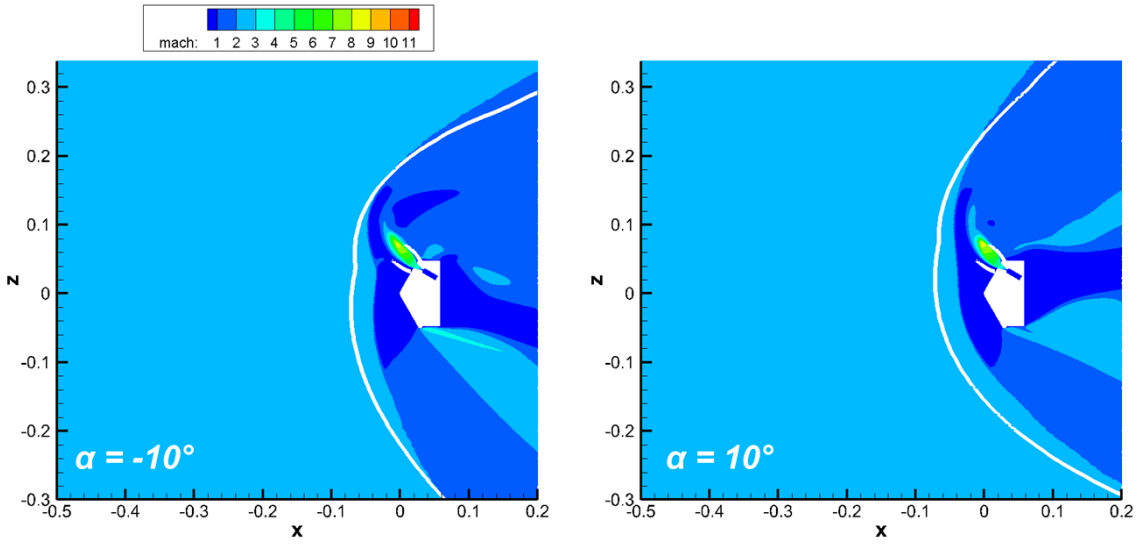

Figure 72: Effect of angle of attack on analytical plume and bow shock structures for the three nozzle configuration with 30° nozzle canting at $C_T = 1$

For $C_T = 10$, the analytical model underpredicts the outboard plume structure regardless of angle of attack, as shown in Figure 73. The inboard plume expansion is slightly overpredicted for both angles of attack, and the bow shock standoff distance is overpredicted due to the variation in plume boundary shape. The radial extent of the plume is significantly underpredicted, as the CFD simulation shows a larger expansion of the plume along the nozzle axis. The axial extent of the plume agrees well for both angles of attack, consistent with the agreement of the inboard barrel shock. As noted for the zero angle of attack comparisons on this geometry, the outboard barrel shock is significantly

affected by an interaction of the plume flow with the surface flow along the vehicle and around the shoulder. This could be the primary source of the discrepancy in the outboard plume shape between the analytical model and the CFD solution.

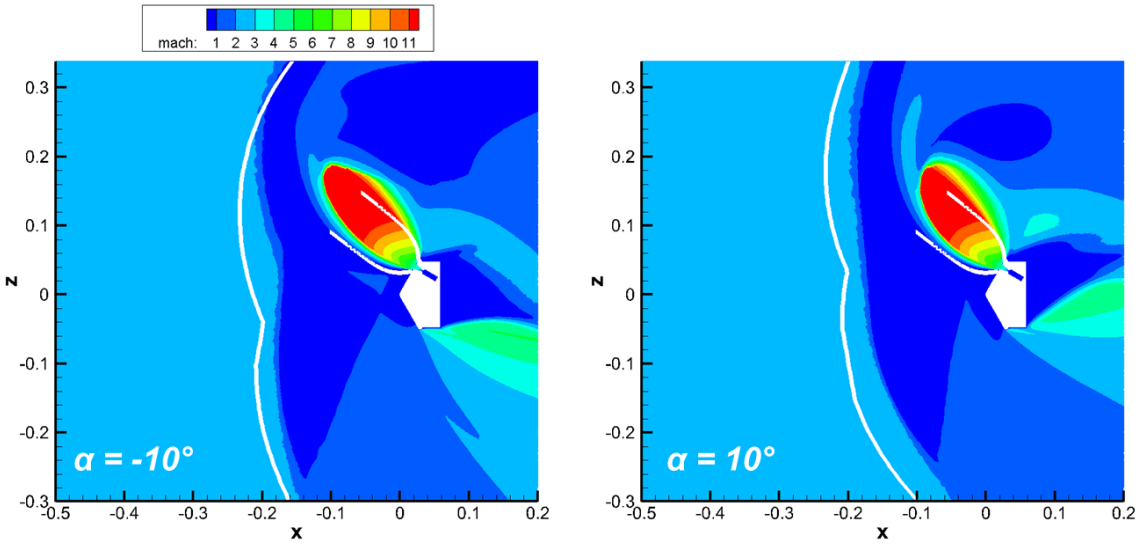

Figure 73: Effect of angle of attack on analytical plume and bow shock structures for the three nozzle configuration with 30° nozzle canting at C_T = 10

4.3.2 Aftbody Canted Nozzles

The aftbody nozzle geometries exhaust into a much different flow environment than when the nozzles are located on the forebody and have less interaction with the bow shock forward of the vehicle. The analytical model captures this lack of interaction with the bow shock structure, as well as possibly predicting plume-surface interactions. The model does not attempt to model plume expansion along the surface, as the axisymmetric plume barrel shock assumes there is no obstruction to the formation of the barrel shock. However, if this shock passes significantly into the vehicle, then plume-surface

interaction may occur as the expected barrel shock will not be able to form as predicted by the analytical model.

Figure 74 shows comparisons of the analytical model to Mach contours for the three nozzle, 30° nozzle canting, aftbody configuration for varying thrust coefficient. For C_T = 1, the plumes do not expand significantly, and the bow shock structure is undisturbed from that predicted by the assumed vehicle obstruction. In the analytical model, the vehicle is treated as a hemispherical body with radius equal to the base radius of the vehicle and a nose location identical to the nose of the actual geometry. The analytical bow shock model results in a consistent overprediction of the bow shock standoff distance for the vehicle. This is due in part to assuming that the vehicle also creates a hemispherical obstruction to the freestream, as well as a similar overprediction of the local bow shock created by the plumes as is seen for the forebody located nozzles. The predicted barrel shock for the analytical model at C_T = 1 captures the initial expansion well, but underpredicts both the axial and radial extents of the plume. The assumption of a hemispherical obstruction for each plume results in the jet flow turning and flowing in the negative X direction, while the CFD plume flow passes further outboard before turning aft.

Increasing thrust to C_T = 4 shows better agreement between the analytical model and the CFD solution. The axial extent upstream of the plume expansion is well captured, as this plume is more underexpanded due to the larger thrust value. The radial extent of the plume is still underpredicted, and the calculated crossflow angle of 9.0° slightly underpredicts the aft deflection of the plume structure. While the bow shock location is overpredicted due to the assumptions related to the hemispherical obstruction for the

vehicle and each plume, the features of the bow shock are similar between the analytical model and the CFD solution. Both show an undisturbed shock near the vehicle axis and a kink in the shock structure due to the effects of the plume flow obstructing the freestream. The kink is more evident on the upper half of the solution, where the flow is directly in plane with a nozzle. A kink also exists on the lower half of the solution, representing the impact of out of plane nozzles on the full three dimensional bow shock.

Further increasing thrust to $C_T = 7$ and $C_T = 10$ show a consistent capturing of the axial extent of the plume, with underprediction of the radial extent and crossflow deflection angle for the jet flow. While the CFD solution for $C_T = 7$ shows a slight increase in bow shock standoff distance at the vehicle axis, the analytical model predicts a large impact on shock structure due to plume obstruction. This creates an analytical bow shock with a larger overall standoff distance rather than a structure similar to the CFD solution showing a more normal shock across the entire flow than is seen at lower thrust values. In the analytical solution for $C_T = 10$, any bow shock formation caused by the vehicle is not captured as the effective obstruction for each plume results in a larger standoff distance. The CFD solution shows a continuation of the $C_T = 7$ result, where the entire bow shock resembles a normal shock and any kinks are smooth transitions rather than the sharp changes in shock angle that the analytical model predicts.

For all four thrust coefficients, the analytical model predicts a barrel shock which significantly passes into the vehicle surface. This can be seen in Figure 74 as the inboard barrel shock emanates from the vehicle surface forward of the nozzle exit, rather than showing the initial expansion near the nozzle. The CFD solutions for these thrust cases all show some degree of plume-surface interaction, supporting that the intersection of the

analytical barrel shock with the vehicle surface can be an indication that plume-surface interaction is to be expected.

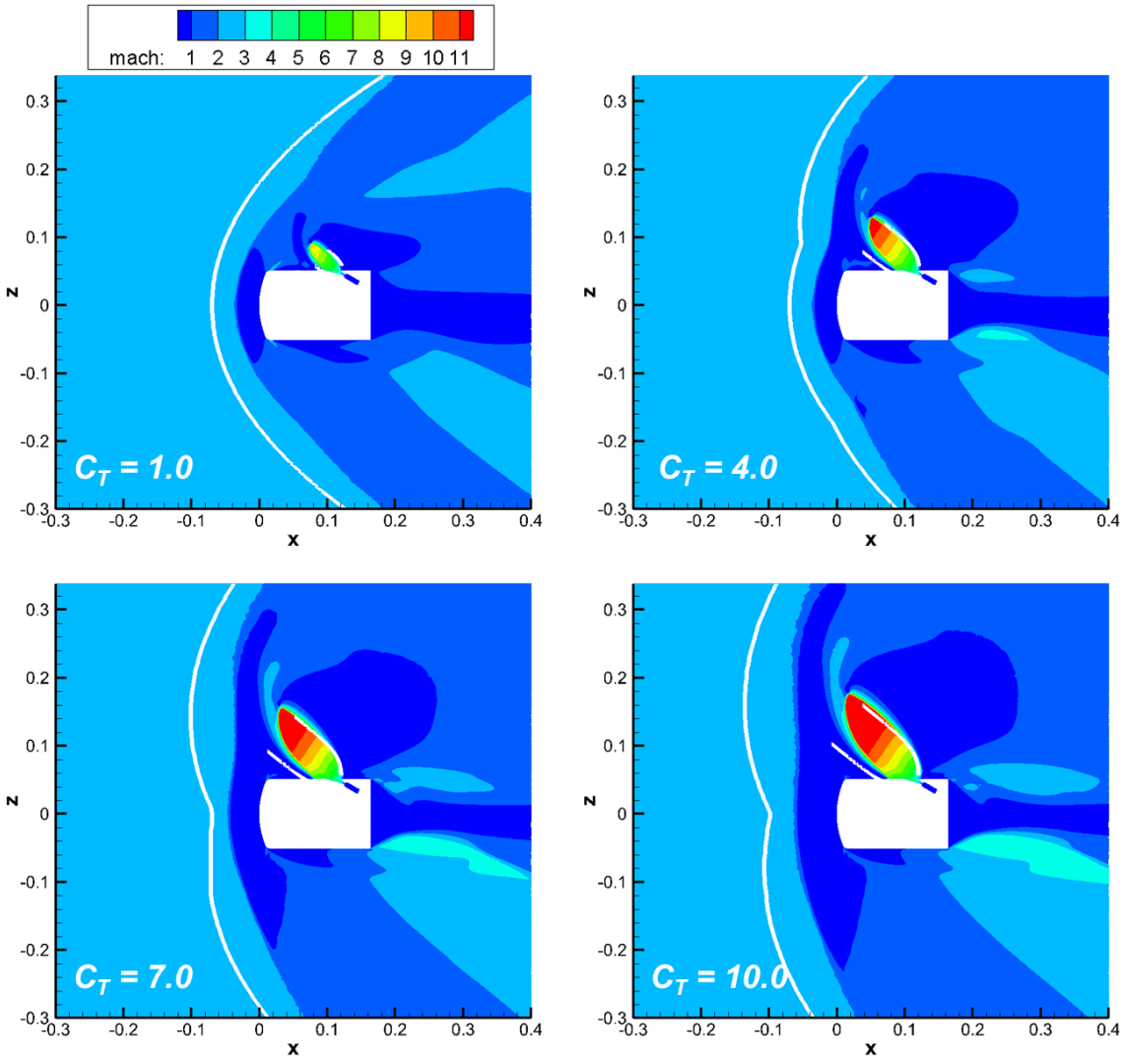

Figure 74: Comparison of plume and bow shock structures for CFD simulations and analytical model (white) for the three nozzle, 30° nozzle canting, aftbody configuration

Figure 71 shows the absolute and percent differences between the analytical model predictions and the CFD solutions for the primary flow features at each thrust condition. The plume radial extent has nearly constant absolute and percent differences, with a

percent difference of around 10%, consistent with the agreement seen in Figure 74. The significant overprediction of bow shock location is seen as a large percent difference, with values over 100% for all C_T values. The relatively undisturbed inboard bow shock for C_T = 1 and C_T = 4 is seen as a constant error in Figure 75. The large magnitude in percent difference for the plume axial extent is due to the small values associated with the plume extending to axial locations near the forebody. The magnitude of the absolute difference increases with thrust, but does not exhibit the large jump seen in the percent difference plot.

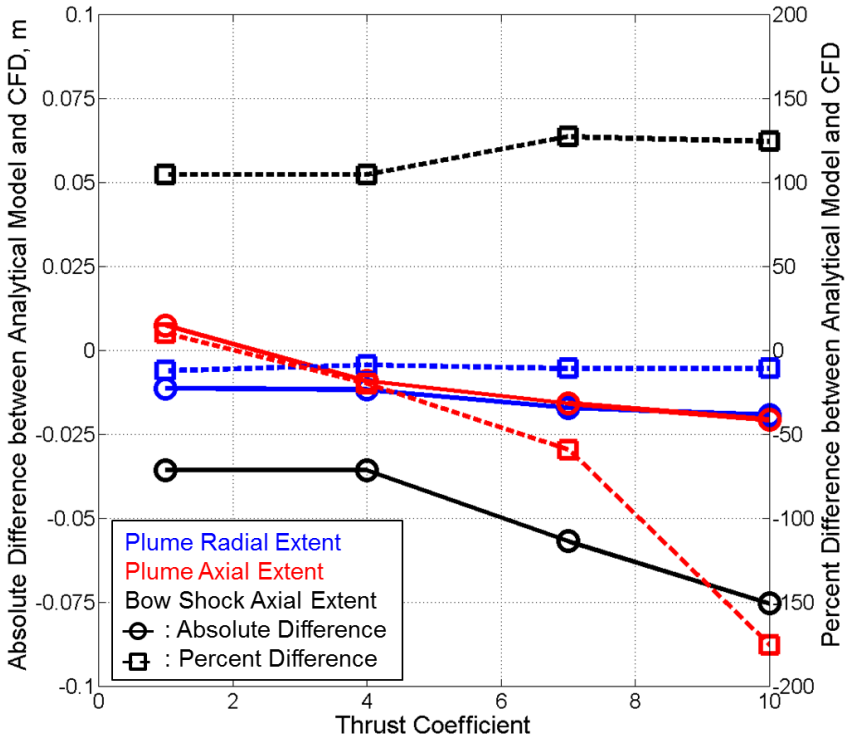

Figure 75: Absolute and percent differences for primary flowfield components between the analytical model and CFD for the three nozzle, 30° nozzle canting, aftbody configuration

Comparisons of the analytical model with CFD solutions for the six nozzle, 30° nozzle canting, aftbody configuration are shown in Figure 76. As with the three nozzle aftbody configuration, the vehicle obstruction results in an overprediction of the shock standoff distance near the vehicle axis for low thrust conditions. The analytical model for that case predicts that the bow shock is nearly undisturbed across the entire shock structure, while the CFD solution shows a shock with a noticeable kink as the freestream flow reacts to the plumes. The reason for this difference is that the analytical model slightly underpredicts the extent of the plume for this case in both the axial and radial directions. As the nozzle design and nozzle location are the same for this geometry as for the three nozzle configuration, the crossflow deflection angle predicted by the analytical model is identical between the two geometries, equal to 9.0°. Increasing thrust to $C_T = 7$ shows the formation of the kink in the bow shock structure due to the plume expansion. The CFD solution shows a smoother transition between the inboard and outboard shock structures than is captured in the analytical model. The outboard barrel shock agrees well across the entire shock, while the inboard barrel shock is overpredicted by the analytical model.

Increasing thrust to $C_T = 10$ and $C_T = 20$ shows the underprediction of crossflow deflection that is also seen in the three nozzle aftbody configuration. While the forebody nozzles show a generally constant crossflow angle with variations in thrust, the aftbody nozzles appear to have a thrust dependent crossflow deflection which is not captured by the velocity triangle method in the analytical model. The axial extent of the plume is slightly overpredicted, consistent with the underprediction in crossflow deflection. If the plume is rotated by a larger angle, then the axial extent will decrease and have better agreement with the CFD solution. The bow shock structure for each of these thrust levels

also shows the effect caused by assuming that the shock is only defined by the furthest extended local shock structure. While the CFD solutions show a smooth shock for each thrust level, the analytical model predicts sharp transitions along the shock boundary. The axial standoff distance for C_T = 10 agrees well, though that is due to the CFD solution showing an increase in standoff distance caused by the increase in plume size. The analytical model for this case predicts the same standoff distance as the lower thrust conditions due to the obstruction caused by the vehicle. C_T = 20 shows that the vehicle no longer influences the shock structure in the analytical model.

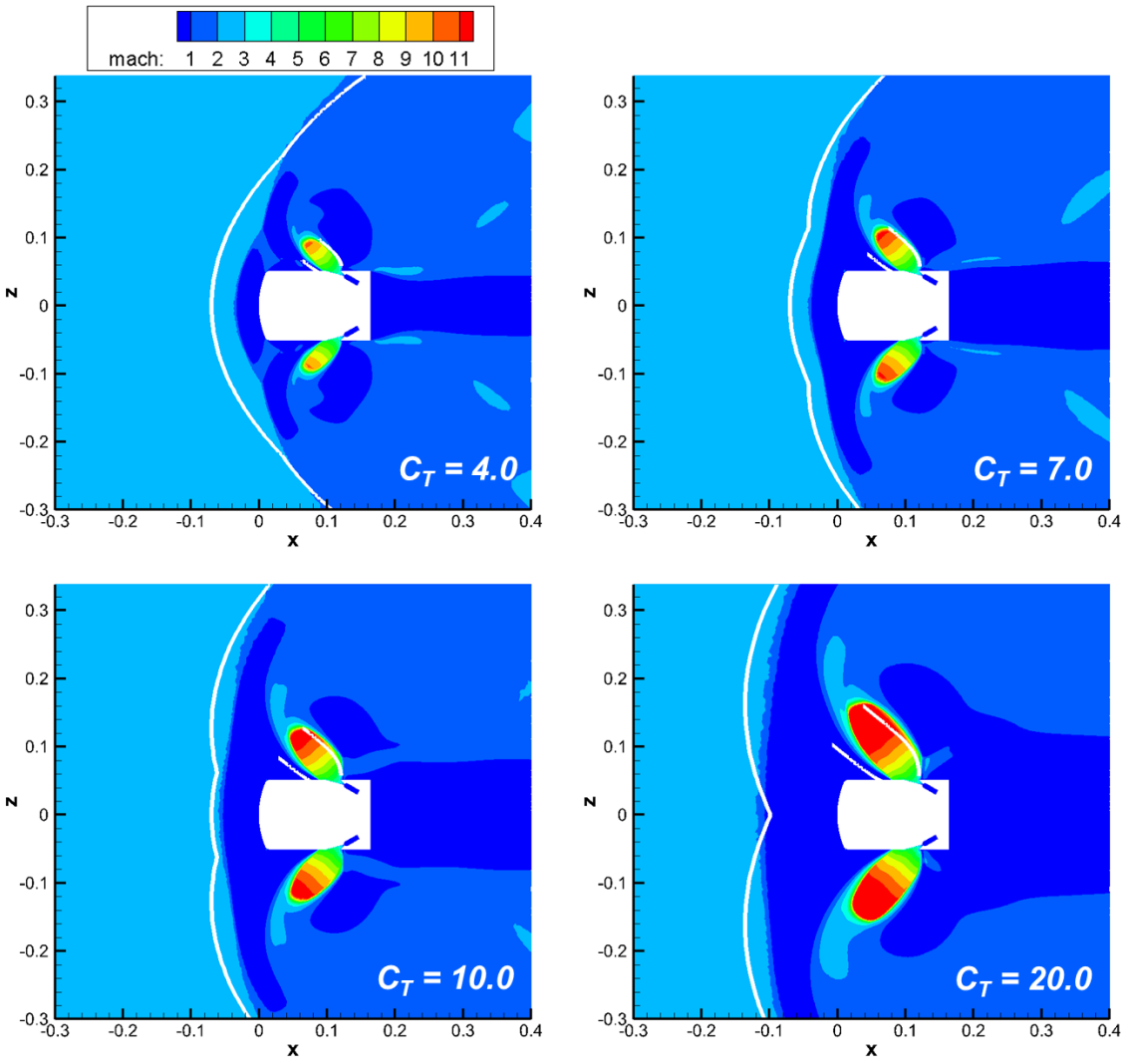

Figure 76: Comparison of plume and bow shock structures for CFD simulations and analytical model (white) for the six nozzle, 30° nozzle canting, aftbody configuration

The maximum bow shock axial extent is overpredicted for all thrust coefficients, as shown in Figure 77. For C_T = 1 and C_T = 4, the percent difference for the bow shock axial extent is constant since both the analytical model and CFD solutions show that the inboard bow shock is unperturbed. As the analytical model transitions from the vehicle causing the maximum bow shock extent to the plumes determining this flow feature, the slopes of the absolute and percent difference plots decrease in magnitude, though the

percent difference is still 21% at C_T = 20. The plume radial extent converges to a nearly constant percent difference near 5% for C_T > 1, confirming that the analytical model captures this feature across all thrust conditions. The magnitude of the absolute difference in plume axial extent increases with thrust, as the crossflow deflection angle calculated by the model is insufficient to accurately capture the plume structure.

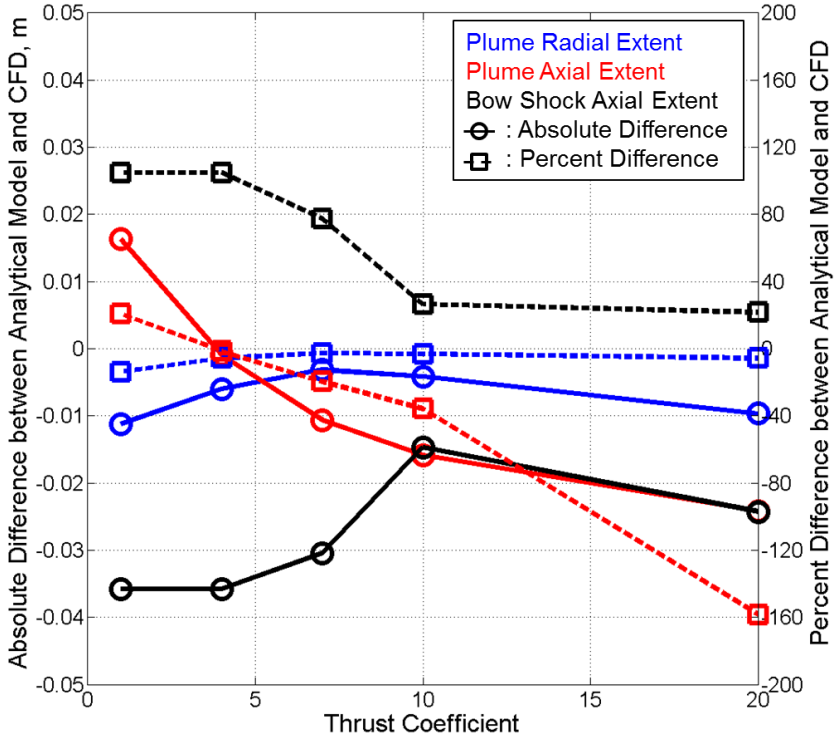

Figure 77: Absolute and percent differences for primary flowfield components between the analytical model and CFD for the six nozzle, 30° nozzle canting, aftbody configuration

Increasing the aftbody nozzle cant angle to 60° creates a nozzle incidence angle to the surface identical to that of the three nozzle, 0° nozzle canting, forebody configuration discussed in Chapter II. However, by having the nozzles on the aftbody, the flow into which the nozzles exhaust is different and the crossflow effects should vary from the

forebody configuration. Figure 78 shows comparisons for the analytical model applied to the six nozzle, 60° nozzle canting, aftbody configuration at various thrust coefficients. The crossflow angle for each of these cases is calculated to be 15.3°, significantly larger than the 7.1° calculated for the three nozzle, 0° nozzle canting, forebody configuration. This increase in crossflow angle is caused by the larger flow velocity along the aftbody surface which exists because the decelerated freestream accelerates around the shoulder of the vehicle.

For C_T = 4, the overall plume boundaries are well captured by the analytical model, indicating that the increased crossflow angle predicted by the model does actually occur in the CFD solution for this thrust coefficient. The analytical model predicts that the bow shock for this condition is unperturbed, as the plumes are directed sufficiently outboard that their effect is negligible. The actual CFD solution shows a kink in the shock structure which is formed by the obstruction created by the decelerated jet flow. This is not captured by the analytical model since the model assumes a hemispherical obstruction centered at the aft plume terminal location, which does not extend far enough radially to create the obstruction seen in the actual flow field.

Increasing thrust to C_T = 7 and C_T = 10 shows a continued trend of capturing the barrel shock well across the entire structure. Both of these analytical results show a bow shock structure that overpredicts the CFD solutions; however, the shape of the bow shock is well captured. The analytical model is nearly parallel to the Mach contour defining the bow shock in the CFD solution, including the kink that forms where the bow shock reacts to the plume obstructions. Increasing thrust to C_T = 20 still shows the well captured barrel shock, with the radial extent better captured than the other thrust coefficients. The

upstream extent of the plume is still well captured, as the crossflow deflection angle orients the analytical plume in the same direction as the CFD solution. The bow shock for this solution shows similar behavior as the six nozzle, 30° nozzle canting, aftbody configuration, where the transition from the inboard shock structure to the outboard structure is not a smooth transition as is seen in the CFD simulation.

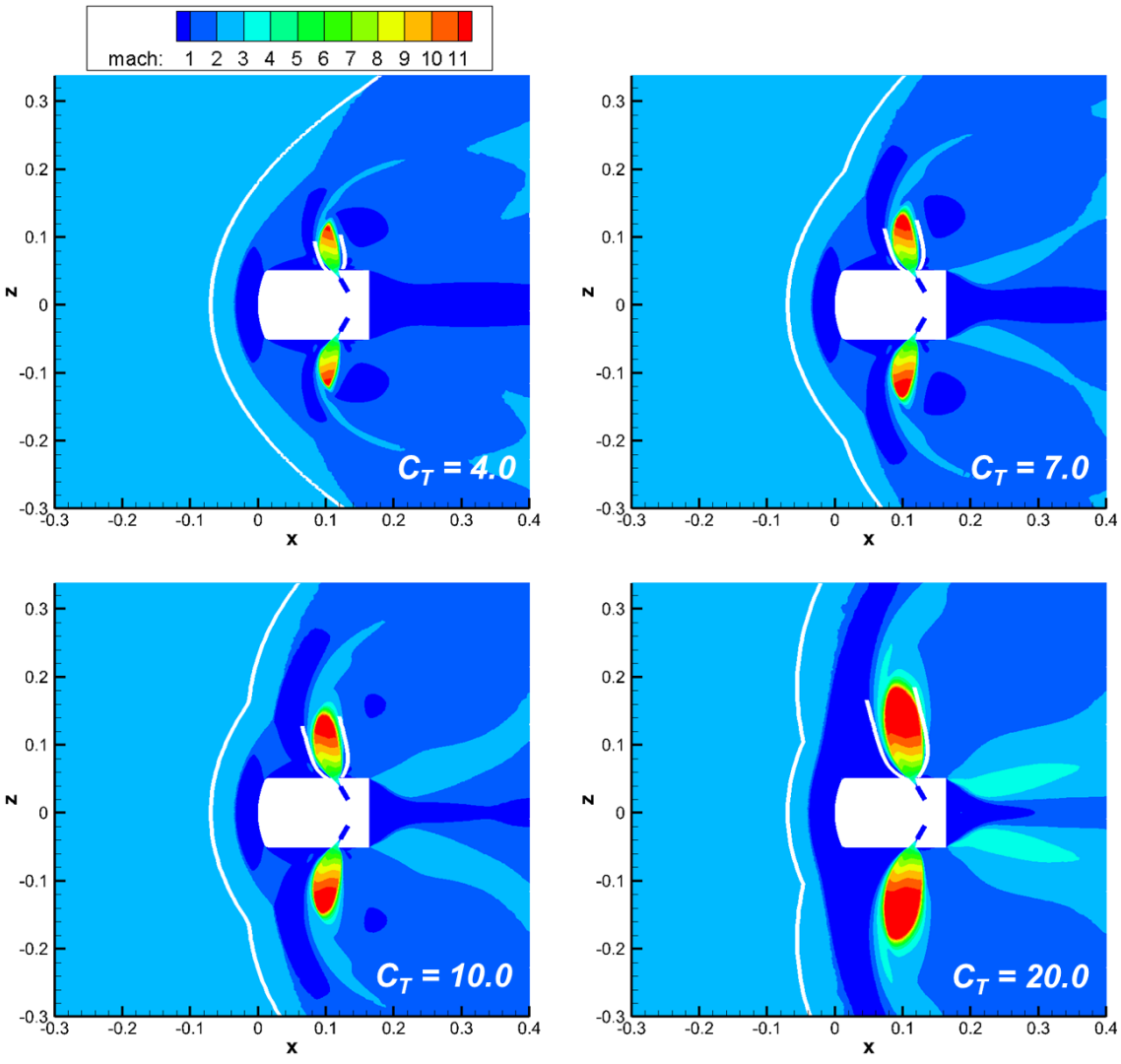

Figure 78: Comparison of plume and bow shock structures for CFD simulations and analytical model (white) for the six nozzle, 60° nozzle canting, aftbody configuration

Across all thrust coefficients, the analytical model predicts an undisturbed inboard bow shock shape, which is also seen in the CFD solutions. This results in a constant percent difference as shown in Figure 79, with the decrease at C_T = 20 a result of a slight increase in the CFD bow shock standoff distance. The plume radial extent is underpredicted across all C_T values, with a peak percent difference of 22% for C_T = 1 and decreasing absolute and percent differences with increasing thrust. The analytical model overpredicts the axial plume extent across all thrust conditions, with both absolute and percent differences increasing with increase thrust. This overprediction is due to the turning of the CFD plume reaching a nearly constant axial extent while the analytical model assumes a constantly expanding plume.

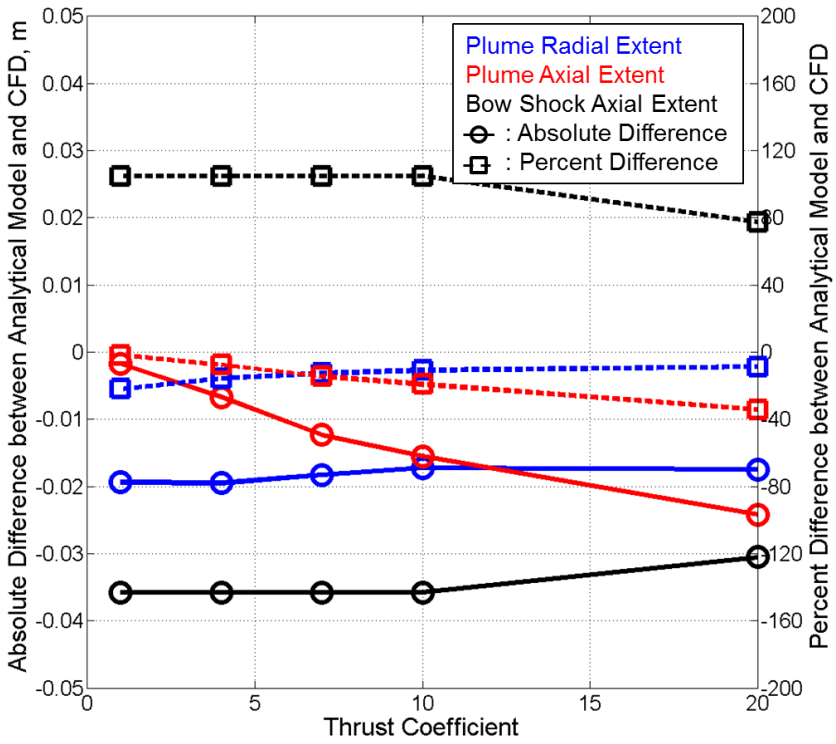

Figure 79: Absolute and percent differences for primary flowfield components between the analytical model and CFD for the six nozzle, 60° nozzle canting, aftbody configuration

4.3.3 Variation in Mach Number

The analytical model has been developed to account for variations in freestream Mach number and its impact on the flowfield structure. Comparisons for $M_\infty = 3$ and $M_\infty = 4$ are shown in Figure 80 for the three nozzle, 30° nozzle canting, aftbody configuration at the thrust conditions given in Table 11. The analytical model predicts a much narrower plume for both Mach numbers than is seen in the CFD solutions and significantly underpredicts the crossflow deflection angle of both plume structures. The terminal shock standoff distance, related to the length of the plume, appears to be well captured by the analytical model, indicating that the assumption of a stagnation pressure balance between the decelerated freestream and jet flows is still an accurate assessment of the plume length. The barrel shock equations used in the analytical model involve a cotangent function which creates a narrow plume structure. While the mass flow rate scaling should allow for a wider plume since the lost mass flow rate of an infinitely long plume is overcome, the significant length to the plume as Mach number increases means that less mass flow rate is effectively lost. Thus the plume is calculated to be narrower than is seen in the CFD solutions.

The maximum expected bow shock standoff distance is slightly overpredicted for both Mach number solutions; however, the overall shape of the bow shock has significant discrepancies. The general shape is correct, in that the visible plume creates a large, local bow shock perturbation forward of the plume structure which transitions to the shock forward and below the vehicle. The location of this transition point is inaccurately captured by the analytical model due to the underprediction of the crossflow deflection

angle. The analytical model predicts an increase in crossflow angle with Mach number, with values of 9.3° for M_∞ = 3 and 10.4° for M_∞ = 4 compared to 9.0° for M_∞ = 2. However, the increased Mach number solutions clearly show that the crossflow deflection angle is affected by more than the velocity triangle formed with the jet exit velocity and the surface flow velocity. If the crossflow angle is increased, the plume will be directed more outboard and have better alignment with the CFD simulations. This will also serve to direct the effective plume obstruction more outboard, increasing the radial location of the bow shock due to the plume obstruction while also decreasing the axial extent of the shock. This type of behavior is more in line with what is seen in the CFD solutions, where the bow shock reaches peak standoff distance farther outboard than is currently predicted by the analytical model.

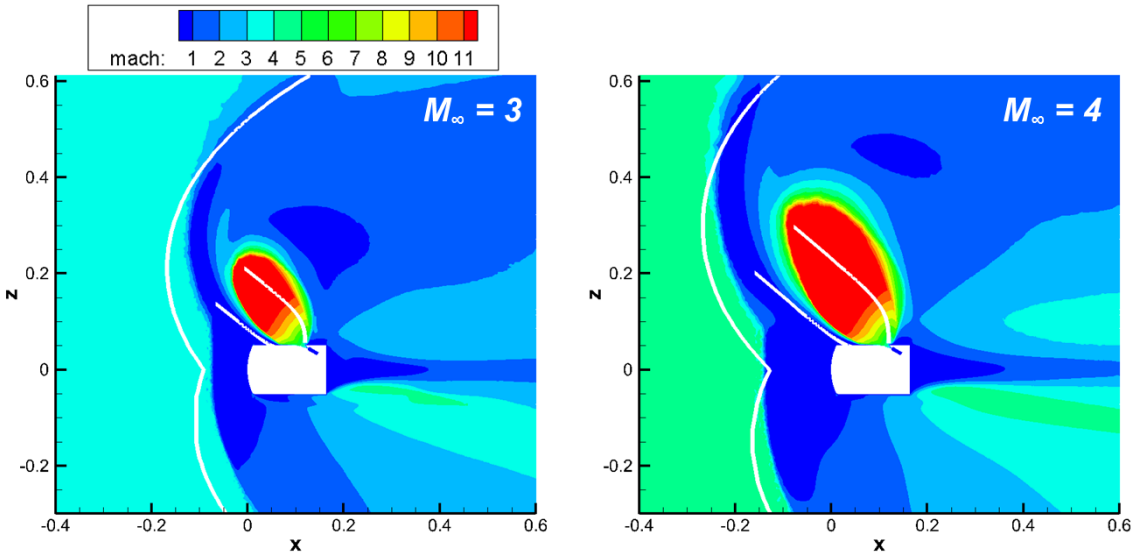

Figure 80: Comparison of plume and bow shock structures for CFD simulations and analytical model (white) for varying freestream Mach number

4.3.4 Variation in Specific Heat Ratio

The ratio of specific heats is also left as an input variable in the analytical model, as many of the governing equations depend on this variable. Figure 81 shows comparisons for γ = 1.2 and γ = 1.3 with the freestream and jet inlet conditions shown in Table 12 on the three nozzle, 10° nozzle canting, forebody configuration. The CFD solutions for these two flows assume a constant γ throughout the entire flow field. For γ = 1.3, the barrel shock agreement is consistent with that seen for γ = 1.4 in Section 4.3.1. The crossflow deflection angle is slightly underpredicted, with a value of 6.5°, but the axial and radial extents of the plume are well captured. The bow shock location is overpredicted by the analytical model, in part due to the underprediction in crossflow angle and in part due to the consistent overprediction associated with assuming a hemispherical obstruction for each plume.

For γ = 1.2, the plumes coalesce in the CFD solution, which has been shown in Section 4.2.5 to be a case which the analytical model is not expected to capture. The analytical model does generally capture the correct direction of the flow, with a calculated crossflow deflection angle of 5.5°. The outboard plume expansion is underpredicted, likely related to the cotangent function in the analytical model that creates narrower plumes. The axial and radial extents of the plume are underpredicted, which is likely a function of the plume coalescence. The bow shock structure shows a slight overprediction of the peak standoff distance, and the analytical shock shape has a kink where the influences of each plume intersect that is not seen in the CFD simulation.

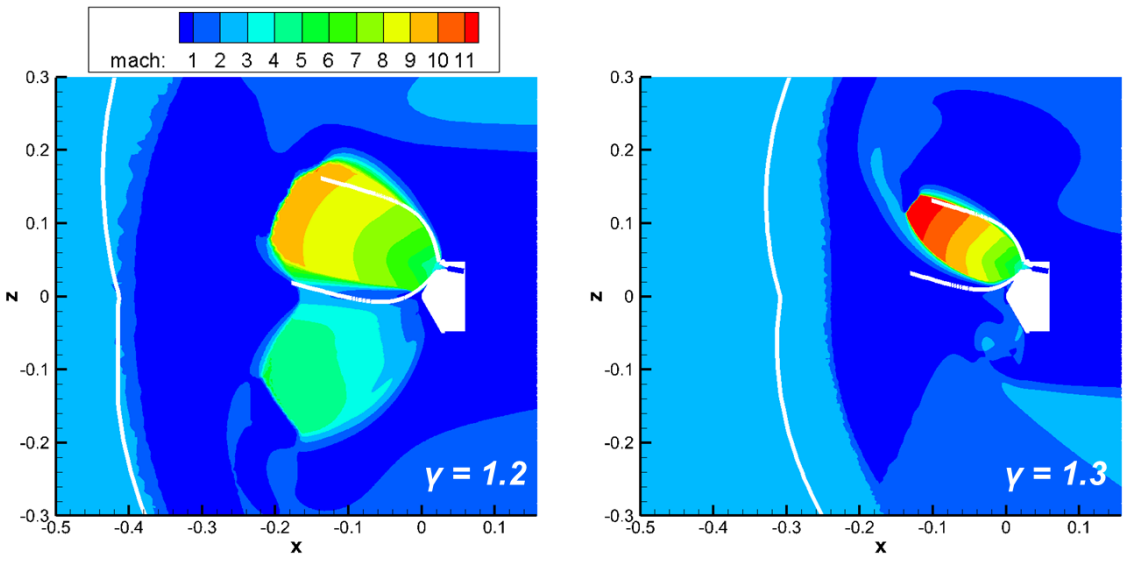

Figure 81: Comparison of plume and bow shock structures for CFD simulations and analytical model (white) for varying ratio of specific heats

4.4 Guidelines for CFD Grid Generation

The analytical model provides a rapid means of determining the flowfield structure for an SRP system, where aeroshell geometry, nozzle configuration, freestream conditions, and thrust level are all input conditions. One use of a given analytical solution is to assist in initial grid generation for the CFD by providing insight into the locations of SRP flow field components. The location of the plume defines a region into which the plume flow is expected to form, and the bow shock structure provides an estimate of the required volume forward of the vehicle to allow for shock formation. An estimate of the maximum cell resolution within the plume region of the computational domain can also be described using the analytical shear layer approximation, with smaller cells near the vehicle surface to capture the plume expansion from the nozzles and any boundary layers that form along the vehicle surface. This methodology has been applied to each

configuration of geometries 3-6 as described in Table 8. A discussion of each grid and the results of the grid generation process are given for each configuration in Chapter V and Chapter VI.

4.4.1 Flow Features and Regions of Interest

The plume boundaries output from the analytical model define a region into which the plume flow is expected to exhaust. How this would be implemented in the grid generation process is a function of the type of grid generation software used to create the computational mesh. The grids used for the CFD solutions in Chapter IV, Chapter V, and Chapter VI have been generated using Gridgen V15.15, and the method described here assumes that type of grid generation. Gridgen allows for the definition of connectors, domains, and blocks within the computational grid, corresponding to 1D, 2D, and 3D grid components respectively. The connectors are used to define the boundary lines of domains, and domains are used to define the boundary surfaces of blocks. The tetrahedral solver within Gridgen creates unstructured cells within a block based on the generated triangular mesh of each bounding domain, with an input variable defining the source strength of the domains on the block's interior tetrahedral formation.

The results of the analytical model for the plume boundaries provide an estimate of the maximum radial and axial extents at which the plumes terminate, as shown in Figure 82. Domains are created to encompass a volume that contains the predicted plume locations for the largest thrust condition run on a given geometry. For the three nozzle configurations, this corresponds to C_T = 10, and for the six nozzle configurations, C_T = 20. A margin has been applied to provide extra computational volume if the analytical

model underpredicts the final plume structure or if plume formation results in an iteration varying plume length.

Once the plume region has been defined, additional blocks can be created to encompass the expected bow shock region, also shown in Figure 82 by the green boundary. The region shown in orange represents a sufficient upstream distance to capture the predicted bow shock with some margin applied, and the outboard distance is set to allow space for the plume flow to decelerate and turn. The analytical model provides an estimate of the transition from a bow shock to a Mach wave, which can be used to define the outermost radius of the computational volume. The freestream inlet plane is set to be further upstream than the predicted analytical model bow shock structure so that sufficient volume is allowed for shock formation. As the accuracy of the analytical model for the bow shock location is not known a priori, a significant margin has been applied in the generation of the computational grids for the configurations in this dissertation to ensure that the entire shock structure is captured.

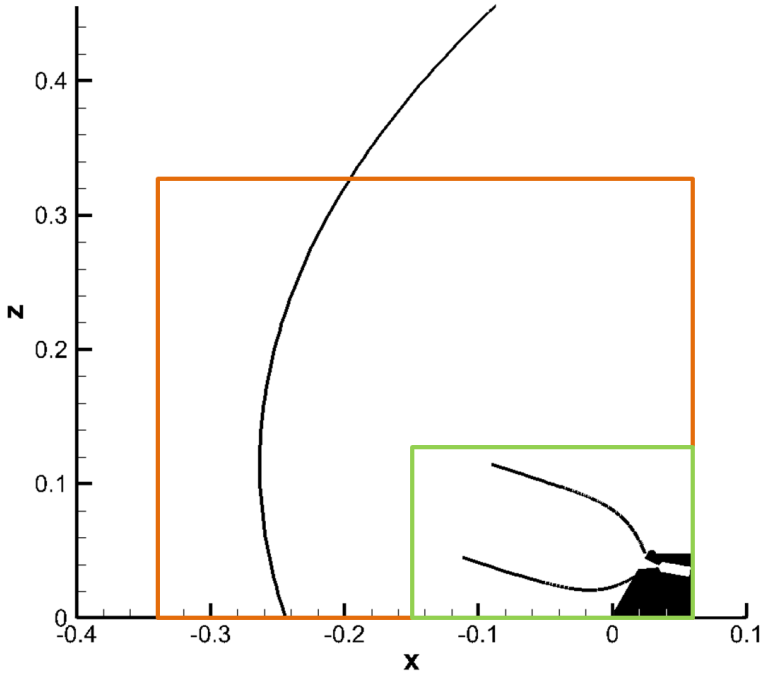

Figure 82: Example application of analytical model (black) for defining plume (green) and bow shock (orange) regions for the 10° nozzle canting forebody configuration at C_T 10

4.4.2 Approximate Grid Resolutions in Plume Region

The analytical shear layer approximation is used to guide cell resolution within the plume region of the computational domain. The maximum shear layer thickness provides an upper bound on the grid spacing within the block, as any cells larger than that spacing will not be able to capture the shear layer formation. This maximum cell length is set along the plume region domains defined in Section 4.4.1 and shown in Figure 83. For this example, the plume is totally contained within the predicted plume region. The bow shock region is sufficiently far upstream such that the shock standoff distance is contained within the predicted region.

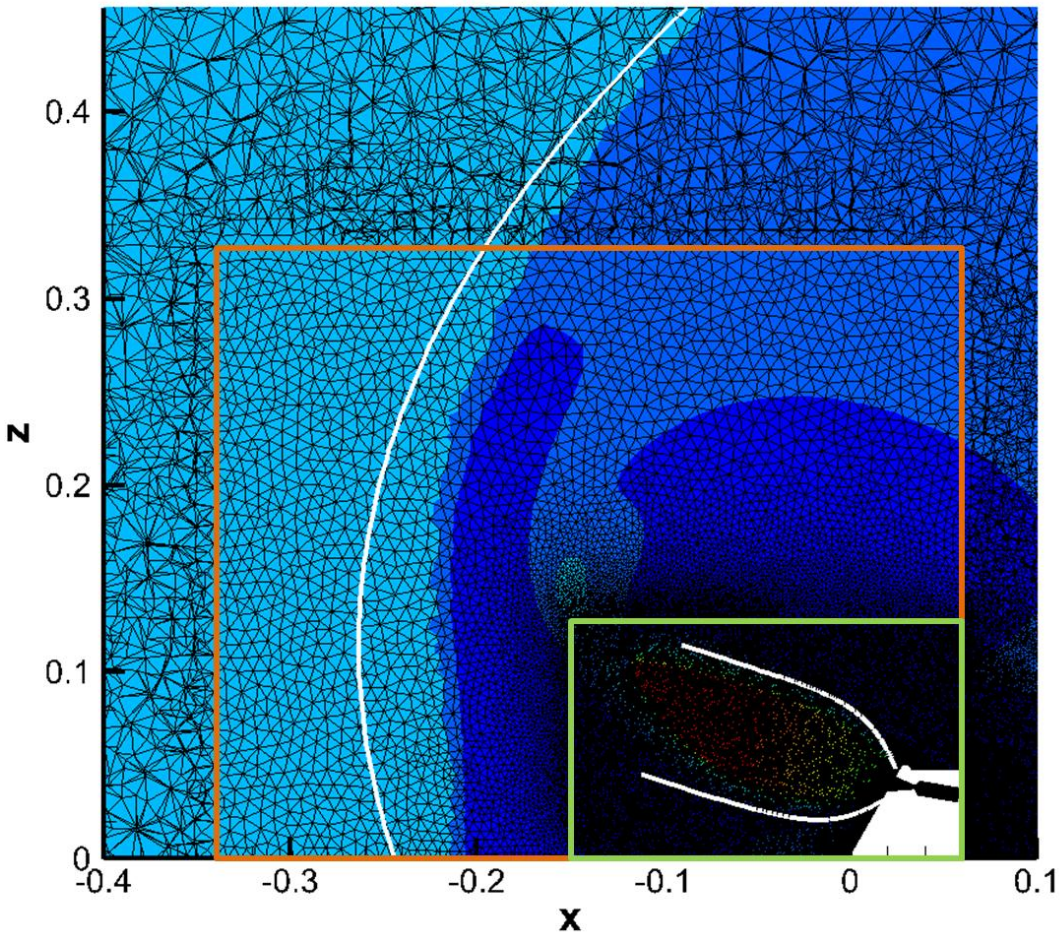

Figure 83: Grid generated using analytical model to define the plume (green) and bow shock (orange) regions with Mach contours shown for C_T = 10 on the 10° nozzle canting configuration

For each of the geometries in Chapter V and Chapter VI, one third of the estimate of the shear layer thickness for the maximum thrust case has been used as the maximum allowable grid spacing within the plume region. This allows for at least three grid cells to cross the maximum shear layer thickness at the extent of the plume region in the computational domain, though with the orientation of unstructured tetrahedrals the actual shear layer will be covered by more cells. The grid spacing at the surface is set to be significantly smaller than this maximum, and each domain on the plume blocks is

allowed to have a strong influence on the tetrahedral solver, meaning that the small cell size will propagate far into the plume region of the flow. This will allow for smaller cells in the initial expansion region of the plume flow, where the shear layer is thinner and a growth of cell size as the plume expands and fills a larger volume.

4.4.3 Near Surface Grid Resolution

The minimum cell spacing is set along the surface of the vehicle, and the reference length for the triangular cells along the surface has been set using engineering judgment through the establishment of the solutions shown in Chapter II. The spacing along the vehicle outer mold line has been set to approximately 5×10^{-4} meters, with a smaller spacing of approximately 2×10^{-4} meters specified along the nozzle surfaces. Cells to capture the boundary layer have been extruded from these surface triangles prior to generating the computational domain for capturing the plume flow. Within the nozzle, anisotropic cells have been used, as pentrahedrals caused errors in generating the mesh within the nozzle. Initial spacing of 1.5×10^{-5} meters with a growth rate of 1.3 have been used to generate 10 layers within the nozzles. For the forebody located nozzles, pentahedral cells have been extruded from the surface triangular cells, with the same initial spacing and growth rate as the nozzle. For the aftbody located nozzles, the pentrahedral cells caused errors in generating the mesh, so anisotropic cells have been extruded from the vehicle triangular surface mesh in addition to the nozzle with the same spacing and growth rate. This surface grid resolution is sufficient to capture the plume structure for analysis of aerodynamic force and moment effects; however increased cell resolution near the

surface would be required to accurately capture heat transfer effects that are beyond the goals of this study.

4.5 Summary

For all eight validation configurations, the analytical model is capable of capturing the maximum radial and axial extents of the plume structure, even if the predicted boundary does not precisely follow the Mach contours in the CFD solutions. Capturing these peak values is useful for preliminary design as the maximum expected plume expansion provides bounds on the regions in the flow field within which the jet flow is expected to exist. The crossflow deflection angle model which perturbs the plume structure is shown to be valid for some configurations. If the incidence angle is low between the nozzle axis and the vehicle surface, such as for the 30° nozzle canting aftbody configurations, then the crossflow model is somewhat valid and provides an underprediction of the perturbation angle of the plume. If the nozzle exhausts nearly normal to the surface, such as for the 30° nozzle canting forebody configuration, then the crossflow model is not valid and underpredicts plume perturbation. Configurations between these two extremes, such as the 0° and 10° nozzle canting forebody configurations as well as the 60° nozzle canting aftbody configuration, show that the velocity triangle approach to modeling crossflow deflection is most valid for modeling plume perturbations.

The analytical model is not valid for conditions where plume coalescence occurs, as the model assumes each plume expands independently of each other. The underprediction of plume structure for these configurations also causes an underprediction in bow shock structure for coalesced plumes. For all other configurations, the maximum bow shock

standoff distance in the analytical model is conservative and overpredicts the CFD solutions. The hemispherical obstruction is valid in terms of shape, though the center of the hemisphere is further outboard in the CFD solutions than is modeled in the analytical approach.

CHAPTER V

FOREBODY NOZZLE CANTING EFFECTS ON FLOWFIELD STRUCTURE AND AERODYNAMIC PERFORMANCE

Nozzle canting on the forebody, as investigated in geometries 3-5 in Chapter IV, displays significant variation in flowfield structure and its subsequent effect on the propulsive-aerodynamic interaction of an SRP system. The underlying forebody and aftbody shape from the Jarvinen and Adams wind tunnel test for the three nozzle configuration [10], and the corresponding computational geometry described in Chapter II are used as the basis for investigating the effects of forebody nozzle canting. Each of the geometries investigated has three nozzles, at the same eighty percent radial location and 120° separation as the wind tunnel configuration. The radius of the conical diverging section as measured from the intersection of the nozzle axis with the vehicle forebody is kept constant for each configuration and the plenum pressure and temperature ratios from Table 2 are used to set the thrust for each nozzle. This results in the same C_T value for each nozzle, although the net deceleration force must include the cosine losses from the nozzle cant angle. For each of geometries 3-5, both the flowfield structure and surface pressure preservation for varying C_T are investigated. For the 10° and 30° nozzle canting geometries, an investigation of the propulsive-aerodynamic interaction at angles of attack is used to determine static stability characteristics.

5.1 Three Nozzle Configuration with 10° Cant Angle

Canting the nozzles by 10° outward represents a modest configuration change from the nominal geometry with no nozzle canting. The nozzles are still scarfed, and the plumes generally have the same structure as are shown in Chapter II. Thrust coefficients of 1, 4, 7, and 10 have been run on this configuration at 0° angle of attack. Additionally, the C_T = 10 case has been run at angles of attack of -10° and 10° to establish static pitch stability characteristics of a high thrust condition.

5.1.1 Zero Angle of Attack Effects on Flowfield Structure and Surface Pressure

Canting the nozzles by 10° results in plume structures which are generally aligned with the nozzle axis for all thrust coefficients examined, as shown in Figure 84. For C_T = 1, each plume is small and the bow shock inboard of the nozzles is relatively undisturbed. The plumes cause local perturbations to the bow shock structure forward of the nozzle exits, as the plume structure represents an additional obstruction to the freestream flow further upstream from the actual vehicle surface. The small plumes result in significant surface pressure preservation inboard of the nozzles, as the combination of small plumes and a jet exhaust directed outboard from the vehicle axis result in little shielding of the forebody.

Increasing the thrust coefficient to C_T = 4 results in larger plumes from each nozzle, which are large enough to significantly offset the bow shock location in front of the entire vehicle. As compared to the lower thrust solution for C_T = 1, the inboard expansion of the plume is larger; however the cant angle causes the plume to still be directed in a generally

outboard direction. This results in a stagnation pressure on the surface similar to the low thrust solution, but the higher pressure region on the forebody has shrunk.

Further increasing thrust to $C_T = 7$ results in a still larger plume as expected, with the bow shock standoff distance increasing relative to the lower thrust conditions. The inboard plume expansion is minimal as the cant angle of the nozzle directs the flow outboard. The peak stagnation pressure has dropped, and the region of high pressure continues to shrink relative to the lower thrust conditions. However, even at this high thrust condition, the modest 10° cant angle is sufficient to create a situation where significant surface pressure is preserved along the forebody.

The highest thrust condition run for this configuration is $C_T = 10$, which shows a similar underlying plume structure as the lower three thrust conditions. Each plume is independent of the others, and the cant angle alleviates the inboard expansion of the jet exhaust flow. While the peak surface pressure is lower for this thrust condition as compared to the other thrust values, the presence of a nonzero surface pressure coefficient over an appreciable area of the forebody indicates that 10° nozzle canting results in a situation where increasing thrust does not necessarily mean a total reduction in the aerodynamic component of deceleration. Rather, the propulsive-aerodynamic interaction becomes more complicated, where aerodynamic drag has a strong dependence on thrust over a wide range of thrusts.

A 10° cant angle does result in a cosine loss to the thrust component of the deceleration force. For this cant angle, the thrust coefficient reported is scaled by 0.985 to determine the net contribution of thrust to the deceleration force. Thus, for $C_T = 10$, the actual deceleration force coefficient provided by thrust would be 9.85, with the

aerodynamic drag contribution added on top of that value. A comparison of the net deceleration force coefficients for all configurations with forebody nozzle canting is performed in Section 5.4.3, which contains the integrated aerodynamic coefficients for the solutions shown in Figure 84.

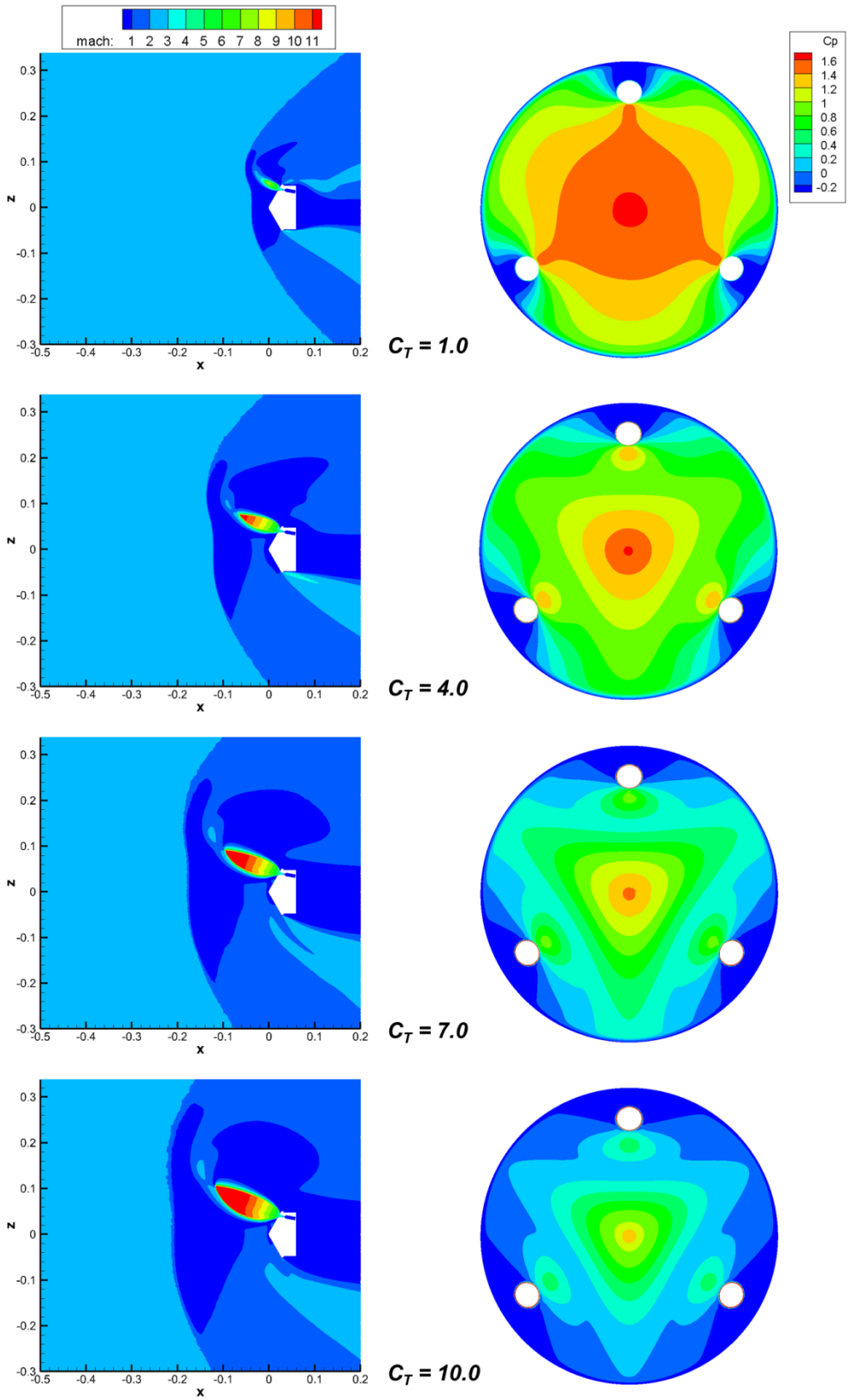

Figure 84: Mach contours and C_P distributions for varying C_T with 10° nozzle canting

5.1.2 Angle of Attack Effects

As angle of attack is varied, the orientation of each plume relative to the freestream flow will differ. Figure 85 shows Mach contours and pressure coefficient distributions for the 10° nozzle canting geometry at angles of attack of -10°, 0°, and 10°. The -10° angle of attack case results in the nozzle located in the *X*-*Z* plane, as shown in the Mach contours, exhausting directly into the freestream flow. However, this does not mean that the plume will revert to a symmetric structure, as the nozzle is not exhausting at the stagnation point of the vehicle. Rather, a small local crossflow is still present into which the nozzle exhausts. This causes a compression of the inboard barrel shock, similar to the effects seen for the geometry with no nozzle canting. For increasing angle of attack, the barrel shock does not noticeably change on either the inboard or outboard side, indicating that the relative angle of the exhaust flow is not strongly dependent on orientation to the freestream, but rather on the orientation of the nozzle axis with the vehicle surface. The terminal region of the plume does show a variation, as the plume appears to form more of a normal shock for increasing angle of attack.

As the plumes do not shield the entire forebody, and the stagnation point remains inboard of the nozzle exits, there is not a large variation in surface pressure with angle of attack. For α = -10°, the peak surface pressure is higher, as the decelerated freestream is less impacted by the out of plane nozzles in this orientation. For α = 10°, the freestream approaches the vehicle from the lower half which contains the out of plane nozzles, and as such the peak surface pressure, and high pressure regions just inboard of the nozzle exits are modified to reflect the slight variations in plume structure due to the change in orientation.

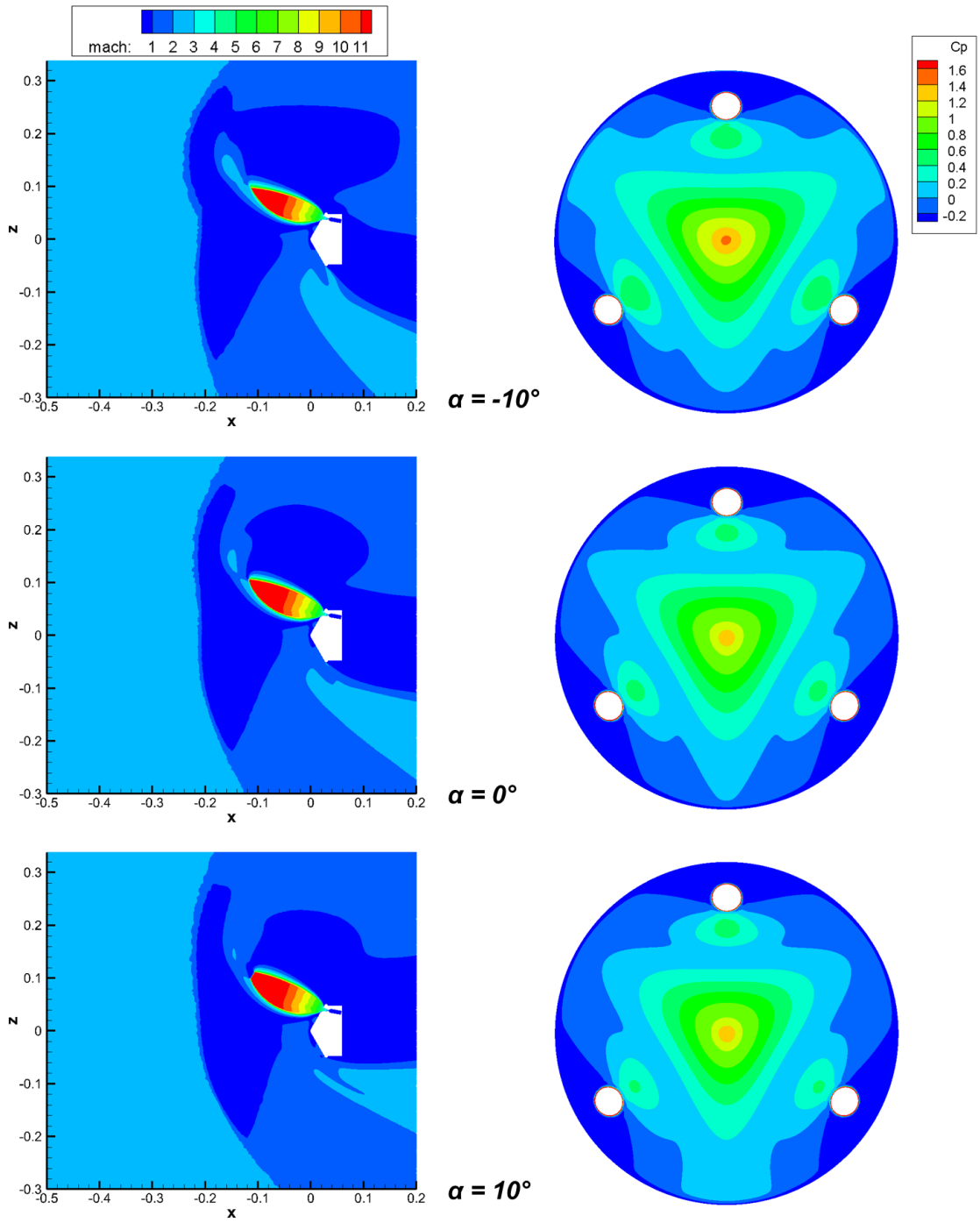

Figure 85: Effect of angle of attack on flowfield structure and surface pressure for C_T = 10 on the 10° nozzle canting geometry

Plots of pitching moment provided by the integrated surface pressure distribution for the forebody and shoulder regions for each angle of attack case are shown in Figure 86 for varying center of mass locations along the vehicle axis. As the nozzle configuration is symmetric about the vehicle axis and each engine provides the same thrust, the thrust moments will cancel each other and are not included in the plots. The maximum axial location allowed corresponds to the intersection of the shoulder and the aftbody, equal to 0.0326 m and consistent with the base location used in the Jarvinen and Adams experiment for measuring the shock standoff distances in the flow field [10]. For performance concerns, this assumption is equivalent to a vehicle with no pressure on the aftbody that would provide additional moments to the system.

At zero angle of attack, the pitching moment is expected to equal zero regardless of axial location since the vehicle, nozzles, and thrust are all symmetric. The only appreciable force or moment on the system should be the axial force component along the vehicle axis, which would provide zero moment for a center of mass also located on the axis. This is true for the 10° nozzle canting geometry, as shown by the blue line in Figure 86. The slight negative value occurs because the computational grid and CFD solution are not perfectly symmetric, so some numerical noise occurs. For static pitch stability, the derivative of the pitching moment with angle of attack should be negative when taken at the center of mass. For the three angle of attack cases examined for this configuration, this derivative is negative. Cases at angles of attack between -10° and 10° may show regions where this vehicle is not statically stable. The results presented in Figure 86 provide a bounded angle of attack region within which the vehicle should remain even if there are local regions of instability that are not captured in this analysis. As the center of

mass location shifts aftward, the derivative decreases, with the trim center of mass location existing far aft of the vehicle for C_T = 10.

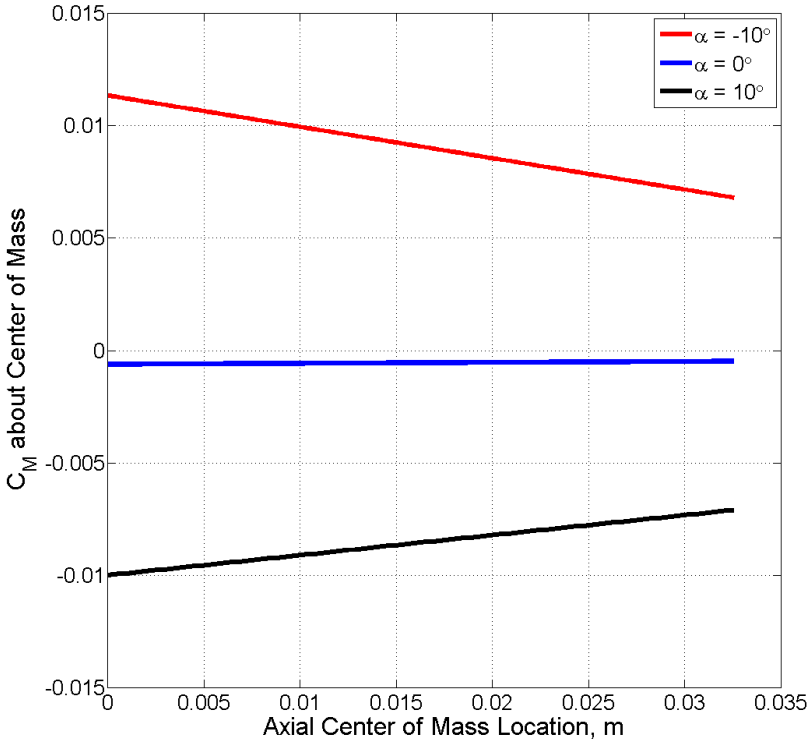

Figure 86: Variation in pitching moment coefficient with center of mass location and angle of attack for C_T = 10 on the 10° nozzle canting geometry

In addition to determining the static pitch stability of the SRP system, the sensitivity of the CG location at which the vehicle trims can be found by solving for the *X* and *Z* coordinates at which the net moment from the aerodynamic and nozzle thrust contributions equals zero. Figure 87 shows these lines plotted with the vehicle shape for reference for angles of attack of -10°, 0°, and 10°. Both a view of the entire vehicle shape and a zoomed view to differentiate the lines for each angle of attack are shown. Regardless of angle of attack, the CG trim lines are nearly horizontal for this thrust

coefficient. This indicates that the ability of the 10° nozzle canting configuration to trim is not sensitive to the location of the CG near the vehicle axis. The large thrust available from the nozzles allows for corrections such that the vehicle can reach trim conditions. Combining this result with Figure 86 showing static pitch stability across the entire axial extent of the vehicle means that the 10° nozzle canting configuration investigated here is not sensitive to CG location. This will impact system design by loosening constraints on packaging, as CG location is not as important for stability concerns.

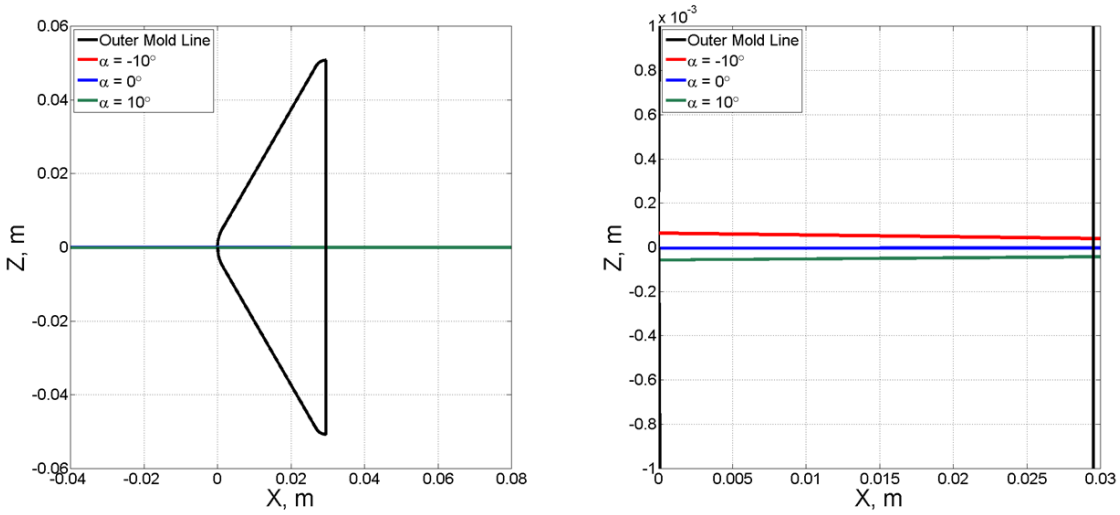

Figure 87: Center of gravity trim lines for varying angles of attack at C_T = 10 on the 10° nozzle canting geometry for the full vehicle view (left) and a zoomed view (right)

5.1.3 Grid Generation

As discussed in Section 4.4, the analytical model has been used to guide the generation of the computational grid for this geometry. Investigating the barrel shock shown in Section 4.3.1 for C_T = 10 on the 10° nozzle canting geometry, the maximum expected plume radial extent is 0.099 m and the maximum expected plume axial extent is -0.112 m. As is

seen in Figure 88, a region has been defined within Gridgen with some margin to the predicted analytical solutions for calculation of the plume boundaries. The final CFD plume falls within the approximate region created from the analytical model, indicating that building a grid using the information from the analytical method works well for this small nozzle cant angle geometry.

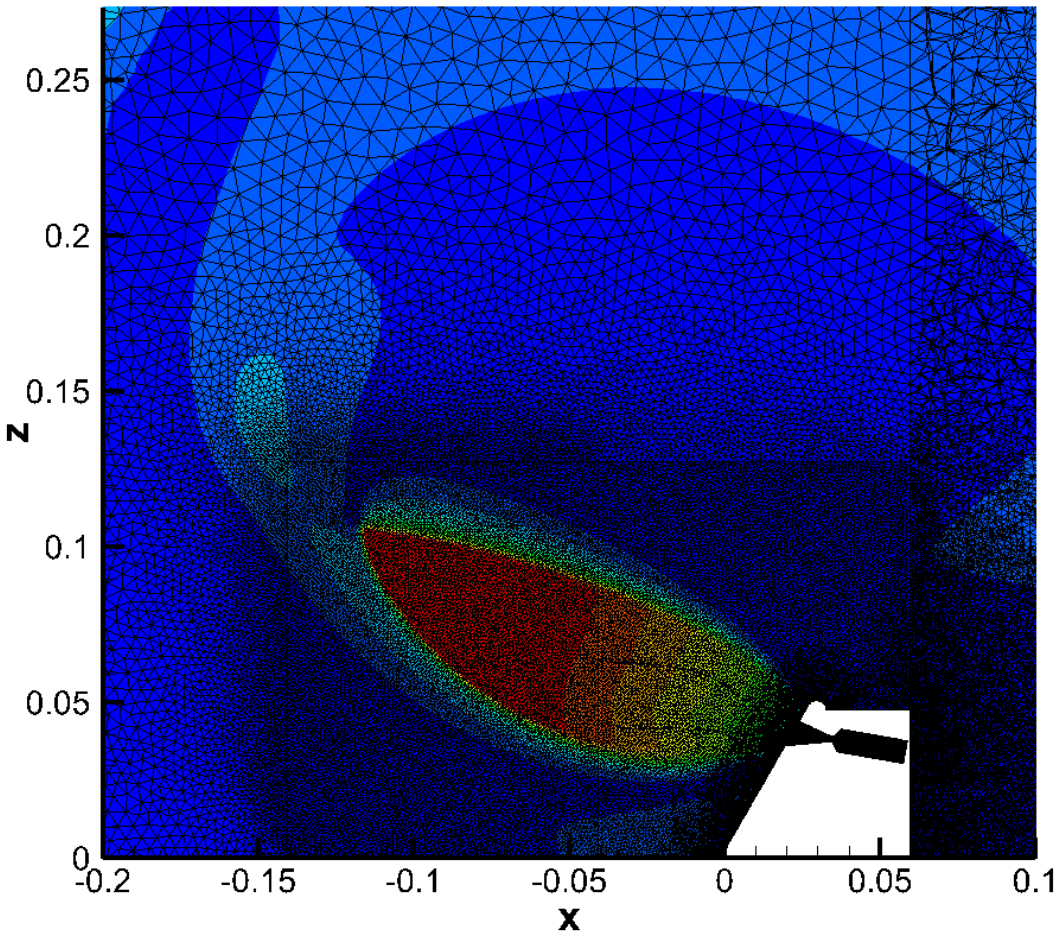

Figure 88: Plume region within computational grid for 10° nozzle canting configuration with C_T = 10 Mach contours shown for reference

As with the plume structure, the analytical model prediction for the bow shock location has been used to guide the definition of a region within Gridgen into which the bow

shock is expected to form. This region is shown in Figure 89 for the 10° nozzle canting geometry. The analytical model overpredicts the bow shock structure as described in Section 4.3.1, so applying a margin to the analytical prediction results in a larger than necessary region for bow shock formation. An overprediction is acceptable in this instance as it guarantees that the bow shock is captured within a region whose resolution is sufficient to resolve the shock. Overall, this grid contains 17.2×10^6 nodes, on the same order as the highest resolution grid used on the 0° nozzle canting geometry in Chapter II.

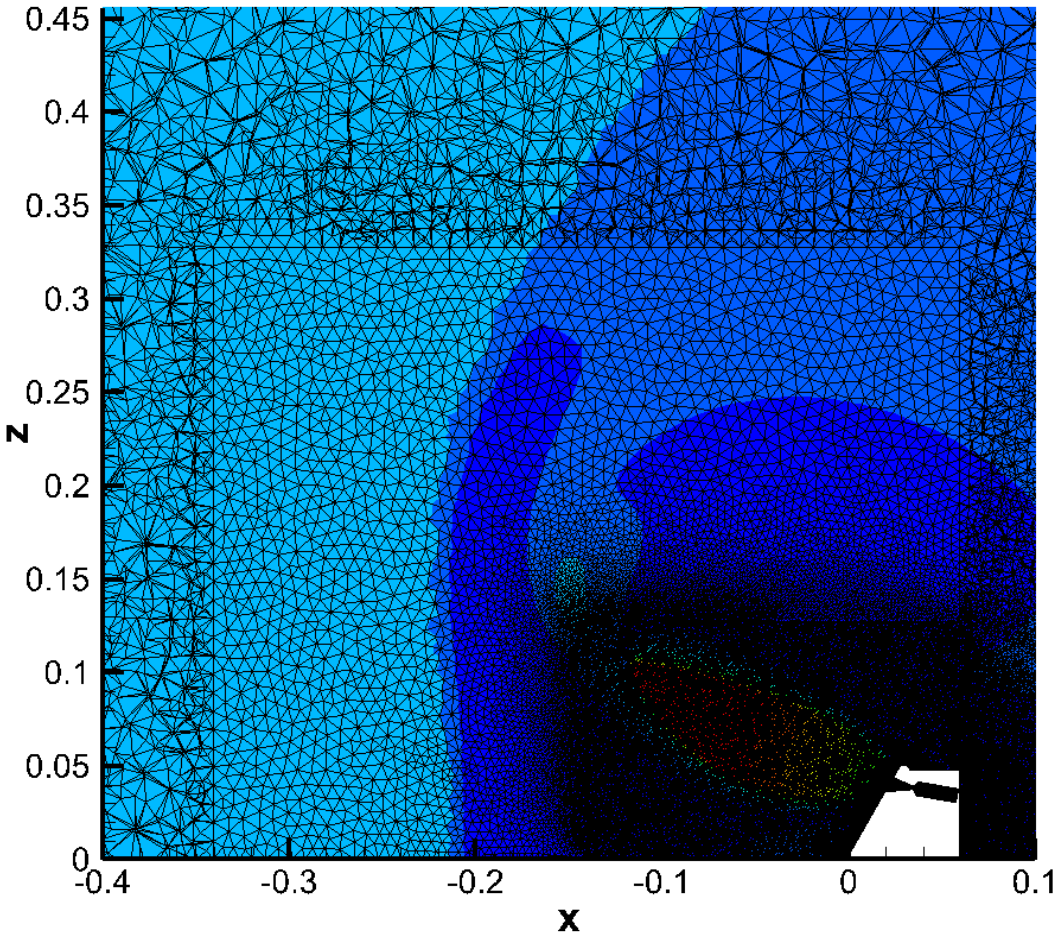

Figure 89: Bow shock region within computational grid for 10° nozzle canting configuration with C_T = 10 Mach contours shown for reference

A view of the *X-Z* plane covering the entire computational domain is shown in Figure 90. The majority of the nodes in the computational mesh are concentrated near the vehicle to capture the plume structure, bow shock structure, and wake flow. The subsonic wake flow closes completely within the computational domain and does not interact with the exit plane boundary. This prevents the exit plane boundary interactions discussed in Chapter II from occurring and potentially modifying the plume structure forward of the vehicle.

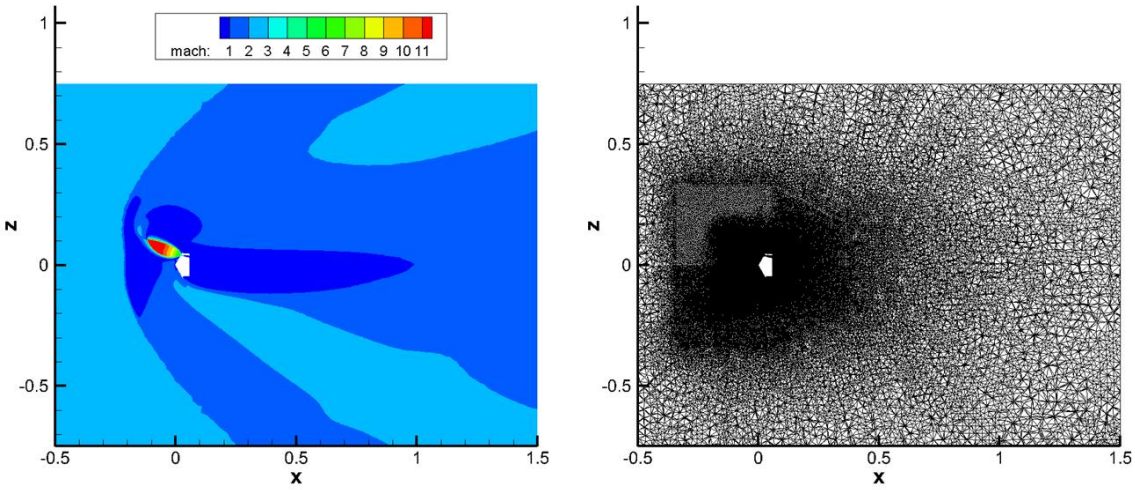

Figure 90: Full computational domain with C_T = 10 Mach contours (left) and computational mesh (right) for the 10° nozzle canting configuration

5.2 Three Nozzle Configuration with 20° Cant Angle

A 20° outward nozzle canting creates a plume structure which differs noticeably from the structure seen for the 0° and 10° nozzle canting geometries, particularly as thrust increases. Thrust coefficients of 1, 4, 7, and 10 have been run at zero angle of attack to determine the variation in flowfield structure and surface pressure for this configuration.

A grid convergence study has been performed on three grids of varying resolution and underlying block structure within Gridgen to ensure that the grid is not the cause of the differing plume structure.

5.2.1 Zero Angle of Attack Effects on Flowfield Structure and Surface Pressure

For the 20° nozzle canting geometry, the nozzle exit velocity in the radial direction is increased and the plume does not extend as far upstream into the freestream flow. This creates a situation where the plume shielding of the forebody decreases substantially, allowing for increased preservation of surface pressure as shown in Figure 91 for varying thrust coefficient. At C_T = 1, the plume is small and the forebody surface pressure is nearly undisturbed. The peak surface pressure is preserved at the nose of the vehicle. The small plume creates a relatively undisturbed bow shock inboard of the nozzle exit and a local bow shock perturbation forward of the nozzle exit due to the presence of the plume.

As thrust is increased to C_T = 4, the plume grows larger and causes the entire bow shock structure to form further from the vehicle. However, since the plume forms along the direction of the nozzle axis, the forebody surface is not shielded sufficiently to lower the surface pressure. As is expected due to each plume creating an effective obstruction to the freestream flow, a small high pressure region forms just inboard of the nozzle exit since the flow along the surface must turn to flow around the plume. While the high pressure region at the nose is smaller than seen for C_T = 1, the peak surface pressure is preserved.

C_T = 7 shows a noticeable difference in the outboard barrel shock as compared to the lower thrust solutions. Rather than constantly expanding until terminal conditions are

reached, the barrel shock has a noticeable kink and a terminal shock appears to form along the outboard portion of the plume. This would be related to the orientation of the plume flow to both the freestream flow direction and the vehicle surface at the nozzle exit. The inboard barrel shock does not exhibit this type of behavior, as this boundary is similar in shape to the lower thrust solutions. The overall axial extent of the plume does not differ significantly from what is expected, as the bow shock standoff distance increases further from the C_T = 4 solution. The difference in outboard barrel shock formation also does not impact the surface pressure trends for this configuration, as the peak surface pressure on the forebody continues to be preserved. Over the entire forebody, an appreciable surface pressure is preserved as well, due to the decrease in forebody shielding from the plume structure.

The C_T = 10 solution exhibits the same outboard barrel shock structure as is seen for C_T = 7. Even at this high thrust condition, the 20° nozzle canting creates a situation where the peak surface pressure at the nose is nearly completely preserved and the pressure over the entire forebody is much greater than the zero pressure coefficient values seen when the nozzles have no canting. The plumes have not coalesced and the decelerated freestream flow still has a flow path to reach the surface of the vehicle. The small high pressure region inboard of the nozzle exits is still present at this thrust condition, as the decelerated freestream turns along the surface and flows outboard until the plume obstruction requires this flow to turn and pass around the plumes.

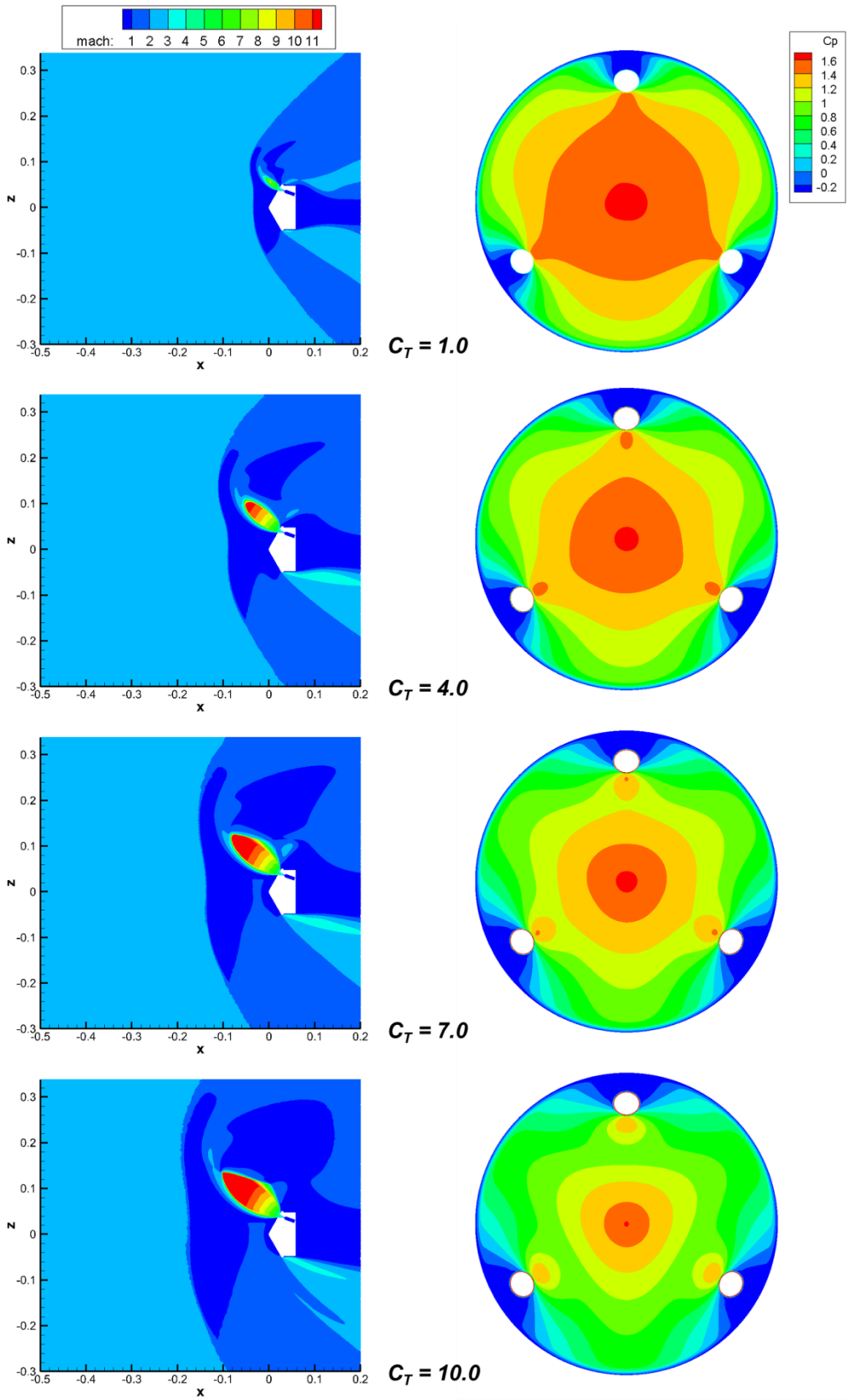

Figure 91: Mach contours and C_P distributions for varying C_T with 20° nozzle canting

5.2.2 Effect of Exhausting Directly into Freestream

Figure 92 shows the Mach contours and surface pressure distribution for the 20° nozzle canting configuration at -20° angle of attack. This results in the nozzle axis for the upper engine being aligned with the freestream. The plume is nearly axisymmetric for this case, with the only perturbation caused by the stagnation point still being located inboard of the nozzle. This causes a crossflow to still exist at the nozzle exit, which compresses the inboard barrel shock. There is a decrease in peak surface pressure due to the shielding provided by the plume exhausting directly into the freestream flow, but not a total loss of pressure over the entire forebody as is seen for the 0° nozzle canting configuration.

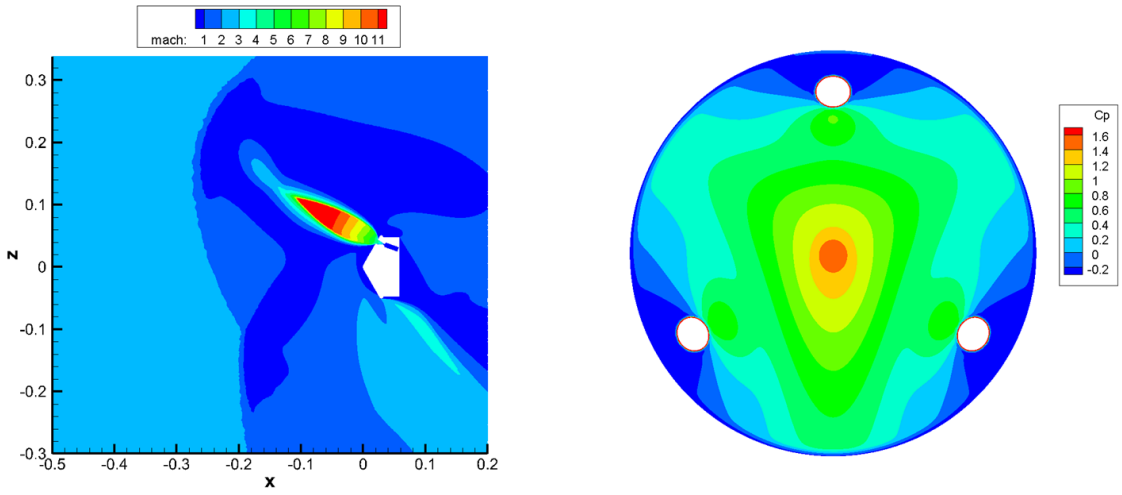

Figure 92: Mach contours and C_P distribution for C_T = 10, α = -20° with 20° nozzle canting

5.2.3 Grid Convergence Study

The unexpected outboard barrel shock structure seen for C_T = 7 and C_T = 10 merits additional investigation to ensure that the CFD simulations are independent of the computational grid. Three different grids have been investigated, where the first and

second grids have a plume modeling region which is roughly defined at the same radius as the outboard terminal shock and contain 14 million and 17 million nodes respectively. The third grid has been generated with a larger plume region to remove the possibility that the boundary between the plume region and the rest of the computational grid might cause the formation of the outboard shock. The third grid contains 17.8×10^6 nodes. The size of the plume region within the grid has been determined using the analytical model to define the plume shape for the 20° nozzle canting configuration operating at $C_T = 10$.

A comparison of the flowfield structures for both $C_T = 1$ and $C_T = 10$ for all three grids is shown in Figure 93. For both thrust conditions, each grid returns essentially the same solution. Any discrepancies are slight and most likely due to the differences in cell alignment between each grid generated with varying boundary conditions and cell resolutions. Particularly for the $C_T = 10$ case, the outboard barrel shock shape is seen for all three grids and the plume extends to the same axial distance across all solutions. This plume structure is a grid converged solution for the 20° nozzle canting configuration.

Figure 94 shows the plume region of the grid for the third grid, with the highest resolution and the largest defined block within Gridgen for the expected plume flow. The analytical model predicts a maximum radial plume extent of 0.119 m and a maximum axial plume extent of -0.112 m. A margin has been applied to these numbers to determine the size of the plume region within the computational grid. The plume is fully encompassed within the region, and the plume barrel shock does not intersect the boundary between the plume region and the remainder of the computational grid as has been noted for the other two grids. The boundary of the plume region does not affect the formation of the outboard terminal shock structure.

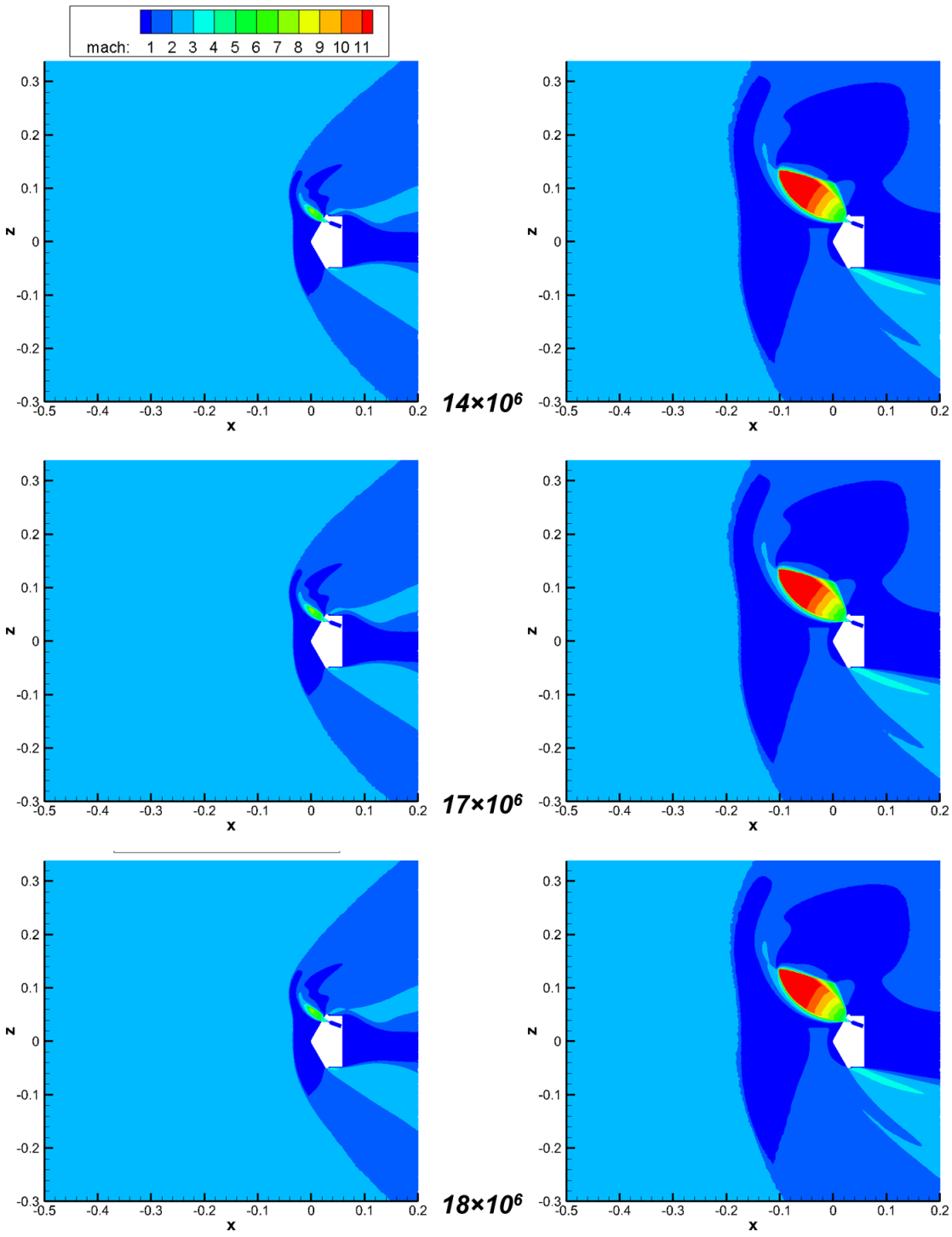

Figure 93: Effect of total number of nodes within computational grid on 20° nozzle canting solutions for C_T = 1 (left) and C_T = 10 (right)

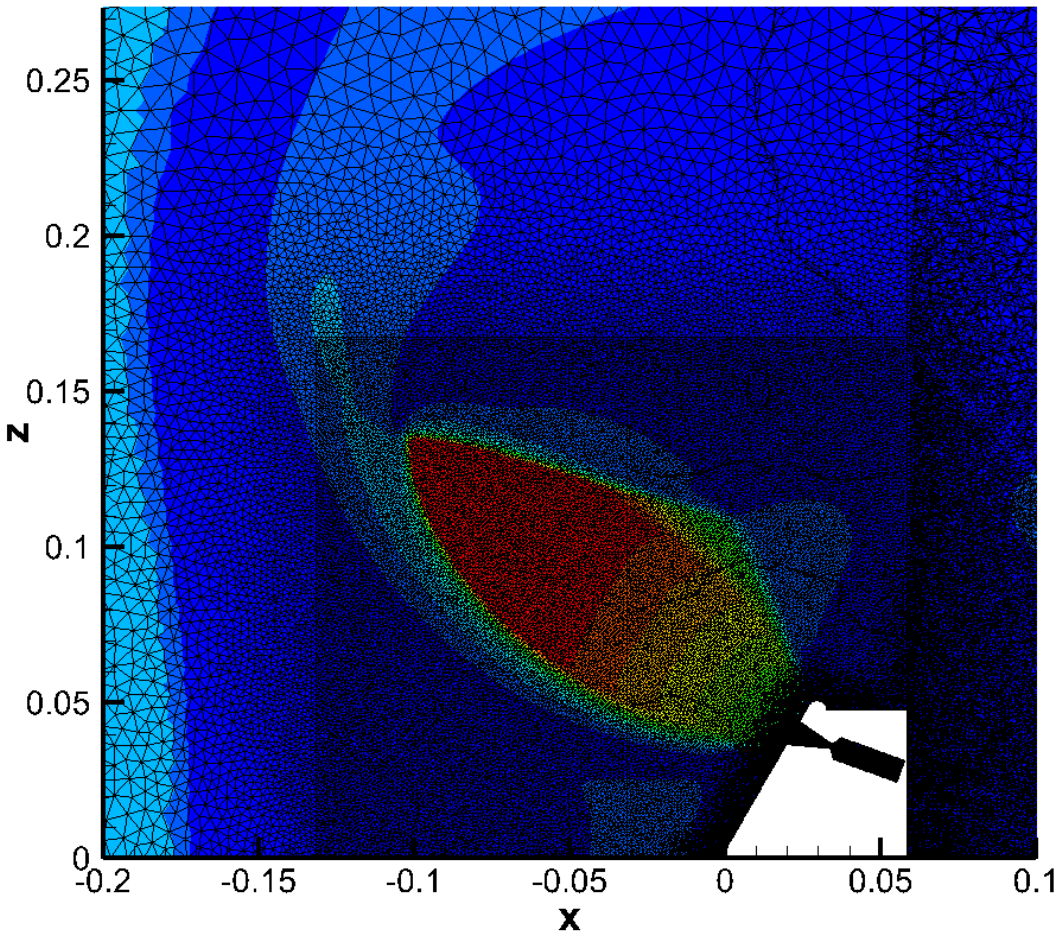

Figure 94: Plume region within computational grid for 20° nozzle canting configuration with C_T = 10 Mach contours shown for reference

A view of the *X*-*Z* plane covering the entire computational domain for the 20° nozzle canting configuration is shown in Figure 95. As with the 10° nozzle canting configuration, the majority of the nodes in the computational mesh are concentrated near the vehicle to capture the plume structure, bow shock structure, and wake flow. The subsonic wake flow closes completely within the computational domain, at a location closer to the vehicle than is seen in Figure 90 for the 10° nozzle canting configuration. This indicates that varying the orientation of the freestream with the nozzle axis and the

plume structure varies the decelerated freestream flow paths sufficiently to alter the wake structure behind the vehicle during SRP.

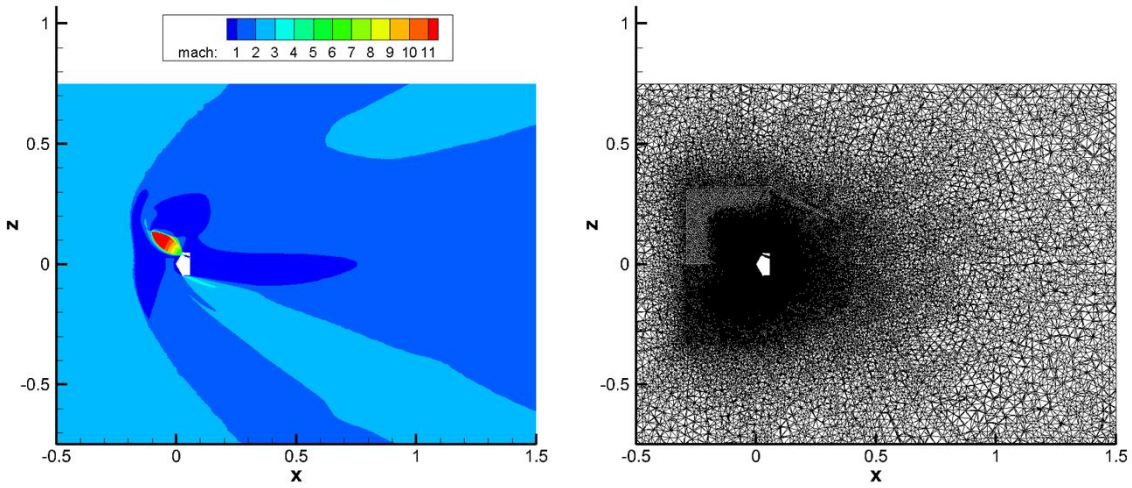

Figure 95: Full computational domain with C_T = 10 Mach contours (left) and computational mesh (right) for the 20° nozzle canting configuration

5.3 Three Nozzle Configuration with 30° Cant Angle

Since the forebody used for all of the canted nozzle configurations is the same 60° sphere-cone used in the Jarvinen and Adams wind tunnel experiment, the 30° nozzle canting configuration creates a flush interaction between the nozzle diverging section and the vehicle surface. There is no scarfing of the nozzle since the nozzle axis is perpendicular to the surface. As with the other cant angle geometries, C_T values of 1, 4, 7, and 10 have been run at zero angle of attack. Additionally, cases at angle of attack have been run for both C_T = 1 and C_T = 10 to establish static pitch stability information for this configuration.

5.3.1 Zero Angle of Attack Effects on Flowfield Structure and Surface Pressure

Increasing the nozzle canting to 30° further changes the flowfield structure as compared to the 0°, 10°, and 20° nozzle canting configurations. The plumes are directed more outboard, which has an effect on both the inboard surface pressure distribution and the outboard flowfield structure, as shown in Figure 96. For C_T = 1, as with the previous geometries, the plume is small and aligned with the nozzle axis. The plume provides little shielding to the forebody, and the bow shock and surface pressure inboard of the nozzles are undisturbed. As the plume expansion is small for this thrust coefficient, the plume does not expand sufficiently to interact with the flow at the shoulder as is seen in the higher thrust solutions.

For C_T = 4, 7, and 10, the flowfield structure changes significantly outboard of the plumes, which is not seen for any other nozzle canting configurations. The outboard barrel shock structure and corresponding shear layer is thicker than is seen in other configurations. This is most likely due to the combination of the crossflow along the vehicle surface and the orientation of the nozzle exit to the surface. The 30° nozzle canting configuration results in nozzles exhausting normal to the surface, which creates the largest angle between the local crossflow and the plume flow. This would create a stronger interaction between these flows than is seen for smaller cant angles. As the plumes are directed more outboard, the surface pressure inboard of the nozzle exits is significantly preserved for all thrust coefficients. The peak surface pressure remains similar and the overall pressure distribution does not drastically decrease.

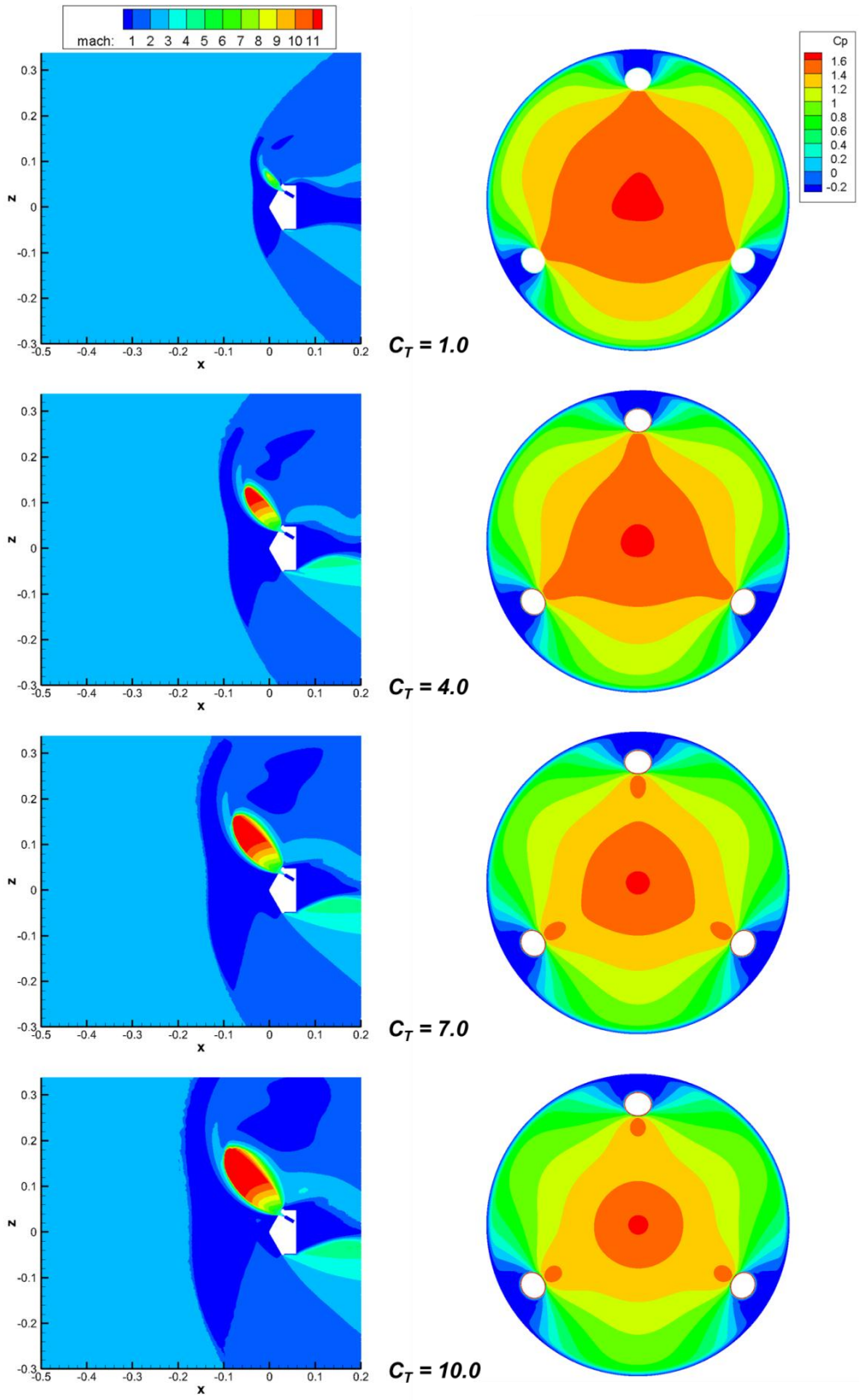

Figure 96: Mach contours and C_P distributions for varying C_T with 30° nozzle canting

The other significant change in the flowfield structure for the 30° nozzle canting configuration is the formation of a high Mach number region in the wake of the flow field. The wake generally resembles that seen for C_T = 1 in Figure 96, where a subsonic core is surrounded by a low speed supersonic flow. For the higher thrust cases where C_T = 4, 7, and 10, the increased radial flow outboard from the plume and the increased size of the outboard free shear layer cause the plume flow to intersect the separated flow region which exists at the shoulder of the vehicle. This is shown in Figure 97 with cross sections of the flow field in planes of constant *X*.

X = 0.000 represents the flow field in the cross section of the flow taken at the nose of the vehicle, and only the plumes are visible. As *X* increases, the vehicle appears in the Mach contours, and the flow along the surface accelerates. At *X* = 0.024, the subsonic flow along the surface is small because the flow is accelerating away from the stagnation point and passing between the plumes. *X* = 0.032 is roughly the location of the shoulder, and the flow along the surface is beginning to separate and accelerate to significant supersonic speeds. As the Mach contours show, the plume flow still exists near the vehicle at this location, and the two supersonic flows begin to merge. Further increasing *X* to 0.036 and 0.040 shows the growth of this interaction, as the flow is greater than Mach 3 around the enter vehicle. The flow is accelerating due to the mass added to the flow field from the plume interacting with the existing shoulder separation flow. Even aft of the vehicle, at *X* = 0.060, this flow region still exists as a high supersonic region. Eventually, this flow passes through a shock in the wake to restore the flow pressure such that it can re-accelerate back to freestream conditions.

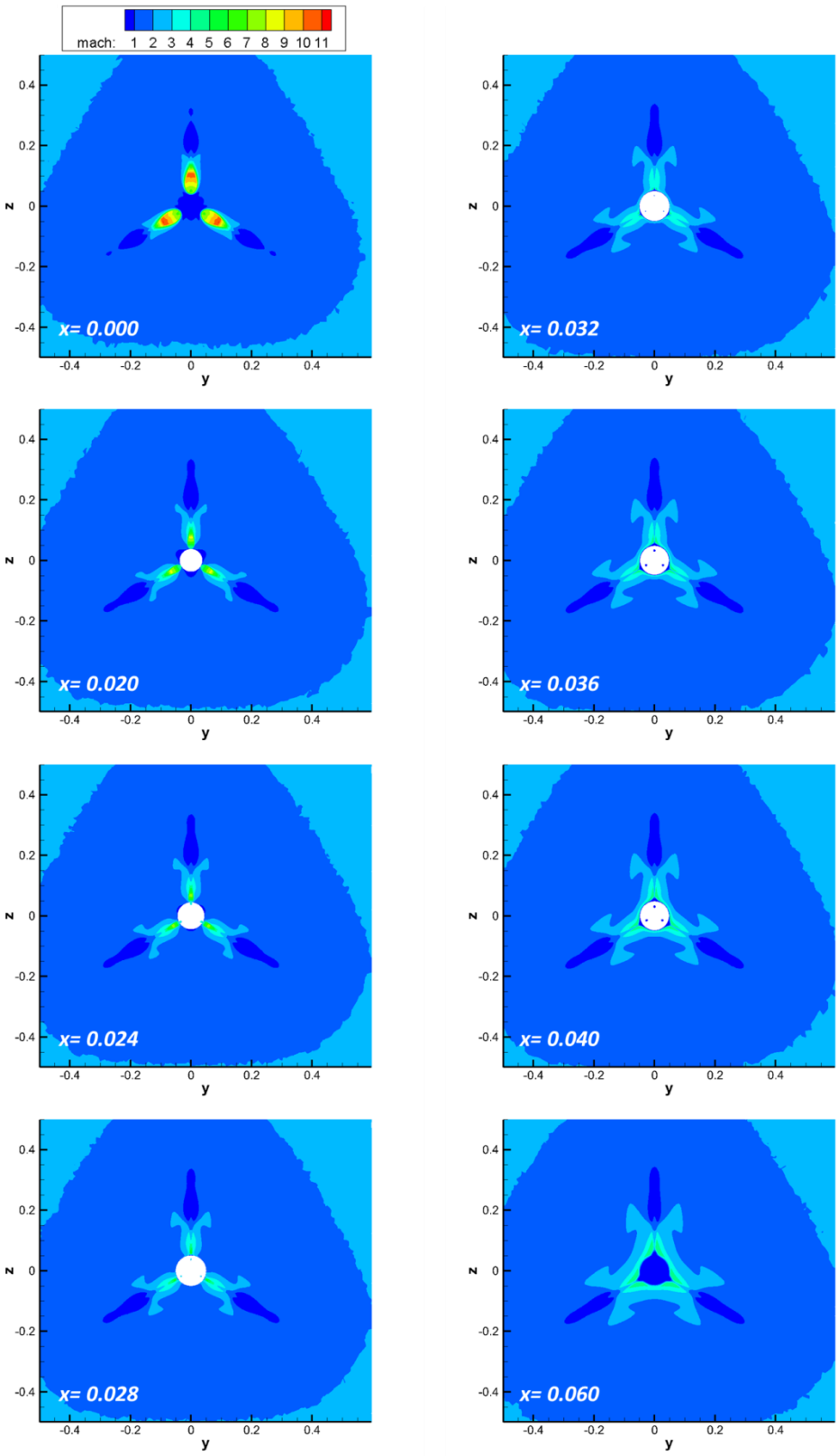

Figure 97: Plume and separated flow interaction for C_T = 10 on the 30° nozzle canting geometry

5.3.2 Low Thrust Angle of Attack Effects

The trend of low thrust conditions providing minimal shielding to the forebody holds true for cases run at an angle of attack too, as shown in Figure 98 for angles of attack of -10°, 0°, and 10° for the 30° nozzle canting geometry. The plume structure is primarily aligned with the nozzle axis, and the expansion of the plume is not sufficient to shield a large portion of the vehicle. Inboard of the plumes a small high pressure region forms, which is consistent with solutions for other nozzle canting configurations. At α = -10°, the stagnation point is expected to shift on the surface due to the variation in approach angle of the freestream flow. This shift in the direction of the upper nozzle causes the two high pressure regions to merge, creating a larger stagnation region on the forebody. For the other two angles of attack, this merging does not occur as the stagnation point is too far removed from the high pressure regions caused by the decelerated freestream passing around the plumes. The out of plane nozzles do not cause this effect for α = 10°, most likely due to the drop in pressure out of the pitch plane. The surface pressure is primarily a function of the incidence angle between the surface and the approaching freestream, which decreases in the out of plane direction more rapidly than within the pitch plane due to the three dimensional geometry.

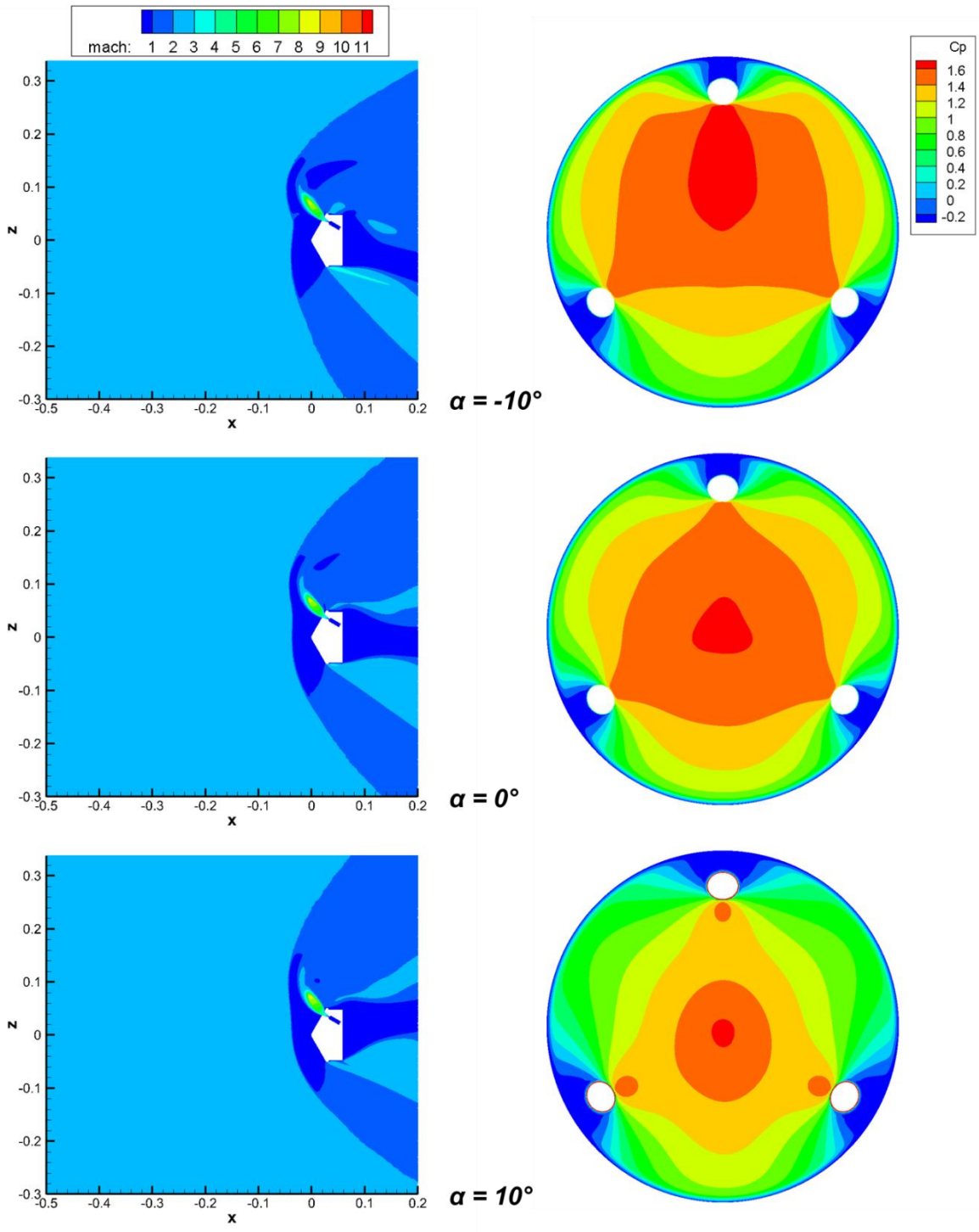

Figure 98: Effect of angle of attack on flowfield structure and surface pressure for $C_T = 1$ on the 30° nozzle canting geometry

Plots of pitching moment as a function of center of mass location and angle of attack for the 30° nozzle canting configuration at C_T = 1 are shown in Figure 99. As with the 10° nozzle canting geometry, the pitching moment at zero angle of attack is expected to be nearly zero since the configuration is symmetric about the vehicle axis. This holds true for the 30° nozzle canting geometry, as the blue line in Figure 99 is nearly zero. The α = -10° curve is consistently higher than the 0° and 10° curves, indicating that this configuration has static pitch stability about the trim zero angle of attack case regardless of center of mass location within the basic sphere-cone geometry. The axial location where the moment is independent of the angle of attack is far aft of the vehicle.

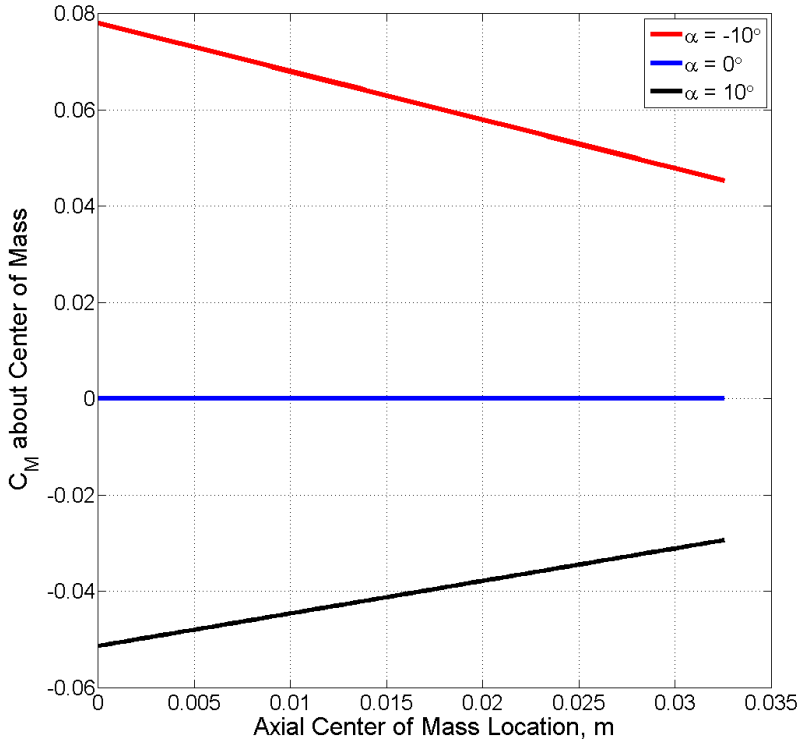

Figure 99: Variation in pitching moment coefficient with center of mass location and angle of attack for C_T = 1 on the 30° nozzle canting geometry

As with the 10° nozzle canting geometry, the variation in CG location at which trim occurs for varying angles of attack has been calculated and plotted in Figure 100. While the CG trim lines are nearly horizontal for C_T = 1 on the 30° nozzle canting geometry, there is a greater spread when compared to the results seen at C_T = 10 on the 10° nozzle canting configuration. The lower thrust provides less control authority for correcting the vehicle trim, and the increase in nozzle cant angle provides reduced thrust for pitching moment control as more thrust is directed in other directions. This result still shows that near-axial CG location is not a significant driver for this particular configuration, as the trim of the vehicle is still not sensitive to the CG location near the vehicle axis at these angles of attack. This configuration also exhibits static stability to the zero angle of attack trim, as shown in Figure 99, so packaging constraints in terms of balancing the CG for the SRP flight regime is not a significant driver for SRP system design.

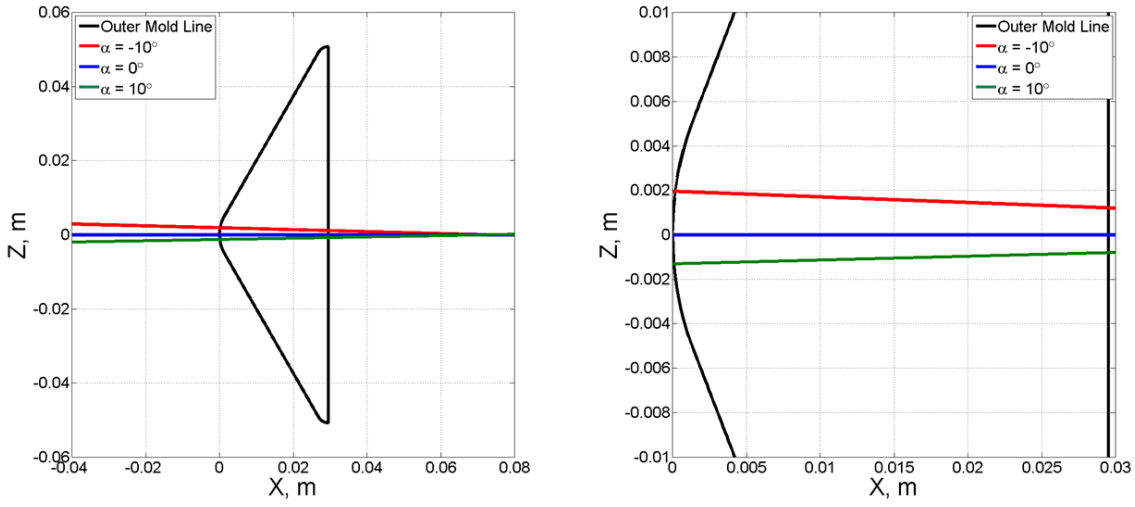

Figure 100: Center of gravity trim lines for varying angles of attack at C_T = 1 on the 30° nozzle canting geometry for the full vehicle view (left) and a zoomed view (right)

5.3.3 High Thrust Angle of Attack Effects

For C_T = 10, the flow field shows a similar structure with angle of attack as is seen for the zero angle of attack case, as shown in Figure 101. The interaction of the plume boundary and the shoulder separation occurs for α = -10°, 0°, and 10° as the plumes for all of these orientations expand sufficiently far aft to reach the shoulder of the vehicle. The orientation of the supersonic wake flow changes with angle of attack, which also alters the size of the subsonic portion of the wake. This wake flow structure does not affect the forebody pressure trends, as the peak surface pressure is preserved for all angles of attack. As with C_T = 1, the -10° angle of attack case shows a merging of the high pressure region directly inboard of the plume with the stagnation region caused by the freestream flow. The larger plume for C_T = 10 does create a lower pressure within this region as compared to the lower thrust condition, as the forebody is more shielded with a wider expansion from the nozzle exhaust.

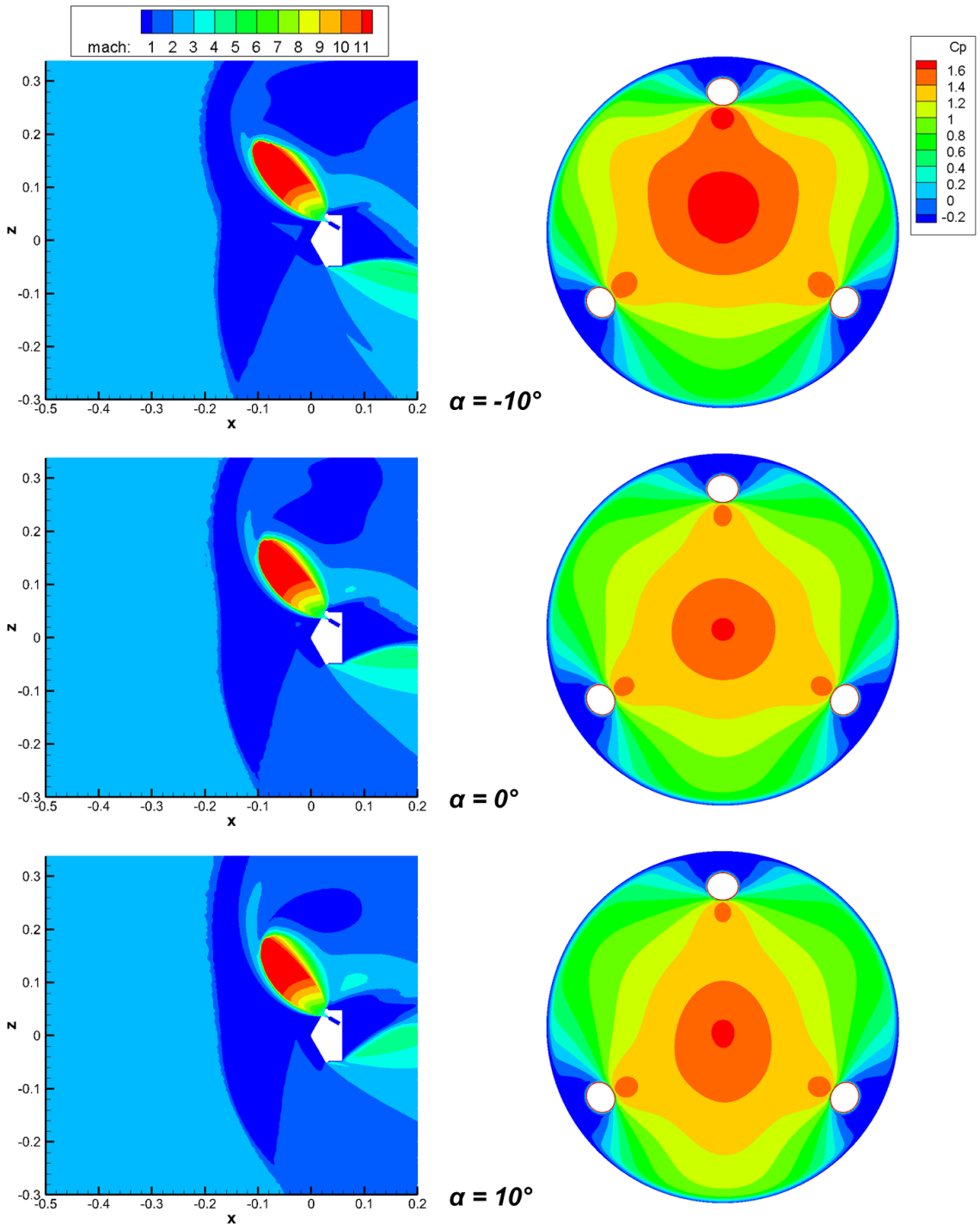

Figure 101: Effect of angle of attack on flowfield structure and surface pressure for C_T = 10 on the 30° nozzle canting geometry

Figure 102 shows the effect of exhausting the upper nozzle directly into the freestream flow, which occurs for this configuration when α = -30°. For both thrust coefficients, the plume is almost exactly axisymmetric because the combination of the nozzle axis aligning with the freestream flow direction and the nozzle exhausting perpendicular to the vehicle surface reduces the local crossflow to nearly zero. Any slight perturbations are most likely due to the fact that the entire line of the conical portion of the vehicle is effectively a stagnation line, which may introduce some small perturbation effects to the plume structure. By creating this situation where the nozzle is effectively performing stagnation point injection, the plume does shield the forebody to a greater extent, reducing the overall surface pressure. For C_T = 1, the highest pressure actually occurs just inboard of the out of plane nozzles, as the stagnation behavior at those points is not shielded by the single axisymmetric plume. This pressure is much lower than the peak surface pressure seen at low angles of attack, and the overall forebody is at a much lower pressure as well. For C_T = 10, the peak surface pressure is near the nose of the vehicle and decreased substantially from the low angle of attack cases, as the larger axisymmetric plume shields most of the forebody. The pressure across the entire surface is also decreased due to this shielding.

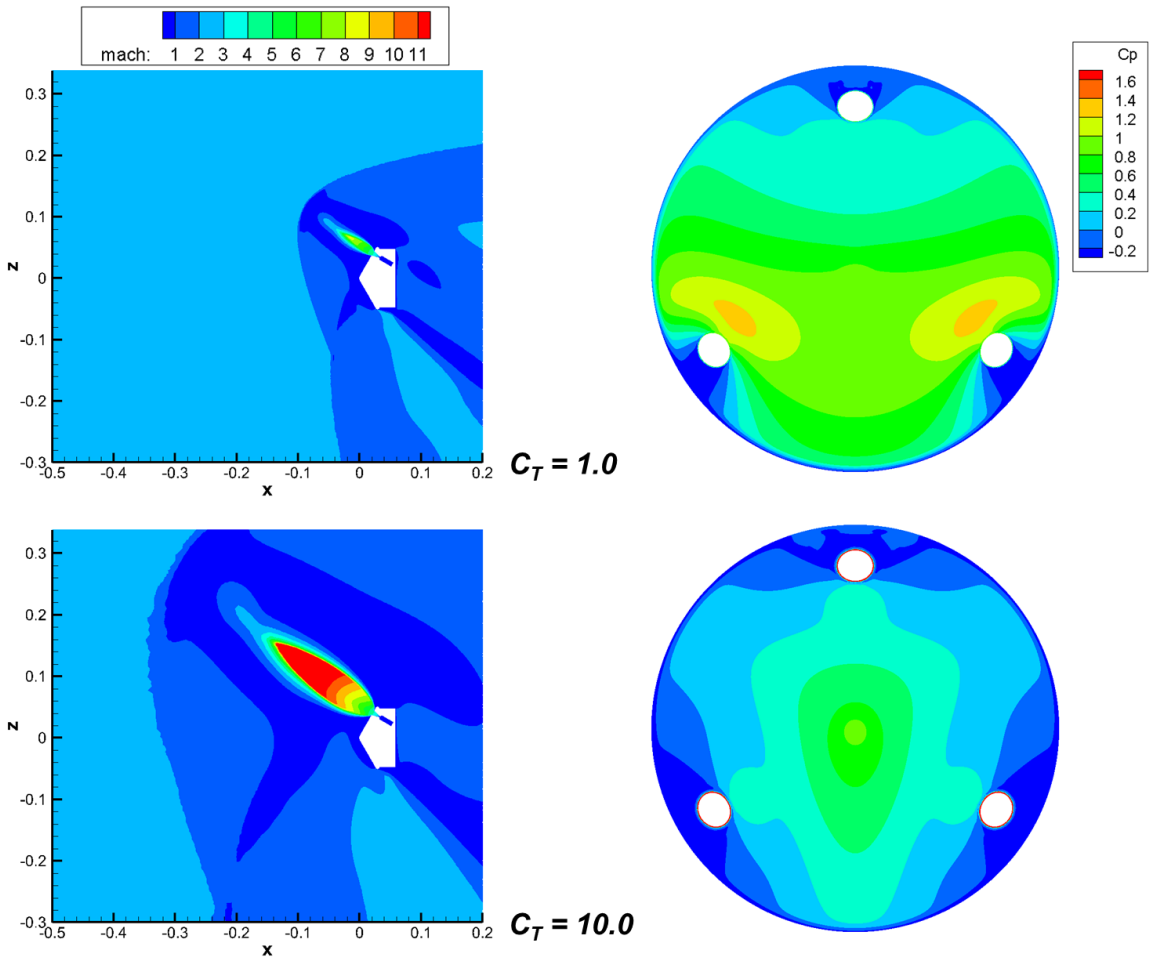

Figure 102: Effect of exhausting plume directly into oncoming freestream at α = -30° for varying C_T on the 30° nozzle canting geometry

Plots of pitching moment as a function of center of mass location and angle of attack for the 30° nozzle canting configuration at C_T = 10 are shown in Figure 103. The trends in static pitch stability are consistent with those seen for the lower thrust C_T = 1 solutions shown in Figure 99. The vehicle has static pitch stability for all center of mass locations along the vehicle axis. Since the pressure is lower at C_T = 10 due to the increased shielding of the forebody, the overall values of the pitching moment are closer to zero for

both angles of attack when compared to the C_T = 1 solutions at the same center of mass location.

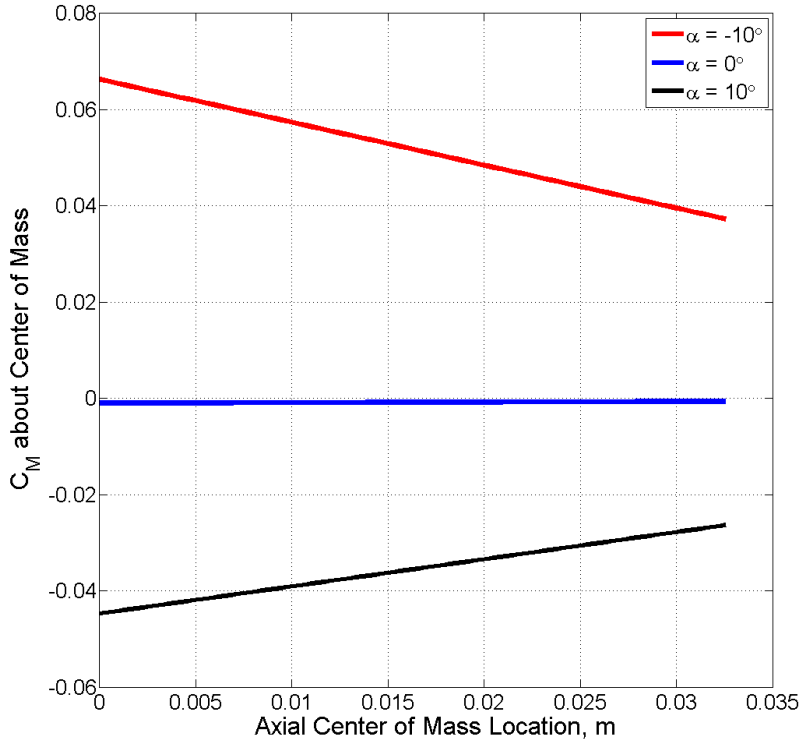

Figure 103: Variation in pitching moment coefficient with center of mass location and angle of attack for C_T = 10 on the 30° nozzle canting geometry

The variation in CG location at which trim occurs for varying angles of attack has been calculated and plotted in Figure 104 for the 30° nozzle canting configuration at C_T = 10. The increase in thrust means that more control from the SRP system is possible, and the vehicle trim is less sensitive to the CG location than is seen for the C_T = 1 condition on the 30° nozzle canting geometry. The effect on nozzle cant angle is evident when compared with the C_T = 10 solution for the 10° nozzle canting geometry, as the slope for the 30° nozzle canting geometry is larger in magnitude for the two angle of attack cases. This is a function of increasing cant angle providing less overall thrust in the directions

that would impact pitch control. Similar to the other results, the combination of low sensitivity to near-axial CG location with static pitch stability means that packaging constraints are not a significant driver of SRP system design for this configuration.

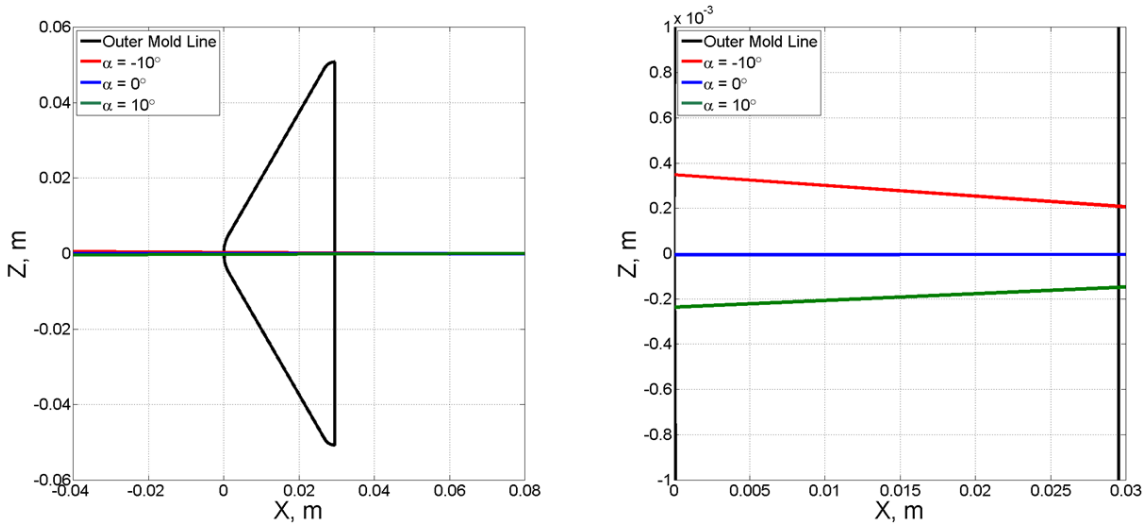

Figure 104: Center of gravity trim lines for varying angles of attack at C_T = 10 on the 30° nozzle canting geometry for the full vehicle view (left) and a zoomed view (right)

5.3.4 Grid Convergence Study

The presence of supersonic flow in the wake merits additional grids to determine if the solution is a result of grid effects. A comparison of solutions for three grids is shown in Figure 105 for C_T = 1 and C_T = 4. The last grid, used for the solutions in Section 5.3.1, contains 17.6×10^6 nodes. For all grids, both thrust conditions result in the same flowfield structure. The C_T = 1 solution does not show the large supersonic flow region in the wake, as the plume is small across all grids. The C_T = 4 solution does show supersonic flow and its subsequent shock in the wake, with similar plume and bow shock structures across all three grids. This phenomenon is not a function of the computational grid, as the formation of this flow feature is consistent and grid converged.

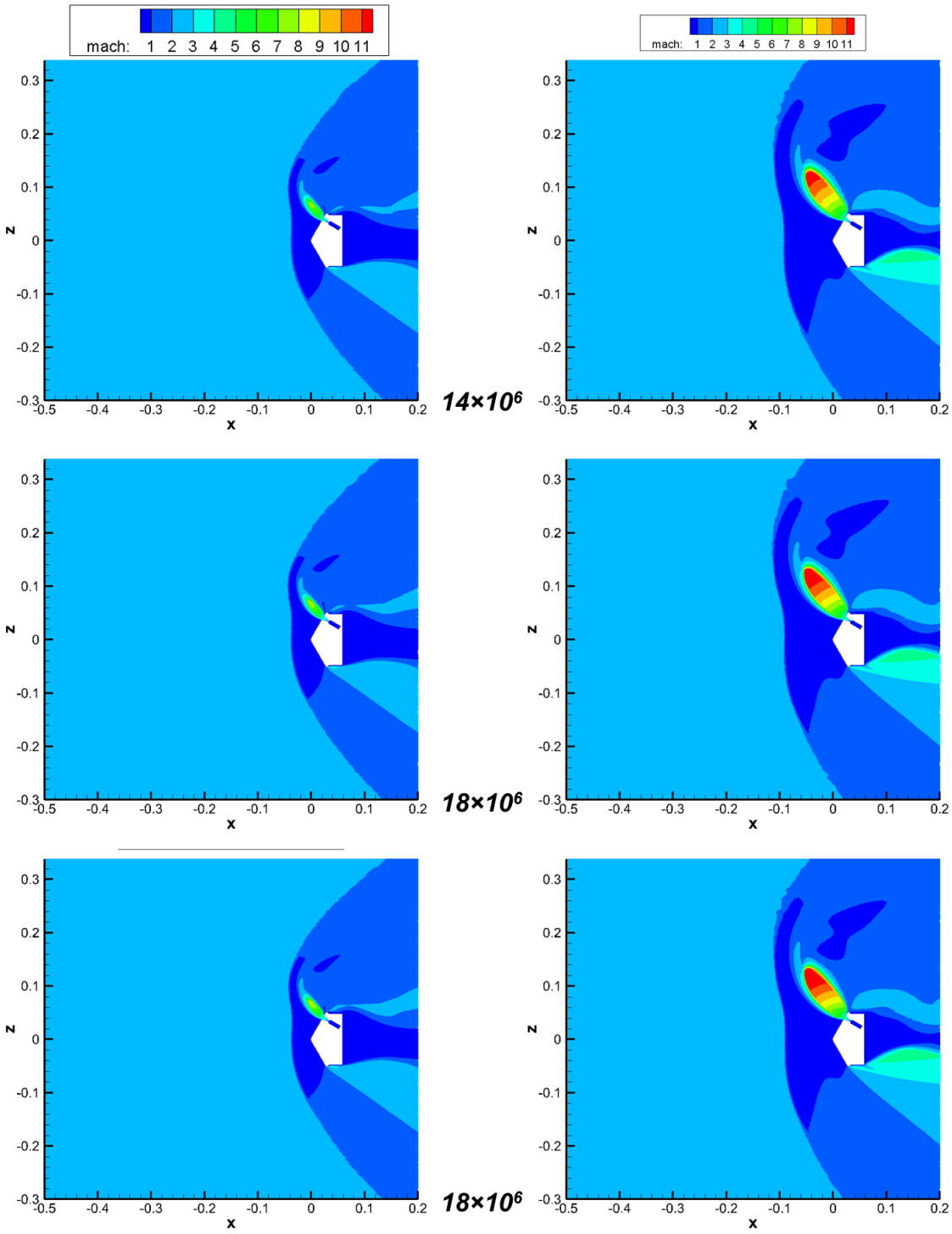

Figure 105: Effect of total number of nodes within computational grid on 30° nozzle canting solutions for C_T = 1 (left) and C_T = 4 (right)

Figure 106 shows the plume region of the final grid as it compares with the calculated plume structure for C_T = 10. The analytical model predicts a maximum plume radial extent of 0.137 m and a maximum plume axial extent of -0.109 m. The axial extent of the plume is well captured by the plume region, but the radial extent the grid does not fully encapsulate the plume structure. By allowing Gridgen to generate cells in each block with a strong scaling function from the block boundaries, sufficient cell resolution is maintained outside the plume region. A growth of the cell size near the termination of the plume may cause the plume to not be sharply defined.

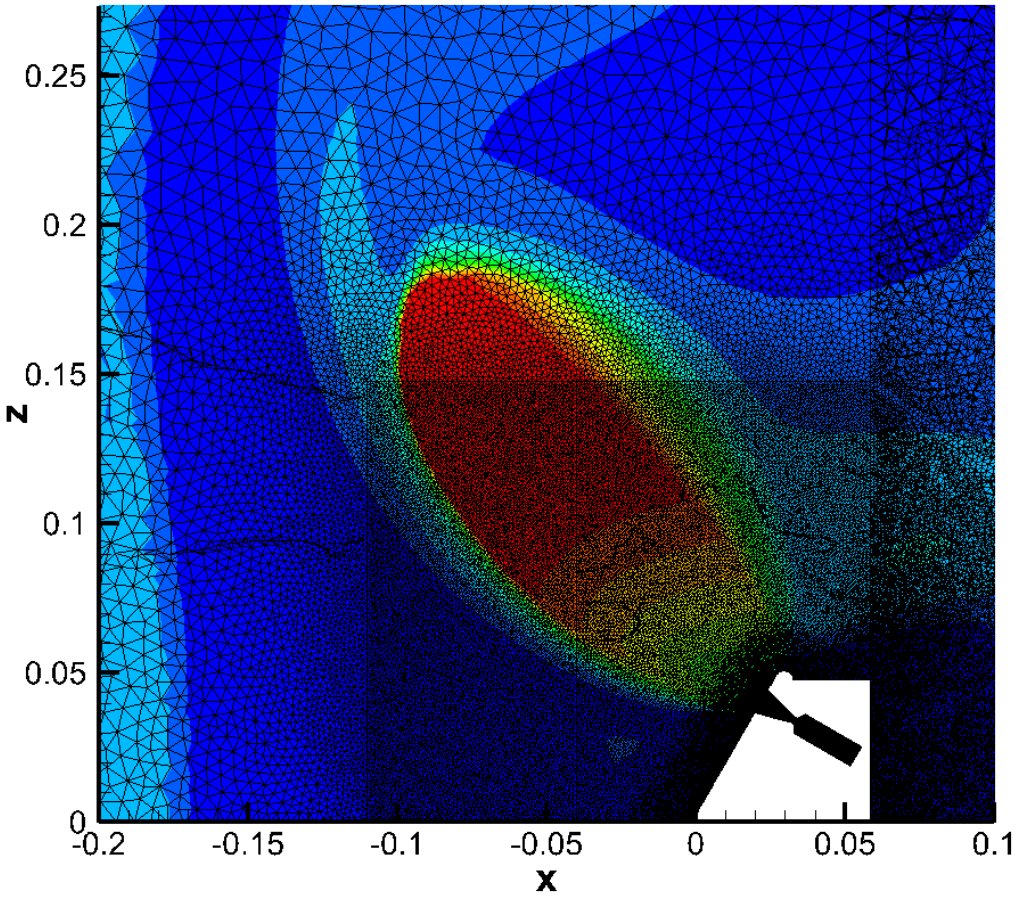

Figure 106: Plume region within computational grid for 30° nozzle canting configuration with C_T = 10 Mach contours shown for reference

As with the 10° and 20° nozzle canting configurations, a view of the entire computational domain for the 30° nozzle canting configuration is shown in Figure 107. The wake structure for this configuration is much different due to the presence of the shock caused by the interaction of the plume expansion with the shoulder separation region of the flow field. The aft extent of the computational domain is larger for this configuration than the other two in case this different wake structure required a longer distance to close the subsonic portion of the wake. As is evident in Figure 107, the subsonic wake region is narrower than is seen in the other two configurations, and the downstream extent of the subsonic wake is similar in distance to the 20° nozzle canting configuration. The mesh for the 30° nozzle canting configuration has a high concentration of nodes near the vehicle to capture the plume, bow shock, and wake structures. This is particularly vital for this configuration due to the complexities associated with the larger plume structures and wake interactions seen across many of the thrust conditions examined.

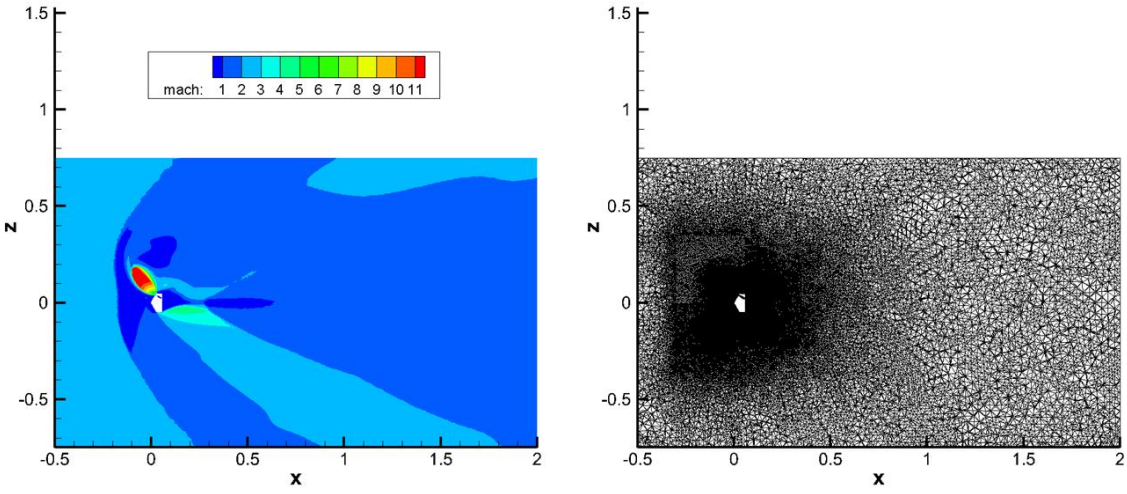

Figure 107: Full computational domain with C_T = 10 Mach contours (left) and computational mesh (right) for the 30° nozzle canting configuration

5.4 Flow Field and Aerodynamic Variation with Cant Angle

Nozzle cant angle is one design consideration that will be taken into account when defining an SRP system for use on an entry vehicle. Understanding the performance variation due to nozzle canting is important for accurately assessing the impact it has on system dynamics. This section provides comparisons of the flow fields and surface pressures for C_T = 1 and C_T = 10 to determine the effects of nozzle canting on the propulsive-aerodynamic interaction. Additionally, the integrated drag and total deceleration forces are plotted to compare the deceleration performance of each forebody nozzle cant angle investigated.

5.4.1 Low Thrust Variation in Flow Field and Surface Pressure

Figure 108 shows the flow field and surface pressure variation with nozzle cant angle for C_T = 1. The plume structure for this low thrust coefficient does not significantly vary relative to the nozzle axis as cant angle changes. As cant angle increases from 0° to 30°, the jet exhaust direction becomes more normal to the surface, and the angle between the local crossflow and the jet exhaust increases since the local crossflow flows tangent to the surface. This causes an increase in the shear of the crossflow on the plume surface as it flows around the plume, causing the outboard plume shear layer to increase in thickness. Since the plume expansion is small, this effect is minor for C_T = 1. The small plume expansion means that the bow shock inboard of the nozzles remains relatively the same across all of the cant angle solutions. The 0° cant angle solution shows a slightly larger bow shock standoff distance at the vehicle axis, but with increasing cant angle this distance converges to a constant standoff. The local bow shock perturbation forward of

the nozzle exit is strongly dependent on nozzle cant angle, as exhausting the plume farther into the freestream flow causes the shock to form farther from the vehicle. The 0° nozzle cant angle solution exhausts the plume farthest into the freestream and has a distinct extension of the bow shock structure. As cant angle increases, the local perturbation to the bow shock varies. The upstream extent of the shock decreases and the radial extent of the shock increases. This causes the shock to appear more like a wide normal shock across the entire region forward of the vehicle. Outboard of the plumes, as the flow gets farther from the obstruction caused by the SRP system; the flow again becomes independent of cant angle.

The surface pressure on the forebody is generally independent of nozzle cant angle for C_T = 1. The peak surface pressure at the nose is the same for all geometries because the decelerated freestream is not shielded by the small plumes. As the nozzle cant angle increases, the plume shielding of the forebody decreases since the jet flow is directed more outboard. This causes the surface pressure on the vehicle to rise across the entire forebody, as seen in Figure 108 by an expansion of the surface C_P contours. The negligible difference in surface pressure distribution for this low thrust condition indicates that the propulsive-aerodynamic interaction is not significantly affected by nozzle cant angle when plume expansion is small.

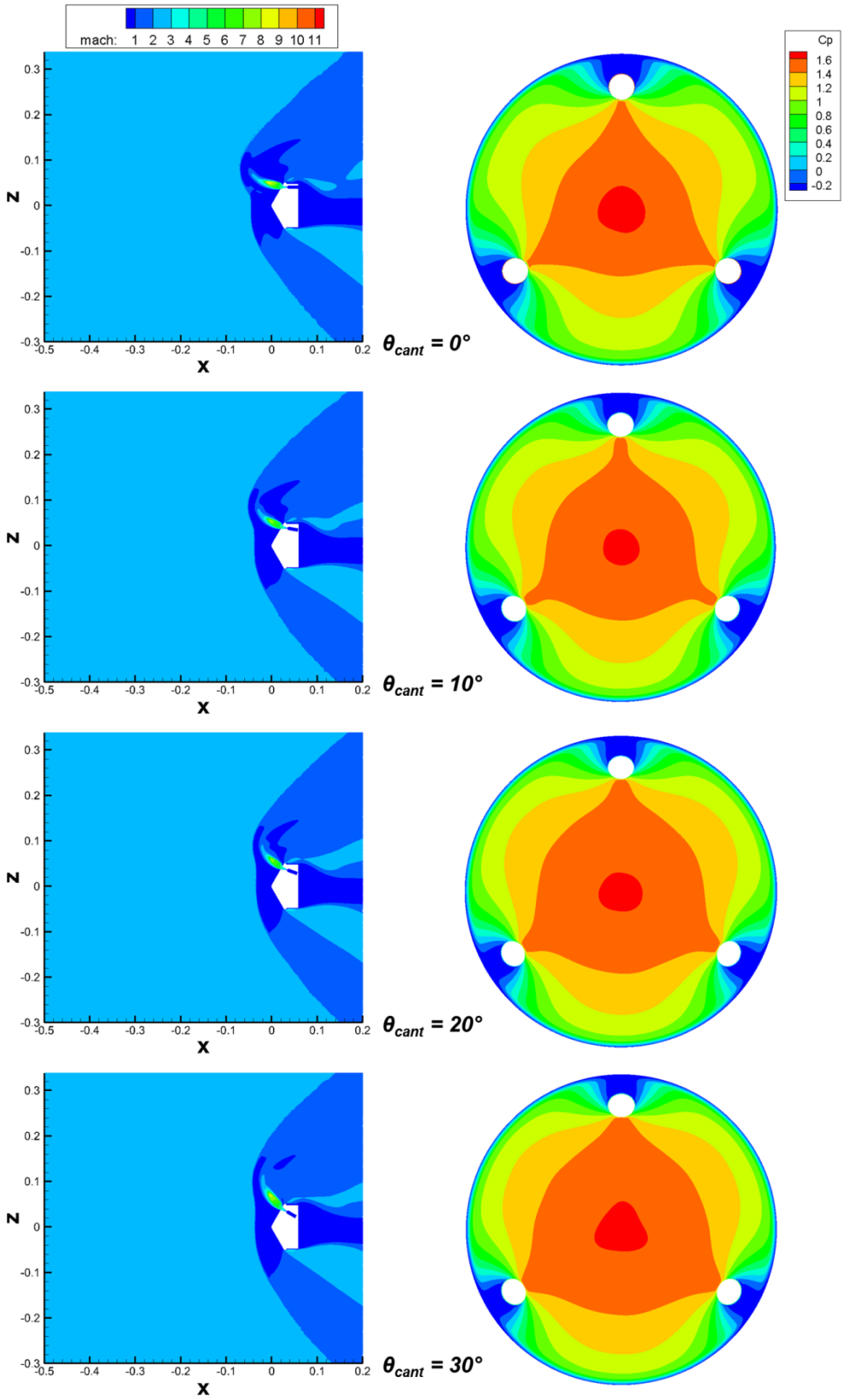

Figure 108: Mach contours and C_P distributions for varying cant angle at $C_T = 1$

5.4.2 High Thrust Variation in Flow Field and Surface Pressure

For the higher thrust of C_T = 10, the flowfield structure and surface pressure show more variation with cant angle as shown in Figure 109. The 0° cant angle solution shows plume coalescence, shielding the entire forebody. Increasing the cant angle to 10° causes the plumes to become independent of each other, and no coalescence occurs. The plume extent upstream into the flow field is similar to that of the 0° nozzle canting solution, but the bow shock standoff distance has been reduced due to the lack of coalescence. Further increasing the cant angle to 20° and 30° causes the bow shock to converge to a nearly constant standoff distance. The local perturbation to the bow shock forward of the nozzles creates a wider and more normal bow shock than is seen for the C_T = 1 solution due to the greater radial extent of the C_T = 10 plumes. As with the low thrust solutions, as the cant angle increases, the jet exhausts more normal to the surface. This creates a stronger crossflow effect, which causes the outboard shear layer thickness to increase and eventually cause an interaction between the plume and shoulder separation flow for the 30° nozzle canting configuration.

The surface pressure distribution for C_T = 10 has a strong dependence on nozzle cant angle. For the 0° canting geometry, the plumes shield the entire forebody and no pressure is present on the vehicle. As cant angle increases, the plumes are directed more outboard and the shielding inboard of the nozzles decreases. This causes a rise in the peak surface pressure and a general increase in pressure across the entire forebody. This will have significant aerodynamic implications, both for the deceleration force on the vehicle and the stability of the system under high thrust conditions. The propulsive-aerodynamic interaction is strongly dependent on both cant angle and thrust level of the SRP system.

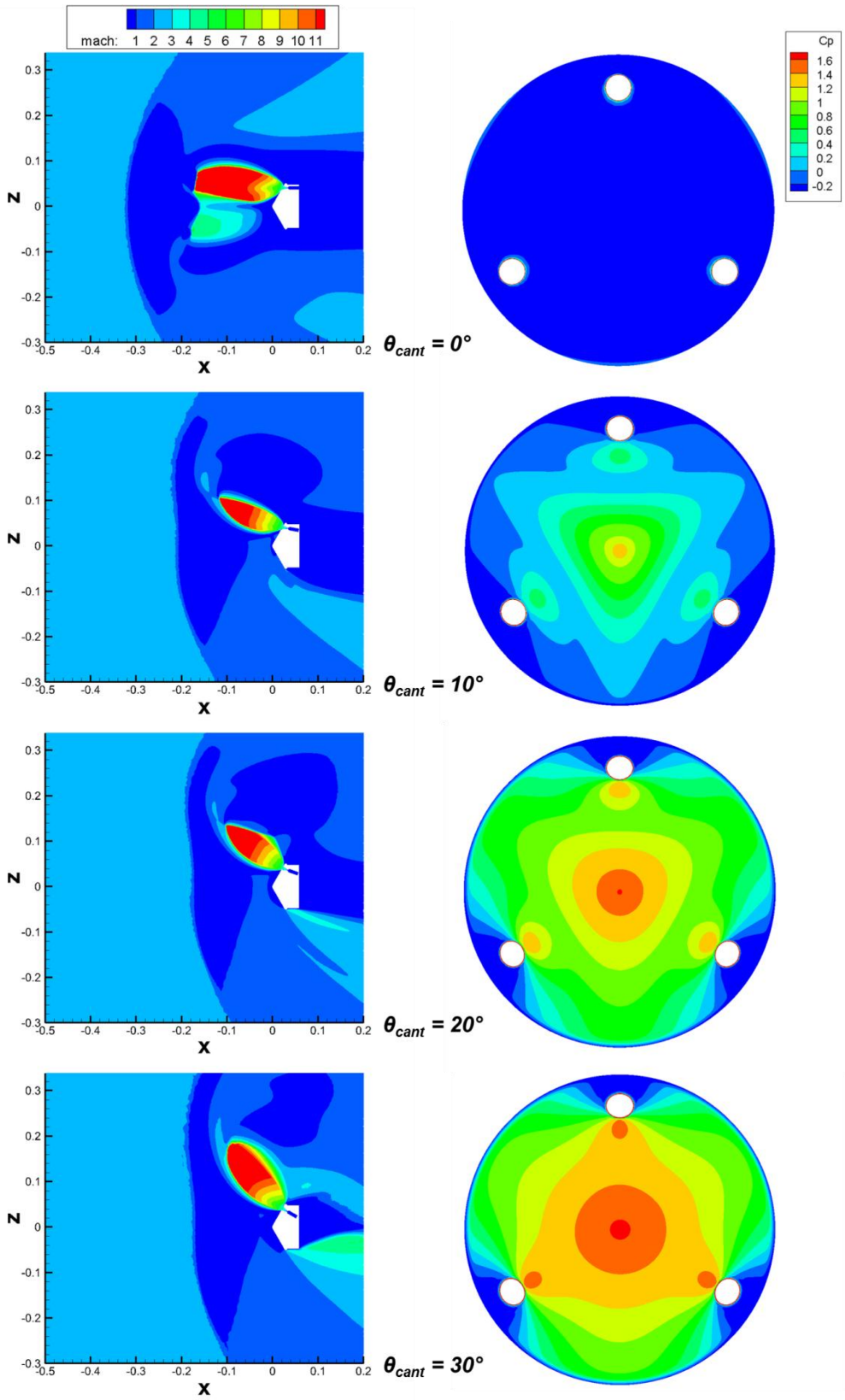

Figure 109: Mach contours and C_P distributions for varying cant angle at $C_T = 10$

5.4.3 Drag Preservation and Net Deceleration Force

The impact of the variation in surface pressure is evident when looking at the drag coefficient of the vehicle as shown in Figure 110 for varying nozzle cant angle and thrust coefficient. In this plot, the zero cant angle thrust coefficient is used for comparison, meaning that the input plenum total pressure is the same for a given C_T value independent of nozzle cant angle. For the zero nozzle canting geometry, the shielding provided by the plumes results in total loss of drag at high thrust coefficients. As cant angle increases, the reduced shielding that increases the surface pressure causes an increase in drag preservation for all thrust coefficients. At low thrust values, such as C_T = 1, this is a minimal effect while at high thrust, such as C_T, the effect of cant angle is more noticeable as the 30° nozzle canting geometry exhibits significant drag preservation.

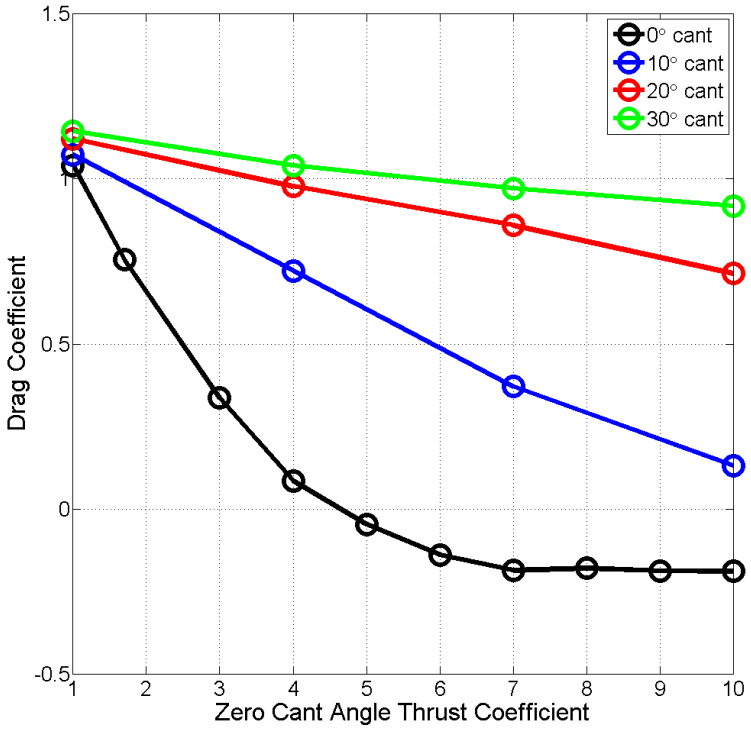

Figure 110: Effects of nozzle cant angle on integrated drag coefficient for forebody canting

Drag coefficient itself does not provide all of the deceleration force. Rather, it is the combination of drag and thrust in the axial direction that decelerates the vehicle. As shown in Figure 111, the inclusion of cosine losses to the thrust due to nozzle canting creates very similar deceleration force performance regardless of cant angle. Both the 10° and 20° nozzle canting geometries leverage the large increase in drag preservation relative to the 0° nozzle canting configuration and relatively low cosine losses to provide the largest total deceleration force across the thrust coefficients examined. Increasing cant angle to 30° does provide more aerodynamic drag, but at the expense of significant cosine losses to the thrust component of deceleration. If this trend were to continue beyond C_T = 10, the 0° nozzle canting should eventually become the most efficient option, as it provides no cosine losses to the thrust deceleration force.

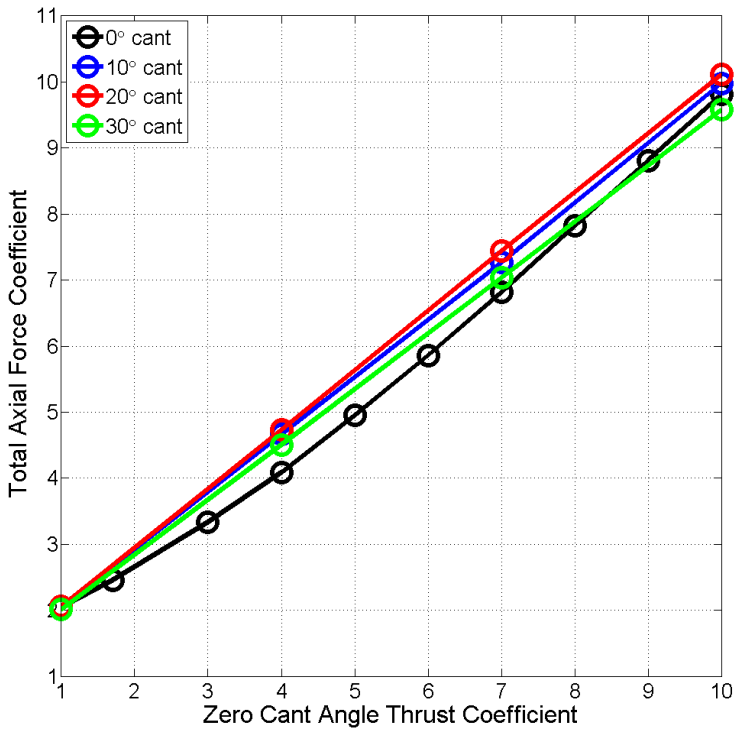

Figure 111: Effects of nozzle cant angle on total axial force coefficient for forebody canting

The data in Figure 111 can be used to determine the difference in required propellant mass as a function of the performance variations due to nozzle canting. Equation (75) shows a deceleration equation of motion, assuming a constant altitude deceleration where flight path angle is zero. Rather than integrate with respect to time, a variable change to integrate with respect to mass is performed to obtain Eq. (76). Rearranging the terms gives Eq. (77), which can be integrated to get a form of the rocket equation as shown in Eq. (78), assuming thrust and drag performance are constant with respect to mass. The mass ratio in Eq. (78) is a function of both the propellant mass and the combined structure and payload mass, as shown in Eq. (79), which can be rearranged to calculate a ratio of propellant mass to the structure and payload mass as shown in Eq. (80).

$$m\frac{dV}{dt} = -T\cos\theta_{cant} - D \tag{75}$$

$$\frac{dV}{dm}\cdot\frac{dm}{dt} = -\left(\frac{1}{m}\right)\cdot\left(T\cos\theta_{cant} + D\right) \tag{76}$$

$$dV = -\left(\frac{T}{\dot{m}}\right)\cdot\left(\frac{T\cos\theta_{cant} + D}{T}\right)\cdot\frac{dm}{m} \tag{77}$$

$$-\frac{C_T}{C_{D,net}}\cdot\left(V_{final} - V_{initial}\right) = g_0 I_{sp}\ln\left(MR\right) \tag{78}$$

$$MR = \frac{m_{pay} + m_s + m_{prop}}{m_{pay} + m_s} \tag{79}$$

$$\frac{m_{prop}}{m_{pay} + m_s} = MR - 1 \tag{80}$$

For given initial and final velocities and engine efficiency, the mass ratio is a function of the ratio of thrust to the net deceleration force. The initial and final velocities are assumed to be 450 and 200 m/s respectively, corresponding to approximately Mach 2 and Mach 0.8 at Mars. The I_{sp} is assumed to be 350 seconds for each engine. For a given thrust level, if the drag is increased then the net deceleration force increases and the mass ratio decreases. This means that less propellant is required to achieve the same change in velocity, as the aerodynamic drag is capable of removing a larger percentage of the vehicle velocity. The CFD data for the 0° nozzle canting configuration is used as the baseline performance level, consistent with the current state of the art in SRP deceleration force modeling. Figure 112 shows the variation in propellant mass required to achieve the same change in velocity for each configuration at varying thrust coefficients, assuming a constant final mass and normalized to the baseline case. A value less than 1 indicates that less propellant is required, as is seen across all C_T values from 1-10 for both the 10° and 20° nozzle canting configurations. The peak propellant mass savings is 14% of the baseline propellant requirement for the 20° nozzle canting configuration near $C_T = 4$. The 30° nozzle canting configuration shows a propellant mass savings for midlevel thrust coefficient values, while $C_T > 8.5$ shows that more propellant is required. This is due to the thrust losses associated with the high cant angle that are not overcome by the drag preserved on the vehicle forebody. For each configuration, if the limiting case at high

thrust is for zero aerodynamic drag, then the curves should eventually asymptote at $1/\cos(\theta_{cant})$, representing the increase in propellant required to overcome the cosine losses to the thrust contribution of deceleration.

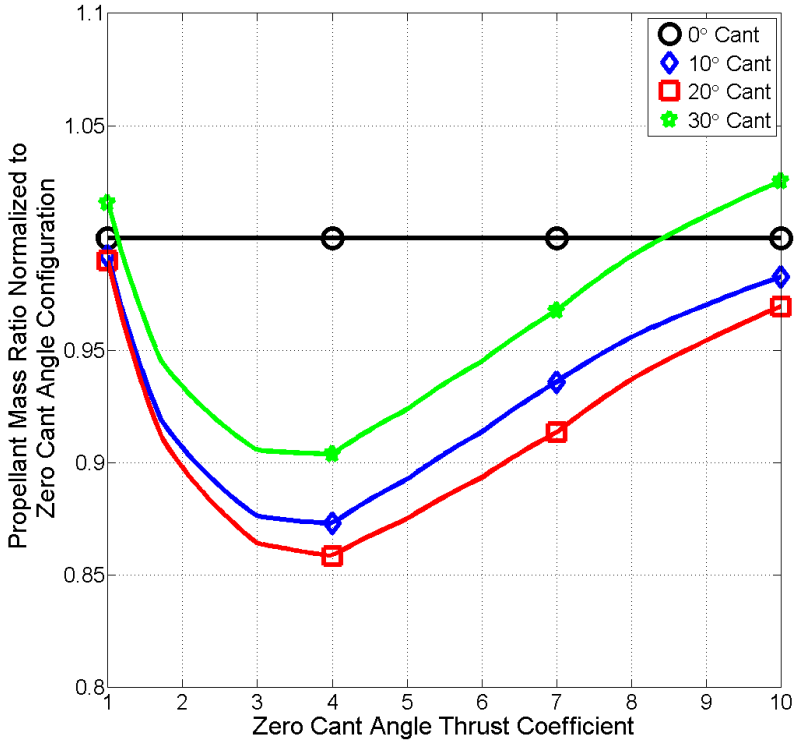

Figure 112: Variation in required propellant mass for forebody nozzle canting configurations relative to the 0° nozzle canting configuration performance at each C_T

5.5 Variation in Specific Heat Ratio

To investigate the dependency of SRP performance on specific heat ratio, three cases are run. Gamma values of 1.2, 1.3, and 1.4 are used to generate the solutions shown in Figure 113. Freestream Mach number, static pressure, and static temperature have been kept constant across all solutions, with values of 2, 1762.3 Pa, and 173.35 K respectively. Total thrust is kept constant, equal to $C_T = 10$ for $\gamma = 1.4$ as shown in Table 12.

As γ decreases, the expansion and size of the plumes greatly increases. γ = 1.4 corresponds to the solution shown in Section 5.1.1 for C_T = 10, where each plume is independent and the forebody surface pressure preservation is significant. Decreasing γ to 1.3 results in a larger plume, particularly along the outboard barrel shock. The inboard compression of the plume is still present due to the stagnation point and local crossflow which form inboard of the nozzle exits. This increase in plume size results in significant shielding of the forebody and the surface pressure drops to nearly zero across the majority of the forebody surface. Further decreasing γ to 1.2 shows a significantly larger plume structure, where the plumes have now coalesced. The outboard plume expansion is much larger than the other solutions, and the shock standoff distance increases dramatically due to the increase in size of the effective obstruction formed by the coalesced plumes. Similar to the single nozzle and three nozzle, 0° nozzle canting configurations, this flow behavior results in total shielding of the forebody and the surface pressure drops to nearly zero across the entire surface. A comparison of the drag performance for each of these configurations is shown in Table 14. The larger plume structures for γ = 1.2 and γ = 1.3 result in significant decreases in drag coefficient.

Table 14: Comparison of deceleration force for varying ratio of specific heats on the 10° nozzle canting configuration

γ	C_T	C_D	$C_{D,net}$
1.4	10	0.13	9.98
1.3	10.8	-0.18	10.46
1.2	11.7	-0.16	11.36

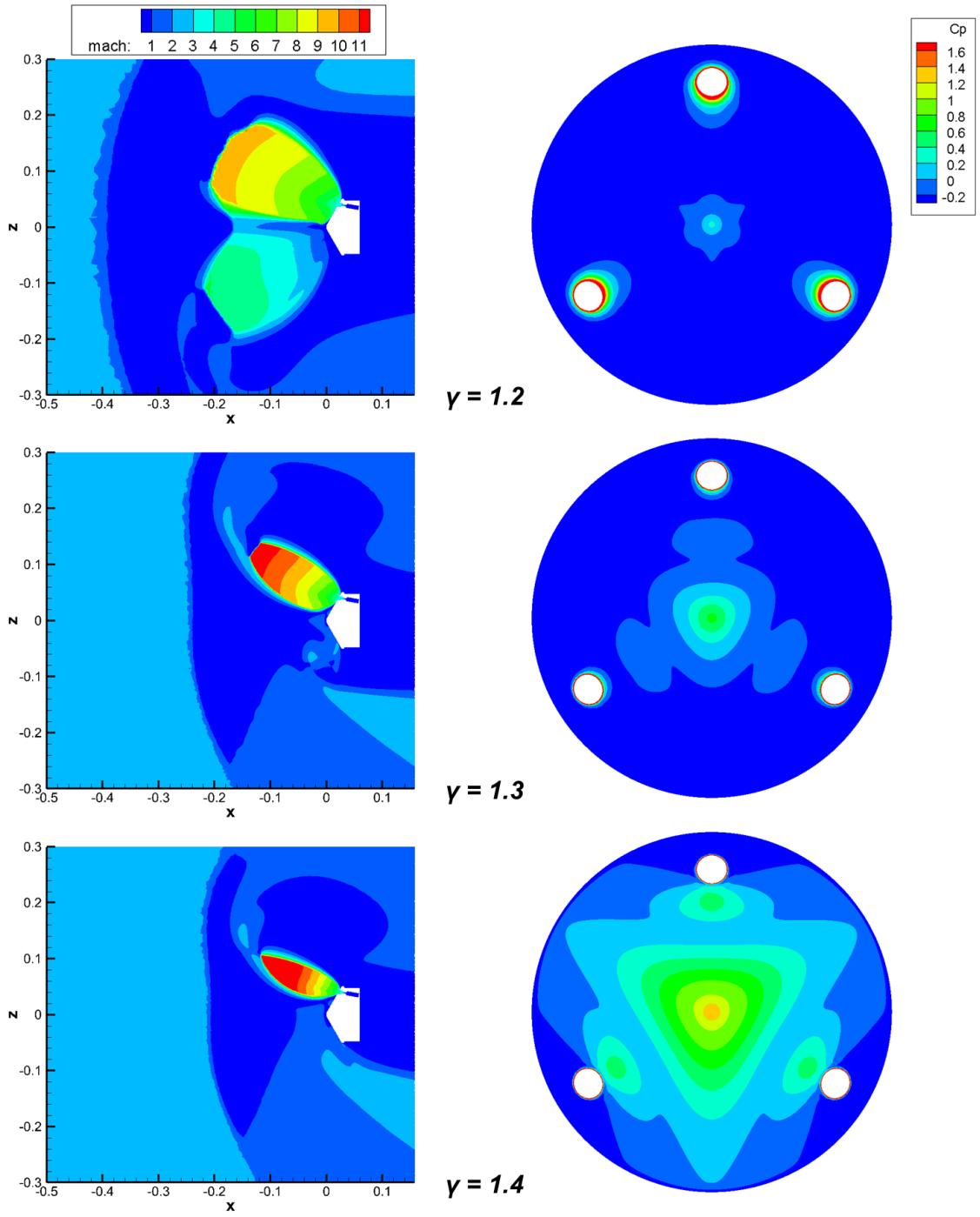

Figure 113: Variation in flowfield structure and surface pressure distribution with γ for the 10° nozzle canting geometry at constant thrust (C_T = 10 for γ = 1.4)

CHAPTER VI

AFTBODY NOZZLE CANTING EFFECTS AND VARIATION IN FREESTREAM FLOW PARAMETERS

Geometries 6-8 in Chapter IV have been created to investigate the effects of nozzles located on the aftbody on SRP performance. These nozzles are necessarily canted, as zero cant angle nozzles integrated directly into the aeroshell structure are infeasible. The forebody geometry for these configurations is assumed to be a 2" base radius Apollo capsule, similar to that used by Daso et al. [29]. A cylindrical aftbody, which will house the nozzles, has been added to the capsule forebody as shown in Figure 114. Both 30° and 60° nozzle canting configurations are examined, where the axis of each cant angle intersects the aeroshell geometry at the same location. The radius of the conical nozzle at this intersection is kept constant, consistent with the forebody nozzle canting configurations examined in Chapter V.

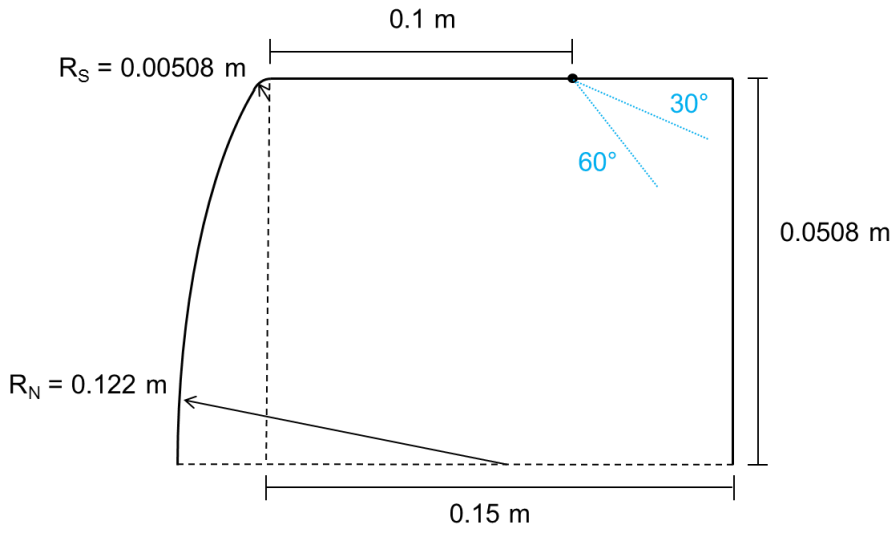

Figure 114: Outer mold line for baseline aftbody geometry with nozzle axes (blue) shown for both the 30° and 60° nozzle canting configurations

The three nozzle, 30° nozzle cant angle geometry provides an extension of the forebody nozzle canting configurations. Both the flowfield structure and surface pressure are obtained for the same thrust coefficients examined in Chapter V to provide direct comparisons of the effect of aftbody nozzle locations. Solutions at angles of attack are also investigated to determine stability characteristics of this configuration. Two six nozzle configurations, one with 30° nozzle canting and one with 60° nozzle canting, are examined to investigate the effects of distributing the thrust over more nozzles. To achieve the same total C_T value with more nozzles, each nozzle has a correspondingly smaller thrust requirement. This results in a smaller plume, which will affect the propulsive-aerodynamic interaction of the SRP system. For the six nozzle, 30° nozzle canting geometry, flowfield structures and surface pressure distributions are found for varying C_T and angle of attack to determine SRP performance and stability characteristics. The same freestream and thrust conditions are run on the six nozzle, 60°

nozzle canting configuration to provide direct comparisons for understanding the effect of aftbody nozzle canting.

6.1 Three Nozzle Configuration with 30° Cant Angle

This configuration extends the trends seen for the three nozzle geometries where the nozzles are located on the forebody. By shifting the nozzles to the aftbody, each plume expansion should be directed more outboard and should not expand such that the forebody is significantly shielded. This will impact the surface pressure distribution and integrated force and moment by providing appreciable aerodynamics even at large thrust values. To be consistent with the forebody geometries investigated in Chapter V, C_T values of 1, 4, 7, and 10 will be investigated at zero angle of attack with the same freestream conditions as given in Section 2.1.2. Additionally, for C_T = 10, solutions at angles of attack of -10° and 10° are investigated to determine stability characteristics of this aftbody configuration.

6.1.1 Zero Angle of Attack Effects on Flowfield Structure and Surface Pressure

Prior to examining the jet on cases, a baseline jet-off solution has been generated as shown in Figure 115. The bow shock structure forward of the vehicle is as expected, and the presence of the nozzles on the aftbody provides minimal interference with the aftbody flow. Including contributions from both the forebody and aftbody results in a drag coefficient of 1.46 for the no thrust condition, where the aftbody includes both the cylinder and its circular back face.

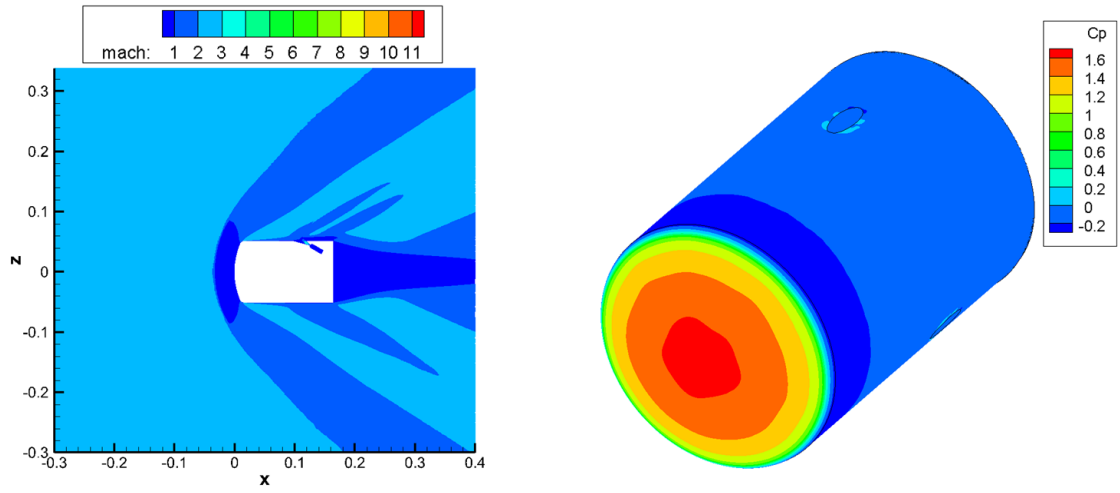

Figure 115: Mach contours and C_P distribution for no thrust condition on the three nozzle, 30° nozzle canting aftbody configuration

Mach contours and surface pressure distributions for varying thrust coefficients are shown in Figure 116. C_T = 1 shows a small plume, which does not extend far enough upstream to disturb the bow shock structure around the forebody. There is a slight deflection of the bow shock far outboard of the vehicle due to the jet flow as it turns to pass behind the vehicle. This undisturbed bow shock creates an unperturbed forebody surface pressure distribution, meaning that the aerodynamic drag force should be completely preserved. The inboard boundary of the plume expands along the vehicle surface, as the angle between the nozzle axis and the aftbody surface is not sufficient to direct the entire plume flow away from the body. This creates a high pressure region on the aftbody just forward of each nozzle, representing an increase in aftbody pressure over the baseline case with no thrust.

Increasing thrust to C_T = 4 shows a larger plume which still does not extend far enough upstream to impact the bow shock structure around the vehicle, preserving the forebody surface pressure distribution. The outboard shock structure is significantly

perturbed, as the larger plume creates a larger effective obstruction to the freestream. The high pressure region forward of each nozzle increases in size, as the plume expands along the surface to a greater extent. Similar trends are seen for an increase in thrust to $C_T = 7$ and $C_T = 10$, as the plume expansion is still not sufficient to reach the vehicle forebody. While the bow shock standoff distance increases slightly for these two cases in response to the larger plumes, the surface pressure on the forebody is fully preserved. The entire front half of the aftbody is covered by a high pressure region due to the plume expansion; however the variation in the C_P distribution with thrust coefficient decreases for these thrust levels. The majority of the plume expansion now occurs off of the vehicle surface as is seen in the Mach contours, and the actual surface region along which the plume expansion flows remains nearly the same for both C_T values. The plume structure for all thrust coefficients results in a plume directed solely outboard of the vehicle, meaning that the forebody will not be shielded as is seen for nozzles located on the forebody of the vehicle. For these thrust conditions, that causes a total preservation of the surface pressure and aerodynamic drag at $\alpha = 0°$.

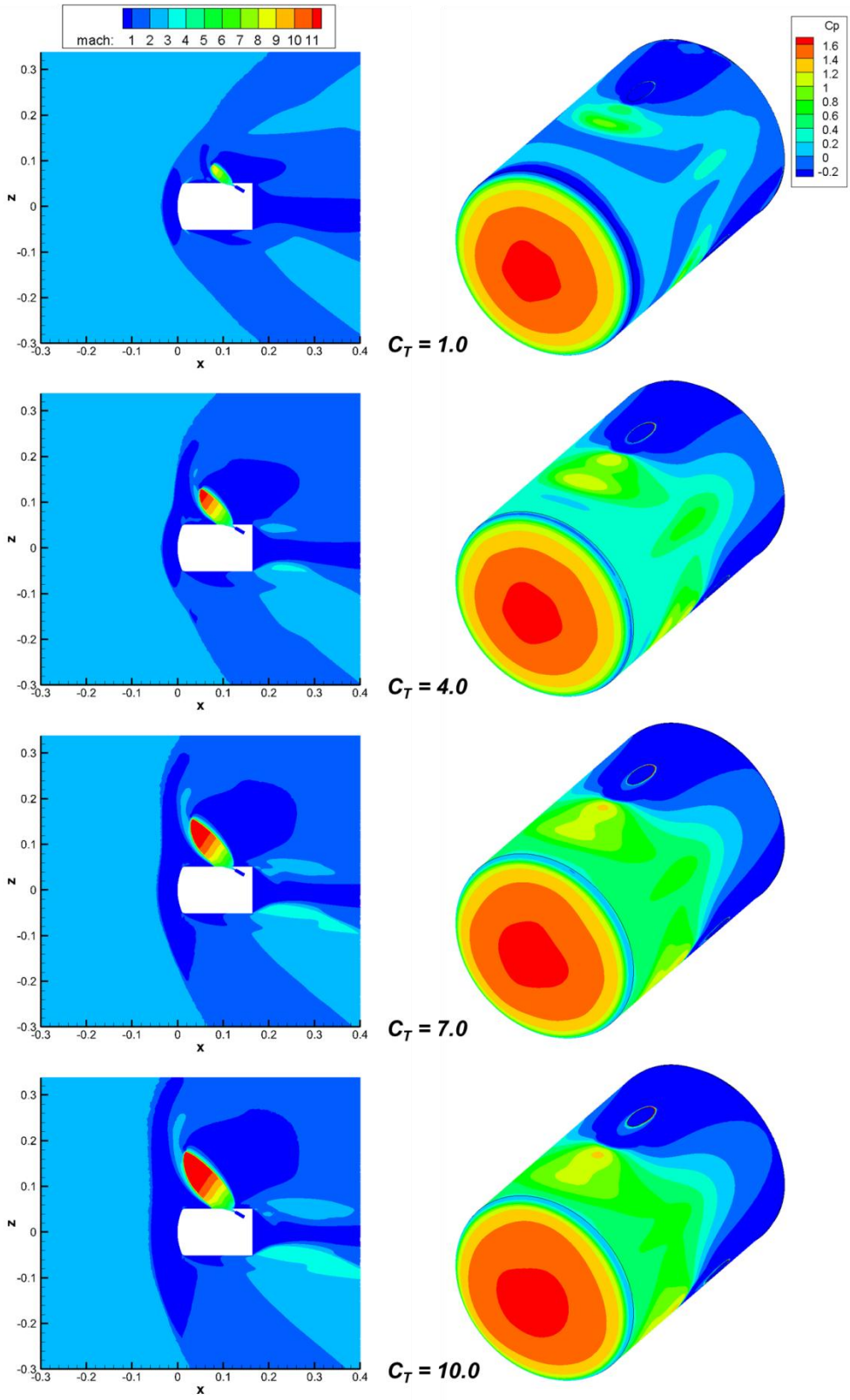

Figure 116: Mach contours and C_P distributions for varying C_T on the three nozzle, 30° nozzle canting, aftbody configuration

6.1.2 Angle of Attack Effects

Solutions for C_T = 10 for angles of attack of -10°, 0°, and 10° are shown in Figure 117. The stagnation point on the forebody shifts with angle of attack in the same manner as is seen for vehicles with no SRP system since the plumes do not reach the forebody and affect the pressure along that surface. A negative angle of attack causes the stagnation point to shift in the positive Z direction, and a positive angle of attack results in the opposite shift. The plume shape is affected by angle of attack as can be seen in the Mach contours. For α = -10°, the nozzle axis is more aligned with the freestream flow, and the resulting plume shape is narrow and nearly aligned with the nozzle axis. As angle of attack increases, the plume becomes more shielded by the vehicle since the orientation of the plume with respect to the freestream flow direction changes and the plume expansion becomes wider.

The high pressure region on the aftbody forward of the nozzles is seen for all three angles of attack investigated. The highest pressure forward of the nozzle is relatively constant across each solution, but the shape of the high pressure region between the nozzles is affected by the orientation of the freestream flow to the vehicle. For α = -10°, a pressure coefficient greater than zero extends to the aftmost nozzle intersection location, while α = 10° shows a forward shift in the transition to zero C_P. This is due to the shift in the stagnation point and the presence of the plumes causing a variation in the flow paths along the surface.

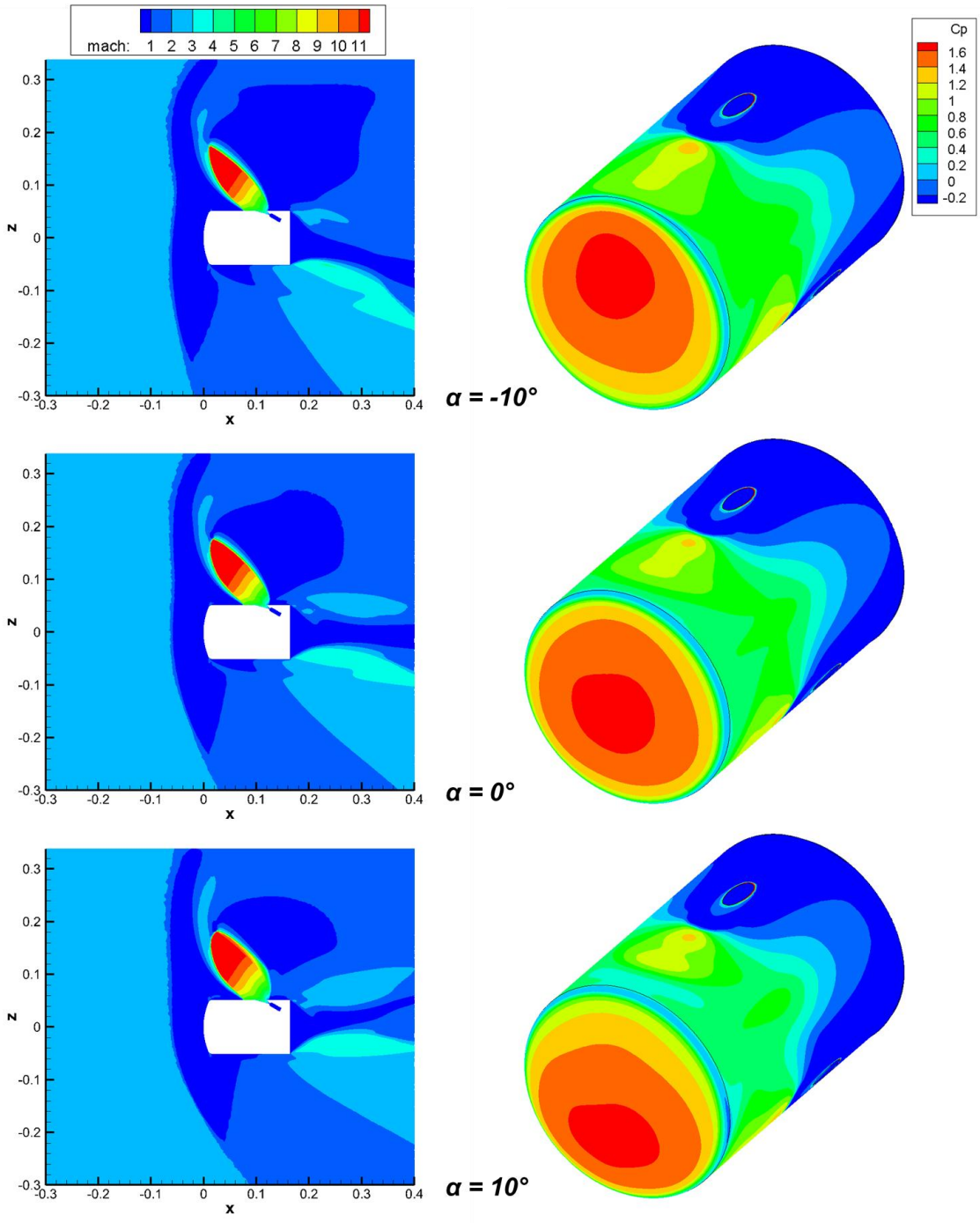

Figure 117: Effect of angle of attack on flowfield structure and surface pressure for C_T = 10 on the three nozzle, 30° nozzle canting, aftbody configuration

As with the forebody nozzle location configurations, a case with α = -30° and C_T = 10 has been investigated to determine the effects of aligning one plume flow directly into the

oncoming freestream, as shown in Figure 118. Since the plume expands along the surface for this configuration, the plume structure is not purely axisymmetric. However, as the plume expansion extends away from the nozzle exit and vehicle, the plume is more axisymmetric than is seen for the other angle of attack solutions, as the freestream flow now has a free stagnation point forward of the plume. This causes an overall reduction in surface pressure, as the decelerated plume flow turning around the vehicle creates a shielding effect on the surface. This is similar behavior to both the forebody nozzle locations and the single nozzle configuration, though the surface pressure is non-negligible for this particular thrust coefficient.

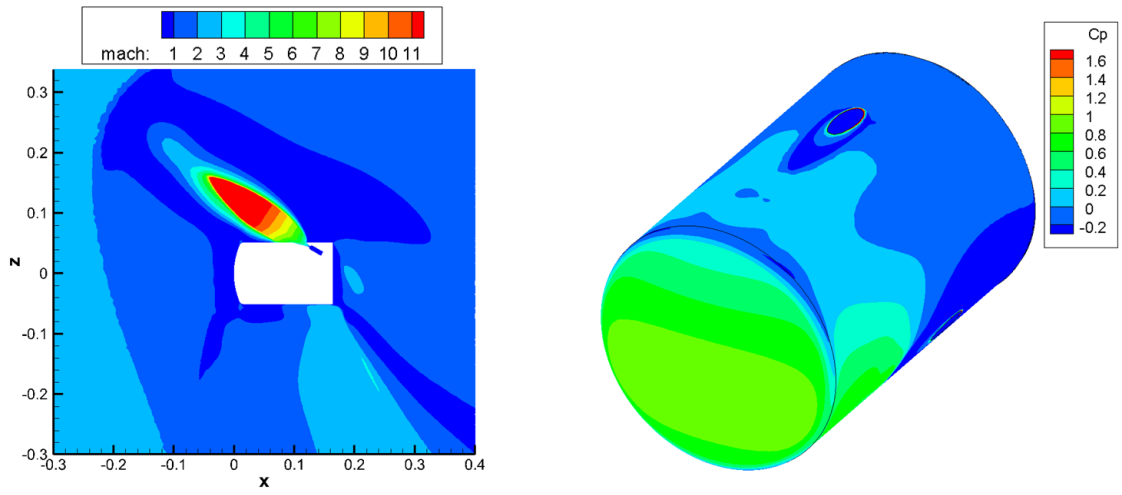

Figure 118: Mach contours and C_P distribution for C_T = 10, α = -30° for the three nozzle, 30° nozzle canting, aftbody configuration

Figure 119 shows the variation in pitching moment coefficient with center of mass location for the three nozzle aftbody configuration with 30° nozzle canting at C_T = 10. The stability performance of this configuration is much different than is seen for the forebody nozzle locations. When the vehicle length is increased, the pressure on the

aftbody provides a sufficient moment to create regions of instability. For CG locations forward of 43% of the vehicle length, the vehicle exhibits static pitch stability because the pitching moment decreases with an increase in angle of attack. For CG locations aft of this point, the trend switches and an increase in angle of attack increases the pitching moment, representing a statically unstable pitch motion. The intersection of each nozzle centerline with the aftbody for this configuration is located at an axial distance of 0.114 m, well aft of the transition from stable to unstable static pitch stability.

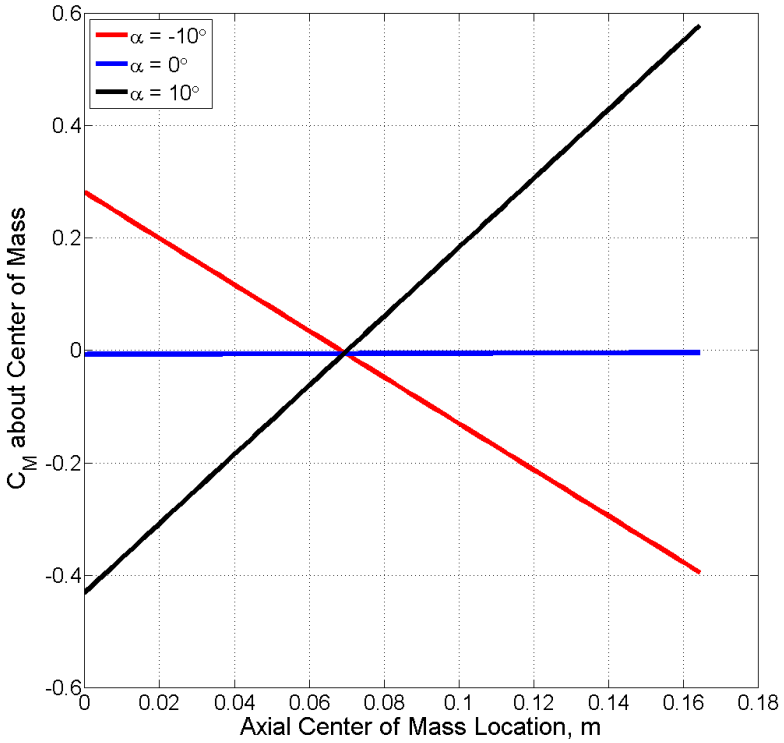

Figure 119: Variation in pitching moment coefficient with center of mass location and angle of attack for C_T = 10 on the three nozzle, 30° nozzle canting, aftbody configuration

Figure 120 shows the variation in CG trim line with angle of attack at C_T = 10. As with the forebody located nozzle configurations, this trim line is generated by solving for the

line of CG locations at which the moments from both aerodynamic and thrust contributions equal zero. While this configuration shows a transition from static pitch stability to static pitch instability, the trim location of the CG is nearly horizontal. This is different than the solutions with no thrust discussed in Section 1.4.3 for a slender vehicle, where the CG trim line was more vertical. Thus, the ability of the vehicle to reach trim conditions is not strongly dependent on the location of the CG in the axial direction. Comparing the slopes of the CG trim lines with those of the forebody nozzle configurations in Chapter V shows that the ability to trim for the aftbody configuration is more dependent on CG location, as the lines have a larger slope magnitude at angle of attack than are seen for the forebody nozzle configurations.

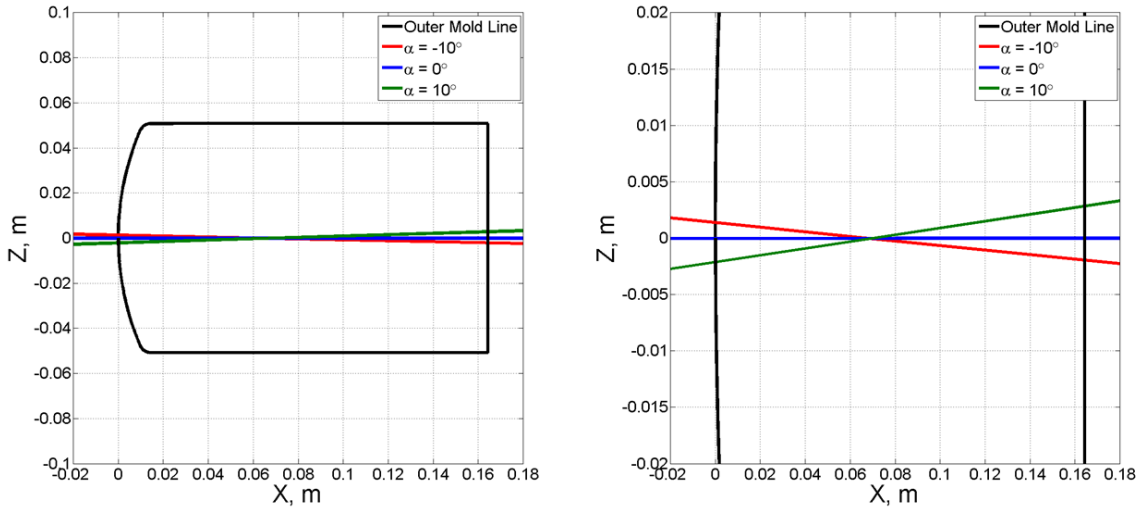

Figure 120: CG trim lines for varying angles of attack at C_T = 10 on the three nozzle, 30° nozzle canting, aftbody configuration for the full vehicle view (left) and a zoomed view (right)

6.1.3 Deceleration Force

The drag coefficient for the baseline, no thrust condition equals 1.46, as noted in Section 6.1.1. Figure 121 shows the variation in drag coefficient with thrust for the three nozzle, 30° nozzle canting, aftbody configuration. Contributions from both the forebody and aftbody are shown, as well as the total C_D for each C_T. Every thrust condition shows a total drag coefficient greater than the baseline case, indicating that the presence of aftbody located nozzles augments the aerodynamic component of the deceleration force in addition to the thrust contribution to deceleration. For low thrust conditions, such as the variation from $C_T = 1$ to $C_T = 4$, the increase in drag is primarily a result of a variation in the aftbody flow caused by the plumes. This is seen in Figure 121 as an increase in the aftbody contribution to the drag coefficient. The forebody component of drag remains nearly constant, as the plumes for these thrust values are not large enough to impact the bow shock structure forward of the vehicle. As thrust increases to $C_T = 7$ and $C_T = 10$, the aftbody contribution to drag is nearly constant with thrust coefficient. While the plumes grow larger in size, the effect on the aftbody surface pressure along the back face of the vehicle is minimal. However, the plumes for these conditions are large enough to interact with the bow shock structure, as shown previously in Figure 116, which creates an increase in the forebody contribution to drag. $C_T = 10$ shows a net drag coefficient of 1.70, a 16% increase over the baseline, no thrust condition. Taking into account the 30° cant angle for the nozzles gives a total deceleration force coefficient of 10.36 for $C_T = 10$, a 4% increase over an assumed performance of thrust directed entirely into the flow with no drag contribution.

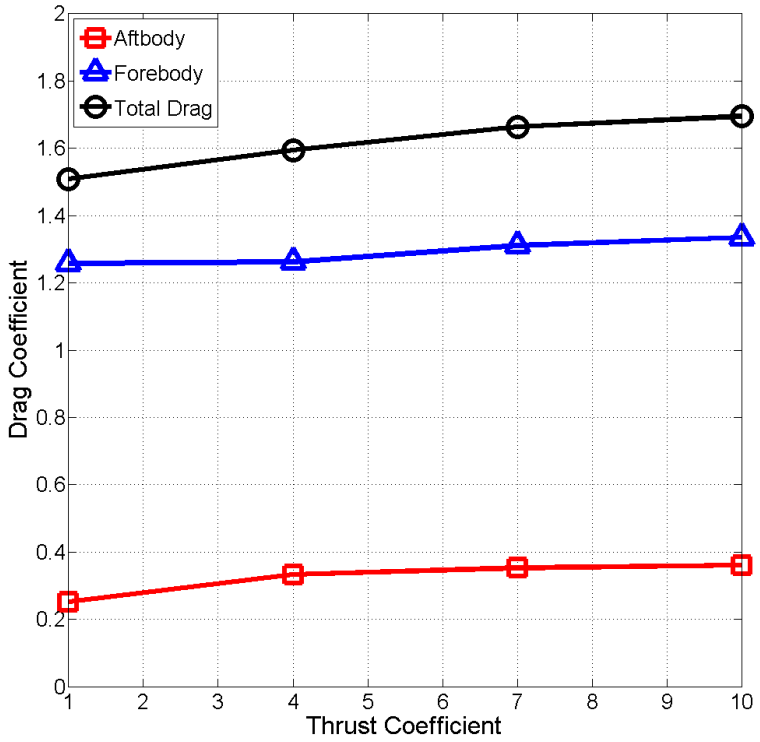

Figure 121: C_D variation with C_T for the three nozzle, 30° nozzle canting, aftbody configuration including aftbody and forebody contributions

6.1.4 Grid Generation

Figure 122 shows the plume region within the computational grid used to generate the solutions for the three nozzle, 30° nozzle cant angle, aftbody configuration. C_T = 10 Mach contours are shown for comparison. As with the forebody configurations, the size of the plume region specified in Gridgen has been based on the analytical model for this thrust condition, which predicts a maximum radial extent of 0.161 m and a maximum axial location of -0.009 m. The axial extent predicted is sufficient to capture the plume structure, as the computational plume region extends further upstream than the plume actually reaches in the CFD solution. The radial extent of the plume region is slightly smaller than the actual plume in the CFD solution; however, the cell size scaling in

Gridgen results in sufficiently small cells in the region just outside the defined plume block boundary. An increase in the margin applied to the analytical model or an increase in the boundary strength for generating the outer grid region would result in smaller cells to capture the entire plume structure. This slight underprediction of plume expansion and smaller grid region does not impact the plume structure substantially, as the plume shape for this thrust condition is consistent with other C_T values on this configuration. Overall, this grid contains 16.6 million nodes.

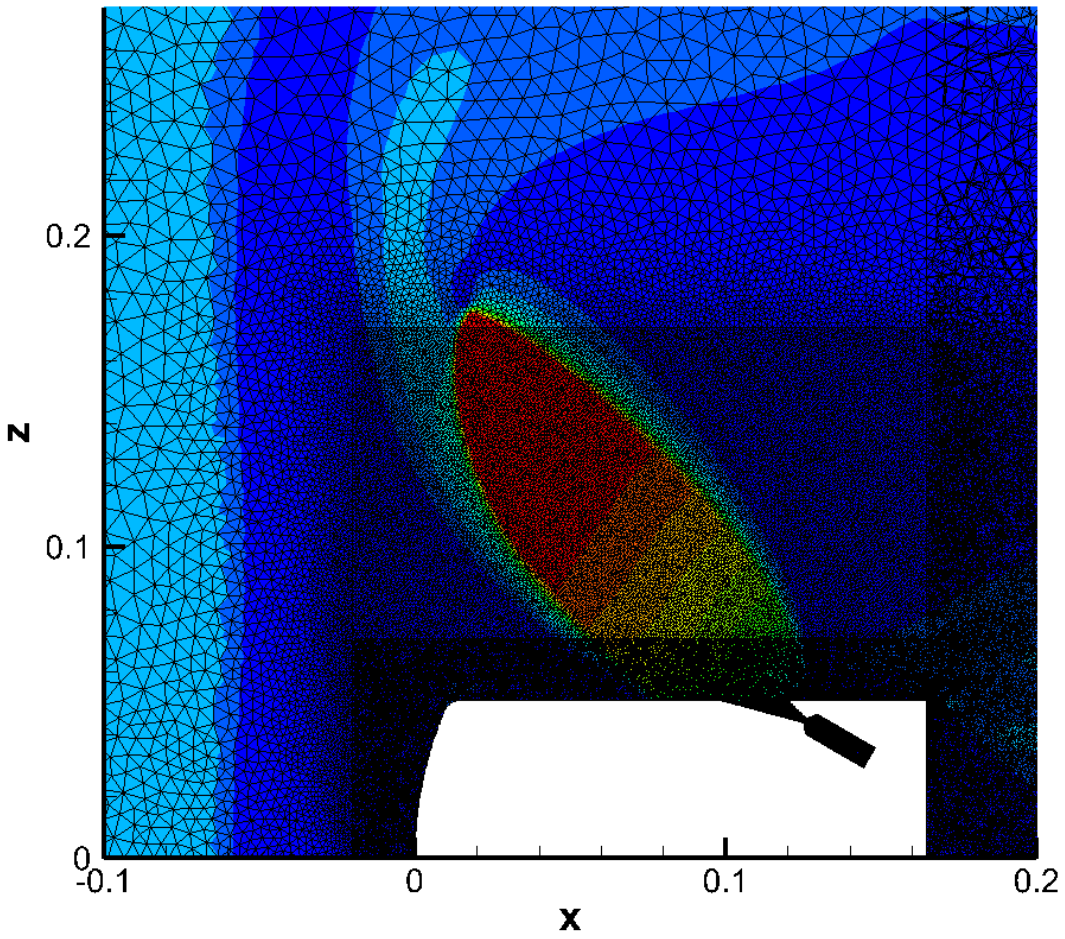

Figure 122: Plume region within computational grid for three nozzle, 30° nozzle canting, aftbody configuration with C_T = 10 Mach contours shown for reference

For the aftbody located nozzles, since the nozzles are located further outboard with the plumes creating a wider obstruction as compared to forebody located nozzles, it was thought that the wake behind the vehicle could have a significantly longer subsonic region, thus the computational domain extends further downstream as shown in Figure 123. The Mach contours for the largest thrust condition, C_T = 10, show that this is a conservative assumption as the subsonic portion of the wake closes at nearly the same axial location aft of the vehicle nose is seen for the 30° nozzle canting configuration with the nozzles located on the forebody. Due to the acceleration of the flow along the aftshell between the nozzles, some supersonic flow exists in the wake near the vehicle and a shock forms to narrow the subsonic wake in a similar manner as is seen in the forebody located nozzles. As with all of the forebody located nozzles, the computational domain has concentrated nodes in the region where the plume, bow shock, and wake are expected to form. The upstream inlet for the freestream flow is conservative compared to the actual bow shock structure, to ensure that the shock does not reach the computational volume upstream boundary and it was not known beforehand that the analytical model would be conservative in its prediction of the bow shock location for this configuration.

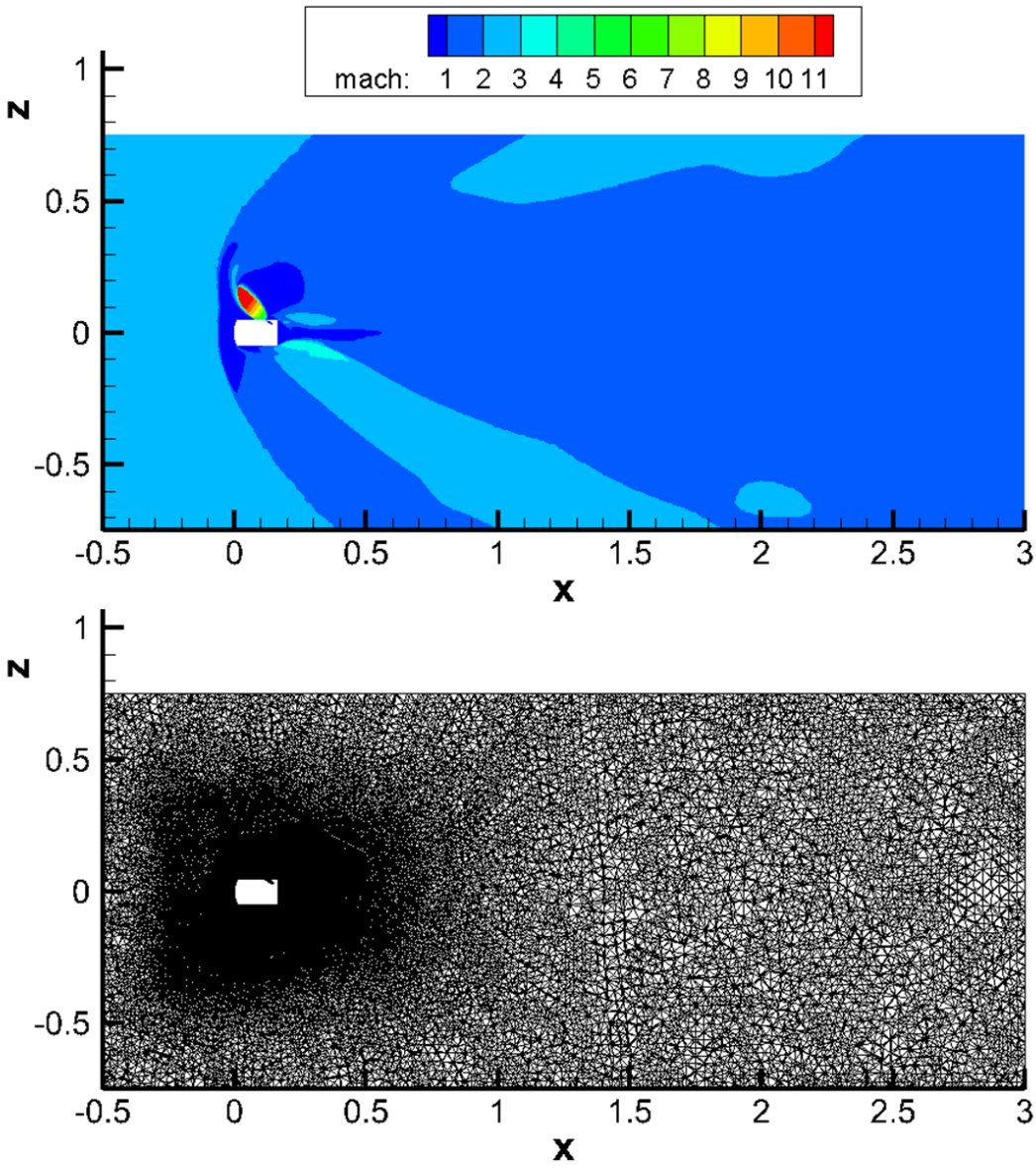

Figure 123: Full computational domain with C_T = 10 Mach contours (top) and computational mesh (bottom) for the three nozzle, 30° nozzle canting, aftbody configuration

6.2 Six Nozzle Configuration with 30° Cant Angle

Distributing the thrust over more nozzles, six for this configuration as compared to three for the configuration discussed in Section 6.1, should result in smaller plumes for a given

thrust coefficient due to each nozzle providing a lower thrust contribution to achieve the same overall deceleration force. This configuration has the same nozzle shape, cant angle, and nozzle axial location as the three nozzle aftbody configuration; only six nozzles are equivalently distributed around the vehicle. C_T = 1, 4, 7, and 10 have been run at zero angle of attack, with cases for C_T = 10 at angles of attack of -10° and 10° also investigated to provide insight into the static pitch stability characteristics of a six nozzle configuration. A case at C_T = 20 and 0° angle of attack has also been run, as this case has the same plenum pressure in each nozzle as the C_T = 10 case for the three nozzle aftbody configuration.

6.2.1 Zero Angle of Attack Effects on Flowfield Structure and Surface Pressure

Flowfield structures and surface pressure distributions for each thrust coefficient at zero angle of attack are shown in Figure 124 for the six nozzle, 30° nozzle canting, aftbody configuration. For C_T = 1, halving the thrust provided by a given nozzle as compared to the three nozzle configuration results in a smaller plume and an overall smaller region of high pressure forward of each nozzle exit. The overall aftbody pressure distribution forward of the nozzle exits is similar to the three nozzle configuration in that the pressure across the aftbody increases as compared to the no thrust condition, even if the plumes do not expand as far forward for the smaller individual thrust values. This indicates that the presence of a plume obstruction, regardless of size, impacts the aftbody flow field such that a pressure rise occurs due to the variation in the aftbody surface flow paths. The forebody surface pressure is unperturbed as the plumes do not expand sufficiently far forward to affect the flow in that region.

Increasing thrust to C_T = 4 shows an identical trend in surface pressure as C_T = 1. Even though the peak aftbody surface pressure is lower than for the three nozzle configuration, the overall aftbody surface pressure increases to a higher C_P value in the vicinity of the vehicle shoulder. Distributing the thrust over more nozzles creates a more constant circumferential obstruction as plumes are spaced every 60° rather than every 120° around the vehicle. This also creates more rounded plumes, as even though the plumes do not coalesce at this thrust coefficient, they do impact the decelerated freestream flow passing between each plume. The bow shock forward of the vehicle and the forebody surface pressure remain undisturbed, as each plume is still too small in expansion to impact that region of the vehicle.

Increasing thrust to C_T = 7 and C_T = 10 continues the trends seen for the lower thrust coefficients. The plume expansions grow larger, primarily affecting the outboard bow shock structure. The shock structure near the nose of the vehicle is mostly undisturbed, and the forebody surface pressure distribution remains constant across all thrust conditions examined. Each plume still shows a rounded shape, indicating that the effective obstruction created by six nozzles creates a much different aftbody flow environment than three nozzles. The peak aftbody surface pressure is lower for both of these thrust values on the six nozzle configuration as compared to the three nozzle aftbody geometry; however the pressure near the shoulder is higher due to the variation in effective obstruction shape. The interaction of the plumes with each other, though not coalescing, is also evident as a band of high pressure forward of the nozzle exits forms that is not seen in the three nozzle configuration, particularly for C_T = 10.

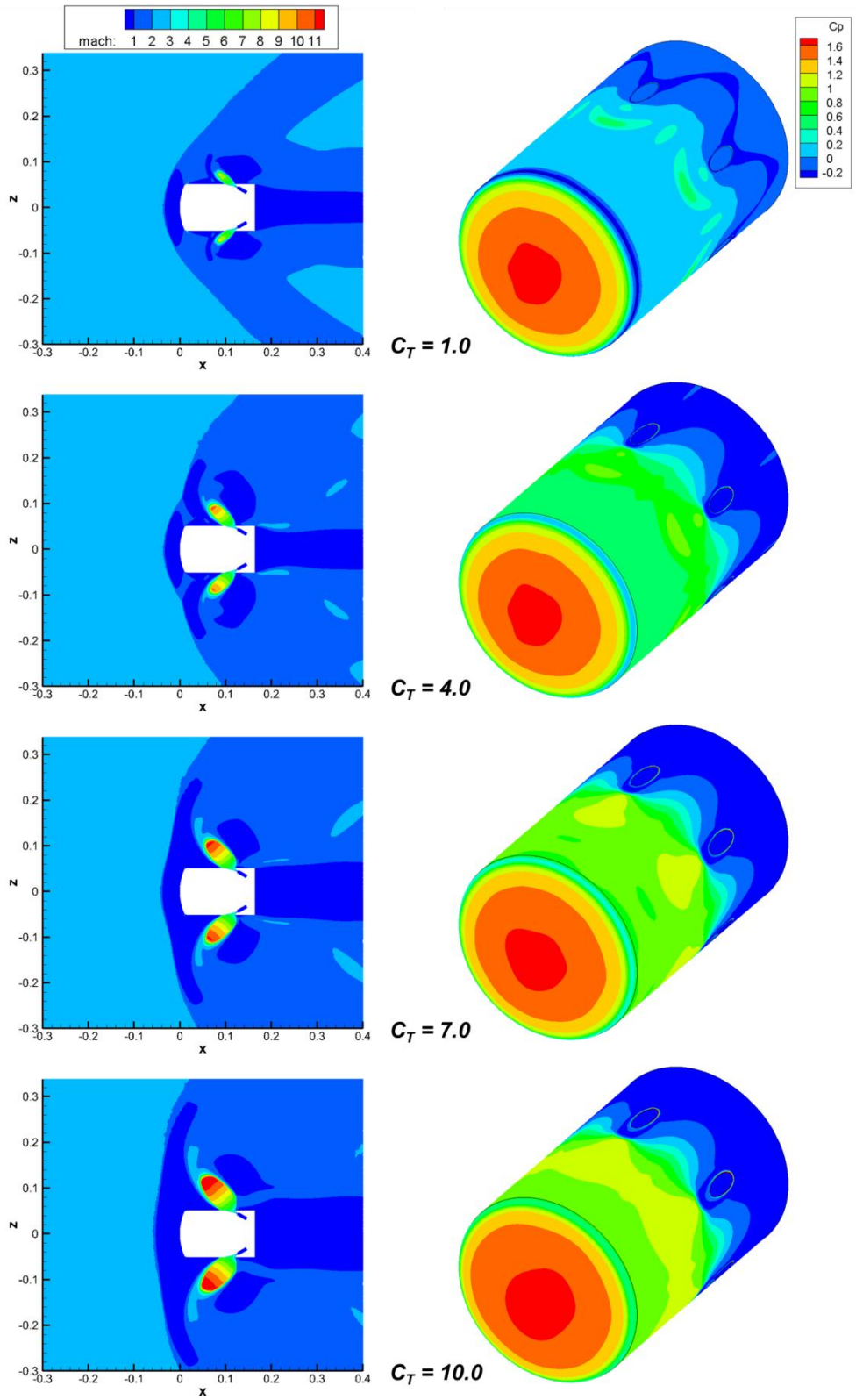

Figure 124: Mach contours and C_P distributions for varying C_T on the six nozzle, 30° nozzle canting, aftbody configuration

Figure 125 shows Mach contours and the surface pressure distribution for C_T = 20, corresponding to the same nozzle plenum pressure ratio as C_T = 10 for the three nozzle configuration. If the plumes have no effect on each other, it is expected that the plume structure for these two cases should be identical; however, the continued trend of rounded plumes is seen for the six nozzle configuration. The plumes affect the aftbody flow path of the decelerated freestream in a much different manner than the three nozzle configuration, which impacts plume expansion and shape. The aftbody pressure forward of the nozzles is significantly higher around the vehicle for the six nozzle configuration, as each plume creates a local stagnation area and the large effective circumferential obstruction created by six plumes increases surface pressure.

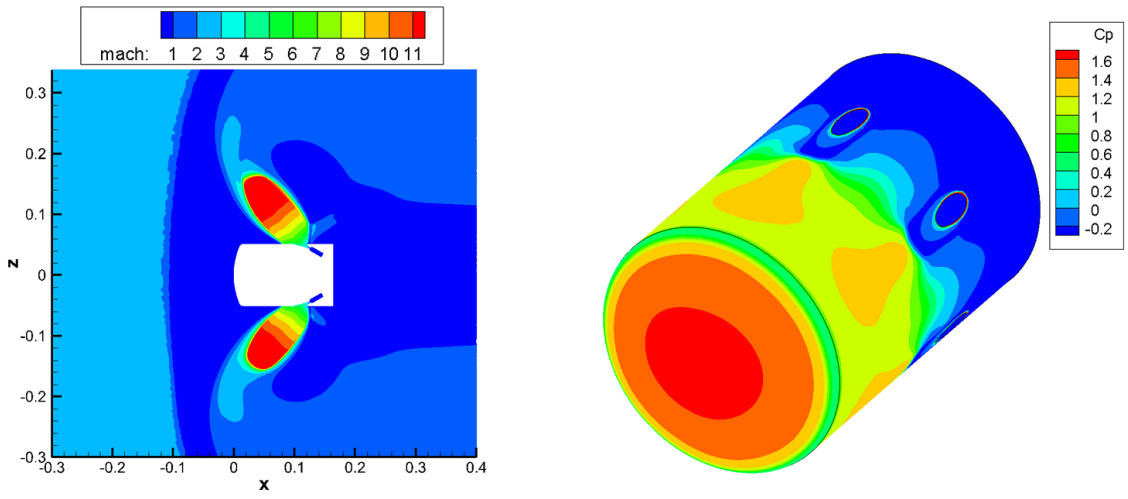

Figure 125: Mach contours and C_P distributions for C_T = 20 on the six nozzle, 30° nozzle canting, aftbody configuration

Figure 126 shows cross sections of the C_T = 10 flow field at varying axial locations along the vehicle. The core of each plume is noticeably independent, meaning that no plume coalescence occurs for this thrust condition; however, this figure illustrates that having

more nozzles results in less volume for the decelerated freestream to pass through as it flows around the vehicle. By narrowing the region between the plumes, the decelerated freestream accelerates from subsonic speeds at X = 0.004 (near the beginning of the plume obstruction as seen by the aftbody flow) to supersonic speeds by X = 0.010 (toward the rearward portion of the plume structure). This is likely the cause of the rounded plume structure in the CFD solutions, as the acceleration of the flow combined with the low incidence angle between the nozzle axis and the aftbody surface will create a strong shear environment over a long length along the plume boundary.

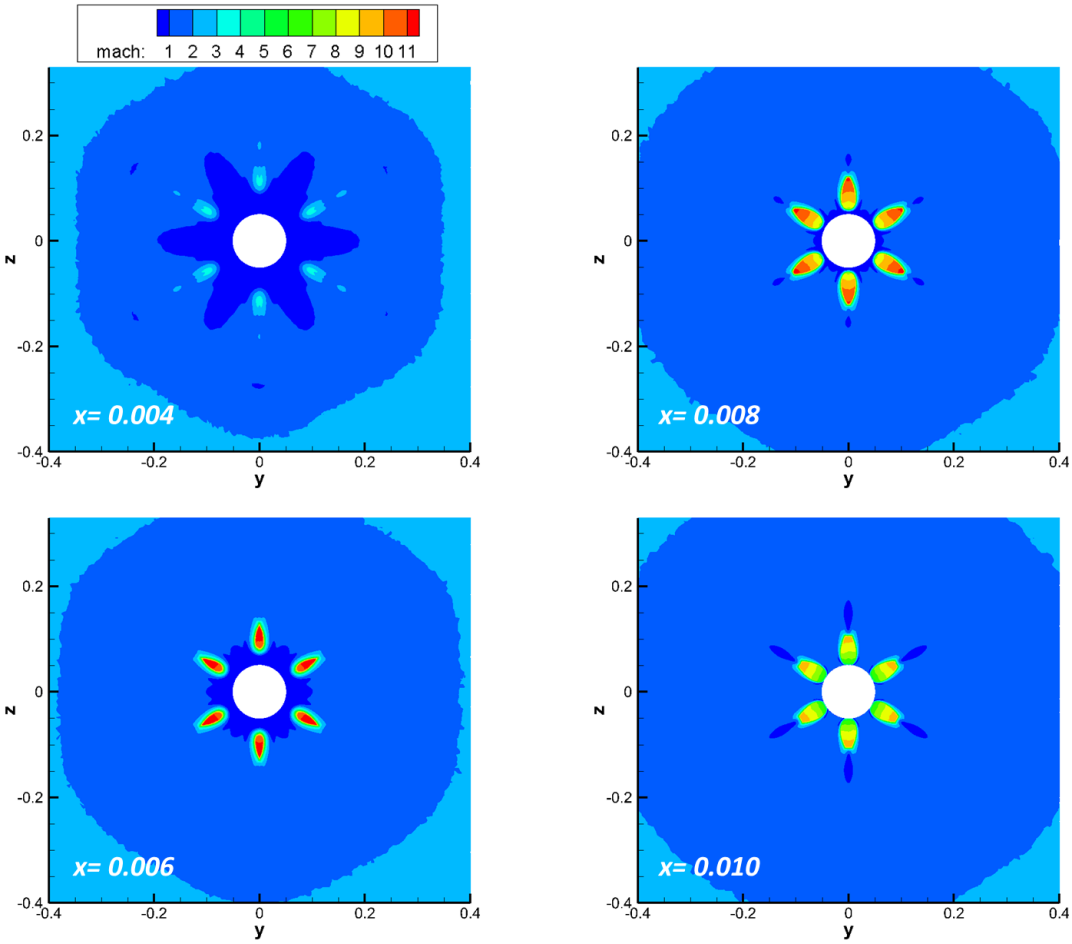

Figure 126: Cross sections of flow field showing proximity of plume structures for C_T = 10 on the six nozzle, 30° nozzle canting, aftbody configuration

6.2.2 Angle of Attack Effects

The smaller plumes that form for the six nozzle geometry have a significant impact on the aftbody pressure distribution when the vehicle flies at an angle of attack as compared to the three nozzle aftbody geometry. Figure 127 shows CFD solutions for C_T = 10 at angles of attack of -10°, 0°, and 10°. The plumes do not significantly modify the forebody pressure distribution for any angle of attack, as the plumes do not extend far enough upstream to shield the forebody.

Since the six nozzle configuration is symmetric about the *X*-*Y* plane, it is expected that the -10° and 10° angle of attack solutions should be mirrors of each other. Investigating the Mach contours in Figure 127 shows this to be the case. The windward plume narrows as the nozzle exit flow becomes more aligned with the oncoming freestream and the local crossflow effects decrease with the shift in the stagnation point on the forebody. The leeward plume becomes shielded by the vehicle body due to the large size of the vehicle and the shift in freestream flow direction, causing this plume to increase its radial expansion. The leeward surface becomes more of a low speed, wake type region where the impact of the supersonic freestream is minimal compared to the windward face. The aftbody surface pressure distribution varies due to this change in flow structure, as the windward side shows a significantly larger band of high pressure forward of the nozzles. The leeward side has a reduction in pressure, consistent with the shielding of the surface due to the vehicle.

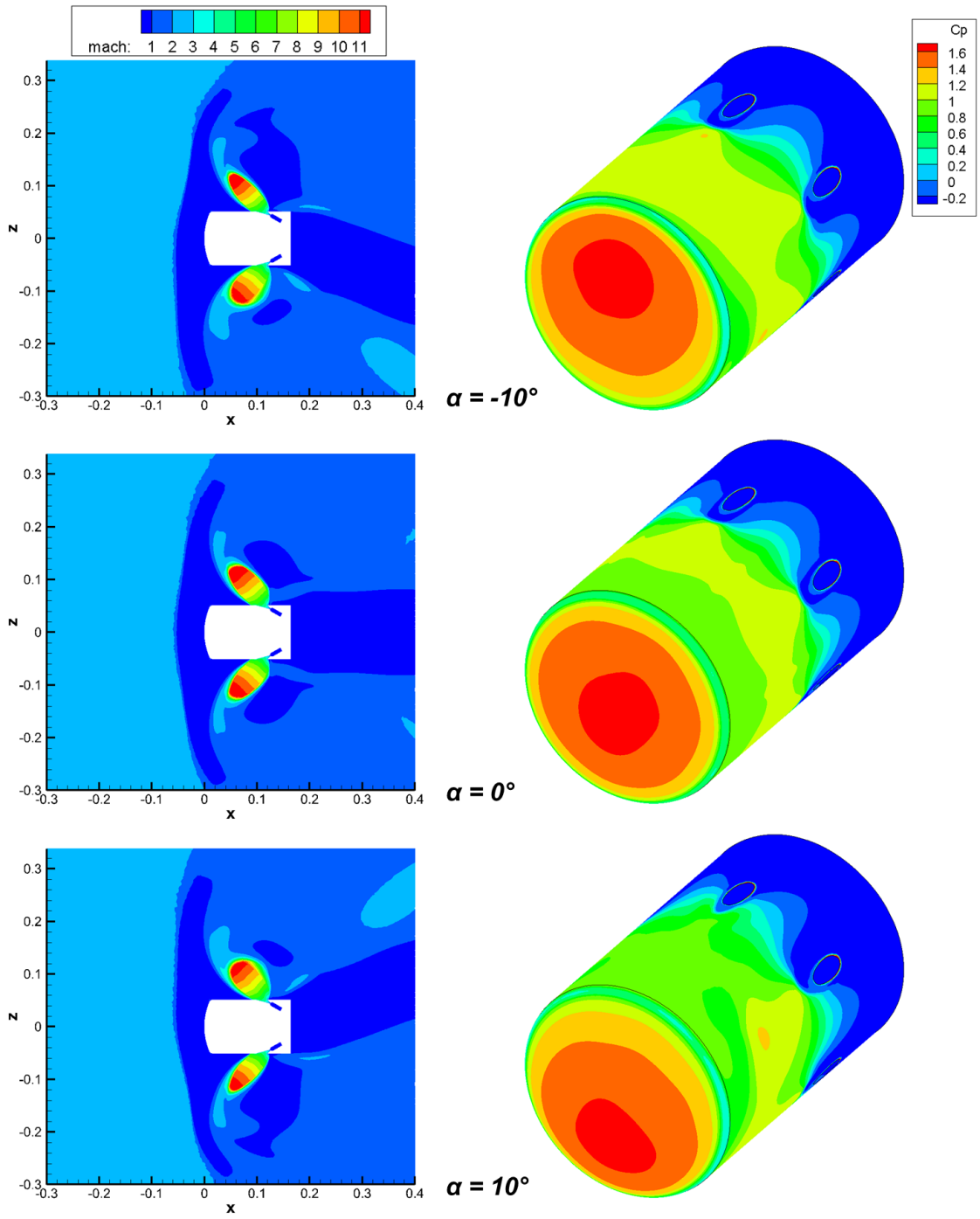

Figure 127: Effect of angle of attack on flowfield structure and surface pressure for C_T = 10 on the six nozzle, 30° nozzle canting, aftbody configuration

The six nozzle aftbody configuration shows similar static pitch stability behavior as the three nozzle aftbody configuration as seen in the plots for pitching moment as a function of axial center of mass location and angle of attack at C_T = 10 shown in Figure 128. For CG locations near the forebody, the vehicle exhibits static pitch stability, with a transition to instability occurring at approximately 37% of the vehicle length. This location is forward of the transition point for the three nozzle aftbody configuration, indicating that distributing thrust over more nozzles provides less volume within this vehicle for the CG to be located and have the vehicle statically stable in pitch. As with the three nozzle aftbody configuration, the nozzles are located aft of the transition point, at X = 0.114 m.

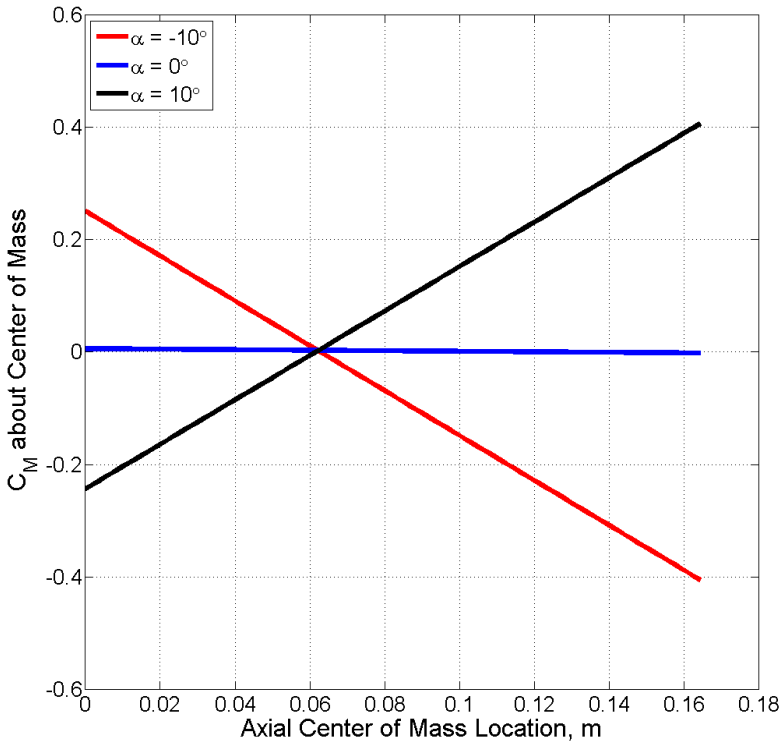

Figure 128: Variation in pitching moment coefficient with center of mass location and angle of attack for C_T = 10 on the six nozzle, 30° nozzle canting, aftbody configuration

Plots of CG trim lines for the six nozzle aftbody configuration at varying angles of attack are shown in Figure 129 for C_T = 10. Consistent with all configurations investigated, the presence of an SRP system provides insensitivity to location along the vehicle axis about which the vehicle can reach trim conditions due to the large moment provided by the nozzles. The CG trim lines for this configuration are slightly less sensitive than those of the three nozzle aftbody configuration as the angle of attack lines have lower slopes and are more horizontal.

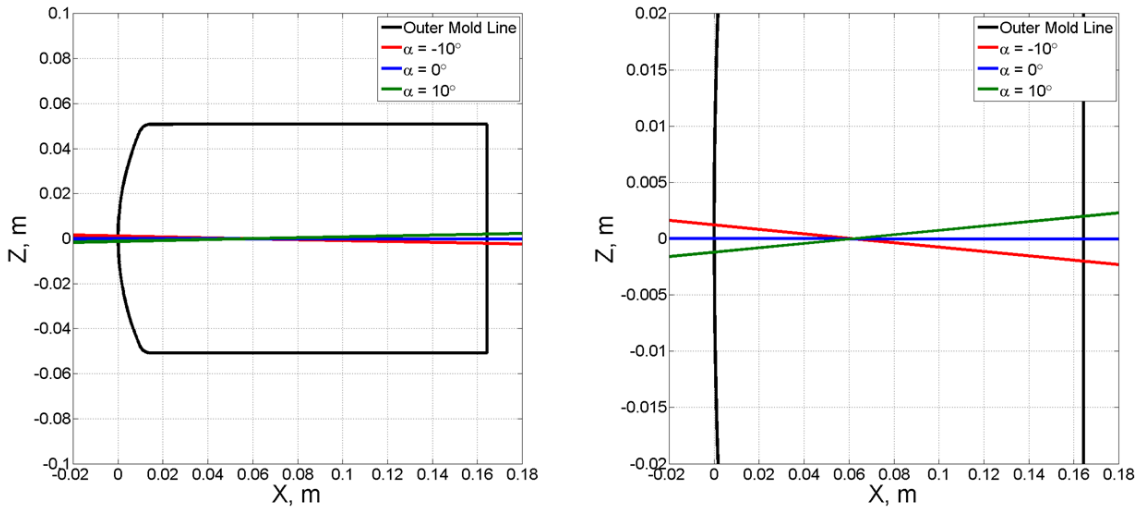

Figure 129: CG trim lines for varying angles of attack at C_T = 10 on the six nozzle, 30° nozzle canting, aftbody configuration for the full vehicle view (left) and a zoomed view (right)

6.2.3 Deceleration Force

Figure 130 shows drag coefficient trends with thrust coefficient for the six nozzle aftbody configuration, including both the aftbody and forebody contributions in addition to the total drag force on the vehicle. As thrust increases, the net aerodynamic drag consistently increases, indicating that there is no loss in aerodynamic performance due to the presence

of plumes in the flow field. For low thrust conditions, the primary cause of the increase in drag is the aftbody contribution, consistent with the results seen for the three nozzle aftbody configuration. For higher thrust conditions, the aftbody drag contribution decreases slightly with an increase in thrust, but the forebody contribution steadily increases. This is due to the plume structure minimally affecting the bow shock forward of the vehicle and causing an increase in forebody surface pressure. For C_T = 20, C_D = 1.67, a 14% increase over the baseline C_D. However, due to the large C_T, the cosine losses to the thrust contribution are significant, and the net deceleration force coefficient is 19.0, a 5% reduction from an assumption where thrust provides all of the deceleration with no losses or aerodynamic contribution. For C_T = 10, the drag coefficient is 1.63, a 12% increase over the baseline and the net deceleration force coefficient is 10.3, a 3% increase over a condition where only thrust provides deceleration with no losses.

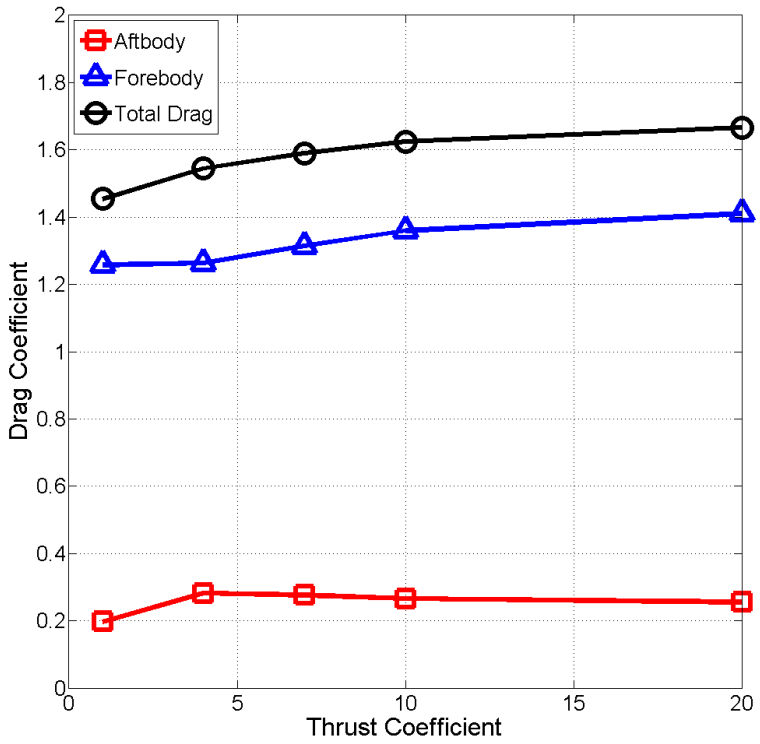

Figure 130: C_D variation with C_T for the six nozzle, 30° nozzle canting, aftbody configuration including aftbody and forebody contributions

6.2.4 Grid Convergence Study

The difference in plume structure for the six nozzle, 30° nozzle canting aftbody configuration as compared to the three nozzle, 30° nozzle canting aftbody configuration necessitates further investigation to determine if the grid is the cause of the rounder plume structure. Two grids have been run on this configuration with solutions for $C_T = 1$ and $C_T = 10$ shown in Figure 131. Both grids show the same flow structure for each thrust condition, indicating that the rounded plume structure is not a function of the computational grid.

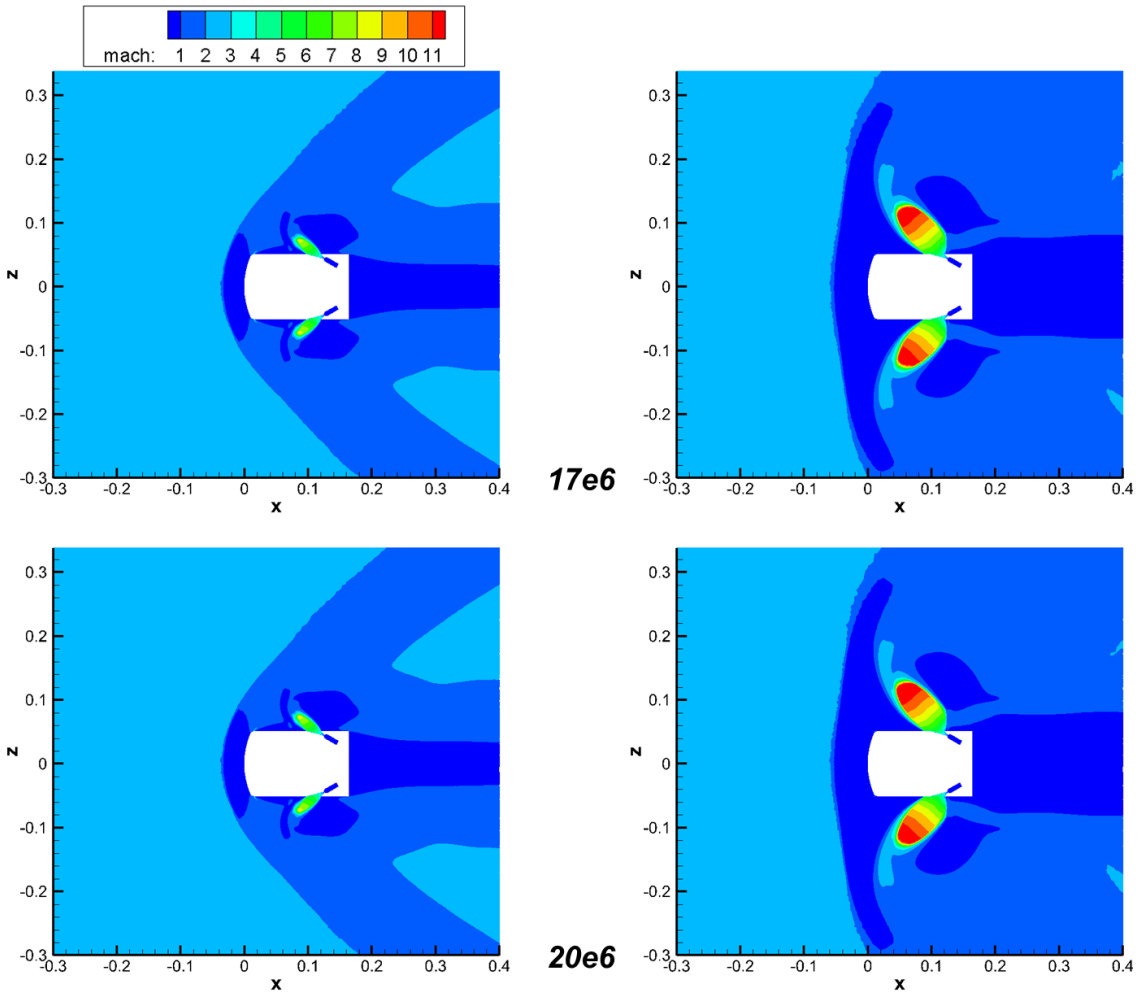

Figure 131: Effect of total number of nodes within computational grid on six nozzle, 30° nozzle canting solutions for C_T = 1 (left) and C_T = 10 (right)

The plume region of the mesh for the six nozzle aftbody configuration is shown in Figure 132 with C_T = 20 Mach contours shown for reference. The analytical model predicts a maximum radial extent of 0.161 m and a maximum axial extent to X = -0.009 m, which has been used to guide the grid generation process. The plume is fully contained within the defined plume block in Gridgen, indicating that basing the grid generation process on the analytical model results in a sufficient grid for solution generation. The grid used for the solutions shown in Section 6.2 contains 16.7 million nodes overall.

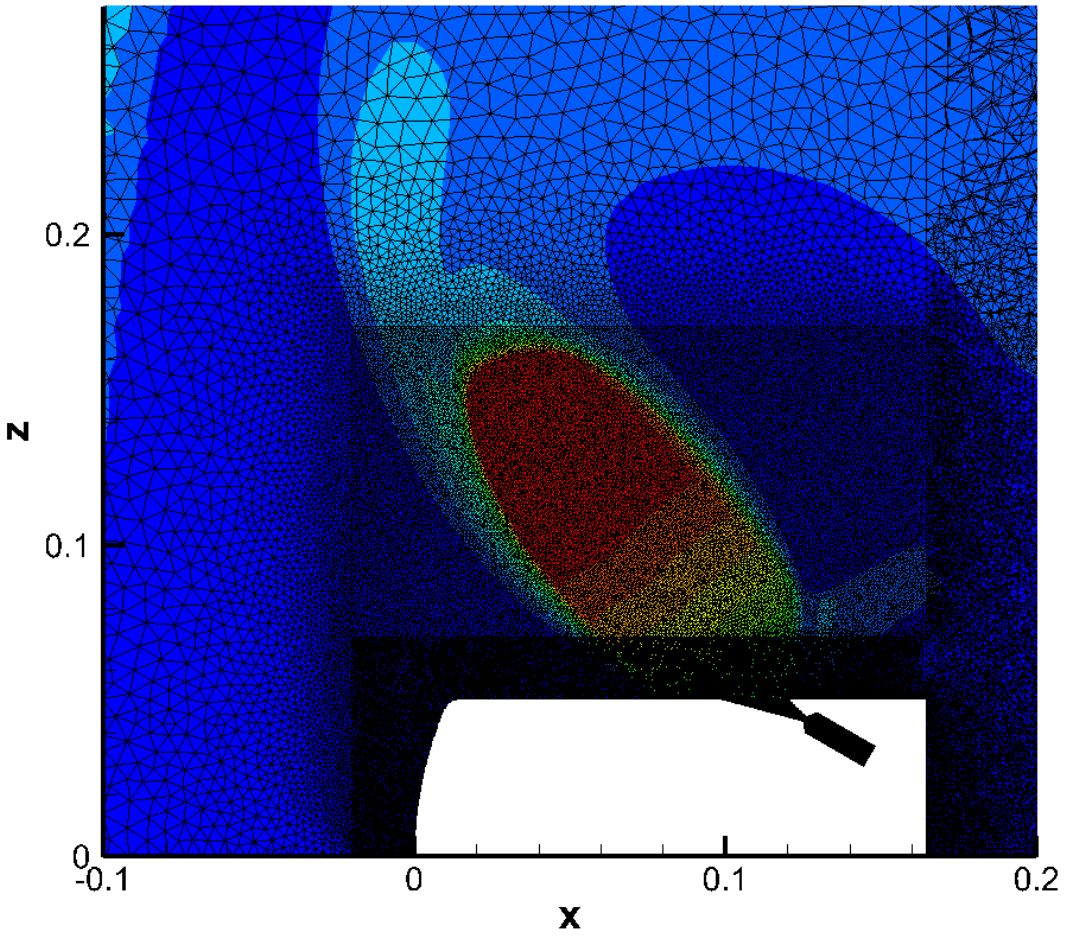

Figure 132: Plume region within computational grid for six nozzle, 30° nozzle canting, aftbody configuration with C_T = 20 Mach contours shown for reference

The six nozzle configuration, having twice the number of nozzles as the three nozzle configuration, results in a larger volume of plume flow creating a more continuous obstruction to the freestream. For the six nozzle, 30° nozzle canting, aftbody configuration, this creates a larger subsonic wake aft of the vehicle than the three nozzle, 30° nozzle canting, aftbody configuration as shown in Figure 133. While the computational downstream boundary is still conservative compared to the location at which the subsonic wake closes in the CFD solution for C_T = 20, this wake flow is more

in line with what was expected prior to running the solutions. There is no supersonic flow in the wake near the vehicle and no shocks are forming in the wake as is seen for the three nozzle, 30° nozzle canting, aftbody configuration. This is due to the larger effective obstruction created by the plumes extending far outboard of the vehicle, and the presence of six plumes rather than three creates a more continuous obstruction to the freestream flow. The subsonic wake extends well downstream of the highest concentration of nodes in the computational mesh; however, this does not appear to impact wake formation.

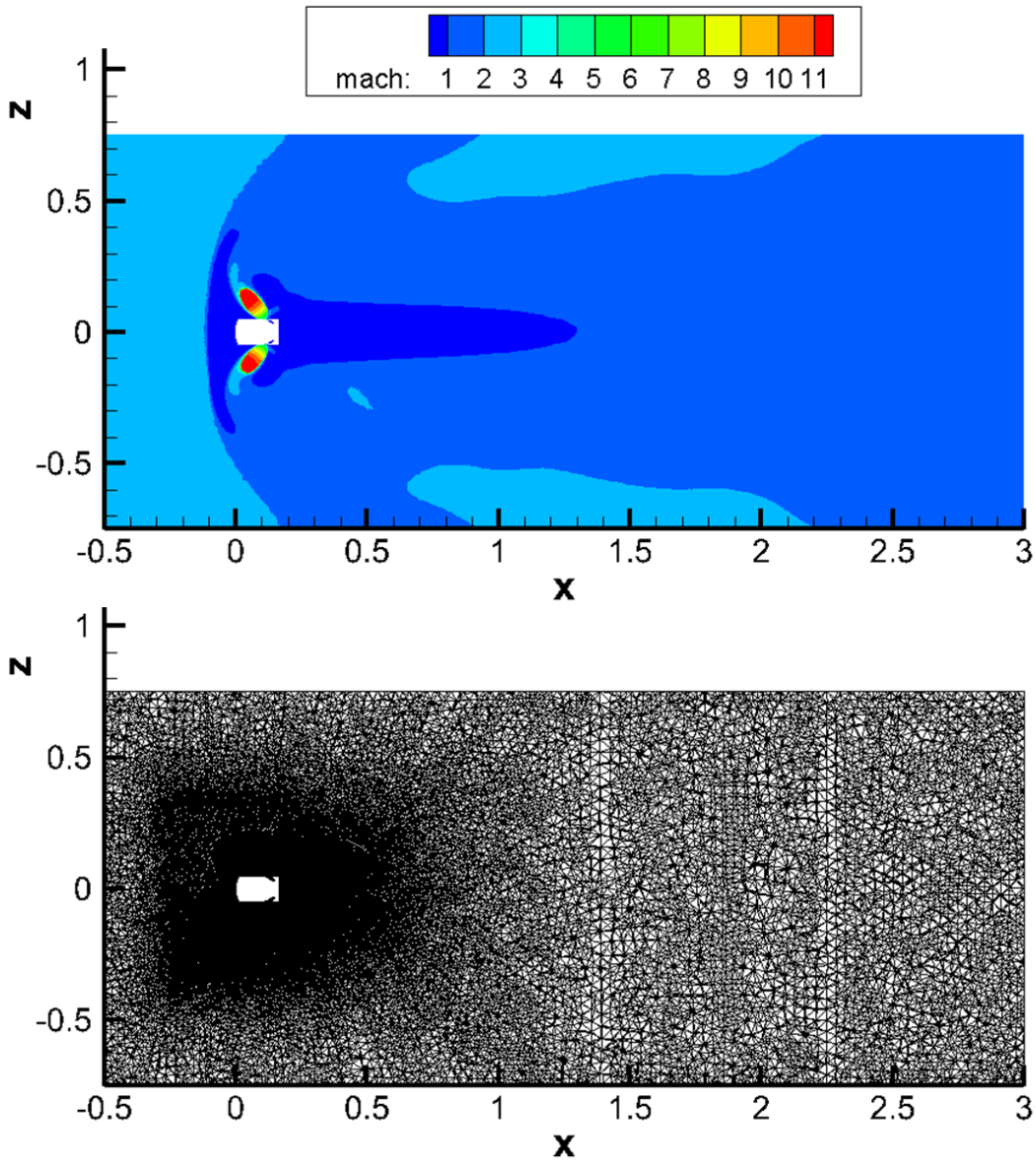

Figure 133: Full computational domain with C_T = 20 Mach contours (top) and computational mesh (bottom) for the six nozzle, 30° nozzle canting, aftbody configuration

6.3 Six Nozzle Configuration with 60° Cant Angle

Increasing the nozzle cant angle from 30° to 60° will create significant thrust losses to deceleration while the plumes will be directed further outboard. This will impact the

aftbody surface pressure, as interaction between the plume and the surface should be reduced if nozzle flow is more normal to the surface. Thrust coefficients of 1, 4, 7, 10, and 20 have been run at zero angle of attack to determine the effects of increasing the nozzle cant angle on SRP performance. Angles of attack of -10° and 10° have also been run for C_T = 10 to establish static pitch stability characteristics for this configuration to determine if increasing cant angle has stability benefits to offset the losses in the thrust contribution to the deceleration force.

6.3.1 Zero Angle of Attack Effects on Flowfield Structure and Surface Pressure

By canting the nozzles at 60° relative to the vehicle axis, the plumes are directed more outboard than forward in the flow field, as shown in Figure 134. For all thrust coefficients, this means that the plumes do not extend far upstream in the flow field. Even for C_T = 10, the plume structure and effective obstruction do not extend half of the distance between the nozzle exit and the vehicle shoulder. The bow shock forward of the vehicle is undisturbed for all thrust coefficients, meaning that the forebody pressure distribution is preserved in all of the CFD solutions. The plume structure for these cases is less rounded than are seen for the six nozzle, 30° nozzle canting configuration because the nozzle exhausts more normal to the surface. The incidence angle of the plume with respect to the surface for the six nozzle, 60° nozzle canting aftbody configuration is equivalent to that of the three nozzle, 0° nozzle canting forebody geometry investigated in Chapter II that also shows a narrower plume structure. Because the plume does not exhaust directly into the freestream flow, the plume structures are not identical between these two geometries as the local crossflow environment differs.

C_T = 1 shows small plumes whose effective obstruction is not sufficiently far forward to impact the shoulder separation and flow acceleration of the decelerated freestream. The low aftbody surface pressure near the shoulder that is seen in the baseline, no thrust condition is preserved due to this distance between the plume boundary and the shoulder. A small higher pressure region still forms forward of the nozzle exits due to the plume expansion, consistent with the aftbody flow needing to turn to pass around the plume structure. Increasing thrust to C_T = 4 causes an increase in the aftbody surface pressure forward of the nozzles, as the plume expansion is large enough to create a noticeable obstruction to the decelerated freestream flow. Both the peak surface pressure and the overall surface pressure are lower than is seen in the CFD solutions for the six nozzle, 30° nozzle canting aftbody configuration because the plumes have less interaction with the surface flow.

Further increasing thrust to C_T = 7 and C_T = 10 continues the trends seen for C_T = 4. The peak and average aftbody surface pressure forward of the nozzles increase with increasing thrust coefficient as the size of the plumes increases. The bow shock structure becomes more normal far outboard of the vehicle in response to the presence of larger plumes, but this disturbance does not reach the shock structure forward of the shoulder. This configuration shows a noticeable difference in the aftbody surface pressure aft of the nozzles, as the pressure is not reduced to a constant negative C_P value. Rather, the plumes exhausting more normal to the surface all for some pressure preservation from the baseline no thrust condition aft of the nozzles due to a change in the shielding behavior of plumes formed by a 60° aftbody nozzle canting.

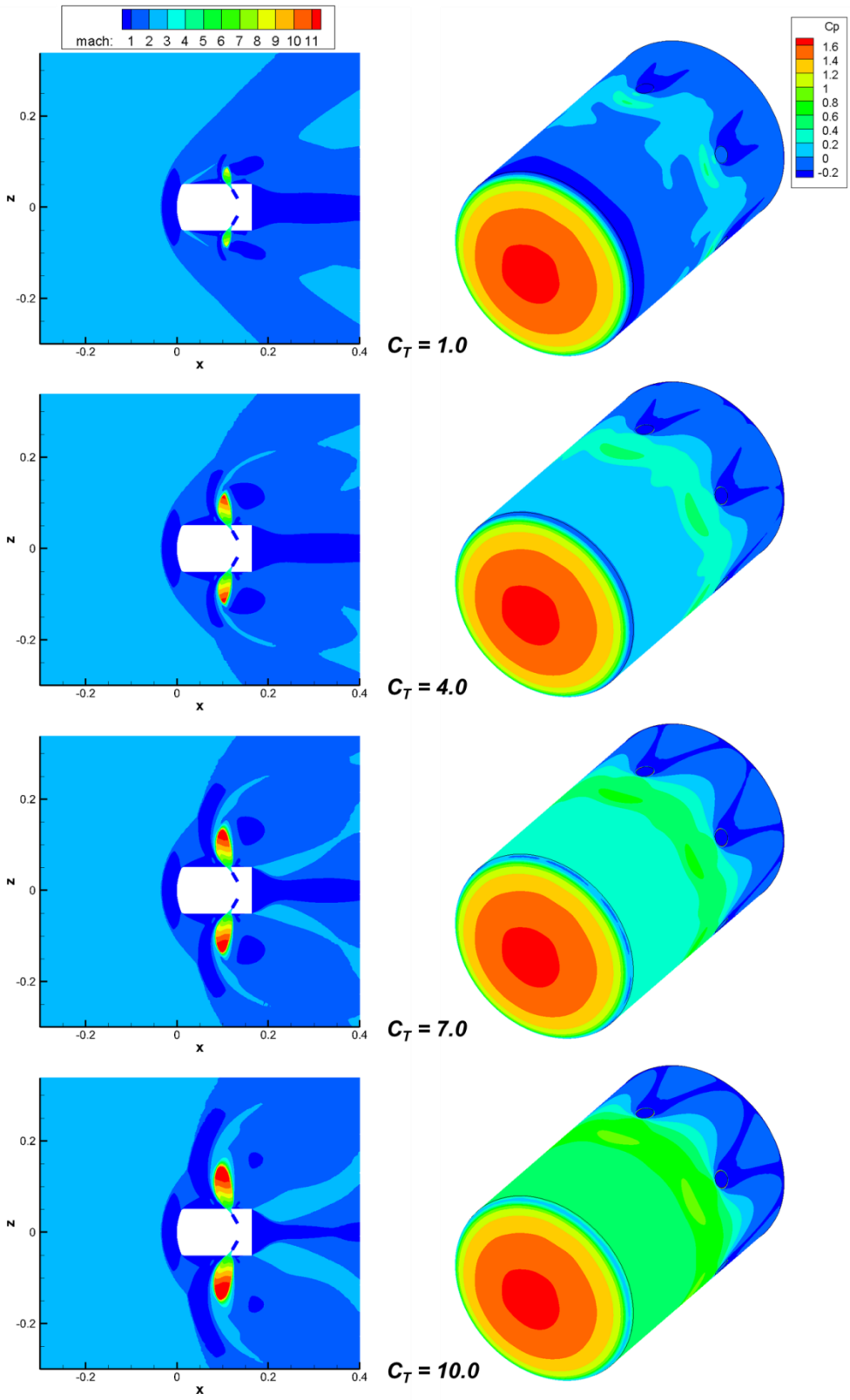

Figure 134: Mach contours and C_P distributions for varying C_T on the six nozzle, 60° nozzle canting, aftbody configuration

Increasing thrust to C_T = 20 shows a similar effect with the plume structure as is seen for the lower thrust conditions. The plume expansion is large, but primarily affects the outboard bow shock structure and leaves the shock forward of the vehicle undisturbed as shown in Figure 135. The forebody surface pressure is preserved, and the increase in aftbody pressure forward of the nozzle continues as the effective obstruction from the plumes grows larger. For this thrust condition, the plumes are large enough to shield the aft portion of the vehicle, resulting in a decrease in pressure aft of the nozzle exits as is seen for both the three and six nozzle, 30° nozzle canting aftbody configurations.

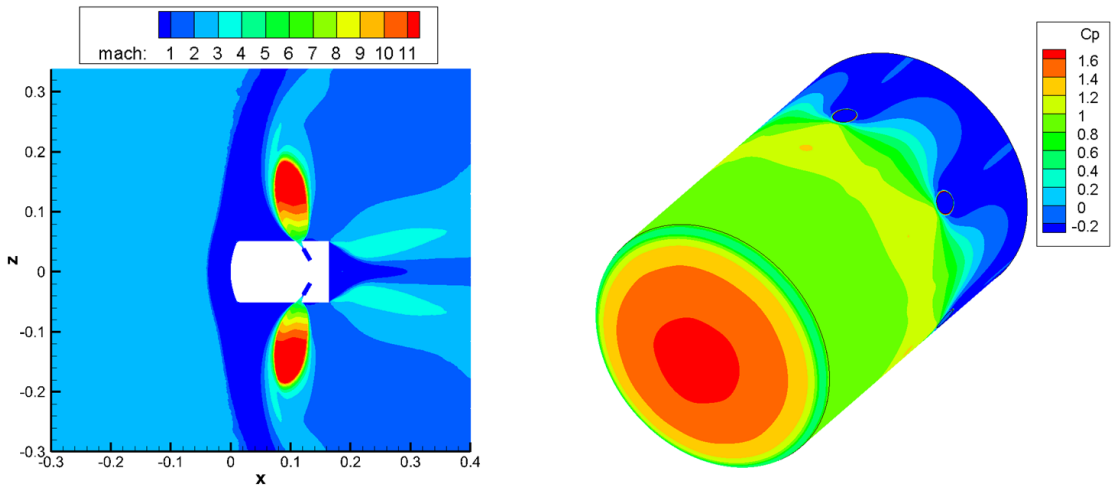

Figure 135: Mach contours and C_P distributions for C_T = 20 on the six nozzle, 60° nozzle canting, aftbody configuration

6.3.2 Angle of Attack Effects

As with the other geometries, solutions for C_T = 10 have been run at angles of attack of -10°, 0°, and 10° to establish the dependency of SRP performance on orientation of the vehicle to the freestream for the six nozzle, 60° nozzle canting configuration. Flowfield structures and surface pressure distributions are shown in Figure 136 for each angle of

attack. As with the six nozzle, 30° nozzle canting, aftbody configuration, the solutions at -10° and 10° are mirrors of each other since the nozzle configuration is symmetric about the *X*-*Y* plane. The windward plume shows a narrower structure, as it is affected by the shift in stagnation point toward its side of the vehicle. The leeward plume is shielded by the vehicle, and the plume expansion increases as the local crossflow is weaker.

The surface pressure distributions show a distinct variation with the orientation of the vehicle to the freestream flow. The leeward side of the vehicle shows a slight loss in aftbody surface pressure forward of the nozzle exits, primarily in the region near the nozzle exit. Near the vehicle shoulder, as is true for the zero angle of attack solutions, the 60° nozzle canting does not result in plumes that extend far upstream and the pressure distribution is nearly the same as is seen for zero angle of attack. On the windward side of the vehicle a high pressure band forms just forward of the nozzle exits. The peak surface pressure in this region is higher than is seen for the 30° nozzle canting configuration, though the size of the band is smaller. Overall, the increase in cant angle does not significantly affect the pressure distribution near the shoulder of the vehicle for the angle of attack cases examined; however, the shift in relative angle of the freestream flow to the vehicle creates a stronger stagnation region forward of the windward plumes as the aftbody flow must pass around the effective obstruction.

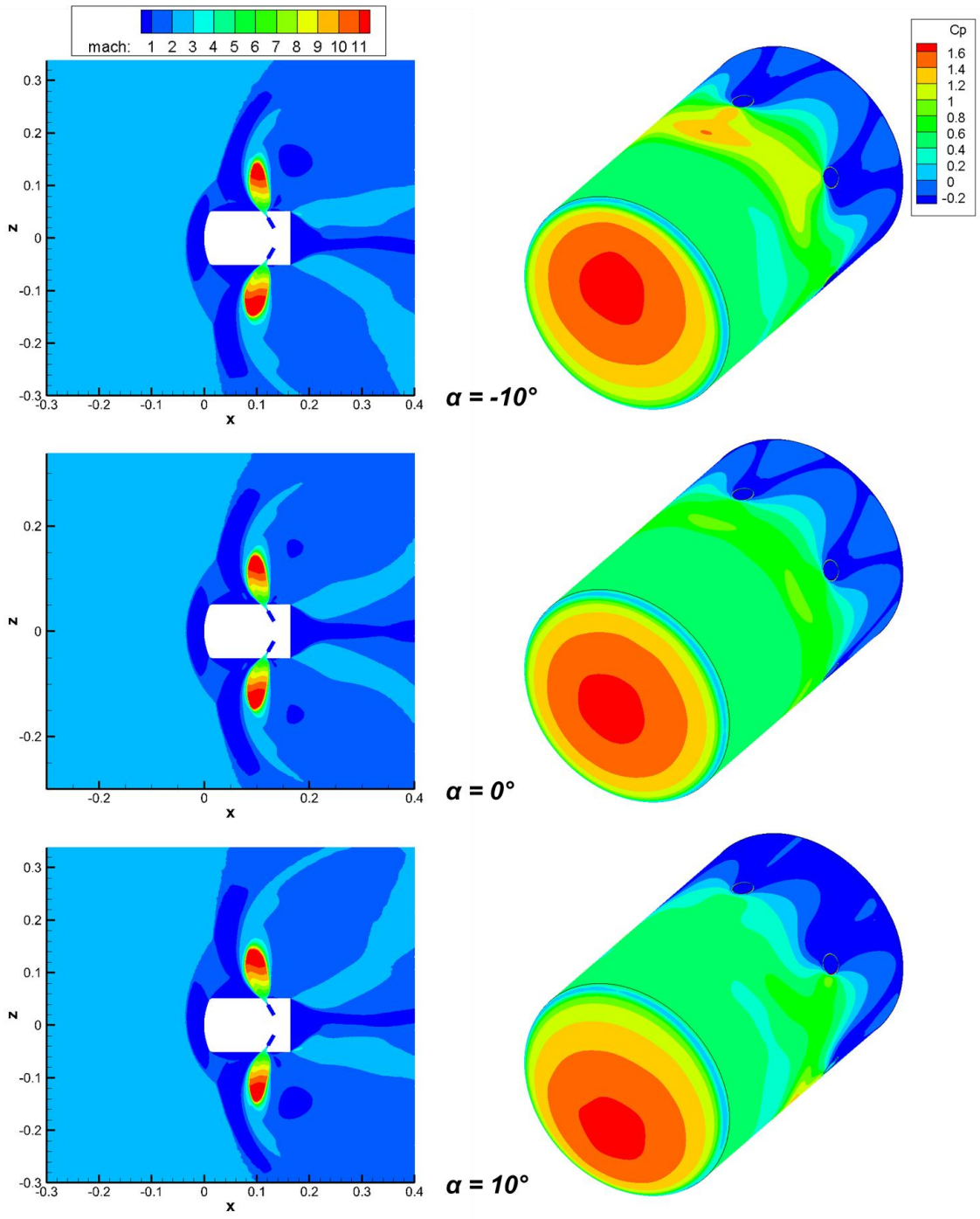

Figure 136: Effect of angle of attack on flowfield structure and surface pressure for C_T = 10 on the six nozzle, 60° nozzle canting, aftbody configuration

Figure 137 shows plots of pitching moment as a function of axial center of mass location for the three angle of attack cases run at C_T = 10 for the six nozzle, 60° nozzle canting,

aftbody configuration. The trend of aftbody nozzle locations exhibiting a transition from static pitch stability to instability continues with an increase in cant angle; however, the transition point shifts along the vehicle axis. For this configuration, the stability transition occurs at 61% of the vehicle length, further aft than is seen for either of the 30° nozzle canting geometries. Increasing the cant angle, while reducing the thrust contribution to deceleration, allows for a larger volume for the center of mass location at which the vehicle is statically stable in pitch motion.

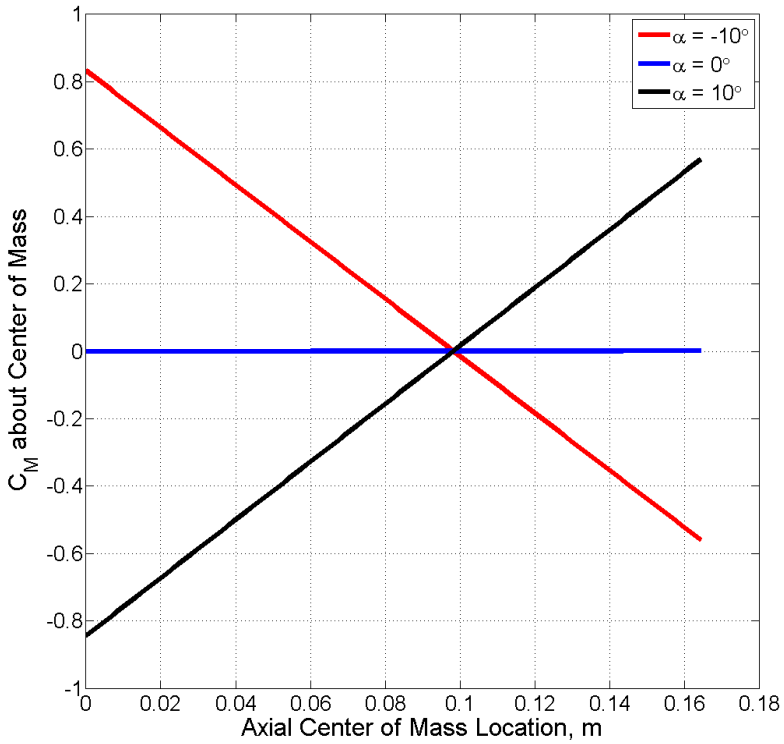

Figure 137: Variation in pitching moment coefficient with center of mass location and angle of attack for C_T = 10 on the six nozzle, 60° nozzle canting, aftbody configuration

Plots of the CG trim lines for varying angle of attack are shown in Figure 138. While the lines are nearly horizontal, indicating that the ability of the vehicle to trim at these angles

of attack is not strongly dependent on CG location near the axis, the magnitude of the slopes of the angle of attack trim lines are larger than is seen for the 30° nozzle canting geometries. The increase in nozzle cant angle provides less moment for trimming the vehicle when the CG is located off axis. The increase in volume for which the vehicle exhibits static pitch stability is offset by an increase in the sensitivity of vehicle trim capabilities to the CG location.

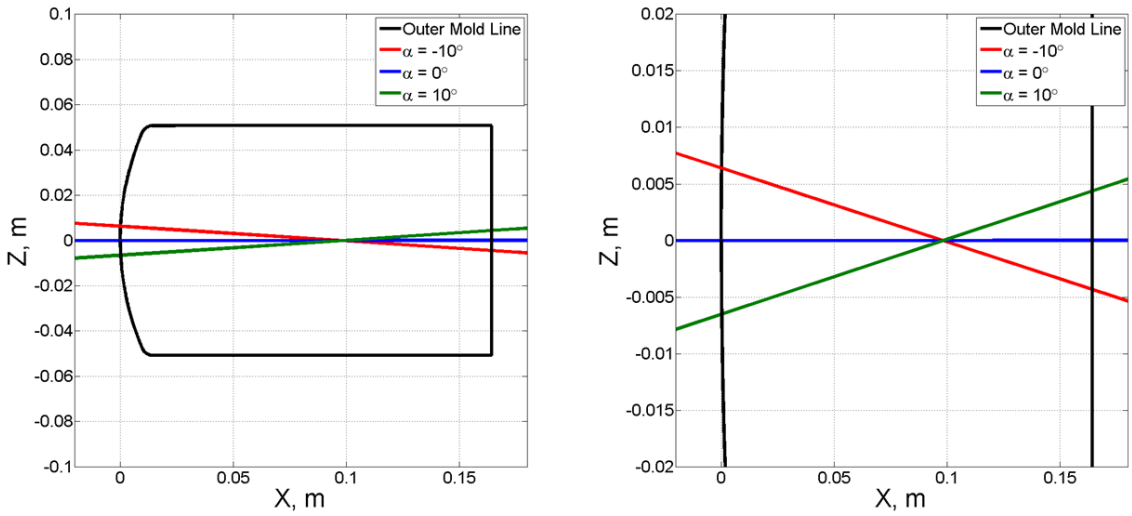

Figure 138: CG trim lines for varying angles of attack at C_T = 10 on the six nozzle, 60° nozzle canting, aftbody configuration for the full vehicle view (left) and a zoomed view (right)

6.3.3 Deceleration Force

Figure 139 shows the variation in drag coefficient with thrust coefficient for the six nozzle, 60° nozzle canting, aftbody configuration. For C_T values ranging from 1-10, the forebody contribution to C_D is nearly constant, as the forebody surface pressure distribution is unperturbed for these cases. The aftbody contribution to drag increases as the pressure on the aft face of the vehicle decreases with larger plume structures. For C_T

= 20, the plumes are large enough to affect the forebody pressure slightly, resulting in an increase in the forebody contribution to drag. Overall, the net deceleration force coefficient increases with thrust for all of the thrust conditions examined. For C_T = 20, the drag coefficient is 1.68, a 15% increase over the baseline case. However, the large cant angle means that the thrust contribution to the deceleration force coefficient is only 10, resulting in a net coefficient of 11.68, a 41.6% decrease from a nominal case where all of the thrust is directed upstream and no aerodynamic contribution is assumed. For C_T = 10, the drag coefficient of 1.60 represents a 9% increase over the baseline drag; however the same steep penalty for nozzle canting applies as the net deceleration force coefficient is only 6.60, a 34% decrease from a thrust only condition with no losses.

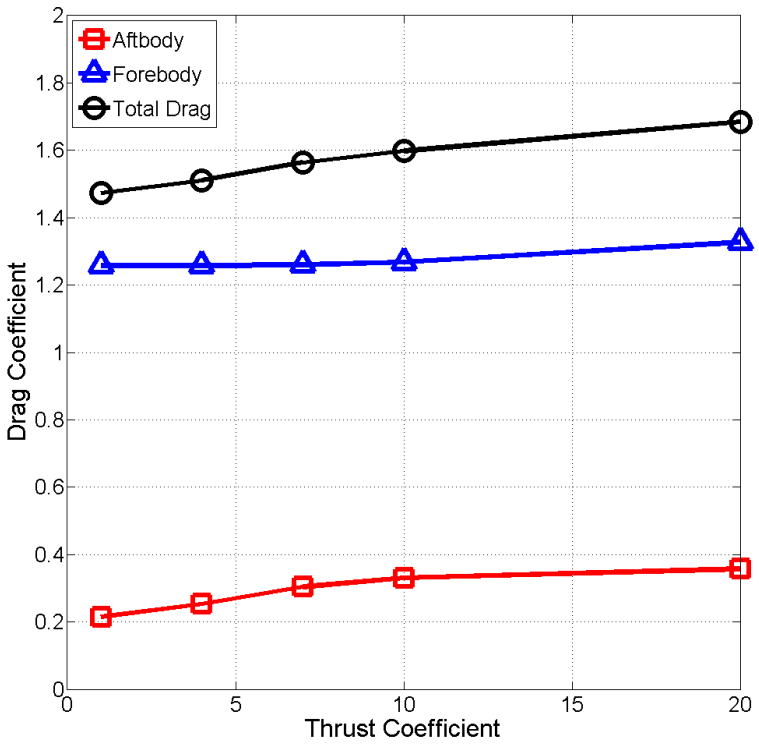

Figure 139: C_D variation with C_T for the six nozzle, 60° nozzle canting, aftbody configuration including aftbody and forebody contributions

6.3.4 Grid Generation

Figure 140 shows the plume region of the computational grid for the six nozzle, 60° nozzle canting, aftbody configuration with C_T = 20 Mach contours shown for reference. This region fully contains the plume structure in both the radial and axial directions, indicating that the information from the analytical model is sufficient for guiding the generation of the computational domain. The analytical model predicts a maximum radial expansion to 0.185 m, and a maximum axial extent to 0.047 m. Some margin has been applied to both of these estimates when defining the plume region within Gridgen, resulting in a radial extent of the region near 0.2 m and an axial extent covering the entire aftbody portion of the vehicle. Overall, this grid contains 19.8 million nodes, consistent with the other computational domains.

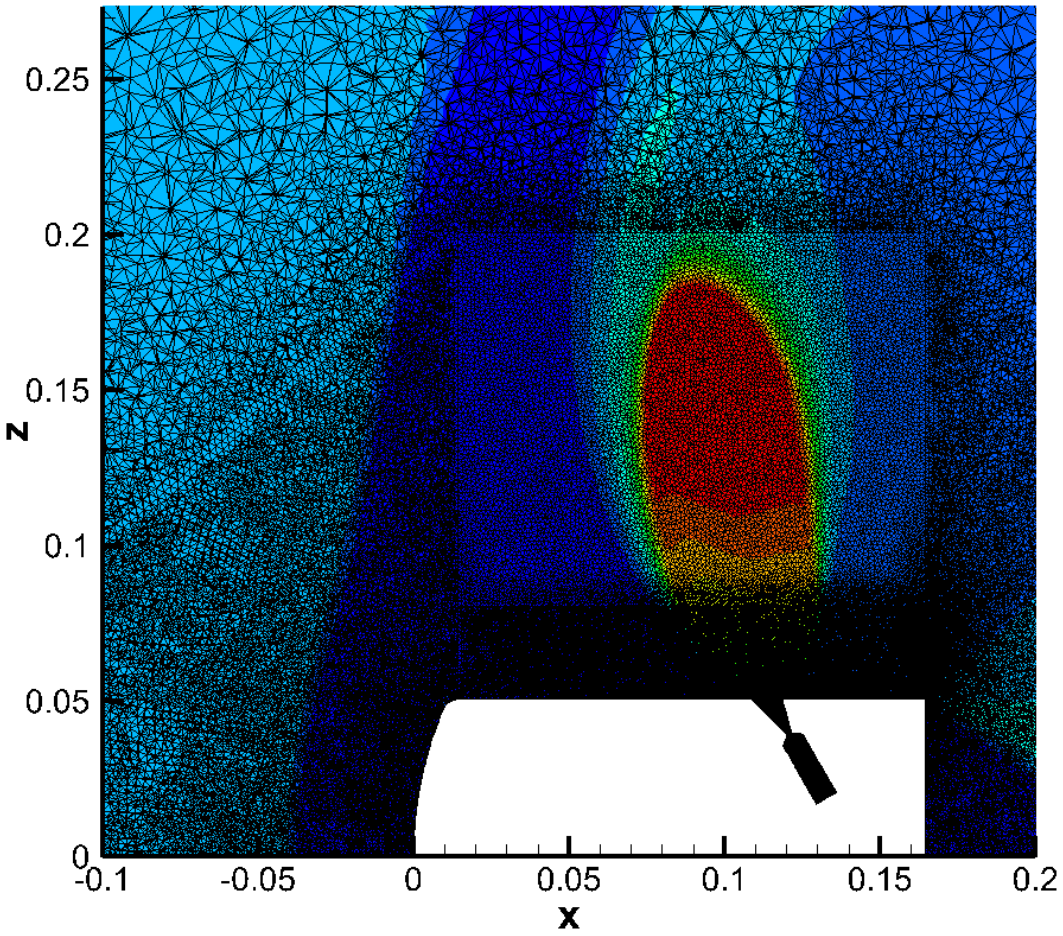

Figure 140: Plume region within computational grid for six nozzle, 60° nozzle canting, aftbody configuration with C_T = 20 Mach contours shown for reference

Increasing cant angle to 60° for the six nozzle aftbody configuration causes the plumes to extend to larger radial distances than the configuration with 30° nozzle canting. It was expected that this would create an even larger effective obstruction to the freestream, and the presence of six plumes would still project a nearly continuous obstruction such that the subsonic wake extended far downstream. In the CFD solution for C_T = 20 shown in Figure 141, the subsonic wake is narrow and short, more consistent with the results seen for the three nozzle, 30° nozzle canting, aftbody configuration than the six nozzle, 30° nozzle canting, aftbody configuration. This is likely due to the 60° nozzle canting

creating a plume exhausting more normal to the surface and presenting a decreased distance for the decelerated freestream to pass along the plume. There is supersonic flow in the wake, causing a narrowing of the subsonic region as is seen for the three nozzle, 30° nozzle canting, aftbody configuration. The wake is contained within the highest concentration of nodes in the mesh due to this decrease in extent of subsonic flow.

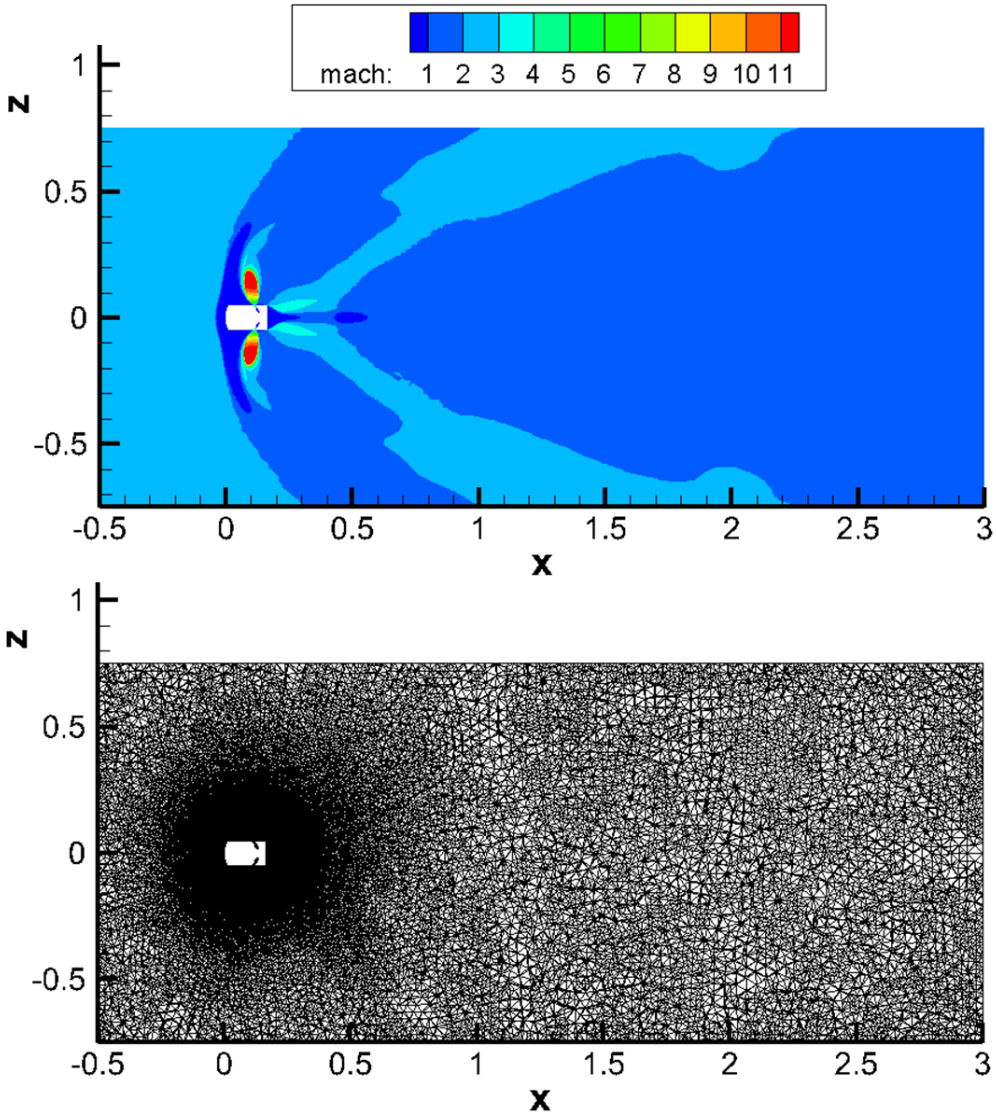

Figure 141: Full computational domain with C_T = 20 Mach contours (top) and computational mesh (bottom) for the six nozzle, 60° nozzle canting, aftbody configuration

6.4 Plume-Surface Interaction Effects

Varying the nozzle cant angle has a strong influence on the interaction of the barrel shock with the surface of the vehicle. This is illustrated in Figure 142 for C_T = 1 and C_T = 10 on the six nozzle aftbody configurations with both 30° and 60° nozzle canting. For C_T = 1, the plume expansion just outside of the nozzle exit is minimal for both configurations and the plume does not significantly interact with the surface on either configuration. This means that the aftbody surface is only seeing flow which originates with the decelerated freestream at the forebody of the vehicle. For C_T = 10, the difference in plume interaction is noticeable between the configurations. For the 30° nozzle canting geometry, the plume actually expands along the surface since the incidence angle between the nozzle axis and the surface tangent is only 30°. The underexpanded plume structure for this thrust condition results in a nozzle exit flow which expands faster than the surface relative to the nozzle axis. The plume flow passes along the surface, meaning that portions of the aftbody only see flow that originates in the nozzle. For 60° nozzle canting, the plume is directed sufficiently outboard that no expansion occurs along the surface. The aftbody for this case only sees flow that originates from the decelerated freestream.

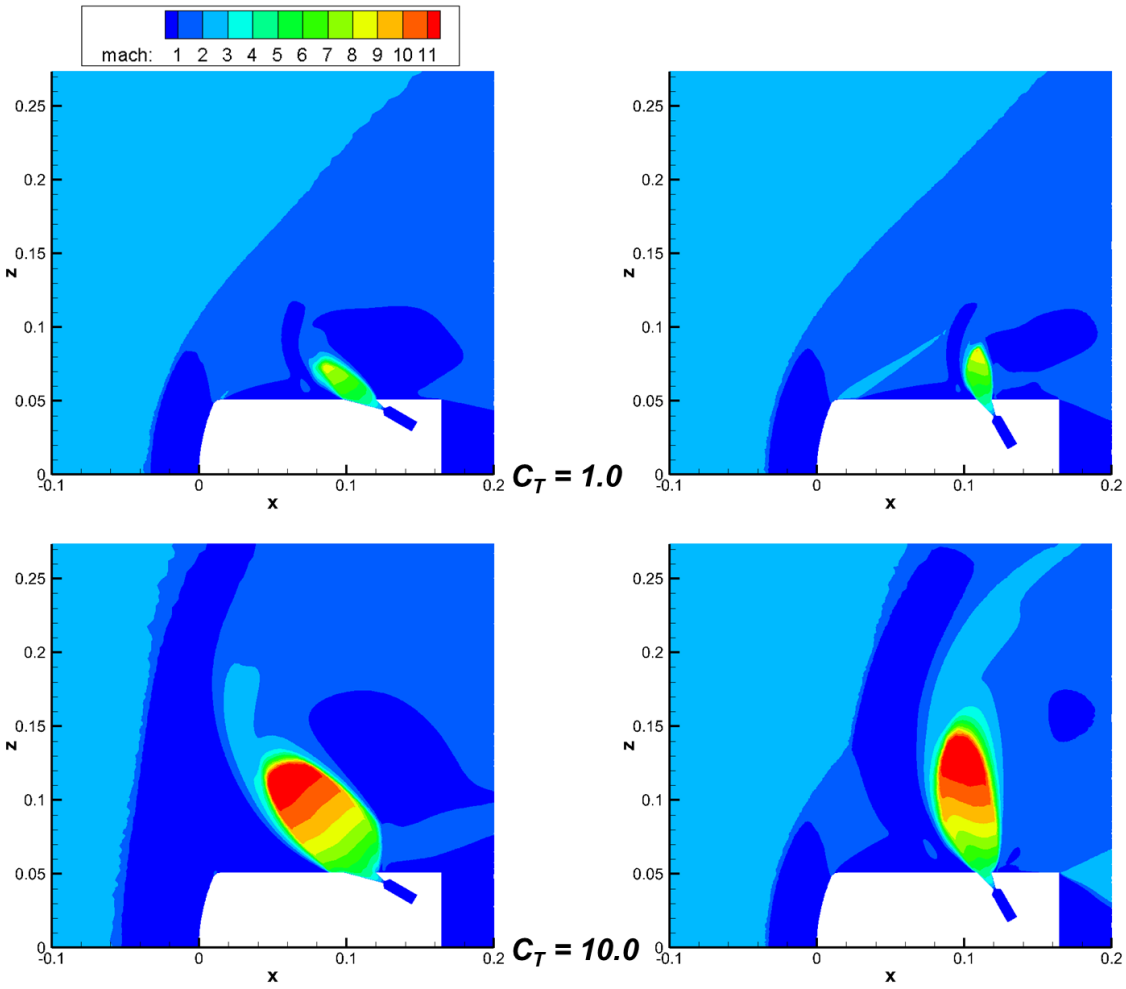

Figure 142: Comparison of flowfield structures between 30° nozzle canting (left) and 60° nozzle canting (right) for six nozzle aftbody configurations

The plume-surface interaction affects the pressure on the aftbody, as shown in Figure 143. For C_T = 1, where neither plume shows significant expansion along the surface, the high pressure created by the plume structure originates at the intersection of the nozzle exit and the surface. There is no separate region near the nozzle exit corresponding to the plume interaction. For C_T = 10, the 30° nozzle canting geometry shows a low pressure region around the nozzle exit corresponding to the area where the plume expands along the surface. The high pressure caused by the plume effective obstruction does not

originate until after this interaction zone. For the 60° nozzle canting geometry, no such low pressure region exists and the decelerated freestream pressure effects extend all the way to the nozzle exit. This region of plume interaction does not have a significant impact when the SRP system is assumed to have a cold gas exhaust and the flow is only assumed to be compressible without modeling any chemistry, as is run in these CFD simulations. However, the presence of this interaction region may have implications for hot gas simulations, where any thermodynamic effects caused by the plume flow on the aftbody could result in thermal design considerations being required for SRP configuration analysis.

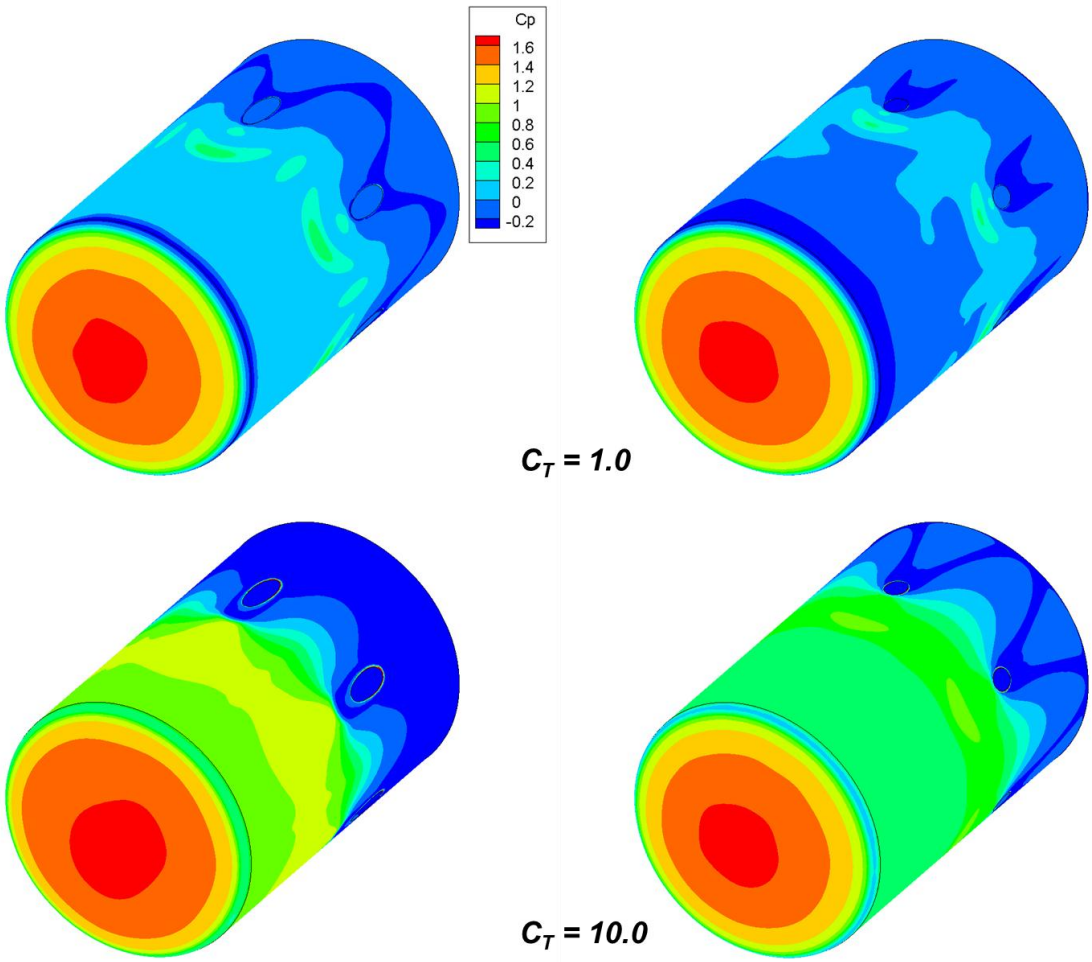

Figure 143: Comparison of pressure distributions between 30° nozzle canting (left) and 60° nozzle canting (right) for six nozzle aftbody configurations

6.5 Aerodynamic Variation with Aftbody Configuration

Total preservation of forebody surface pressure results in an appreciable aerodynamic drag coefficient for all thrust coefficients as shown in Figure 144. All three configurations show an increase in drag coefficient with C_T due to the creation of a more normal bow shock forward of the vehicle. Distributing thrust over more nozzles results in smaller plumes which have less interaction with the bow shock structure for a given

thrust coefficient, resulting in a decrease in C_D for configurations with more nozzles. At C_T = 1, increasing nozzle cant angle modifies the aftbody flow structure and creates a higher drag coefficient. For C_T values in the range of 4-10, the 30° nozzle canting configuration creates a higher drag due to an increase in the forebody contribution to drag that is not seen for these conditions on the 60° nozzle canting configuration.

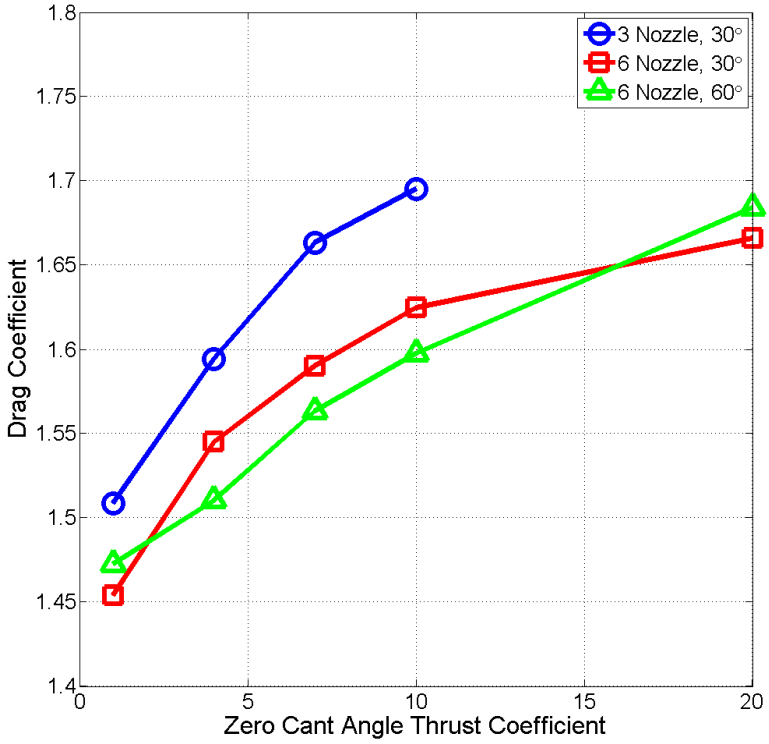

Figure 144: Effects of configuration on integrated drag coefficient for aftbody located nozzles

Total axial force coefficient as a function of thrust for each of the aftbody configurations is shown in Figure 145. The two configurations with 30° nozzle canting show similar performance, as the thrust losses are identical and the drag performance is similar between each configuration. The 3 nozzle configuration does have a slightly higher total

axial force coefficient for C_T values from 1-10, as the drag is higher for each of these cases. Increasing cant angle to 60° shows the impact of significant thrust losses as a decrease in the total axial force coefficient. This cant angle represents a 50% reduction in thrust contribution to deceleration, which is too large for the aerodynamic drag to overcome for increasing thrust coefficient. At C_T = 1, the loss in net deceleration is not as large for this configuration, as the drag is still a significant percentage of the total axial force and is capable of countering the increase in thrust losses.

Figure 145: Effects of configuration on total axial force coefficient for aftbody located nozzles

Using the same method described in Section 5.4.3 to determine propellant mass requirements and using the forebody 0° nozzle canting configuration as the baseline

performance, a comparison of the aftbody configuration propellant requirements can be found as shown in Figure 146. Both of the 30° nozzle canting configurations show a reduction in required propellant mass to achieve the same change in velocity due to the drag augmentation across the full range of thrust coefficients examined. The peak propellant savings is 20% of the baseline propellant mass near C_T = 3. The 60° nozzle canting configuration shows a higher propellant requirement for all thrust coefficients. This is due to the large thrust loss associated with the large cant angle, which is not overcome by the preserved aerodynamic drag. At C_T = 10, the 60° nozzle canting configuration requires 50% more propellant.

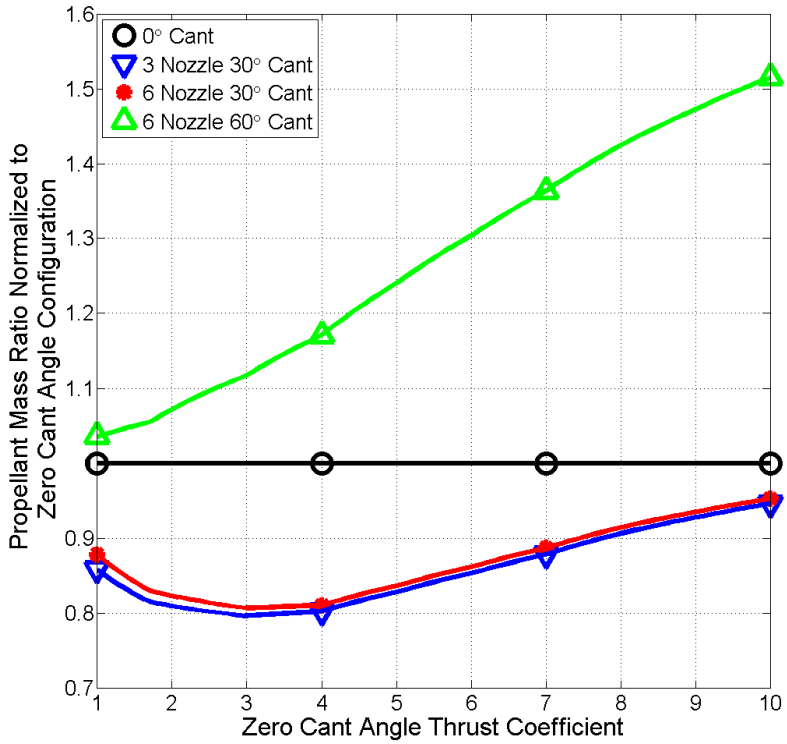

Figure 146: Variation in required propellant mass for aftbody located nozzle configurations relative to the 3 nozzle, 30° nozzle canting configuration performance at each C_T

6.6 Effect of Varying Mach Number

Holding thrust constant, for the same ratio of specific heats, and keeping the same nozzle design means that the plenum stagnation pressure does not vary. Keeping the freestream total pressure constant while increasing Mach number means that the freestream static pressure decreases, and the plume expansion for a given thrust value should change. Figure 147 shows these effects for the three nozzle, 30° nozzle canting, aftbody configuration. As Mach number is increased from 2-4, the plume expansion grows larger because the stagnation pressure of the region into which the nozzles exhaust decreases. Thus the plume, with unvaried nozzle exit conditions, will exhibit a larger underexpanded behavior. For this aftbody nozzle location, the plumes are directed significantly outboard, and as such do not shield the forebody. For all Mach numbers, the plumes expand along some distance of the surface, which increases with increasing Mach number, due to the incidence angle of the nozzle axis with the aftbody surface.

The surface pressure distribution varies significantly with freestream Mach number. Along the aftbody, the peak surface pressure forward of the nozzle exits remains nearly constant across all Mach numbers investigated; however, the pressure across the aftbody generally increases with Mach number. As plumes grow larger, the location of the peak surface pressure shifts forward due to increased plume expansion altering the location of the effective obstruction to the freestream flow. For $M_\infty = 4$, this peak surface pressure has shifted to the shoulder of the vehicle due to the plume extending further upstream than the vehicle forebody. Aft of the nozzle exits, the aftbody pressure also increases with increasing Mach number. This is also due to increased plume expansion and the variation in how plumes are affecting the aftbody flow paths of the decelerated freestream.

On the forebody, the pressure distribution increases with an increase in Mach number. For M_∞ = 3, much of the forebody has a pressure coefficient greater than the stagnation C_P value for the M_∞ = 2 case. Further increasing to M_∞ = 4 results in an even larger area exhibiting this high pressure region, as the plumes have modified the bow shock structure and forebody flow paths such that pressure is maintained in the decelerated freestream flow. The drag performance of this configuration at each Mach number is shown in Table 15, and confirms the results seen in the surface pressure distribution plots. The forebody contribution to the drag coefficient increases with increasing Mach number; however the increase in aftbody surface pressure along the aft face results in a decrease in the aftbody contribution to the drag coefficient. Overall, these two contributions effectively cancel each other and the total drag performance of the vehicle is similar across all Mach numbers. The data in Table 11 shows that C_T varies from 10 when M_∞ = 2 to 48.5 for M_∞ = 4 when thrust is held constant, meaning that the 30° cosine loss to the thrust performance is not balanced by drag preservation on the vehicle. For M_∞ = 4, the net deceleration force coefficient is 43.8, a 10% reduction from a condition where thrust provides all of the deceleration with no losses and no drag contribution.

Table 15: Aerodynamic drag performance for the three nozzle, 30° nozzle canting, aftbody configuration with varying freestream Mach number

	Mach 2	Mach 3	Mach 4
Forebody C_D	1.34	1.49	1.63
Aftbody C_D	0.36	0.19	0.14
Total C_D	1.70	1.68	1.77

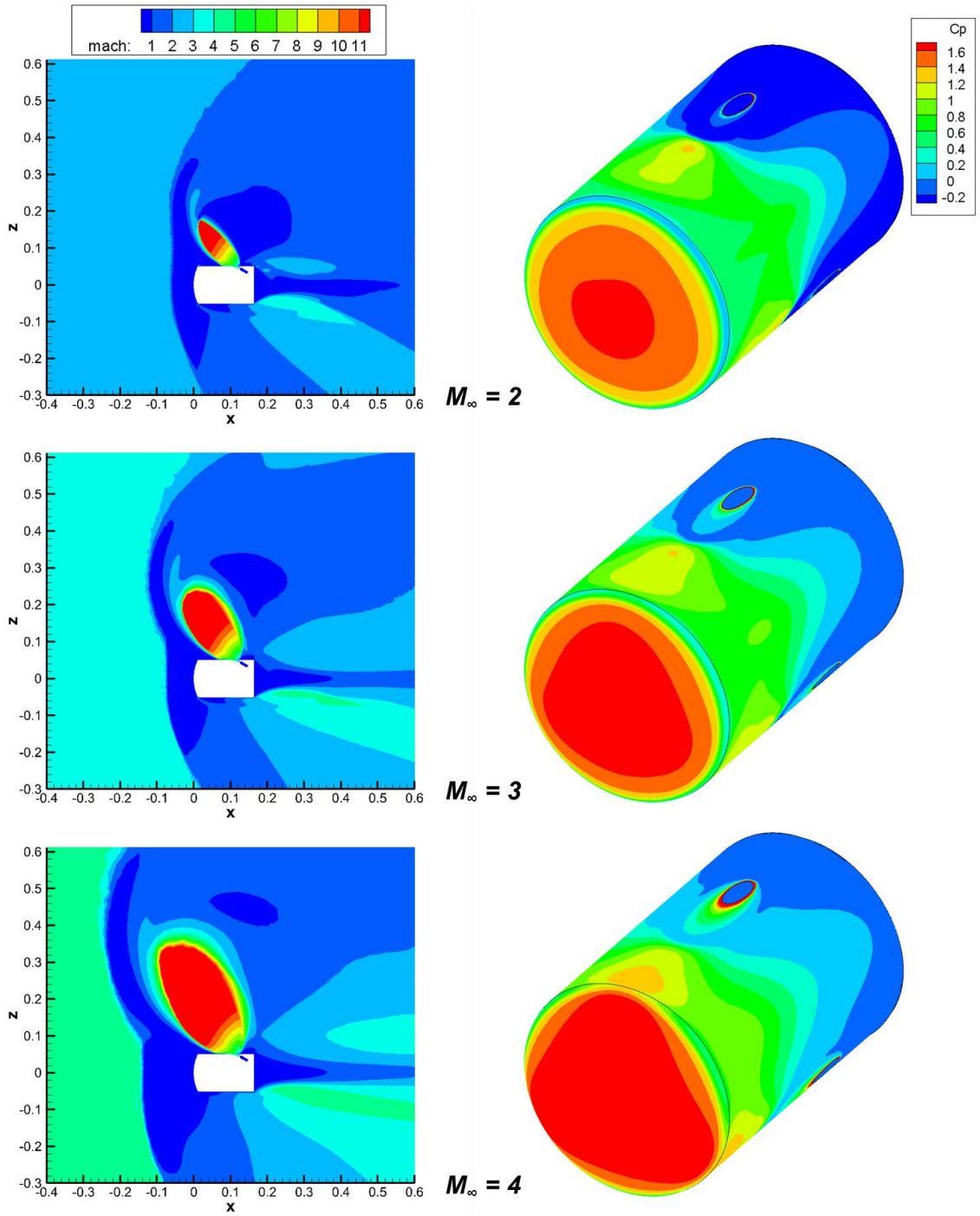

Figure 147: Variation in flowfield structure and surface pressure distribution with M_∞ for the three nozzle, 30° nozzle canting, aftbody configuration at constant thrust (C_T = 10 for M_∞ = 2)

CHAPTER VII

SUMMARY AND FUTURE WORK

7.1 Summary of Contributions

7.1.1 List of Contributions

This work focuses on analyzing the propulsive-aerodynamic interaction associated with a vehicle employing supersonic retropropulsion. Configuration effects on vehicle aerodynamic forces and moments are investigated using both an analytical approach to modeling the SRP flow field and a CFD approach to determine flowfield structure and propulsive-aerodynamic performance. The contributions of this thesis are:

1. **Development and validation of an analytical approach to modeling SRP flowfield structures**

   The developed analytical model leverages existing analytical approaches for various components of an SRP flow field to create an integrated, adapted model of the flow field for a given SRP configuration. Past analytical methods for plume terminal shock location, barrel shock, free shear layer, and bow shock structure have been adapted and expanded to capture SRP relevant flow conditions. A crossflow model has been developed to capture perturbations to individual plume structures. The analytical model has been validated against eight vehicle and nozzle configurations using CFD results as validation data.

2. **Determine the effects of nozzle canting for forebody located nozzles on the propulsive-aerodynamic interaction of an SRP system**

   CFD has been used to analyze the effects of nozzle cant angle on plume and bow shock structure for forebody located nozzles. The propulsive-aerodynamic interaction has also been examined, including both the variation in total deceleration force and static pitch stability for varying nozzle cant angle. The propellant mass impact of each configuration has been compared to a baseline configuration defined to be the computational results for a model based on a three nozzle wind tunnel experimental configuration. This analysis shows that modest nozzle cant angles can result in a lower propellant mass requirement for a similar final mass.

3. **Determine the effects of aftbody located nozzles on SRP performance by varying the number of nozzles and nozzle cant angle**

   CFD has also been used to analyze the effects of distributing thrust over varying number of nozzles for configurations where the nozzles are located on the aftbody of a slender entry vehicle. Two nozzle cant angles have been investigated to assess the implications of plume-surface interaction on SRP performance. The propulsive-aerodynamic interaction for these configurations has been analyzed to determine the variation in total deceleration force and static pitch stability with configuration, noting that aerodynamic drag is augmented by aftbody located nozzles for the thrust conditions examined. Propellant mass impact of each configuration has been compared to the same baseline configuration as for the

forebody located nozzles; showing that the drag augmentation present in aftbody located nozzles at 30° nozzle canting reduces the propellant mass required for deceleration across all thrust conditions examined assuming a similar final mass.

4. **Create guidelines for generating computational meshes for SRP configurations using results from the analytical model**

   Grid convergence studies provide insight into the effects of exit plane location and cell resolution on modeling SRP flow fields and show that the computational domain must be sufficiently large to capture the subsonic region of the wake. Analytical predictions of the plume and bow shock structure have been used to set boundaries for setting cell resolutions within the computational domain by defining regions of interest in the flow field. The analytical free shear layer model has been used to guide required cell sizes within the plume region of the flow field for capturing relevant SRP plume flow features.

7.1.2 Development of the Analytical Model for SRP Flow Fields

The analytical model developed in this dissertation creates a model of an SRP flow field by employing a piecewise construction of the primary flow field components. First, the terminal shock location for each plume in the configuration is found using the equations developed by Sibulkin and Gallaher [52] for radial jet flow emanating from a common source point. Because this model assumes the plume exhausts into a vacuum, additional equations are added to perform a stagnation pressure balance between the decelerated freestream flow through an assumed normal bow shock and the decelerated jet flow

through a normal terminal shock. This sets the terminal shock conditions, including the density ratio which is required for the Sibulkin and Gallaher equation for determining terminal shock standoff distance from the nozzle exit.

Next, the equations developed by Charwat [51] are used to define the barrel shock for each nozzle. A Prandtl-Meyer expansion at the nozzle exit is used to calculate the flow conditions along the barrel shock, which allows for calculation of the barrel shock radius as a function of distance along the nozzle axis away from the intersection of the axis with the vehicle surface. The Charwat model assumes an infinitely long plume, so additional steps are taken to include the fact that an SRP plume actually terminates with a shock. The barrel shock is truncated at the terminal shock location, and a mass flow rate is calculated through both the barrel shock and the jet terminal shock to scale the plume such that this outward flow rate balances with the input mass flow rate in the plenum of the nozzle.

A free shear layer is calculated along each barrel shock using the turbulent boundary equations for a flat plate, with the barrel shock modeled as a solid boundary. Because the plume shape is rounded and not a flat plate, the arc length of the plume is used as the distance traveled by the flow, and the boundary layer thickness is applied normal to the curvature of the shock.

To calculate the deflection of the plume due to the local crossflow created by the decelerated freestream flowing along the vehicle surface, the subsonic panel method described by Anderson [90] has been used to calculate pressure and velocity along the vehicle surface. As this method requires a subsonic freestream, the actual supersonic freestream flow is assumed to decelerate through a normal shock, with the resulting

subsonic conditions behind the shock used as an effective freestream for the subsonic panel method. To calculate the deflection angle, the resulting surface velocity from the subsonic panel method is used in conjunction with the calculated nozzle exit velocity to create a velocity triangle approximation to the plume deflection angle.

For definition of the bow shock structure, the shape equations of Van Dyke [62] are applied for a hemispherical obstruction. In order to apply these equations, each plume is treated as an independent obstruction in the flow field, and an effective hemispherical obstruction is created for each plume with radius equal to the diameter of the scaled terminal shock and a center point located at the most outboard extent of the plume structure. This hemispherical obstruction is used to define a local bow shock for each plume using Van Dyke's approach. To create the full three-dimensional shock structure, all of the local bow shocks are combined assuming that the furthest offset shock from the vehicle at a radial and angular location relative to the vehicle axis is the shock that will form in the flow field.

7.1.3 Comparison of the Analytical Predictions with CFD Solutions

Across all eight configurations, the axial and radial extents of the plume structure are generally well captured by the components of the barrel shock model. The mass flow rate scaled barrel shock captures the expansion diameter of the plume as a function of distance from the nozzle exit for all geometries, as long as the plumes are essentially independent of each other. The crossflow angle calculation agrees well for configurations where the incidence angle between the nozzle axis and surface is small, and becomes less accurate as the nozzle exhausts more normal to the surface. The analytical plume model

is not capable of capturing plume coalescence or plume flow along the surface because the barrel shock method assumes an axisymmetric plume exhausting into a stagnation region without any perturbations to the jet flow.

The bow shock for all configurations with independent plume structures consistently overpredicts the shock standoff distance from the vehicle. The assumption of a hemispherical obstruction overpredicts the out of plane expansion of each plume, causing an increase in bow shock standoff distance in the out of plane direction. For the purposes of providing an initial estimate of an SRP flow field, overprediction of bow shock location is conservative as the actual plumes will not cause as large of an effect on the flow structure. Across all seven multiple nozzle configurations examined, the bow shock prediction is consistently conservative, indicating that this property of the analytical model should be configuration independent, so long as the plumes do not coalesce.

Overall, the analytical model is most valid for the range of configurations investigated where the incidence angle of the nozzle axis with the vehicle surface is not low enough to cause significant scarfing and not high enough to exhaust nearly normal to the surface. This condition occurs for the 0°, 10°, and 20° forebody nozzle canting configurations, and the six nozzle, 60° nozzle canting aftbody configuration. The 30° forebody nozzle canting configuration shows significant interaction between the plume flow and the shoulder expansion that is not captured in the analytical model. The two aftbody configurations with 30° nozzle canting have significantly scarfed nozzles, while the analytical model assumes an axisymmetric plume which will not form for a scarfed nozzle. Even for these configurations where the analytical model is less valid, portions of

the flow are still well captured, such as the axial plume extent for the 30° forebody configuration or the plume radial extent for the 30° aftbody configurations.

7.1.4 The Effect of Nozzle Canting for Forebody Located Nozzles

For three nozzles located on a 60° sphere-cone employing SRP, the cant angle of the nozzles has a significant impact on the propulsive-aerodynamic interaction created by an SRP system. For low thrust conditions, where the plumes are small due to being slightly underexpanded, the aerodynamic performance is nearly the same across nozzle cant angles from 0°-30°. There is not a significant decrease in aerodynamic drag performance for these cases, and the vehicle's static pitch stability characteristics are preserved, as the angle of attack solutions for the 30° nozzle canting show a negative slope of pitching moment coefficient with respect to angle of attack regardless of near-axial CG location along the vehicle axis. The presence of an SRP system also results in the trim capabilities of the vehicle being insensitive to near-axial CG location along the axis. As long as the CG is located near the symmetry axis of the vehicle, the entry system will be able to reach trim conditions.

For higher thrust conditions, the propulsive-aerodynamic interaction is strongly dependent on nozzle cant angle. Increasing the canting of each nozzle results in the jet flow being directed more outboard and the surface pressure on the forebody is preserved to a greater degree. While 0° nozzle canting shows no aerodynamic drag for C_T = 10, 30° nozzle canting shows 72% of the baseline no-thrust aerodynamic drag being preserved on the forebody. For both the 10° and 30° nozzle canting configurations, the static pitch stability characteristics are also preserved. Angle of attack solutions show a negative

slope for the pitching moment coefficient as a function of angle of attack regardless of near-axial CG location. The 30° nozzle canting configuration has a larger magnitude for $C_{M\alpha}$ than the 10° nozzle canting configuration at C_T = 10, indicating that the reduced pressure for lower cant angles causes a reduction in the pitch stability derivative. Both configurations also show an insensitivity to axial CG location for trim capability, as the thrust provided by the nozzles generates sufficient moment to reach trim conditions regardless of aerodynamic moment contributions. The 10° nozzle canting configuration provides less sensitivity than the 30° nozzle canting configuration at C_T = 10, since more of the thrust is directed along the vehicle axis and creates a larger pitch moment.

There is a tradeoff for increased aerodynamic drag performance in that canting the nozzles reduces the thrust contribution to deceleration due to some thrust force being directed outboard. For C_T values from 1-10, the 10° and 20° nozzle canting configurations show a higher total deceleration force coefficient than the 0° and 30° nozzle canting configurations. This increase in deceleration force coefficient results in a lower propellant requirement to achieve a desired change in velocity during SRP operation assuming a constant final mass. For thrust increases beyond the limit investigated in this dissertation, the cosine losses due to nozzle canting will eventually be larger than what the aerodynamic drag preservation can provide, meaning that there should be a transition point where nozzles exhausting directly into the freestream provides the highest total deceleration force, even with a total loss in aerodynamic drag.

7.1.5 The Effect of Canting and Number of Nozzles for Aftbody Nozzles

Nozzles located on the aftbody of an entry vehicle create a much different flow field than is seen for forebody located nozzles. Aftbody nozzles exhaust into a region of the flow field which does not result in a strong interaction between the plume flow and the bow shock. For three nozzles with a 30° cant angle, the forebody surface pressure is preserved regardless of thrust coefficient across C_T = 1-10, and the aerodynamic drag coefficient increases slightly with thrust coefficient. For C_T = 10, CFD solutions at angles of attack show that there is a transition from static pitch stability to instability depending on the location of the CG along the vehicle axis. Locations near the nose exhibit static pitch stability, while locations further aft exhibit pitch instability. The high thrust created by the C_T = 10 condition provides sufficient control authority to make trim capabilities of the vehicle insensitive to CG location along the axis for this configuration.

Increasing the number of nozzles to six while keeping the cant angle equal to 30° results in a lower thrust provided by each nozzle for a given total thrust coefficient as compared to the three nozzle configuration. Smaller thrust requirements for a nozzle create a smaller plume due to the variations in nozzle exit pressure, which further impacts the propulsive-aerodynamic interaction of the SRP system. For C_T = 1-10, the inboard bow shock structure is nearly undisturbed, the forebody surface pressure is preserved across all thrust coefficients, and the aerodynamic drag for each thrust condition increases with increasing C_T. The plumes still expand along the aftbody surface, creating a rise in pressure along the aftbody forward of the nozzles. The static pitch stability of this configuration is similar to the three nozzle configuration in that there is a transition from static stability to instability as CG location varies along the axis. The location at

which this transition occurs is slightly further forward for the six nozzle configuration than the three nozzle configuration. The trim capabilities are similar between the two configurations, as the six nozzle configuration also shows insensitivity to axial CG location.

The last aftbody configuration examined in this dissertation has six nozzles with a 60° cant angle for each nozzle. This directs the jet flow more outboard, resulting in even less interaction between the plumes and the bow shock than is seen for lower cant angles, and the plume-surface interaction is eliminated. The increase in cant angle results in significant cosine losses to the thrust contribution to deceleration as compared to the 30° nozzle canting configurations, and the similar aerodynamic drag performance means that the 60° nozzle canting geometry provides a lower total deceleration force for a given thrust level. However, there is a benefit to increased nozzle canting in static pitch stability performance, as the transition point from static pitch stability to instability shifts further aft along the vehicle axis than is seen for either aftbody configuration with 30° nozzle canting.

Figure 148 shows the propellant mass performance for all seven multiple nozzle configurations, as detailed in Figure 112 and Figure 146 for each class of configuration. In general, aftbody nozzle locations appear to show great promise including significant performance benefits in Mars SRP applications by decreasing the propellant required to achieve a given change in velocity assuming a similar final mass for each configuration.

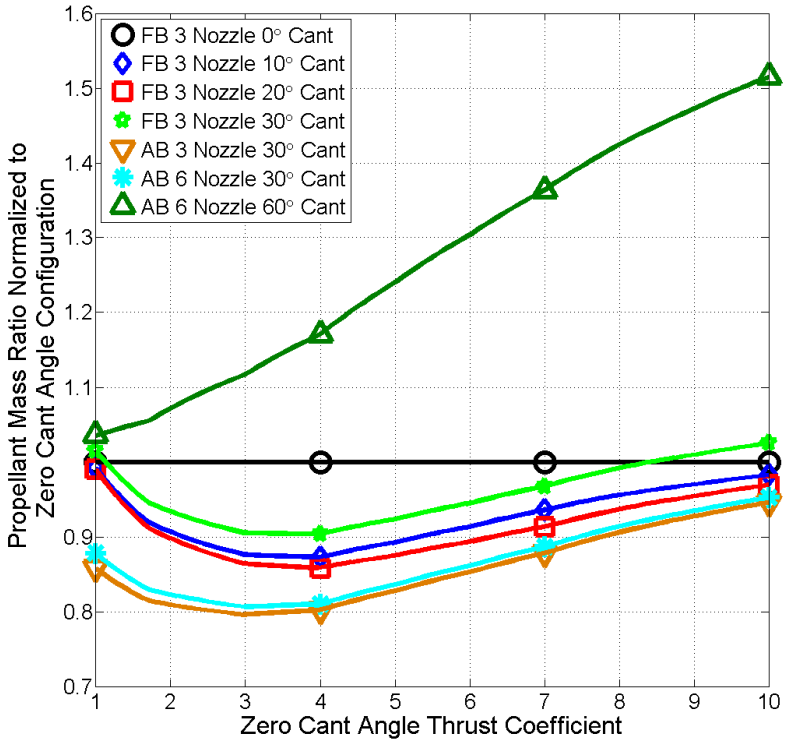

Figure 148: Required propellant mass comparison of the seven multiple nozzle configurations

7.1.6 Use of the Analytical Model in System Design and CFD Simulations

The analytical model provides two primary uses for SRP analysis at various times during system design. Early in the design phase, when configuration trades are being performed, the analytical model provides rapid estimates of flowfield structure for configurations of interest, providing insight into anticipated SRP performance. Investigating perturbations to the bow shock structure allows for qualitative assessment of aerodynamic performance for varying configurations as less perturbation to the inboard bow shock has been shown to show similar drag performance as a no thrust condition in this dissertation. Additionally, the plume structure predictions can indicate possible plume-surface interaction for a given nozzle cant angle. If the predicted barrel shock significantly

intersects the vehicle outer mold line, then plume-surface interaction is more likely to occur for that system and increased investigation would be required.

Later in the design phase, when higher fidelity, time intensive CFD analyses are being performed, the analytical model can be used to guide the creation of a computational mesh for a given configuration. Knowledge of where the plumes should be located allow for definition of boundaries within the computational domain that should contain plume flow for each nozzle. Estimates of the shear layer thickness provide upper bounds on cell size for the plume region that should be sufficient to capture key flow features in the jet flow. Knowledge of bow shock structure prior to grid generation guides the location of the freestream boundaries required to capture the entire SRP flow field. The transition point from a bow shock to a Mach wave sets an outboard distance required to contain the shock structure, and the standoff distance of the bow shock prediction sets the distance upstream at which the freestream inlet plane needs to be located to contain the shock structure. Creating an initial grid which is capable of accurately modeling SRP flow fields reduces the analysis time required for CFD by reducing the number of grids required to generate a grid converged solution. For more complex CFD methodologies, such as grid adaptation, accurately capturing flow features on the base grid provides a better initial solution to the adaptation process. For the three forebody located nozzles with positive nozzle canting geometries and three aftbody located nozzle geometries, using the analytical model to guide grid generation shows that that subsequent grid is sufficient for modeling the SRP flows at the thrust levels investigated.

7.2 Future Work

The work presented in this dissertation has shown that SRP performance is a strong function of vehicle and nozzle configuration. The eight configurations examined are a limited subset of possible configurations. Establishing that the trends in SRP performance found in this investigation extend to other possible configurations would further the understanding of SRP systems. The developed analytical model shows overall good agreement with the resulting flow fields for these configurations at varying thrust levels; however, some areas of improvement to the model have been identified as potential avenues of investigation for future analyses.

7.2.1 Further Improvements in the Analytical Model

While the analytical model developed in this dissertation is capable of modeling SRP flow fields for a variety of configurations, there are areas of improvement that are evident in the validation against CFD solutions. One such area of improvement is the crossflow deflection angle calculation. In the analytical model, this angle is approximated using a velocity triangle created by the nozzle exit flow and the surface flow velocity that would exist if no thrust is present. The jet flow velocity vector is independent of nozzle thrust, as the expansion through the nozzle diverging section does not vary with jet total pressure as long as the plume is underexpanded. Comparisons for the 20° and 30° forebody nozzle canting geometries show that there appears to be a thrust dependency to the crossflow deflection angle, as the agreement in direction of jet flow between the analytical result and CFD solution worsens with increasing thrust. As the incidence angle between the nozzle axis and the surface increases such that the nozzle exhausts more normal to the

surface, such as for the 30° forebody nozzle canting configuration, the crossflow calculation underpredicts the actual deflection angle in the CFD solutions. This indicates that there may be additional factors that influence crossflow other than relative velocities, such as momentum exchange along the plume boundary and pressure effects from the presence of other plumes in the flow field modifying the flow paths of the decelerated freestream flow.

The CFD solutions for plumes created by the multiple nozzle configurations, as long as the plumes do not coalesce, show a plume structure that is more complex than the axisymmetric barrel shock assumed by the analytical model. The inboard barrel shock is more compressed by the flow approaching the plume, resulting in an asymmetric plume and an overprediction of the barrel shock by the analytical model. Further understanding of the processes affecting the plume structure as a function of orientation of the three-dimensional barrel shock to the flow field may allow for further analytical methods to capture this flow feature by varying the boundary conditions along the plume boundary as a function of the location around the three-dimensional plume.

The bow shock locations created by the analytical model show a consistent overprediction as compared to the CFD solutions. This is partially due to the underprediction of crossflow angle, as directing the plume more outboard would subsequently reduce the bow shock standoff distance. Another source of this overprediction is the assumption of a hemispherical obstruction created by the decelerated plume flow. Figure 149 shows two thrust conditions on the three nozzle, 0° nozzle canting, forebody configuration with CFD streamlines shown to highlight the effective obstruction of the plume flow. The streamlines do create a nearly hemispherical

obstruction; however, the center of the computational obstruction is further outboard than the assumed center along the analytical barrel shock. The analytical model assumes the turning radius of the flow at the hemispherical center is zero, while the CFD solutions show that there is some nonzero turning angle that shifts the hemispherical center outboard. The size of the boundary between the decelerated freestream and jet flows is also different between the two solutions. The local perturbation to the bow shock assumed by the analytical model appears to be reasonable; however, modifications to the effective obstruction and resultant bow shock could show better agreement with the flow field seen in the computational solutions.

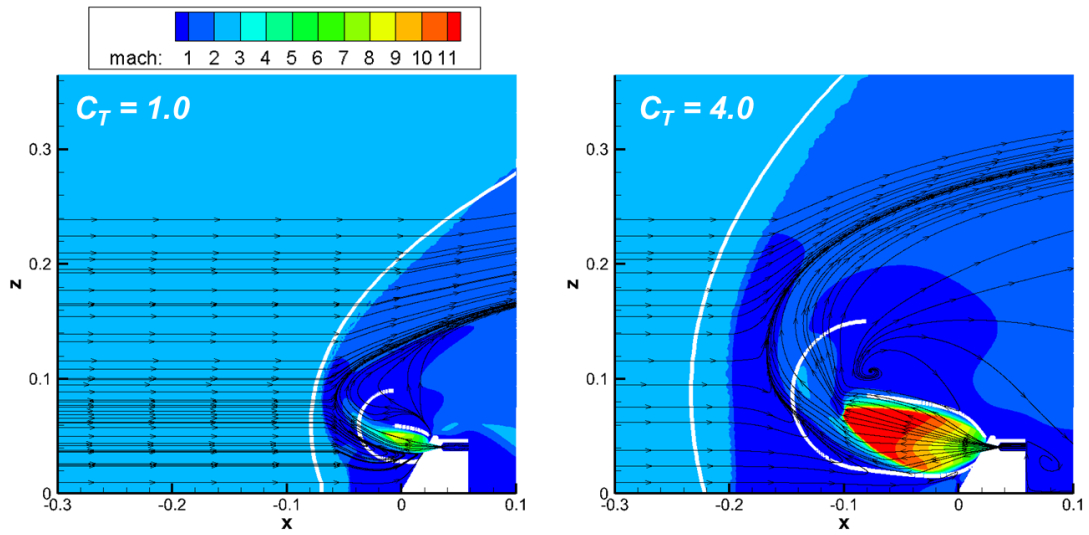

Figure 149: Comparison of assumed hemispherical obstruction with CFD streamlines for the three nozzle, 0° nozzle canting, forebody configuration

The bow shock predictions in the analytical model do not account for any smoothing of the transition from the local perturbation from each plume that is seen in the CFD solutions. As thrust increases for many of the configurations investigated, the

computational bow shocks show a nearly normal shock with a smooth shock shape. The analytical model creates kinks in the shock structure rather than a smooth shock, due in part to the assumption of a hemispherical obstruction for each plume rather than a continuous obstruction containing the plume boundaries, decelerated jet flows, and the vehicle. Improvements in the analytical modeling of the physics governing bow shock formation around the full obstruction created by the vehicle and plumes should better capture these features.

The developed analytical model does not attempt to capture the surface pressure effects caused by an input SRP configuration. Using the analytical predictions of the plume and shock structure to define regions on the vehicle which exhibit varying pressure effects, similar in concept to the work performed by Skeen [REF] as described in Section 1.3.3, may allow for prediction of surface pressures and their resulting aerodynamic forces and moments. This would further allow the analytical model to be used as a quantitative SRP configuration screening tool as the propulsive-aerodynamic interaction would be modeled for use in performance analyses.

7.2.2 Performance Characterization of SRP Configurations

The CFD results used for validation of the analytical model in this thesis have been generated using a steady-state approach to modeling the SRP flow physics. To investigate a higher fidelity, time accurate solution with CFD, additional grid resolution and input parameters are required. Examining the extensibility of the analytical model to providing insight into the required grid resolutions for these conditions in addition to determining if the predicted steady state flow field provides reasonable boundaries within the flow field

for capturing time varying plume and shock structures would provide further support for using the analytical model as a precursor to CFD analysis.

The thrust conditions and nozzle design for each of the validation geometries with nozzle canting are kept consistent with those of the three nozzle, 0° nozzle canting, forebody configuration. The steady-state CFD solutions provide aerodynamic performance data as a function of thrust coefficient and configuration; however, the impacts of these aerodynamic performance trends on vehicle performance are only examined at constant altitude deceleration as part of this thesis. Integrating the aerodynamic drag and pitching moment variation with thrust coefficient and freestream conditions for canted nozzle geometries with a trajectory simulation will provide further insight into the effects that configuration has on overall performance of the entry system throughout the EDL timeline. Propellant mass, deceleration timeline, and landing location are all dependent on the thrust level of the system. The aftbody configurations in particular show appreciable drag preservation, even for high thrust coefficients, that may have positive impacts on required propellant mass and system performance beyond what has currently been assumed for SRP systems.

Design of an SRP system will involve many variables, including number of nozzles, their location and cant angle, aeroshell geometry, and nozzle design to achieve required thrust levels. Preliminary investigation of these parameters with CFD simulations has been performed in this dissertation to demonstrate that configuration has a significant impact on the propulsive-aerodynamic interaction inherent to an SRP system. Studying additional configurations will extend the knowledge of performance trends of SRP with respect to these parameters. For example, forebody surface pressure is dependent on the

angle of the surface to the freestream flow vector, where sharper geometries exhibit lower pressures at zero angle of attack. The three aftbody configurations investigated in this dissertation all show an increase in forebody pressure for a blunt capsule forebody. If this trend is consistent regardless of forebody shape, then shapes which nominally show a lower drag coefficient may be capable of increased aerodynamic drag performance through modification of the shock structure by an SRP system.

7.2.3 Extension to Flight-Like Configurations

All of the configurations investigated in this dissertation are subscale models of the size that would be used for wind tunnel experiments. Examining the trends in flowfield structure and aerodynamic performance for larger vehicles with larger nozzles would further the understanding of the extensibility of SRP modeling to flight-sized vehicles. Additionally, with SRP being planned for use at Mars employing combustion engines, investigating the performance in atmospheric conditions other than air with nozzles exhausting combustion products rather than a cold gas will help determine if the aerodynamic trends seen for subscale models is applicable to a flight system. The analytical model is developed such that aeroshell geometry, freestream flow properties, and nozzle flow properties can be set as input conditions, meaning that analytical analysis of flight-like configurations is possible. By using one specific heat ratio representing jet exhaust composition for all calculations involving jet flow, and another specific heat ratio for all calculations involving the freestream flow, the analytical model could be used to predict flows with multiple gas compositions, though the accuracy of the model for these types of flows would need to be determined. Higher fidelity approaches to modeling SRP

performance under these configurations will depend on CFD and wind tunnel capabilities and the required performance defined by SRP system design. If the trends for realistic gas compositions are similar to those seen in analysis for a freestream of air with a cold gas exhaust, then the results of this dissertation and other SRP investigations can be used as performance data for a flight-like configuration. The analysis methodology developed in this dissertation can be adapted to other flow conditions as well if the aerodynamic performance is strongly dependent on atmospheric conditions during actual flight.

APPENDIX A: PUBLICATIONS

Journal Articles

Published:

1. Cordell, C. E., Jr., and Braun, R. D., "Steady State Modeling of Supersonic Retropropulsion Plume Structures," *Journal of Spacecraft and Rockets*, Vol. 50, No. 4, 2013, pp. 763-770.
2. Korzun, A. M., Cordell, C. E., Jr., and Braun, R. D., "Computational Aerodynamic Predictions of Supersonic Retropropulsion Flowfields," *Journal of Spacecraft and Rockets*, Vol. 50, No. 5, 2013, pp. 950-960.

Planned:

3. "An Analytical Approach to Modeling Supersonic Retropropulsion Flow Field Components" To be submitted to *Journal of Spacecraft and Rockets* by April 2014.

   This paper will discuss the full flow field model, including the barrel shock, crossflow deflection, and bow shock structure. Validations against various configurations will be used to demonstrate the applicability of the model.

4. "Effect of Nozzle Canting on Supersonic Retropropulsion Performance for Forebody Located Nozzles" To be submitted to *Journal of Spacecraft and Rockets* by December 2013.

   This paper will discuss the trends seen in SRP performance for the forebody located nozzle configurations with varying nozzle cant angle.

CFD solutions for varying thrust coefficients will be discussed for flowfield structure, and the aerodynamic drag and pitching moment variations will be discussed.

5. "Effect of Aftbody Located Nozzles on Supersonic Retropropulsion Flowfield Structures and Aerodynamic Performance" To be submitted to *Journal of Spacecraft and Rockets* by February 2014.

   This paper will discuss the trends seen in SRP performance for the aftbody located nozzle configurations with varying number of nozzles and nozzle cant angle. CFD solutions for varying thrust coefficients will be discussed for flowfield structure, and the aerodynamic drag and pitching moment variations will be discussed.

Conference Papers

Published:

1. Korzun, A. M., Cordell, C. E., Jr., and Braun, R. D., "Comparison of Inviscid and Viscous Aerodynamic Predictions of Supersonic Retropropulsion Flowfields," AIAA 2010-5048, June 2010.
2. Cordell, C. E., Jr., Clark, I. G., and Braun, R. D., "CFD Verification of Supersonic Retropropulsion for a Central and Peripheral Configuration," IEEEAC Paper 2011-1190, March 2011.

Accepted:

3. Cordell, C. E., Jr., and Braun, R.D., "An Analytical Approach to Modeling Supersonic Retropropulsion Flow Field Components," AIAA Science and Technology Forum and Exposition 2014, January 2014.

APPENDIX B: BOW SHOCK BLUNTNESS DATA

This table provides the shock bluntness data for an assumed hemispherical obstruction for varying Mach number and ratio of specific heats as calculated in Ref. [62]. For a given freestream Mach number and γ value, the tabulated data is interpolated to define the variable B_S in the analytical model.

Table 16: Shock bluntness data for varying gamma and Mach number [62]

Mach Number	$\gamma = 1$	$\gamma = 1.4$	$\gamma = 1.67$
1.2	-3.28	-3.32	-3.30
1.5	-0.69	-0.73	-0.71
2	0.01	0.08	-0.06
3	0.35	0.22	0.25
4	0.51	0.35	0.38
6	0.67	0.43	0.47
10	0.80	0.46	0.49

REFERENCES

[1] Korzun, A. M., Cordell, C. E. Jr., and Braun, R. D., "Comparison of Inviscid and Viscous Aerodynamic Predictions of Supersonic Retropropulsion Flowfields," AIAA Paper 2010-5048, July 2010.

[2] Braun, R. D., and Manning, R. M., "Mars Exploration Entry, Descent, and Landing Challenges," *Journal of Spacecraft and Rockets*, Vol. 44, No. 2, 2007, pp. 310-323. doi: 10.2514/1.25116

[3] Zang, T. A., et al., "Overview of the NASA Entry, Descent, and Landing Systems Analysis Study," AIAA Paper 2010-8649, August 2010.

[4] Adler, M., Wright, M., Campbell, C., Clark, I., Engelund, W., and Rivellini, T., "Entry, Descent, and Landing Roadmap Technology Area 09," NASA, November 2010.

[5] Sutton, G. P., and Biblarz, O., *Rocket Propulsion Elements*, 8th ed., Hoboken: Wiley, 2010, pp. 69-72. Print.

[6] Chang, I. S., and Chow, W. L., "Mach Disk from Underexpanded Axisymmetric Nozzle Flow," *AIAA Journal*, Vol. 12, No. 8, 1974.
doi: 10.2514/3.49415

[7] Peters, C. E., and Phares, W. J., "The Structure of Plumes from Moderately Underexpanded Supersonic Nozzles," AIAA Paper 70-229, January 1970.

[8] Wilkes, J. A., Glass, C. E., Danehy, P. M., and Nowak, R. J., "Fluorescence Imaging of Underexpanded Jets and Comparison with CFD," AIAA Paper 2006-910, January 2006.

[9] Abbett, M., "Mach Disk in Underexpanded Exhaust Plumes," *AIAA Journal*, Vol. 9, No. 8, 1971.
doi: 10.2514/1.48335

[10] Jarvinen, P. O., and Adams, R. H., "The Aerodynamic Characteristics of Large Angled Cones with Retrorockets," NAS 7-576, February 1970.

[11] Vogler, R. D., "Surface Pressure Distributions Induced on a Flat Plate by a Cold Air Jet Issuing Perpendicularly from the Plate and Normal to a Low-Speed Free-Stream Flow," NASA TN D-1629, March 1963.

[12] Shaw, C. S., and Margason, R. J., "An Experimental Investigation of a Highly Underexpanded Sonic Jet Ejecting from a Flat Plate into a Subsonic Crossflow," NASA TN D-7314, December 1973.

[13] Fearn, R. L., and Weston, R. P., "Induced Pressure Distribution of a Jet in Crossflow," NASA TN D-7916, July 1975.

[14] Demuren, A. O., "Characteristics of 3D Turbulent Jets in Crossflow," NASA-TM-104337, April 1991.

[15] Orth, R. C., Schetz, J. A., and Billig, F. S., "The Interaction and Penetration of Gaseous Jets in Supersonic Flow," NASA CR-1386, July 1969.

[16] Viti, V., Neel, R., and Schetz, J. A., "Detailed Flow Physics of the Supersonic Jet Interaction Flow Field," *Physics of Fluids*, Vol. 21, No. 4, 2009, pp. 1-16.
doi: 10.1063/1.3112736

[17] Edquist, K. T., et al., "Development of Supersonic Retro-Propulsion for Future Mars Entry, Descent, and Landing Systems," AIAA Paper 2010-5046, July 2010.

[18] Korzun, A. M., Braun, R. D., and Cruz, J. R., "Survey of Supersonic Retropropulsion Technology for Mars Entry, Descent, and Landing," *Journal of Spacecraft and Rockets,* Vol. 46, No. 5, 2009, pp. 929-937.
doi: 10.2514/1.41161

[19] Gnoffo, P. A., "Planetary-Entry Gas Dynamics," *Annual Review of Fluid Mechanics,* Vol. 31, 1999, pp. 459-494.

[20] Love, E. S., and Grigsby, C. E., "Some Studies of Axisymmetric Free Jets Exhausting from Sonic and Supersonic Nozzles into Still Air and Into Supersonic Freestreams," NACA RM-L54L31, May 1955.

[21] Love, E.S., Grigsby, C. E., Lee, L. P., and Woodling, M. J., "Experimental and Theoretical Studies of Axisymmetric Free Jets," NASA TR R-6, 1959.

[22] Charczenko, N., and Hennessey, K. W., "Investigation of a Retrorocket Exhausting from the Nose of a Blunt Body into a Supersonic Freestream," NASA TN D-751, September 1961.

[23] Venukumar, B., Jagadeesh, G., and Reddy, K. P., "Counterflow Drag Reduction by Supersonic Jet for a Blunt Body in Hypersonic Flow," *Physics of Fluids*, Vol. 18, 2006.
doi:10.1063/1.2401623

[24] Romeo, D. J., and Sterrett, J. R., "Exploratory Investigation of the Effect of a Forward Facing Jet on the Bow Shock of a Blunt Body in a Mach Number 6 Free Stream," NASA TN D-1605, February 1963.

[25] Barber, E. A., "An Experimental Investigation of Stagnation Point Injection," *Journal of Spacecraft and Rockets,* Vol. 2, No. 5, 1965, pp. 770-774.

[26] McGhee, R. J., "Effects of a Retronozzle Located at the Apex of a 140° Blunt Cone at Mach Numbers of 3.00, 4.50, and 6.00," NASA TN D-6002, January 1971.

[27] Peterson, V. L., and McKenzie, R. L., "Effects of Simulated Retrorockets on the Aerodynamic Characteristics of a Body of Revolution at Mach Numbers from 0.25 to 1.90," NASA TN D-1300, May 1962.

[28] Keyes, J. W., and Hefner, J. N., "Effect of Forward-Facing Jets on Aerodynamic Characteristics of Blunt Configurations at Mach 6," *Journal of Spacecraft and Rockets*, Vol. 4, No. 4, 1967, pp 533-534.
doi:10.2514/3.28900

[29] Daso, E. O., et al., "The Dynamics of Shock Dispersion and Interactions in Supersonic Freestreams with Counterflowing Jets," AIAA Paper 2007-1423, January 2007.

[30] McDaniel, J. C., Codoni, J. R., Reed, E. M., Alkandry, H., and Boyd, I. D., "Propulsion Deceleration Studies using Planar Laser-Induced Iodine Fluorescence and Computational Fluid Dynamics," AIAA Paper 2011-2549, May 2011.

[31] Codoni, J. R., Reed, E. M., McDaniel, J. C., Alkandry, H., and Boyd, I. D., "Investigations of Peripheral 4-Jet Sonic and Supersonic Propulsive Deceleration Jets on a Mars Science Laboratory Aeroshell," AIAA Paper 2011-1036, January 2011.

[32] Berry, S. A., et al., "Supersonic Retro-Propulsion Experimental Design for Computational Fluid Dynamics Model Validation," IEEEAC Paper 2011-1499, March 2011.

[33] Berry, S. A., Rhode, M. N., Edquist, K. T., and Player, C. J., "Supersonic Retropropulsion Experimental Results from the NASA Langley Unitary Plan Wind Tunnel," AIAA Paper 2011-3489, June 2011.

[34] Berry, S. A., Rhode, M. N., and Edquist, K. T., "Supersonic Retropropulsion Experimental Results from the NASA Ames 9- x 7-Foot Supersonic Wind Tunnel," AIIA Paper 2012-2704, June 2012.

[35] Rhode, M. N., and Oberkampf, W. L., "Estimation of Uncertainties for a Supersonic Retro-Propulsion Model Validation Experiment in a Wind Tunnel," AIAA Paper 2012-2707, June 2012.

[36] Bakhtian, N. M., and Aftosmis, M. J., "Parametric Study of Peripheral Nozzle Configurations for Supersonic Retropropulsion," *Journal of Spacecraft and Rockets*, Vol. 47, No. 6, 2010, pp. 935-950.
doi: 10.2514/1.48887

[37] Bakhtian, N. M., and Aftosmis, M. J., "Analysis of Inviscid Simulations for the Study of Supersonic Retropropulsion," AIAA Paper 2011-3194, June 2011.

[38] Trumble, K. A., et al., "An Initial Assessment of Navier-Stokes Codes Applied to Supersonic Retro-Propulsion," AIAA Paper 2010-5047, July 2010.

[39] Cordell, C. E., Jr., Clark, I. G., and Braun, R. D., "CFD Verification of Supersonic Retropropulsion for a Central and Peripheral Configuration," IEEEAC Paper 2011-1190, March 2011.

[40] Alkandry, H., Boyd, I. D., Reed, E. M., Codoni, J. R., and McDaniel, J. C., "Interactions of Single-Nozzle Supersonic Propulsive Deceleration Jets on mars Entry Aeroshells," AIAA Paper 2011-138, January 2011.

[41] Alkandry, H., Boyd, I. D., Codoni, J. R., Reed, E. M., and McDaniel, J. C., "Numerical Investigation of Multi-Nozzle Propulsive Deceleration Jets for Mars Entry Aeroshells," AIAA Paper 2011-3953, June 2011.

[42] Kleb, B., et al., "Toward Supersonic Retropropulsion CFD Validation," AIAA Paper 2011-3490, June 2011.

[43] Korzun, A. M., Clark, I. G., and Braun, R. D., "Application of a Reynolds-Averaged Navier-Stokes Approach to Supersonic Retropropulsion Flowfields," AIAA Paper 2011-3193, June 2011.

[44] Schauerhamer, D. G., et al., "Continuing Validation of Computational Fluid Dynamics for Supersonic Retropropulsion," AIAA Paper 2012-0864, January 2012.

[45] Zarchi, K. A., Schauerhamer, D. G., Kleb, W., Carlson, J.-R., and Edquist, K., "Computational Fluid Dynamics Validation and Post-test Analysis of Supersonic Retropropulsion in the Ames 9x7 Unitary Tunnel," AIAA Paper 2012-2705, June 2012.

[46] Alden, H. L., and Habert, R. H., "Gas Dynamics of High-Altitude Rocket Plumes," AFCRL-64-677, July 1964.

[47] Albini, F. A., "Approximate Computation of Underexpanded Jet Structure," *AIAA Journal*, Vol. 3, No. 8, 1965, pp. 1535-1537.
doi: 10.2514/3.3194

[48] Hubbard, E. W., "Approximate Calculation of Highly Underexpanded Jets," *AIAA Journal*, Vol. 4, No. 10, 1966, pp. 1877-1879.
doi: 10.2514/3.3809

[49] Boynton, F. P., "Highly Underexpanded Jet Structure: Exact and Approximate Calculations," *AIAA Journal,* Vol. 5, No. 9, 1967, pp. 1703-1704.
doi: 10.2514/3.4283

[50] Hill, J. A. F., and Draper, J. S., "Analytical Approximation for the Flow from a Nozzle into a Vacuum," *Journal of Spacecraft and Rockets*, Vol. 3, No. 10, 1966, pp. 1552-1554.
doi: 10.2514/3.28700

[51] Charwat, A. F., "Boundary of Underexpanded Axisymmetric Jets Issuing into Still Air," *AIAA Journal*, Vol. 2, No. 1, 1964, pp. 161-163.
doi: 10.2514/3.4159

[52] Sibulkin, M., and Gallaher, W. H., "Far-Field Approximation for a Nozzle Exhausting into a Vacuum," *AIAA Journal*, Vol. 1, No. 6, 1963, pp.1452-1453.
doi: 10.2514/3.1835

[53] Salas, M. D., "The Numerical Calculation of Inviscid Plume Flow Fields," AIAA Paper 74-523, June 1974.

[54] Abbett, M., "The Mach Disc in Underexpanded Exhaust Plumes," AIAA Paper 70-231, January 1970.

[55] Finley, P. J., "The Flow of a Jet from a Body Opposing a Supersonic Free Stream," *Journal of Fluid Mechanics*, Vol. 26, No. 2, 1966, pp. 337-368.

[56] Korzun, A. M., *Aerodynamic and Performance Characterization of Supersonic Retropropulsion for Application to Planetary Entry and Descent*, Diss, Georgia Institute of Technology, 2012.

[57] Bakhtian, N. M., and Aftosmis, M. J., "Maximum Attainable Drag Limits for Atmospheric Entry via Supersonic Retropropulsion," 8th International Planetary Probe Workshop, 2011.

[58] Skeen, M. A., *Conceptual Modeling and Analysis of Drag-Augmented Supersonic Retropropulsion for Application in Mars Entry, Descent, and Landing Vehicles*, Thesis, University of Colorado, 2013.

[59] Romeo, D. J., and Sterrett, J. R., "Flow Field for Sonic Jet Exhausting Counter to a Hypersonic Mainstream," *AIAA Journal*, Vol. 3, No. 3, 1965, pp. 544-546.

[60] Gilles, S. E., and Kallis, J. M., "Penetration Distance of Retrorocket Exhaust Plumes into an Oncoming Stream," CR TDR-269(4181)-2, USAF, 1964.

[61] Love, E. S., "A Reexamination of the Use of Simple Concepts for Predicting the Shape and Location of Detached Shock Waves," NACA TN 4170, December 1957.

[62] Van Dyke, M. D., and Gordon, H. D., "Supersonic Flow past a Family of Blunt Axisymmetric Bodies," NASA TR R-1, October 1958.

[63] Drake, B. G. (Editor), "Human Exploration of Mars, Design Reference Architecture 5.0," Mars Architecture Steering Group, NASA Headquarters, NASA SP-2009-566, July 2009.

[64] Howard, A., Stanley, D., and Williams-Byrd, J., "Mars Exploration Entry and Descent and Landing Technology Assessment Figures of Merit," AIAA Paper 2010-8676, August 2010.

[65] Zang, T. A. (Editor), "Entry, Descent, and Landing Systems Analysis Study: Phase 1 Report," EDL Systems Analysis Team, NASA TM-2010-216720, July 2010.

[66] Cianciolo, A. D., Davis, J. L., Shidner, J. D., and Powell, R. W., "Entry, Descent and Landing Systems Analysis: Exploration Class Simulation Overview and Results," AIAA Paper 2010-7970, August 2010.

[67] Korzun, A. M., and Braun, R. D., "Performance Characterization of Supersonic Retropropulsion for High-Mass Mars Entry Systems," *Journal of Spacecraft and Rockets*, Vol. 47, No. 5, 2010, pp. 836-848.
doi: 10.2514/1.49803

[68] Steinfeldt, B. A., Theisinger, J. E., Korzun, A. M., Clark, I. G., Grant, M. J., and Braun, R. D., "High Mass Mars Entry, Descent, and Landing Architecture Assessment," AIAA Paper 2009-6684, September 2009.

[69] Mandalia, A., and Braun, R. D., "Descent Phase Divert Maneuvers for Future Robotic and High Mass Mars Missions," Accepted to AIAA Science and Technology Forum and Exposition, January 2014.

[70] Christian, J. A., Wells, G., Lafleur, J., Verges, A., and Braun, R. D., "Extension of Traditional Entry, Descent, and Landing Technologies for Human Mars Exploration," *Journal of Spacecraft and Rockets*, Vol. 45, No. 1, 2008, pp. 130-141.
doi: 10.2514/1.31929

[71] Grant, M. J., Steinfeldt, B. A., Braun, R. D., and Barton, G. H., "Smart Divert: A New Entry, Descent, and Landing Architecture," AIAA Paper 2009-522, January 2009.

[72] Grenich, A. F. and Woods, W. C., "Flow Field Investigation of Atmospheric Braking for High Drag Vehicles with Forward Facing Jets," AIAA Paper 1981-293, January 1981.

[73] "Elon Musk on SpaceX's Reusable Rocket Plans," *Popular Mechanics*, February 2012.
http://www.popularmechanics.com/science/space/rockets/elon-musk-on-spacexs-reusable-rocket-plans-6653023 [retrieved October 3, 2013].

[74] Samareh, J. A., and Komar, D. R., "Parametric Mass Modeling for Mars Entry, Descent and Landing Systems Analysis Study," AIAA Paper 2011-1038, January 2011.

[75] Buck, G. M., Watkins, A. N., Danehy, P. M., Inman, J. A., Alderfer, D. W., and Dyakonov, A. A., "Experimental Measurement of RCS Jet Interaction Effects on a Capsule Entry Vehicle," AIAA Paper 2008-1229, January 2008.

[76] Danehy, P. M., Inman, J. A., Alderfer, D. W., and Buck, G. M., "Visualization of Flowfield Modification by RCS Jets on a Capsule Entry Vehicle," AIAA Paper 2008-1231, January 2008.

[77] Grover, M. R., Cichy, B. D., and Desai, P. N., "Overview of the Phoenix Entry, Descent, and Landing System Architecture," *Journal of Spacecraft and Rockets*, Vol. 48, No. 5, 2011, pp. 706-712.
doi: 10.2514/1.46548

[78] Dyakonov, A. A., Schoenenberger, M., Scallion, W. I., van Norman, J. W., Novak, L. A., and Tang, C. Y., "Aerodynamic Interference Due to MSL Reaction Control System," AIAA Paper 2009-3915, June 2009.

[79] Johansen, C. T., Danehy, P. M., Ashcraft, S. W., Bathel, B. F., Inman, J. A., and Jones, S. B., "Planar Laser-Induced Fluorescence of Mars Science Laboratory Reaction Control System Jets," *Journal of Spacecraft and Rockets*, Vol. 50, No. 4, 2013, pp. 781-792.
doi: 10.2514/1.A32214

[80] Lilley, J. S., "Performance Analysis of Scarfed Nozzles," AIAA Paper 1984-1416, June 1984.

[81] "Space Exploration Technologies Corporation – Dragon," 2012.
http://www.spacex.com/dragon.php [retrieved April 2012].

[82] "Dragon Offers Ticket to Mars," November 2011.
http://www.nature.com/news/2011/111107/full/479162a.html [retrieved April 2012].

[83] Braun, R.D., Mitcheltree, R. A., and Cheatwood, F. M., "Mars Microprobe Entry Analysis," *Proceedings from the 1997 IEEE Aerospace Conference*, February 1997.

[84] Mitcheltree, R. A., Moss, J. N., Cheatwood, F. M., Greene, F. A., and Braun, R. D., "Aerodynamics of the Mars Microprobe Entry Vehicles," AIAA Paper 1997-3658, August 1997.

[85] Tunnell, P. J., "The Static and Dynamic Stability Derivatives of a Blunt Half-Cone Entry Configuration at Mach Numbers from 0.70 to 3.50," NASA TM X-577, August 1961.

[86] Schoenenberger, M., Cheatwood, F. M., and Desai, P. N., "Static Aerodynamics of the Mars Exploration Rover Entry Capsule," AIAA Paper 2005-0056, January 2005.

[87] Grant, M. J., and Braun, R. D., "Analytic Hypersonic Aerodynamics for Conceptual Design of Entry Vehicles," AIAA Paper 2010-1212, January 2010.

[88] Grant, M. J., *Rapid Simultaneous Hypersonic Aerodynamic and Trajectory Optimization for Conceptual Design*, Diss, Georgia Institute of Technology, 2012.

[89] "FUN3D Manual," April 2012. fun3d.larc.nasa.gov [retrieved April 2012].

[90] Anderson, J. D., *Fundamentals of Aerodynamics*, 4th ed., New York: McGraw-Hill, 2007, pp. 264-273, 922. Print.